Doctoral Dissertation
Doctoral Program in Metrology (38^{th}cycle)

Advancing Optical Lattice Clocks: Accurate Measurements on a Bosonic System and Development of a Hybrid Cavity-Lattice Clock

By

Juan Pablo Salvatierra

******

Supervisor(s):
Dr. Filippo Levi, Supervisor
Dr. Marco G. Tarallo, Co-Supervisor

Doctoral Examination Committee:
Prof. Francesco Scazza, Referee, UniTS - Università di Trieste
Dr. Marco Schioppo, Referee, NPL - National Physical Laboratory

Politecnico di Torino
2026

Declaration

I hereby declare that, the contents and organization of this dissertation constitute my own original work and does not compromise in any way the rights of third parties, including those relating to the security of personal data.

Juan Pablo Salvatierra
2026

* This dissertation is presented in partial fulfillment of the requirements for **Ph.D. degree** in the Graduate School of Politecnico di Torino (ScuDo).

Abstract

This thesis presents advances on the bosonic ^{88}Sr optical lattice clock operated at INRiM, the Italian National Metrology Institute. Exploiting the recently upgraded clock laser frequency stability, and after realizing several improvements within the existing clock apparatus, this work presents a detailed characterization of the key systematic shifts affecting the clock, such as the quadratic Zeeman shift and the clock laser light shift, which are notoriously relevant for bosonic clocks. The lattice light AC Stark shift and other key systematics are also evaluated. The total fractional frequency uncertainty is evaluated to be 3.9×10^{-16}, representing a nearly two orders of magnitude improvement with respect to the previous clock uncertainty budget assessment.

Beyond its metrological evaluation, the optical lattice clock is used to investigate the interactions properties of ^{88}Sr by measuring collisional losses, decoherence, and density dependent frequency shifts in both one and two-dimensional optical lattices. Through these measurements, this work offers novel insights on the elastic interaction properties between excited-excited and ground-excited ^{88}Sr atoms, which allowed to provide estimates of the strength and sign of the relevant scattering parameters.

In the final part, this thesis introduces the design and mechanical implementation of a cavity-enhanced extension of the optical lattice clock, which represents the future direction towards INRiM strontium clock is evolving to. The proposed system combines a magic-wavelength optical lattice with a cavity-QED architecture targeting strong, homogeneous, and collective coupling on the $^1\mathrm{S}_0 \leftrightarrow {}^3\mathrm{P}_1$ intercombination transition of strontium. This configuration enables non-destructive measurement schemes and the generation of collective atomic states, such as spin-squeezed states, with the potential to reduce quantum projection noise and improve clock stability. Furthermore, the system also provides a platform for exploring collective light-

matter phenomena, such as superradiant emission on both the red cooling and clock transitions.

Contents

Chapter 1

Introduction

1.1 Atomic frequency standards

The ability to measure time with increasing precision is at the base of a vast range of science and technology, from navigation and communication systems, to tests of fundamental physics. This section introduces the fundamental operating principles of clocks and atomic frequency standards, follows their development, discusses the main factors determining the clocks performance, and provides an overview of the current status and emerging directions in the field of frequency metrology.

1.1.1 Principles of operation

A clock can be viewed as a physical system that produces a periodic signal of frequency ν_L and a mechanism that counts its cycles. Its two essential elements are the *Local Oscillator* (LO), which provides a stable oscillating signal at a frequency ν_L, and a feedback loop that references the LO to a more stable periodic phenomenon. In atomic clocks, the reference is a well defined atomic transition of frequency ν_0, which is determined by the fundamental properties of the atom in consideration, and therefore ultimately reproducible anywhere else in space and time.

In an atomic clock the stabilization works as follow: the LO frequency is compared with the atomic transition, generating a signal, typically of spectroscopic nature, that serves as a discriminator. The error signal, proportional to $\nu_L - \nu_0$,is then used to steer the LO frequency via a control loop so that the LO reproduces the atomic resonance, with additional environmental induced systematic effects that must be accounted for. This stabilized output, once corrected for the systematic effects, defines the *atomic frequency standard*, while the combination of the oscillator and counter forms the clock itself, as schematically shown in Fig. 1.1.

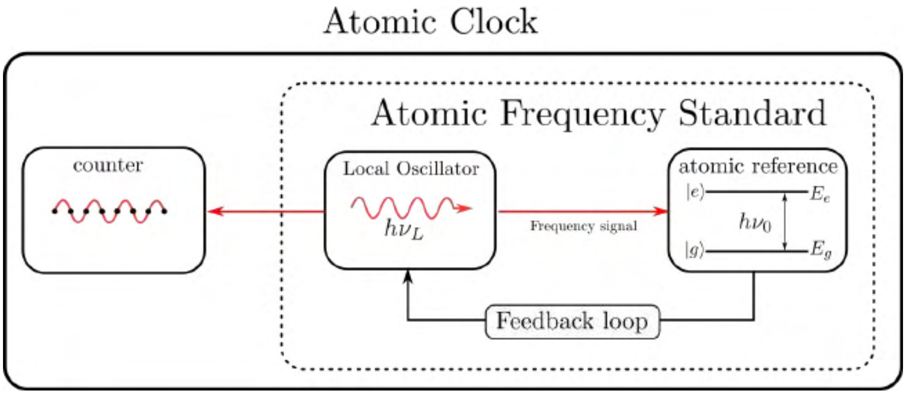

Fig. 1.1 Principle of operation of an atomic clock. The local oscillator is stabilized to an atomic transition via a frequency discriminator and feedback loop, generating a stable reference.

The clock performance is commonly characterized by two figures of merit: *stability* and *accuracy*. Stability describes the amount of noise of a clock and therefore characterize its statistical uncertainty. The stability of frequency standards, and oscillators in general, is commonly quantified by the Allan deviation $\sigma_y(\tau)$ (see for example [1]), a statistical tool that characterize the oscillator noise at different observation timescales, allowing to also distinguish between different noise processes affecting the oscillator. While in general oscillators suffer from different kind of noises, an atomic frequency standard is typically affected by white frequency noise. In this case its statistical uncertainty decreases with the measuring time τ as:

$$\sigma_y(\tau) \propto \frac{1}{\mathrm{SNR}} \frac{\Delta\nu}{\nu_0} \sqrt{\frac{T_c}{\tau}} \tag{1.1}$$

where $Q = \nu_0/\Delta\nu$ is the oscillator quality factor, SNR is the signal-to-noise ratio, and T_c is the clock cycle time. Accuracy, on the other hand, describes how closely the realized frequency faithfully reproduces the unperturbed atomic transition frequency ν_0. Therefore, it quantifies the introduced systematic environmental perturbations, for example arising from unwanted magnetic and electric fields, blackbody radiation, atomic interactions, and other technical biases.

1.1.2 Historical development

The first atomic frequency standards emerged from the combination of quantum resonance techniques and microwave technology, following the work of Rabi on atomic beam magnetic resonance [2] and Ramsey's separated oscillatory fields method [3]. The first practical caesium clock was realized by Essen and Parry in 1955 at the National Physical Laboratory [4]. This led in 1967 to the redefinition of the International System of Units (SI) second based on the ^{133}Cs ground state hyperfine transition, in the microwave region, later refined in wording in 2019 [5]:

> "The second, symbol s, is the SI unit of time. It is defined by taking the fixed numerical value of the caesium frequency $\Delta\nu_{\mathrm{Cs}}$, the unperturbed ground-state hyperfine transition frequency of the caesium-133 atom, to be 9 192 631 770 when expressed in the unit Hz, which is equal to s^{-1}."

Technological advances in laser cooling and trapping of neutral atoms [6–9] later allowed the realization of caesium fountain clocks [10, 11], which still represent the most accurate primary frequency standards, with fractional frequency uncertainties of $\simeq 2 \times 10^{-16}$ [12–16].

The explicit dependence of clock stability performances on the quality factor Q in Eq.(1.1) provides a direct motivation for pursuing the realization of reference oscillators characterized by increasingly higher frequencies. For a given linewidth $\Delta\nu$, optical transitions offer quality factors $10^4 - 10^5$ times better than microwave transitions just by the increase of the nominal frequency ν_0, and consequently a corresponding improvement in fractional frequency fluctuations. However, achieving this, required many decades devoted to overcome many technological challenges. Particularly important were the development of the appropriate coherent visible light sources and the development of ultra-stable lasers by means of high-finesse optical cavities [17–19] used as a frequency reference to reduce laser noise, which together enabled precision spectroscopy of optical transitions. The remaining problem of how to count such high frequencies, was finally overcome with the invention of the optical frequency comb in the early 2000s [20–22]. This crucial technological advancement closed the gap between the optical and microwave domains, providing a coherent link that allowed optical frequencies to be easily measured. Together, these breakthroughs laid the foundation for the development of atomic clocks based on optical transitions, the so-called *optical clocks*, which now surpass microwave standards by more than two orders of magnitude in both accuracy and stability.

1.1.3 Modern optical clocks

Optical clocks combine laser cooling, optical trapping, ultra-stable lasers, and frequency comb technologies to achieve fractional uncertainties at or below 10^{-18}, and instabilities near $10^{-17}/\sqrt{\tau}$ [23–26]. The two dominant clocks architectures are based on neutral atoms ensembles trapped in optical lattices and clocks based on single trapped ions. Each offers distinct advantages in terms of sensitivity to systematic perturbations, achievable frequency instability, and engineering complexity. Below follows a general picture of these systems, their limitations and potential new directions that the frequency metrology community is currently exploring.

Stability limits. Clock stability is fundamentally bounded by quantum projection noise (QPN), which arises due to fluctuations of the atomic population and the destructive nature of the detection process. For N uncorrelated atoms, the QPN limited fractional instability scales as [27]

$$\sigma_y(\tau) \sim \frac{1}{Q}\frac{1}{\sqrt{N}}\sqrt{\frac{T_c}{\tau}}, \tag{1.2}$$

where $Q = \nu_0/\Delta\nu$ and T_c is the cycle time. The scaling $N^{-1/2}$ represent the so-called *standard quantum limit* (SQL). Lattice clocks mitigate QPN by interrogating 10^3–10^4 atoms, while ion clocks are limited by single-ion statistics. Another limit, of technical origin and usually predominant over the QPN, is posed by the interrogation laser phase noise. Its influence is determined by the cyclic nature of the clock operation, with dead times, which results in aliasing of the clock laser noise through the Dick effect [28]. The use of exceptionally low phase noise lasers is crucial to suppress this effect. The fundamental clock laser noise floor is determined by thermal Brownian motion of the reference cavity and mirrors coatings [19, 29] and can be reduced for example by carefully engineering long reference cavities [30]. Also, the introduction of cryogenic silicon cavities and crystalline mirror coatings have reduced this thermal noise floor to the 10^{-17} level [31–33], potentially enabling interrogation times of several seconds.

Neutral atoms optical lattice clocks. The optical lattice clock, pioneered by H. Katori, confines atoms in a standing wave potential tuned to the *magic wavelength*, where the differential AC Stark shift of the clock transition, induced by the trap itself, vanishes at first order [34, 35]. As will be detailed in Sec.2.4.1, this confinement technique enables Doppler and recoil free probing of the atomic transition and thus opens the path to the realization of high accuracy optical frequency standards. Alkaline-earth-like atoms such as Sr and Yb are typically chosen for their narrow $^1S_0 \leftrightarrow {}^3P_0$ clock transitions and the robust technology available for their manipulation. Most lattice clocks employ *fermionic* isotopes: their non-zero nuclear spin naturally allows weak single photon excitation of the clock transition, which can also be probed with removed first order Zeeman shift by using spin-polarized fermions. This, also allows to benefit from Pauli suppression of s-wave interactions between atoms in the same spin state, thus partially avoiding the systematic perturbation induced by atom-atom interactions. By contrast, *bosonic* isotopes lack this suppression and their clock transitions are strictly forbidden, but can be induced by magnetic-field mixing or multi-photon schemes [36–41]. These systems are attractive due to the virtually infinite natural lifetime of the clock state, a reduced complexity in state preparation thanks to the simpler energy level structure, and the typically higher natural abundance. However, this system have been historically challenging to be operated at high accuracy levels, due to complexity introduced by the clock transition inducing technique and because of large atomic interaction effects. Typically the largest contribution of uncertainty in neutral atoms clocks originates from the blackbody radiation (BBR) shift, arising from the AC Stark shift of the atomic states induced by the thermal radiation emitted by the environment. This effect can be substantially reduced through operation in a low temperature environment[23, 42, 43], but it also typically requires in-vacuum thermometry systems and a refined modeling of the environment emissivity [44, 45]. Other significant effects include DC and AC Stark shifts from trapping and probe fields, and quadratic Zeeman shifts.

Single ion optical clocks. The first ion clocks, such as Hg^+ [46] and Ca^+, exploited a single ion Paul trap [47] to perform laser cooling to the ground state [48]. Similarly to the optical lattice, the ion trapping potential enables to probe the atomic transition with suppresed motional effects such as the Doppler and recoils shifts [46]. Several ion clocks exploit electric quadrupole (E2) clock transitions, including those in $^{171}Yb^+$, $^{88}Sr^+$, and $^{40}Ca^+$. One of the major benefits of ion-clocks lays in the sample preparation, which it does not require re-trapping the ion at every clock interrogation, making them the primary candidates for commercial solutions [49]. In terms of accuracy, these systems are inherently sensitive to the electric quadrupole shift arising from the non-zero total angular momentum of the clock states, as well as to perturbations induced by the trapping potential [50]. The Al^+ quantum-logic clock [51, 52], whose clock states present zero total angular momentum, employs a co-trapped logic ion for both sympathetic cooling and state readout of the Al^+ ion, which otherwise lack the possibility of direct laser cooling and state readout. The $^{171}Yb^+$ ion, besides the narrow E2 transition, offers the possibility to address the ultra-narrow octupole (E3) transition [24, 53] which reduces sensitivity to higher-order Stark and quadrupole shifts. Additionally, the lack of an electron in ion clocks reduces the atomic polarizability, leading to suppressed sensitivity to BBR shift. Despite the outstanding accuracy demonstrated by ion clocks, their main limitation remains the short term stability which is constrained by QPN.

Frequency comparisons and transportable systems. Phase-stabilized fiber links allows for coherent transfer of optical signals over continental scales with fractional instabilities below 10^{-19} [54, 55]. By connecting national metrology institutes across Europe, fiber links support large scale coordinated comparison campaigns to verify the agreement between independent optical clocks at unprecedented levels [56] by direct measurements of optical frequency ratios. This allows the construction of a network of optical frequencies, that can be compared independently from the caesium primary standards, and form the basis for the future "optical second" [57]. Free-space links have also been demonstrated to be effective for the local comparison of optical frequency standards between neighboring institutes [58]. In parallel, transportable optical lattice clocks [59–61] extend high-accuracy clocks comparisons beyond laboratory environments, and enable applications such as field tests of gravitational redshift [62] and chronometric geodesy [54, 60, 63, 64], probing geopotential differences of a few centimeters.

Active and Squeezed clocks. The possibility of exploiting collective atomic phenomena is being considered to overcome limitations in both the interrogation laser and the atomic system. In this sense, coupling the atomic system to an optical cavity, thus entering the cavity quantum electrodynamics (cQED) framework, has revealed to be a promising strategy. A particularly interesting phenomena is *superradiant* *lasing* [65, 66]: a regime in which a properly excited atomic ensemble behaves as single collective dipole that can coherently and collectively decay into an optical cavity mode. If the cavity loss rate allows a fast escape of the emitted photons, the coherence properties of the light will be mainly determined by the atomic transition properties rather than the optical resonator itself. This paves the way to the realization of ultra-stable laser sources directly emitting on an atomic transition with unprecedented stability, and eventually the development of optical masers [67, 68]. On the other hand, the controlled generation of many-body collective atomic states aims at overcoming the projection noise through the preparation of spin-squeezed states [69, 70], for instance via cavity feedback or cavity-aided quantum non-demolition measurements. The realization of strongly correlated atomic states on the clock two-level system, allows the population imbalance between the clock states to be determined with reduced uncertainty below the SQL [71–73] and has been recently demonstrated to provide metrological advantage in direct optical clocks comparisons [74]. Interestingly, the same cavity mediated interactions have been recently exploited the other way around: the reduced uncertainty of a collective atomic state is transferred to the interrogation laser of an optical clock, resulting an reduced phase noise that improves the optical clock performance [75].

Emerging directions. Multi-ion clocks [76] aim to combine the high accuracy provided by single ion clocks with ensemble-like stability. At a more fundamental level, there have recently been first realizations of nuclear clocks based on the ^{229}Th isomeric transition [77–79] in the vacuum ultraviolet (VUV) range, aiming to exploit its extremely high clock frequency and insensitivity of the nuclear transitions to typical systematic effects limiting clocks based on electronic transitions. Recent direct optical excitation and absolute frequency measurements at the 10^{-16} level [80, 81] mark a milestones toward the realization of nuclear clocks. Highly charged ions (HCIs) represent another frontier. Due to their high net charge and tightly bound electrons these systems present small polarizabilities, and show strong relativistic effects.This makes their clock transition extremely sensitive to potential variations of the fine structure constant, and therefore a promising tool for testing variation of fundamental constants [82–84].

1.2 Thesis overview

This thesis presents the work I carried out at INRiM, the Italian National Metrology Institute, on the bosonic ^{88}Sr optical lattice clock. The construction of the clock apparatus began as a collaboration between INRiM, UNITN, and CNR-INO in 2017 [85], and its first accuracy budget evaluation in 2021-2022 determined a fractional frequency uncertainty of 2×10^{-14} [86].

One of the aims of my work in this context was improving the clock accuracy budget targeting a total fractional frequency uncertainty at or below the 10^{-15} level, and in parallel study the atom-atom interaction properties of ^{88}Sr in an optical lattice. In particular, by leveraging the ^{88}Sr notoriously strong density dependent effects on the clock transition, I was able to gain new insights on the relevant elastic scattering parameters of this isotope. Beyond this, part of this work aimed at advancing and finalizing the design phase of the experiment upgrade, which aims at developing an hybrid cavity-lattice clock to explore the possible metrological advantages introduced by the interactions of atoms with an optical cavity.

The thesis is organized as follows:

Chapter 2 introduces fundamental concepts about strontium atoms trapped in optical lattices and provides the physical framework for understanding and explaining the experimental results that follow.

Chapter 3 describes the experimental apparatus of the ^{88}Sr optical lattice clock highlighting the major contributions of this work, ranging from the installation of new lasers sources to improvements on the experiment control system, which eventually led to an overall enhancement of the robustness and reliability of the setup.

Chapter 4 presents the detailed evaluation of the key systematic frequency shifts affecting the INRiM ^{88}Sr optical lattice clock. Particular focus is posed on the control and evaluation of the quadratic Zeeman shift and the clock laser light shift, which are the major effects. Additional systematic effects such as the lattice light AC Stark shift and the blackbody radiation shift are also discussed.

Chapter 5 is devoted to the investigation of the interaction properties of ^{88}Sr confined in harmonic potentials. Measurements of inelastic losses, decoherence, and density-dependent frequency shifts are presented in both one and two dimensional optical lattices configurations. The experimental results provide insight into the relevant s-wave scattering lengths.

Chapter 6 introduces the concept and design of the hybrid cavity-lattice clock. The chapter outlines the motivation, describes the architecture of the system, and present the mechanical design of the main in-vacuum components.

Chapter 2

Ultracold strontium in optical lattices

Strontium (Sr) is a chemical element with atomic number Z=38 belonging to group II of the periodic table, it is thus an alkaline-earth atom (AEA) and has two electrons in its outermost shell. It has four stable isotopes: ^{84}Sr,^{86}Sr,^{87}Sr,^{88}Sr which key properties are reported in Tab.2.1. Letting A be the atomic mass number, the total number of fermions that compose an atom is N = A+Z, therefore all the strontium isotopes are bosonic particles beside ^{87}Sr, for which N is odd. The A = 87 isotope is thus fermionic and, according to the nuclear shell model, has a large nuclear spin $I = 9/2$ coming from the unpaired neutron in the orbital $1g_{9/2}$ (see Refs. [87, 88]). In contrast, all the other isotopes have paired nucleons, resulting in a total nuclear spin $I = 0$ and lack of hyperfine structure.

Table 2.1 Mass, natural abundance, and nuclear spin of stable Sr isotopes extracted from [89]. $\mu_N = 5.0507837393(16) \times 10^{-27}$ J/T is the nuclear magneton, and $\mathrm{u} = 1.66053906892(52) \times 10^{-27}$ kg is the atomic mass unit.

Isotope	Mass / u	Abundance / %	Nuclear Spin	μ/μ_N
^{84}Sr	83.913425(3)	0.56(1)	0	0
^{86}Sr	85.9092602(12)	9.86(1)	0	0
^{87}Sr	86.908871(12)	7.00(1)	9/2	$-1.0936030(13)$
^{88}Sr	87.9056121(12)	82.58(1)	0	0

2.1 Relevant transitions and properties

The distinctive electronic structure of strontium is one of the primary reasons it has become a central element in the development of atomic clocks [35, 90–93], quantum degenerate gases[94–96], neutral-atoms based quantum computation and simulation [97–99]. Because strontium has two valence electrons, its excited states are organized into singlet (total spin $S = 0$) and triplet (total spin $S = 1$) states. This structure supports a strong electric-dipole (E1) transition within the singlet states, which is used for first stage Doppler cooling [100] and atomic population detection, as well as a set of intercombination transitions that connect the singlet and the lowest energy triplet manifold. These latter transitions are nominally spin-forbidden but can become weakly allowed through spin-orbit coupling or hyperfine mixing, providing exceptionally narrow transitions that enable narrow-line laser cooling [101–103] and serve as excellent candidates for optical clock transitions.

These properties are common to all group-II elements, yet they are not exclusive to them. Several other two-electrons systems, including Yb, Cd, and Hg, share a similar electronic structure and are usually referred to as alkaline-earth-like atoms. These systems play a similarly important role in precision metrology and emerging quantum technologies. A comprehensive overview of the physics of such atoms, with particular emphasis on strontium, is given in Ref. [104].

Most of the following information about the cooling and repumping transitions is relevant for both bosonic and fermionic strontium atoms, with additional minor complications for the latter due to the presence of hyperfine structure. Figure 2.1 shows a partial energy levels diagram for ^{88}Sr and highlights the transitions relevant to this work.

Laser cooling transitions. The strong E1 transition $5s^2\,{}^1\mathrm{S}_0 \leftrightarrow 5s5p\,{}^1\mathrm{P}_1$ at 461 nm is used to drive the first magneto-optical-trap (MOT) stage, commonly referred to as the "blue MOT". Thanks to the relatively short lifetime of the $5s5p\,{}^1\mathrm{P}_1$ state [105], this transition supports high photon-scattering rates and is therefore well suited for capturing the fast atoms emerging from an oven. For the same reason, the achievable temperature is limited to a few mK. To reach the μK temperature range, a second MOT stage, the "red MOT", is performed by addressing the $5s^2\,{}^1\mathrm{S}_0 \leftrightarrow 5s5p\,{}^3\mathrm{P}_1$ transition, which has a natural linewidth of only 7.5 kHz. Operating on such a narrow

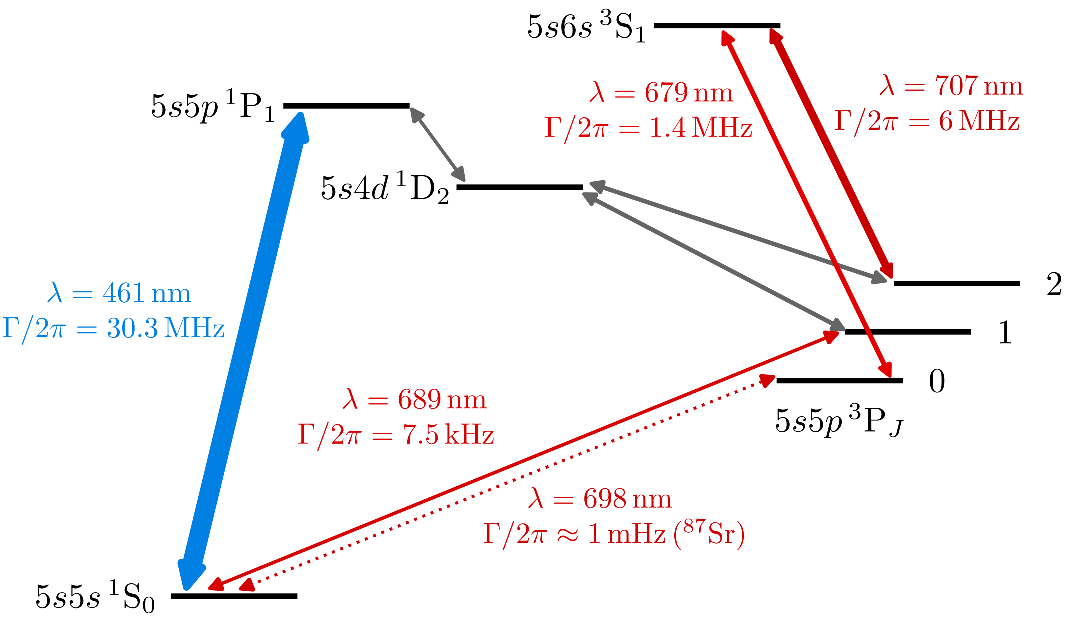

Fig. 2.1 Simplified energy levels diagram for ^{88}Sr with the transitions relevant for this work. Transitions linewidths are estimated from lifetime measurements [105–110].

line makes the energy scale of the cooling process fundamentally different from that of broad-line MOTs, and, most importantly, tunable through the laser detuning Δ and the trap beams intensity. By appropriately varying these parameters, the system can be driven from a Doppler-dominated regime into one where the photon-recoil energy sets the energy scale. In this regime, the cooling dynamics become sensitive to individual absorption-emission events, and temperatures can be pushed below the single-photon recoil limit, down to 200 nK [102, 103].

Repumping transitions. The $5s^2\,^1S_0 \leftrightarrow 5s5p\,^1P_1$ transition is not perfectly closed: a small fraction of the atoms (branching ratio $\sim 1:50000$) decays from $5s5p\,^1P_1$ into the $5s4d\,^1D_2$ state and subsequently into $5s5p\,^3P_1$ and $5s5p\,^3P_2$, limiting the MOT lifetime and loading capacity. Atoms that decay into $5s5p\,^3P_1$ rapidly rejoin the cooling cycle [107], whereas those that fall into the ultra-long-lived $5s5p\,^3P_2$ state are effectively lost, as their dominant decay channel is an extremely weak magnetic-octupole (M2) transition directly back to the ground state [111, 112]. To close the $5s^2\,^1S_0 \leftrightarrow 5s5p\,^1P_1$ a repumping scheme is required to bring the $5s5p\,^3P_2$ population back to $5s^2\,^1S_0$.

The most widespread approach employs 707 nm and 679 nm light to address the E1 transitions $5s5p\,^3\mathrm{P}_2 \leftrightarrow 5s6s\,^3\mathrm{S}_1$ and $5s5p\,^3\mathrm{P}_0 \leftrightarrow 5s6s\,^3\mathrm{S}_1$, respectively, ensuring that atoms eventually return through $5s5p\,^3\mathrm{P}_1$ to the ground state. Several alternative repumping schemes have been proposed and demonstrated [113–117], most of which rely on a single laser and suffer from residual loss channels that fail to fully close the cooling cycle. In contrast, a recent study [118] shows that directly exciting the $5s4d\,^1\mathrm{D}_2 \leftrightarrow 5s8p\,^1\mathrm{P}_1$ transition at 448 nm completely eliminates decay into the metastable $5s5p\,^3\mathrm{P}$ manifold, providing an effective and fully closed single-laser repumping solution. However since detecting the $5s5p\,^3\mathrm{P}_0$ state population is a fundamental step in the atomic clock operation, and there are no single-laser effective repumping schemes to fully drive the $5s5p\,^3\mathrm{P}_0$ atoms down to the ground state, the standard combination of 707 nm and 679 nm repumpers is usually chosen. Another possibility could be to use the 707 nm in combination with a 2.6 µm laser addressing the $^3\mathrm{P}_0 \leftrightarrow {}^3\mathrm{D}_1$ transition [119], which therefore plays an equivalent role of the 679 nm laser. In this work we use the 707 nm and 679 nm repumping lasers almost exclusively for the clock state population detection and not for MOT number of atom enhancement.

Clock transition. Finally, the $5s^2\,^1\mathrm{S}_0 \leftrightarrow 5s5p\,^3\mathrm{P}_0$ is the clock transition, and the $5s5p\,^3\mathrm{P}_0$ is the clock state. For all the bosonic isotopes of Sr, and in general of all the AEAs, this transition is completely forbidden since the clock state is not affected by spin-orbit coupling and there is no other mixing mechanism that opens clock state E1 decay channels to the ground state. The only decay path remains a E1M1 two photon process with a predicted natural linewidth $\Gamma = 2\pi \times 0.88$ pHz ($\tau \simeq 5.7 \times 10^3$ years) [112]. However, the transition can be induced by external fields, as will be discussed in Sec. 2.2.
In the fermionic isotope ^{87}Sr, hyperfine mixing, induced by the presence of a non-zero nuclear magnetic moment, opens a weak E1 coupling channel between the clock states that results in a finite lifetime of the $5s5p\,^3\mathrm{P}_0$ state corresponding to a measured natural linewidth of $\gamma = 1.35(3)$ mHz [109, 110].

Both ^{88}Sr and ^{87}Sr clock transition frequencies are part of the accepted frequency standards as secondary representation of the second (SRS) by the International Committee for Weights and Measures (CIPM). The recommended values have been updated in 2021 to:

$$\nu_{^{88}Sr} = 429\,228\,066\,418\,007.01(8)\,\mathrm{Hz}$$
$$\nu_{^{87}Sr} = 429\,228\,004\,229\,872.99(8)\,\mathrm{Hz}.$$

For ^{88}Sr the result arise from 3 absolute frequency measurements and 2 optical frequency ratios, while for ^{87}Sr 15 absolute frequency measurements and 25 optical frequency ratios were considered [120]. The uncertainty for these value is limited by the current $\sim 2 \times 10^{-16}$ accuracy of the primary Cs frequency standards.

2.2 Addressing the clock transition in ^{88}Sr

How to induce a controlled and finite lifetime to the ^{3}P$_0$ state in bosonic alkaline-earth atoms, while keeping the perturbation on the system low, was an active research topic during the early stages of optical clocks development around 20 years ago. Several proposals were introduced, mainly by the JILA and NIST groups [36–41], and mostly involving multi-photon coupling schemes to mix the ^{3}P$_0$ with a combination of ^{1}P$_1$, ^{3}P$_1$, and ^{3}P$_2$ states. A thorough discussion of some of these methods and their implications for clock accuracy can be found in [121]. To the best of my knowledge most of these approaches remain experimentally unrealized. Only very recently, in 2025, three-photon excitation of the $5s^2\,{}^1\mathrm{S}_0 \leftrightarrow 5s5p\,{}^3\mathrm{P}_0$ has been demonstrated in ^{88}Sr [122, 123] using schemes similar to the one originally proposed in [37]. The primary reason for the limited experimental adoption of the early proposed multi-photon schemes is practicality. This is also why the *magnetic induced spectroscopy* (MIS) technique proposed in [38] and first experimentally demonstrated with ^{174}Yb atoms [124], prevailed among the others, despite not being ideal in terms of accuracy implications [121]. Beside bosonic strontium [125] and ytterbium [124], optical clocks with bosonic ^{24}Mg [126], and more recently ^{198}Hg [127] have been realized.

In our clock we also use the MIS mixing technique, which is detailed in [38] where also the results of calculations of experimentally relevant parameters for Sr, Yb, Ca, and Mg are given. Here the idea behind MIS technique and relevant implications on the introduced clock transitions shifts are reported.

Magnetic field induced spectroscopy. The technique requires applying a static magnetic field $\vec{B}$ that couples the ^{3}P$_0$ and ^{3}P$_1$ states with the matrix element $\Omega_B = \langle {}^3P_0 \mid \hat{\mu} \cdot \vec{B} | {}^3P_1 \rangle / \hbar$ where $\hat{\mu}$ is the magnetic-dipole operator. Letting Δ_{10} denote the fine-structure splitting between ^{3}P$_0$ and ^{3}P$_1$, the new clock state acquires a ^{3}P$_1$ component weighted by Ω_B/Δ_{10} [38], which easily satisfies $|\Omega_B/\Delta_{10}| \ll 1$ for practical values of the applied field. In this configuration, the new state can decay to the ground state ^{1}S$_0$ via a single-photon emission.

When driving the system with a linearly polarized optical field $\vec{E}$ (i.e., the clock laser), the resulting Rabi frequency depends linearly on the applied fields and can be expressed as [38]:

$$\Omega = \frac{\langle||d||\rangle\langle||\mu||\rangle}{\hbar^2 \Delta_{10}} \vec{E} \cdot \vec{B} = 2\pi \times \alpha \sqrt{I_c} |\vec{B}| \cos\theta \tag{2.1}$$

where $\langle||d||\rangle$ and $\langle||\mu||\rangle$ are respectively the reduced matrix elements of the electric and magnetic dipole moments, θ is the angle between the applied electric and magnetic fields, I is the clock laser intensity, and α characterizes the induced Rabi frequency per unit of each field. The value of α for ^{88}Sr is estimated as $\alpha = 198\,\mathrm{Hz}/(T\sqrt{\mathrm{mW/cm^2}})$ [38]. For reference, assuming an applied magnetic field of 1 mT, a clock laser intensity of approximately 25.5 mW cm^{-2} is required to achieve Rabi frequencies of the order of 1 Hz, comparable to those typically employed in fermionic clocks. In an optical lattice clock, a natural choice is to align the fields parallel to each other to maximize the coupling ($\cos\theta = 1$) while keeping them orthogonal to the lattice axis.

Both the clock laser electric field and the applied bias magnetic field introduce systematic frequency shifts to the unperturbed clock transition [38]:

$$\Delta_B = \beta |\vec{B}|^2, \tag{2.2a}$$

$$\Delta_L = \kappa I_c, \tag{2.2b}$$

where the coefficients β and κ depend on the atomic species. Notably, both shifts are quadratic in the respective fields although the mixing strength increases linearly with them. For ^{88}Sr, the coefficient in Eq.(2.2b) is calculated in [38] as $\kappa = -18\,\mathrm{mHz\,mW^{-1}\,cm^2}$ with an estimated uncertainty of a few $\mathrm{mHz\,mW^{-1}\,cm^2}$ (not better specified). From a practical perspective, this is not a strong limitation, since the shift can be evaluated using the measured optical power and extrapolated to the desired intensity. Precisely measuring κ, however, is experimentally challenging, as it requires accurate knowledge of the laser beam geometry, polarization, and trap-related inhomogeneities.

The quadratic Zeeman coefficient for ^{88}Sr is estimated in [38] as $\beta_{88} = -23.3\,\mathrm{MHz\,T^{-2}}$. The only experimental measurement on ^{88}Sr was performed at LNE-SYRTE [128], yielding $\beta_{88} = -23.3(5)\,\mathrm{MHz\,T^{-2}}$. More recently, an *ab initio* calculation [129] provided updated second-order Zeeman coefficients for ^{88}Sr and for all the possible transitions $|^1\mathrm{S}_0, F = 9/2, m_F\rangle \leftrightarrow |^3\mathrm{P}_0, F = 9/2, m_F\rangle$ in ^{87}Sr. The results yeld equal values when considering $m_F = \pm 9/2$ in ^{87}Sr: $\beta_{88} = \beta_{87}^{\pm 9/2} = -23.38(5)\,\mathrm{MHz\,T^{-2}}$, and show excellent agreement with the currently most precise measurement ($\beta_{87}^{\pm 9/2} = -23.38(3)\,\mathrm{MHz\,T^{-2}}$) [25] on ^{87}Sr.

2.3 Optical dipole potentials

Optical lattices are a particular case of a wider class of neutral atoms traps generally named *optical dipole traps* [130] (ODT), since the trapping mechanism relies on the dipole interaction of atoms with far-detuned laser light with respect to the main dipole allowed transition, which for strontium is the $5s^2\,{}^1\mathrm{S}_0 \leftrightarrow 5s5p\,{}^1\mathrm{P}_1$. A far-detuned beam, with intensity $I(\mathbf{r})$, allows to suppress the dissipative component $F_{\mathrm{diss}} \propto I(\vec{r})$ [131] of the resulting force that is exploited for example in the production of MOTs and optical molasses, thus leaving the main force component to be the reactive one $F_{\mathrm{reac}} \propto -\nabla I(\mathbf{r})$. The spatial intensity $I(\mathbf{r})$ can be interpreted as a nearly conservative potential U as [130]

$$U = -\frac{1}{2\varepsilon_0 c}\mathrm{Re}\left[\alpha(\omega)\right] I, \tag{2.3}$$

that can be tailored by choosing the involved laser beams shape, crossing angles, and relative phase. In Eq. (2.3) α is the induced complex dynamic polarizability, which depends on the radiation frequency ω, c is the vacuum speed of light and ε_0 is the vacuum permittivity.

The electric field spatial distribution of single laser beam of wavevector $\mathbf{k} = k\hat{\mathbf{k}} = 2\pi/\lambda\hat{\mathbf{k}} = \omega c\hat{\mathbf{k}}$, with polarization $\hat{\mathbf{e}}$ is usually described by the fundamental TEM$_{00}$

transverse Gaussian mode with cylindrical symmetry

$$\mathbf{E}(\rho,\zeta,t)=\hat{\mathbf{e}}\frac{E_0}{2}\frac{w_0}{w(\zeta)}\exp\left(\frac{-\rho^2}{w^2(\zeta)}\right)\exp\left[-i\left(k\zeta+k\frac{\rho^2}{2R(\zeta)}-\psi(\zeta)+\omega t\right)\right]+c.c. \tag{2.4}$$

where the generalized axial coordinate ζ and radial coordinate ρ are derived from the spatial coordinates $\mathbf{r}=(x,y,z)$, via $\zeta=\hat{\mathbf{k}}\cdot\mathbf{r}$ and $\rho=|\mathbf{r}-(\hat{\mathbf{k}}\cdot\mathbf{r})\hat{\mathbf{k}}|$. Here, w_0 is the beam waist and $z_R=\pi w_0^2/\lambda$ is the corresponding Rayleigh range. The quantity $w(\zeta)=w_0\sqrt{1+(\zeta/z_R)^2}$ is the beam radius, describing how the Gaussian beam expands due to diffraction, $R(\zeta)=\zeta\left[1+(z_R/\zeta)^2\right]$ is the radius of curvature of the phase front, which is infinite at the waist and becomes approximately spherical far from it, and $\psi(\zeta)=\arctan(\zeta/z_R)$ is the Gouy phase, an additional phase shift acquired by the beam as it propagates through the focus. The corresponding intensity is thus

$$I(\rho,\zeta)=I_0\frac{w_0^2}{w^2(\zeta)}\exp\left(\frac{-2\rho^2}{w^2(\zeta)}\right)\qquad ,I_0=\frac{1}{2}c\varepsilon_0E_0^2=\frac{2P_0}{\pi w_0^2} \tag{2.5}$$

where P_0 is the total power of the laser beam.

Now, starting from Eq. (2.3) and Eq. (2.5) we can summarize the properties of a few pedagogical cases that will be useful during this work.

2.3.1 Gravitationally sagged optical dipole trap

Let's consider a single Gaussian beam with waist w_0, propagating along the z direction, and let gravity act along the y direction through the gravitational acceleration g. The total potential experienced by an atom with mass m will then be

$$U(\mathbf{r})=-U_0\left(\frac{w_0}{w(z)}\right)^2\exp\left(-2\frac{(x^2+y^2)}{w^2(z)}\right)+mgy, \tag{2.6}$$

where U_0 is the peak trap depth. The major confining action of U comes from the exponential gradient of the radial intensity profile, while along the propagation direction the confinement is generally too weak unless the beam is extremely tightly focused as in an optical tweezer ($w_0\simeq\lambda$). In the absence of the gravitational term, the potential in Eq. (2.6) produces near-harmonic confinement in the x and y

directions with the characteristic frequency

$$\omega_{0r}^2 = \omega_x^2 = \omega_y^2 = \frac{4U_0}{mw_0^2}\,. \tag{2.7}$$

The presence of gravity introduce a minimum trap depth condition that can be evaluated through $max(F_y) \geq mg$, and reduces the effective radial trap frequencies by modifying the potential curvature. The maximum force that U can produce will be of course at $x = z = 0$ and by imposing $\partial_y F_y = 0$ one find that $y_{max} = w_0/2$, and the minimum trap depth as

$$U_{0,\mathrm{min}} = \frac{\sqrt{e}}{2} mgw_0 \approx 86 \times \left(\frac{w_0}{\mu\mathrm{m}}\right) \mathrm{nK}, \tag{2.8}$$

using the mass of ^{88}Sr. Also, the presence of the linear term in y shifts the equilibrium position defined by $\partial_y U = 0$ which in the vicinity of the waist and assuming small sag gives

$$y_{\mathrm{eq}} \simeq -\frac{mgw_0^2}{4U_0}. \tag{2.9}$$

However, when $U_0 \rightarrow U_{0,min}$ Eq. (2.9) fails and results in up to 40% difference from a numerical evaluation of $\partial_y U = 0$. A more general solution can be found for the equilibrium position y_{eq} of the potential $U(0,y,0)$ by solving the transcendental equation

$$\left.\frac{\partial U}{\partial y}\right|_{(0,y,0)} = \frac{4U_0}{w_0^2} y e^{-2y^2/w_0^2} + mg = 0\,. \tag{2.10}$$

Substituting $u = -2y^2/w_0^2$ and squaring, Eq. (2.10) can be rewritten in the form

$$2ue^{2u} = -\left(\frac{mgw_0}{2U_0}\right)^2 = -\beta^2\,, \tag{2.11}$$

which can be solved in terms of the Lambert W function [132], obtaining for the equilibrium position

$$y_{\mathrm{eq}} = \frac{w_0}{2}\mathrm{Re}\left[i\sqrt{W_0\left(-\beta^2\right)}\right]\,, \tag{2.12}$$

where W_0 is the principal branch of the Lambert W function, and the complex square root cut is taken along the negative real axis. The expression found for y_{eq} holds for $\beta^2 \geq 1/e$, which leads to the same minimum trap depth condition result of Eq. (2.8). Using Eq. (2.12) realistic values of the trap frequencies ω_x and ω_y can be computed evaluating $m\omega_i^2 = \partial_i^2 U\big|_{(0,y_{\text{eq}},0)}$:

$$\begin{aligned}
\omega_x^2 &= \frac{4U_0}{mw_0^2} e^{-2y_{\text{eq}}^2/w_0^2} = \omega_{0r}^2 e^{-2y_{\text{eq}}^2/w_0^2} \\
\omega_y^2 &= \frac{4U_0}{mw_0^2} e^{-2y_{\text{eq}}^2/w_0^2} \left(1 - \frac{2}{w_0^2} y_{\text{eq}}^2\right) = \omega_x^2 \left(1 - \frac{2}{w_0^2} y_{\text{eq}}^2\right)
\end{aligned} \tag{2.13}$$

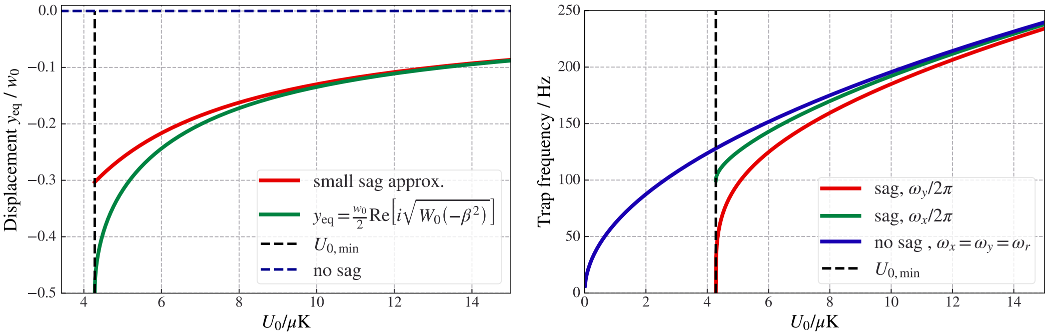

Fig. 2.2 Equilibrium position (left) and trap frequencies (right) of a dipole trap subject to gravitational sag. The beam is here assumed to have w_0 =50 µm. See main text for details.

A graphical representation of the effect of gravitational sag is reported in Fig. 2.2. These effects must be properly accounted for if for example one desires to estimate the beam waist via trap frequency measurements.

2.3.2 The optical lattice

The confinement provided by single beam optical dipole traps is relatively weak and covers a space region which scale is set by the beam waist and its Rayleigh range. This, as will be shown in the next section, is not enough to provide a metrologically helpful confinement to perform Doppler and recoil free spectroscopy of narrow atomic transitions. A straight forward way to realize tighter and more localized confinement it to exploit coherent superposition of fields described by Eq. (2.4), obtaining tight and periodic potentials where the scale is dominated by the wavelength: an *optical lattice*.

The standard way to realize an optical lattice is by taking two counter-propagating Gaussian laser beams (usually achieved with a back-reflector), in this way the optical potential (assuming perfectly equal beams propagating along the z-axis and no losses) is obtained via Eq. (2.3) and Eq. (2.4)

$$U(r,z) = -U_0 \left(\frac{w_0}{w(z)} \right)^2 e^{-\frac{2r^2}{w^2(z)}} \cos^2 \left(kz + k\frac{r^2}{2R(z)} - \psi(z) \right), \tag{2.14}$$

which can be expanded for $r \ll w_0$ and $z \ll z_R$, to better highlight its harmonic properties near the minima, as

$$\begin{aligned} U(r,z) &\simeq -U_0 \cos^2(kz) \left(1 - 2\frac{r^2}{w_0^2} - \frac{z^2}{z_R^2} \right) \\ &\simeq -U_0 \left(1 - k^2 z^2 - \frac{2}{w_0^2} r^2 \right). \end{aligned} \tag{2.15}$$

Thus, the potential is formed by a series of wells with periodicity $\lambda/2$ and atoms confined at the minima behave as harmonic oscillators with trap frequencies

$$\nu_z = \frac{1}{2\pi}\sqrt{\frac{2k^2U_0}{m}} = \frac{2}{h}\sqrt{U_0 E_r}\,,\ \nu_r = \frac{1}{2\pi}\sqrt{\frac{4U_0}{mw_0^2}} = \frac{\lambda}{\sqrt{2}\pi w_0}\nu_z\,, \tag{2.16}$$

where $E_r = (\hbar k)^2/2m = h\nu_r \simeq h \times 3426\,\mathrm{Hz}$ is the recoil energy for strontium trapped at 813.4 nm. If the lattice is horizontally oriented, the gravitational potential affects in the same way the radial trap frequencies, which can still be calculated via Eq. (2.13). However, the minimum trap depth condition will require four time less power (neglecting losses) if a single bakcreflected beam is used to create the lattice. On the other hand, the axial confinement is not particularly sensitive to the lattice orientation.

2.3.3 2D lattice geometries

Combining an increasing number of beams and tweaking their relative orientation allows to engineer the trap geometry and dimensionality, examples of two dimensional traps are depicted in Fig. 2.3.

The lattice geometry discussed until now is commonly referred to as 1D lattice, as the strong wavelength-scale confinement only happens along one direction. Higher dimensionality lattices can be realized by providing the same tight confinement over more spatial directions, and can be helpful in studying and eventually suppress the atom-atom interaction that happens within a single lattice site [93, 133, 134]. Possible 2D lattices configurations are depicted in Fig. 2.3a and Fig. 2.3b, which shows the interference patterns arising from optical latteces crossing at a 90° angle. In Fig. 2.3b, the two lattice are polarized along the same direction and assumed perfectly in phase. The parallel polarization and the absence of detuning ensure a full interference pattern $I \propto \cos^2(kx)\cos^2(ky)$ that it is difficult to maintain in free-space, indeed similar potentials are usually realized by means of optical resonators (see for example [135, 136]). Finally, Fig. 2.3a depicts the situation of our experiment 2D lattice configuration, where we overlap two orthogonal lattices that are non interfering and have a large detuning. The two lattices in our experiment have also different waists w_{0x} and w_{0y}, and hare intensity unbalanced, thus resulting in individual peak potential depths U_{0x} and U_{0y}. Since the two lattice are non interfering the total potential near the crossing points is approximated to

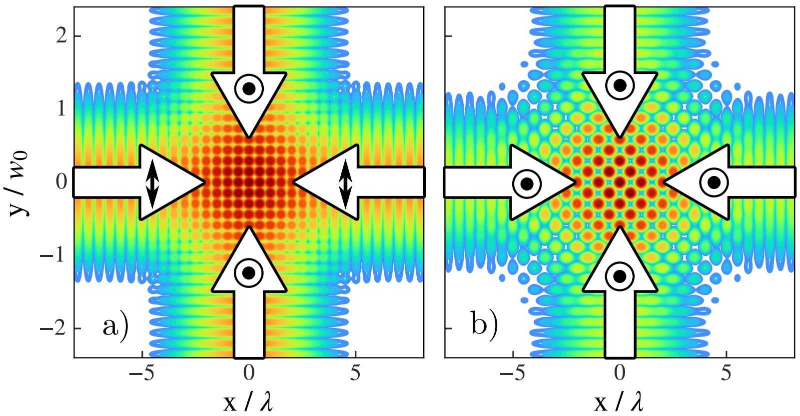

Fig. 2.3 a) 2D lattice intensity pattern from two overlapped orthogonal non interfering lattices. b) same as a) but with interfering lattices.

$$U_{2D} = U_x + U_y \simeq \left(U_{0x}k^2 + \frac{2U_{0y}}{w_{0y}^2} \right) x^2 + \left(U_{0y}k^2 + \frac{2U_{0x}}{w_{0x}^2} \right) y^2 + \left(\frac{2U_{0x}}{w_{0x}^2} + \frac{2U_{0y}}{w_{0y}^2} \right) z^2 \tag{2.17}$$

with trap frequencies given by the quadrature sum of each lattice trap frequency along a given direction

$$
\begin{aligned}
\omega_x &= \sqrt{\frac{2U_{0x}k^2}{m} + \frac{4U_{0y}}{mw_{0y}^2}} = \sqrt{\omega_{ax,x}^2 + \omega_{r,y}^2} \\
\omega_y &= \sqrt{\frac{2U_{0y}k^2}{m} + \frac{4U_{0x}}{mw_{0x}^2}} = \sqrt{\omega_{ax,y}^2 + \omega_{r,x}^2} \\
\omega_z &= \sqrt{\frac{4U_{0x}}{mw_{0x}^2} + \frac{4U_{0y}}{mw_{0y}^2}} = \sqrt{\omega_{r,x}^2 + \omega_{r,y}^2}
\end{aligned}
\tag{2.18}
$$

where $\omega_{ax,i}$ ($\omega_{r,i}$) is the axial (radial) trap frequency of the single lattice which axial direction is i.

2.4 Clock spectroscopy in an optical lattice

This section briefly outlines the benefits of confining atoms in an harmonic potential to perform high accuracy spectroscopy of atomic transitions, and introduces concepts that will be useful in the chapters that follow.

A simple argument to start with is considering the light absorption process by an atom in free space, whose unperturbed resonance is at ω_0, moving with velocity $\mathbf{v}$. Denoting with $\mathbf{k}$ the wavevector of the electromagnetic radiation interacting with the atoms, the absorption of light happens at the radiation frequency

$$
\omega_{abs} = \omega_0 + \frac{\hbar k^2}{2M} + \mathbf{k} \cdot \mathbf{v} - \frac{1}{2}\frac{v^2}{c^2}\omega_0 \tag{2.19}
$$

where M is the atomic mass, c is the speed of light, and $\hbar$ is the reduced Planck constant. From Eq.2.19 the atomic transition appears shifted by two additional terms related to motion: the first and second order Doppler shifts given by $\mathbf{k} \cdot \mathbf{v} - \frac{1}{2}\frac{v^2}{c^2}\omega_0$ and the recoil shift given by $\hbar k^2/2M$.

Cooling atoms and confining them in a small region of space helps to suppress these motion-related shifts, in particular the first order Doppler and the recoil shifts, by reaching the so-called *Lambd-Dicke regime* [137]. Residual second order Doppler shift remains due to the finite temperature of the atomic system.

2.4.1 Lamb-Dicke regime

Atoms trapped in a 1D lattice potential described by Eq. (2.14) experience a spatially dependent light shift that modifies the clock states as depicted in Fig. 2.4. In the vicinity of a lattice site minima, the atomic motion is quantized with characteristic frequencies given by Eq. (2.16), and consequently an axial occupation number n_z and radial occupation number n_r might be introduced in the picture. The clock laser, in first approximation described as a plane wave $e^{i(k_c z-\omega_c t)}$ propagates along the lattice axis, making the axial motion dynamics to be the dominant one in the description of the atom-light interaction. If the characteristic spatial extension of the atomic wavefunction $z_0 = \sqrt{\hbar/2m\omega_z}$ along the probing direction is much smaller then the probe laser wavelength, the system is in the strong-binding or Lamb-Dicke regime [137, 138]. Introducing the Lamb-Dicke parameter $\eta = k_c z_0 \ll 1$ and the harmonic oscillator ladder operators $\hat{a}$ and $\hat{a}^\dagger$, we can see how in this regime the clock laser coupling to the motional states, described by the momentum translation operator $e^{ik_c\hat{z}} = e^{i\eta(\hat{a}+\hat{a}^\dagger)}$, is suppressed. The clock laser mediated transition probability between motional states $n_z = n$ and $n_z' = m$ can be expressed as

$$\begin{aligned} A_{mn} &\equiv |\langle m| e^{i\eta(\hat{a}+\hat{a}^\dagger)} |n\rangle|^2 \\ &\simeq |\langle m|\mathbb{I}|n\rangle + i\eta\,\langle m|(\hat{a}+\hat{a}^\dagger)|n\rangle + O(\eta^2)|^2 \\ &\simeq \delta_{m,n} + \eta^2\,[n\delta_{m,n-1} + (n+1)\delta_{m,n+1}] \end{aligned} \tag{2.20}$$

where δ_{ij} id the Kronecker delta. Thus, three main absorption features are present: the Doppler-free pure electronic ($\Delta n_z = 0$) clock transition, and two motional sidebands corresponding to transitions where the clock laser induce the gain or loss of a vibrational quanta ($\Delta n_z = \pm 1$). This single characteristic is at the base of the pioneering improvement that optical lattices brought to the frequency metrology field, allowing to probe narrow atomic transitions with suppressed Doppler, recoil and line pulling effects. A comprehensive description of the clock laser-atom interaction dynamics in this context is provided in [139]. Here the authors also show how the shape and intensity of the observed sidebands are valuable tool to extract information about the axial and radial atomic temperatures T_z and T_r inside the lattice.

Without providing details on the derivation, here we just report the description we use in our experiment to handle the sidebands excitation spectra in terms of the

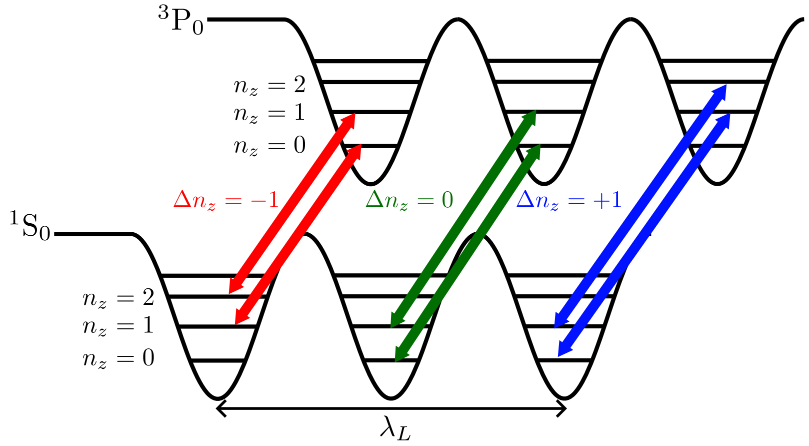

Fig. 2.4 Lamb-Dicke regime in a 1D optical lattice. The clock transition is purely electronic and compose by all the possible transitions between vibrational levels with the same quantum number n_z. The other main features of the excitation spectra are the red ($\Delta n_z = -1$) and blue ($\Delta n_z = +1$) sidebands, corresponding to all the possible transitions were a vibrational quanta is lost (red) or gained (blue).

absorption cross sections σ_{red} ($\Delta n_z = -1$) and σ_{blue} ($\Delta n_z = 1$)

$$\begin{aligned}
\sigma_{blue}(\delta) &= \sum_{n_z=0}^{N_z} e^{-E_{nz}/k_B T_z} \frac{\alpha^2}{\tilde{\gamma}(n_z)} \left[1 - \frac{\delta}{\tilde{\gamma}(n_z)}\right] e^{-\alpha\left[1-\frac{\delta}{\tilde{\gamma}(n_z)}\right]} \Theta\left[\tilde{\gamma}(n_z) - \delta\right] \\
\sigma_{red}(\delta) &= \left[1 - \frac{e^{-E_0/k_B T_z}}{\sum_{n_z=0}^{Nz} e^{-E_{nz}/k_B T_z}}\right] \sigma_{blue}(\delta) \\
\tilde{\gamma}(n_z) &= \nu_z - \nu_{rec}(n_z + 1) \\
\alpha &= \frac{h\nu_z \tilde{\gamma}(n_z)}{\nu_{rec} k_B T_r} \\
E_{nz} &= h\nu_z(n_z + \frac{1}{2}) - \frac{\nu_{rec}}{2}(n_z^2 + n_z + 1).
\end{aligned} \tag{2.21}$$

Most of the quantities in Eq. (2.21) were previously defined, while Θ is the Heaviside theta function, $\nu_{rec} = E_r/h$ is the lattice photon recoil frequency, δ is the clock laser detuning from the clock clock transition, and the maximum number of trap states N_z up to which the sum is performed is parametrized as $N_z = \sqrt{U_0/h\nu_z}$.

Recently, more accurate treatments on the theoretical model behind the sidebands excitation spectra have been proposed [140, 141], specifically addressing the role of motion along the radial degrees of freedom. These works aim to provide a more accurate temperature extraction from the sidebands spectra with the goal of improving the lattice light shift models predictions, which is necessary to accurately estimate effects at the 10^{-18} level. At the current accuracy of our experiment these sophisticated treatments are not used. Besides, the main relevant experimental quantity we are interested in extracting from the sideband spectra is the axial trap frequency, and for this the model summarized here is sufficient. To access information about the temperature of the system we mainly rely on time-of-flight (TOF) expansion measurements. This provides us an estimate of the temperature along the weakly confined radial direction, which represent the major finite-temperature correction when deriving the atomic density within a lattice site.

2.4.2 Lattice AC Stark shift

The presence of the optical lattice, as already mentioned, induces an AC Stark shift of the atomic energy levels. For a lattice laser of angular frequency ω_L and electric field amplitude $E(\mathbf{r})$, the light shift of an internal state $|i\rangle$ can be written as

$$\Delta E_i(\mathbf{r}) = -\frac{1}{4}\,\alpha_i(\omega_L)\,|E(\mathbf{r})|^2, \tag{2.22}$$

where $\alpha_i(\omega_L)$ is the dynamic polarizability of the state. The resulting shift of the clock transition frequency is determined by the differential polarizability

$$\Delta\nu_{\text{lat}} = -\frac{1}{4h}\Delta\alpha(\omega_L)\,|E(\mathbf{r})|^2, \tag{2.23}$$

with $\Delta\alpha = \alpha_e - \alpha_g$ denoting the differential polarizability between the clock states.

The frequency dependence of $\Delta\alpha(\omega_L)$ is at the base of the definition of the *magic wavelength* [34, 35], at which the scalar electric-dipole (E1) polarizabilities of the two clock states are equal, $\Delta\alpha(\omega_m) = 0$. At this magic wavelength the clock transition is insensitive, to first order, to fluctuations in the lattice intensity. For bosonic strontium isotopes, such as ^{88}Sr, the lattice light shift modelling is simplified by the absence of nuclear spin: there is no hyperfine structure and, consequently, no vector or tensor components of the atomic polarizability [142]. As a result, the lattice-induced shift does not depend on the polarization state of the lattice light or on its orientation with respect to an external magnetic field.

Although the E1 light shift is cancelled at the magic wavelength, residual lattice light shifts remain. Treatment of these effects in ^{88}Sr is provided in the model developed by Katori *et al.* [143]. We employ this method to perform our preliminary lattice light shift evaluation in Chapter 4. The model considers higher-order contributions arising from magnetic dipole (M1) and electric quadrupole (E2) interactions, as well as hyperpolarizability terms, that lead to a non-zero differential shift even at λ_m described with Eq. (2.24). The model parameters are: the scalar dipole polarizability near the magic wavelength α^{E1}, its differential sensitivity to deviations from the magic wavelength $\partial/\partial\nu(\Delta\alpha^{\mathrm{E1}})$, the differential multipolar polarizability $\Delta\alpha^{\mathrm{qm}}$ and hyperpolarizability $\Delta\beta(\xi)$ coefficients, and are expressed as follow:

$$\begin{aligned} h\Delta\nu_{\mathrm{ACStark}} \approx & \left(\frac{\partial\Delta\alpha^{\mathrm{E1}}}{\partial\nu}\,\delta\nu - \Delta\alpha^{\mathrm{qm}}\right)(2n_z+1)\sqrt{\frac{E_R}{4\alpha^{\mathrm{E1}}}}\,I^{1/2} \\ & - \left[\frac{\partial\Delta\alpha^{\mathrm{E1}}}{\partial\nu}\,\delta\nu + \Delta\beta(\xi)(2n_z^2+2n_z+1)\right]\frac{3E_R}{4\alpha^{\mathrm{E1}}}\,I \\ & + \Delta\beta(\xi)(2n_z+1)\sqrt{\frac{E_R}{\alpha^{\mathrm{E1}}}}\,I^{3/2} \\ & - \Delta\beta(\xi)\,I^2, \end{aligned} \tag{2.24}$$

where the intensity I is intended as the single lattice beam intensity.

2.5 Atomic interactions in optical lattices

This section presents some fundamental concepts about scattering processes in ultracold atomic ensambles, and introduce the theoretical framework that was used during this work for the interpretation of the experimental results presented in chapter 5 for the collisional induced frequency shift, also frequently called density shift.

2.5.1 Collisional processes

The importance of atomic interactions in an optical lattice depends on the quantum statistics of the trapped particles and therefore differs between bosonic and fermionic systems. For spin-polarized fermionic atoms, the antisymmetry of the total wavefunction forbids s-wave scattering. This, strongly suppresses collisional interactions in the ultracold regime and leaves higher-partial-wave processes as only weak (but measurable) residual contributions [50, 144], that can be further suppressed by lowering the system temperature. In contrast, in bosonic atoms s-wave collisions are allowed, and dominate the interaction physics at low temperatures. As a result, the interaction effects are significantly more pronounced in bosonic lattice clocks. This affects the coherence properties of the system and leads to significant systematic frequency shifts.

In lattice clocks atomic interactions arise predominantly from binary collisions between atoms occupying the same lattice site. These collisional processes can be divided into elastic and inelastic contributions, which, although originating from the same underlying interatomic potentials, results in qualitatively different physical effects. Elastic collisions conserve both the total atom number and the internal-state populations, and their principal consequence is to shift the energies of the the system and introduce dephasing. Inelastic collisions, by contrast, involve irreversible processes in which colliding atoms are removed from the trap or transferred to other states, and lead to atom loss and decoherence. In bosonic ^{88}Sr, inelastic collisions involving $^3P_0 + {}^3P_0$ and $^1S_0 + {}^3P_0$ mixtures of atoms have been shown to play a particularly important role [145, 146]. The nature of these inelastic losses in ultracold strontium is mainly attributed to principle-quantum-number-changing collisions that results in one of the two interacting atoms to fall back into the ground state, while the other goes into a higher electronic state, for example the $5s6s\,{}^3S_1$, that eventually decays to the lowest energy level [146].

For atoms confined to the lowest vibrational band of a deep and magic wavelength optical lattice, with only two internal states α and β available, elastic interactions are described in terms of on-site two-body interaction energies $U_{\alpha\beta}$, which quantify the interaction between two atoms in internal states α and β. These energies are determined by both the low energy scattering properties and the degree of spatial confinement, and assuming contact interactions within a single lattice site, can be expressed as [131, 147]

$$U_{\alpha\beta} = g_{\alpha\beta} \int d^3\mathbf{r}\, |w(\mathbf{r})|^4, \tag{2.25}$$

where $w(\mathbf{r})$ denotes the localized Wannier wavefunction associated with a single lattice site, α and β can be either the ground (g) or excited (e) states. In Eq. (2.25) the implicit assumption that the two interacting bosons occupy the same spatial Wannier orbital is made. Moreover, the magic trapping condition ensures that both electronic states experience the same trap depth, and therefore allowing the overlap integral in Eq. (2.25) to be computed with a single Wannier state even for interspecies interactions. The effective low-energy coupling constant $g_{\alpha\beta}$ is related to the s-wave scattering length $a_{\alpha\beta}$ by

$$g_{\alpha\beta} = \frac{4\pi\hbar^2}{m} a_{\alpha\beta}, \tag{2.26}$$

with m the atomic mass. The values of $U_{\alpha\beta}$ set the scale for elastic interaction effects in the lattice and therefore determine the magnitude of the density shifts observed in bosonic optical lattice clocks. The elastic interaction properties, hence the scattering lengths value, of ^{88}Sr are not fully understood. The ground state scattering length has been precisely measured by photoassociation spectroscopy and determined to be $a_{gg} = -1.4(6)\,a_0$ [148]. This small and negative value is a positive attribute for precision measurements because the interaction is small, on the other hand it prevents to reach quantum degeneracy by evaporative cooling. The excited state scattering length modulus $|a_{ee}|$ is known with a 50% uncertainty: $|a_{ee}| = 100\,a_0$, determined via inelastic and elastic collision rates measurements in a crossed beam ODT [146], while there is no direct experimental determination of the mixed a_{eg} scattering length.

The expected density dependence of the interaction energies is encoded in the spatial integral in Eq. (2.25), quantifying the wavefunctions spread over the lattice site and therefore representing an effective volume. Using the tight binding approximation, where atoms can be considered effectively localized within a single lattice site with a spatial wavefunction well approximated by an harmonic oscillator state , the integral in Eq. (2.25) can be easily calculated in the 3D harmonic-oscillator approximation and in the zero temperature limit, where only the ground state of the oscillator is populated in the state $|0,0,0\rangle$, resulting in the single particle density, or equivalently the inverse of the effective lattice site volume

$$n_0 = \int d^3\mathbf{r}\,|w(\mathbf{r})|^4 \equiv \frac{1}{V_0} \simeq \frac{1}{(2\pi)^{3/2} l_0^x l_0^y l_0^z}, \tag{2.27}$$

where l_0^i is the harmonic oscillator 1/e width $l_0^i = \sqrt{2(\langle \widehat{x_i^2}\rangle - \langle \hat{x}_i\rangle^2)} = \sqrt{\hbar/m\omega_i}$. To account for the finite temperature of the system, following the arguments presented in [149], the effective volume can be inflated by considering non-zero occupation numbers n_i of the harmonic oscillator and assuming a Boltzmann thermal distribution, thus writing the effective oscillator lengths as

$$L_i = \sqrt{\frac{\hbar}{m\omega_i}} \times \sqrt{2\langle n_i \rangle + 1} \quad , \quad \langle n_i \rangle = \left[\exp\left(\frac{\hbar\omega_i}{k_B T} \right) - 1 \right]^{-1} . \tag{2.28}$$

Combining the last two sets of equations, we can write the explicit formula that is used throughout this manuscript to estimate the effective lattice site volume as

$$V_{\text{site}} = (2\pi)^{3/2} \prod_i \sqrt{\frac{\hbar}{m\omega_i}} \times \sqrt{2\langle n_i \rangle + 1}. \tag{2.29}$$

The combined effects of collisional losses and density-dependent decoherence in a bosonic ^{88}Sr optical lattice clock have been previously studied and brought together in [145, 150], where these processes are described using a single-particle density matrix (SPDM) approach that follows the non-unitary evolution

$$\dot{\rho} = -\frac{i}{\hbar}[H, \rho] + \mathscr{R}(\rho), \tag{2.30}$$

that combines coherent laser driven evolution of the SPDM ρ via the hamiltonian H, with collisions induced dissipative and dephasing processes, and technical noises agglomerated in the relaxation matrix $\mathscr{R}$, which components are [145]:

$$\begin{aligned} \mathscr{R}(\rho)_{11} &= -(\Gamma + \gamma_{ge}\rho_{22})\,\rho_{11} \\ \mathscr{R}(\rho)_{22} &= -(\Gamma + \gamma_{ge}\rho_{11} + \gamma_{ee}\rho_{22})\,\rho_{22} \\ \mathscr{R}(\rho)_{12} &= -\left[\frac{\gamma_{ge}(\rho_{11} + \rho_{22})}{2} + \frac{\gamma_{ee}\rho_{22}}{2} + \Gamma + L + \gamma_{\text{dep}}\rho_{11} \right] \rho_{12}. \end{aligned} \tag{2.31}$$

Here Γ denotes the background gas limited loss rate, while γ_{ge} and γ_{ee} are the two-body inelastic loss coefficients for ground-excited and excited-excited collisions, respectively. The coefficient L represents an effective laser linewidth including phase noise and spatial inhomogeneities, while the purely phenomenological parameter γ_{dep} describes a density dependent elastic dephasing inserted by the authors to explain their high-density observations. This parameter should be semiclassicaly related to the loss rate $n\sigma v_T$, where n is the atomic density, σ is the scattering cross-section, related to the scattering lengths, and v_T is the average thermal velocity of the atoms. These dephasing processes are attributed in [151] to mode-changing *lateral collisions*:

interaction processes where there is a relatively large momentum transfer between the two colliding particles that results in coherence decay.

2.5.2 Density shift - many body spin $1/2$ model

In this section and the following, we derive the model that is being later used to interpret the results of collisional shifts measurements. We start by considering a many-body description of N identical bosonic atoms within a lattice site, with two relevant internal states $\alpha, \beta \in \{g, e\}$. For such a system, the second-quantized Hamiltonian reads

$$\begin{aligned} \hat{H} = & \sum_{\alpha} \int d^3r \, \hat{\psi}_{\alpha}^{\dagger}(\mathbf{r}) \left(-\frac{\hbar^2}{2m} \nabla^2 + V_{\text{ext}}(\mathbf{r}) \right) \hat{\psi}_{\alpha}(\mathbf{r}) \\ & + \frac{1}{2} \sum_{\alpha\beta} \int d^3r d^3r' \, \hat{\psi}_{\alpha}^{\dagger}(\mathbf{r}) \hat{\psi}_{\beta}^{\dagger}(\mathbf{r}') V_{\alpha\beta}(\mathbf{r} - \mathbf{r}') \hat{\psi}_{\beta}(\mathbf{r}') \hat{\psi}_{\alpha}(\mathbf{r}). \end{aligned} \tag{2.32}$$

Assuming tight confinement within a single lattice site, we may start by expanding the field operators using a single Wannier mode $\hat{\psi}_{\alpha}(\mathbf{r}) = w(\mathbf{r})\hat{a}_{\alpha}$, where $\hat{a}_{\alpha}$ annihilates a boson in internal state α at that site. For contact interactions $V_{\alpha\beta}(\mathbf{r} - \mathbf{r}') = g_{\alpha\beta}\delta(\mathbf{r} - \mathbf{r}')$ the second term of Eq.(2.32), representing the interaction Hamiltonian $\hat{H}_{\text{int}}$ reduces to

$$\begin{aligned} \hat{H}_{\text{int}} &= \frac{1}{2} \sum_{\alpha\beta} U_{\alpha\beta} \hat{a}_{\alpha}^{\dagger} \hat{a}_{\beta}^{\dagger} \hat{a}_{\beta} \hat{a}_{\alpha} \\ &= \sum_{\alpha \in e,g} \frac{U_{\alpha\alpha}}{2} \hat{n}_{\alpha}(\hat{n}_{\alpha} - 1) + U_{eg} \hat{n}_e \hat{n}_g \end{aligned} \tag{2.33}$$

with $U_{\alpha\beta}$ given by Eqs. (2.25), (2.26) while $\hat{n}_{\alpha} = \hat{a}_{\alpha}^{\dagger} \hat{a}_{\alpha}$ is the number operator for bosons in the state α. The first term usually represent the interaction energy in the Bose-Hubbard model [147].

The interacting two-level bosonic system can be mapped onto a collective spin-$1/2$ model [152] by defining

$$\hat{S}_z = \frac{1}{2}(\hat{n}_e - \hat{n}_g), \qquad \hat{S}_x = \frac{1}{2}(\hat{a}_e^{\dagger} \hat{a}_g + \hat{a}_g^{\dagger} \hat{a}_e), \tag{2.34}$$

with fixed total particle number $\hat{n}_e + \hat{n}_g = N$. Finally, including coherent laser driving with Rabi frequency Ω and detuning δ, the effective total Hamiltonian becomes

$$\hat{H}_{tot} = -\hbar\delta\hat{S}_z + \hbar\Omega\hat{S}_x + C(N-1)\hat{S}_z + \chi\hat{S}_z^2, \tag{2.35}$$

where the interaction parameters are

$$C = \frac{U_{ee} - U_{gg}}{2\hbar}, \qquad \chi = \frac{U_{ee} + U_{gg} - 2U_{eg}}{2\hbar}. \tag{2.36}$$

It must be noted that this approach, particularly the single coherent mode expansion of the bosonic fields operator and the requirement of fixed N, leads to miss an important part of the interaction picture between bosonic atoms by loosing the ability to reproduce the exchange symmetry that typically characterizes a thermal bosonic ensemble. From a closer look at the operator $\hat{H}_{\mathrm{int}}$, we recognize that when computing its expectation values for a generic, thermal bosonic gas, this would be strictly related to the evaluation of the second-order correlation function

$$\alpha^{(2)}_{\alpha\beta} = \frac{\langle \hat{a}^\dagger_\alpha \hat{a}^\dagger_\beta \hat{a}_\beta \hat{a}_\alpha \rangle}{\langle \hat{n}_\alpha \rangle \langle \hat{n}_\beta \rangle}, \tag{2.37}$$

which, for any α, β combination is equal to 2 for the system under consideration: non-condensed, weakly interacting, thermal bosonic gas with coherently populated and symmetric internal states α and β. The assumption performed at the beginning, however, prevents this exchange symmetry to arise, and it must be introduced for example by re-normalizing the interaction energies including an extra $\alpha^{(2)}_{\alpha\beta}$ in the coupling strengths defined by Eq.(2.26), leading to

$$g_{\alpha\beta} \to g'_{\alpha\beta} = \alpha^{(2)}_{\alpha\beta} g_{\alpha\beta}. \tag{2.38}$$

A more detailed treatment including multi-mode expansion of the bosonic field operators and subsequent thermal averaging over the thermally populated states would lead to a similar result [152].

Chapter 3

INRiM ^{88}Sr Optical Lattice clock

This chapter illustrates the experimental apparatus of the INRiM ^{88}Sr optical lattice clock. An overview of the system and the delivered optical radiations to the science chamber is given in Sec. 3.1. Sections 3.2 and 3.3 introduce the detection system and the experiment control architecture, with a focus on the changes made during this work with respect to [85] and previous arrangements in general.
Section 3.4 describes the generation and distribution across the experiment of all the necessary optical radiations, and section 3.5 shows how the frequency stabilization of such radiations is handled.

3.1 Physics package and apparatus overview

Vacuum system and atomic source. The physics package of the ^{88}Sr optical lattice clock is composed by the vacuum system including the atomic source and the science chamber, the coils surrounding it, and the optical system used to shape and manipulate the necessary laser beams interacting with the atomic ensemble. A picture of the physics package is shown in Fig. 3.1. The vacuum system was realized in collaboration with Trento University [153] and it consists of two vacuum regions connected by a differential pumping channel (DPC) which allows us to maintain different pressure levels: high vacuum (HV) in the atomic source region, and ultra-high vacuum (UHV) in the science chamber, where the atoms are cooled, trapped, and probed. The HV and UHV conditions are maintained by $200\,\mathrm{L\,s^{-1}}$ and $500\,\mathrm{L\,s^{-1}}$ ion-getter pumps respectively (NextTorr D200, NextTorr D500). The whole system is realized in stainless steel (AISI-304). The science chamber has an octagonal shape, and all the optical accesses are provided via BK7-silica glass viewports. Seven CF40 viewports are displaced along the octagon faces, while two CF63 viewports provide optical accesses from the top and bottom of the chamber. During the operation condition, the pressure levels achieved in both vacuum regions is $P_{\mathrm{UHV,HV}} \lesssim 1 \times 10^{-10}$ mbar, limited by the minimum detectable pressure of the pumps drivers.

The atomic source is based on a collimated thermal atomic beam produced by an oven operating at $T_{\mathrm{oven}} = 460\,^{\circ}\mathrm{C}$. The atomic flux from the oven is directed orthogonally with respect to the main vacuum chamber, leading the atoms towards a region where they undergoe a pre-cooling stage using a sideband-enhanced 2D-MOT [154]. The 2D-MOT produces a transversely cooled, cigar-shaped atomic cloud trapped along the zero-field axis of a quadrupole-like magnetic field generated by four stacks of permanent magnets.

The 2D-MOT beams have two spectral components: the standard red-detuned beams required for the MOT, detuned at about half the transition linewidth, and additional sideband beams that are roughly twice as red-detuned from the $^1S_0 \rightarrow {}^1P_1$ transition. The presence of these sideband beams allows a larger fraction of atoms to be slowed down at this stage, resulting in a brighter and higher-flux atomic source [154].

After the transverse cooling, atoms are optically pushed into the science cell using a resonant push beam. Inside this region, they are further cooled in the blue and red 3D MOT stages, before being trapped in the optical lattice. At the maximum available optical powers, the atomic source provides an estimated flux and MOT loading rate of $\Phi = 1.5(2) \times 10^9\,\mathrm{atoms/s}$ and $L_{\mathrm{MOT}} = 7.3(9) \times 10^8\,\mathrm{atoms/s}$ respectively [154]. Control over the final number of trapped atoms in the lattice is mainly achieved by tuning the intensities of the 2D-MOT and push beams.

The design of the 2D-MOT based atomic source provides several practical advantages: it significantly reduces the number of hot thermal atoms entering the interrogation region and minimizes the black-body radiation shift of the clock transition caused by heat from the oven. Comprehensive details and characterization of the atomic source can be found in [85, 154].

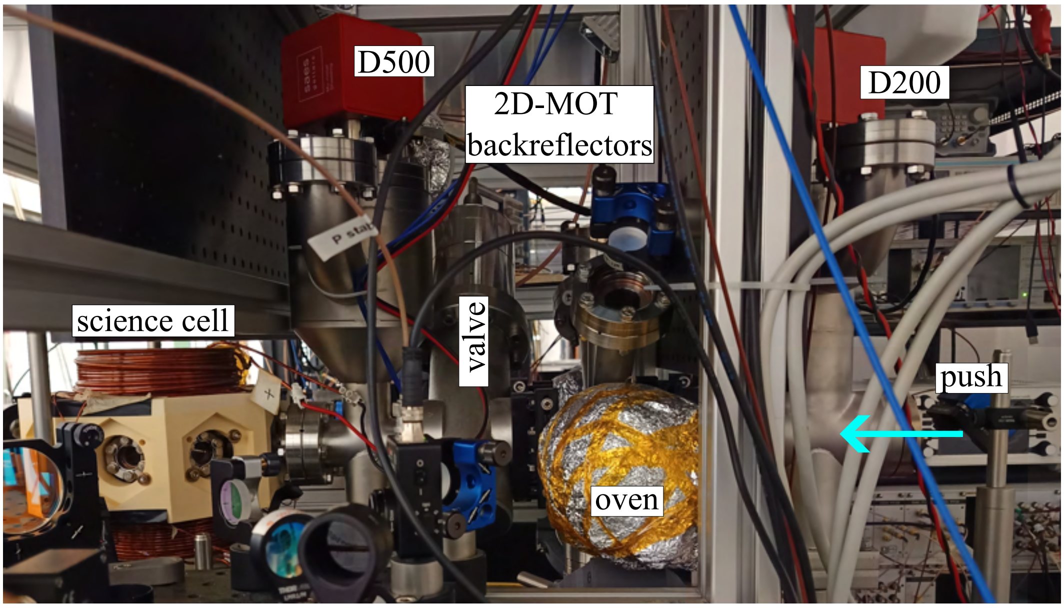

Fig. 3.1 Picture of the physics package.

Magnetic fields. The coils system for generating and controlling magnetic fields in our experiment is schematized in Fig. 3.2. A set of circular coils (solid copper wire, not water cooled) provides the necessary quadrupole and homogeneous magnetic fields needed for MOT and clock interrogation respectively. At the maximum operating current of $I_{\mathrm{max}} = 10\,\mathrm{A}$ the system can reach a gradient of $40\,\mathrm{G\,cm^{-1}}$ and static field of $|B|_{\mathrm{max}} \approx 100\,\mathrm{G}$. The coils can be switched between anti-Heltmoltz (quadrupole field) and Helmoltz (homogeneous field) configuration by applying a TTL control signal to an H-bridge loaded with one of the coils. The current I supplied to the coils is provided by a power supply (Delta Elektronika ES015-10) remotely controlled via a DAC connected to the main experiment control board. A fast magnetic field switch-off is guaranteed by an insulated-gate bipolar transistor (IGBT), which gate voltage is controlled with a DAC. As part of this work, an additional H-bridge controlling the overall current flow direction was implemented to optionally allow reversal of the magnetic field polarity during clock operation.

Additional magnetic fields, static during the clock operation, are applied via three orthogonal sets of compensation coils. The driving circuit shown in Fig. 3.2 for these sets of coils it was actually used only during the quadratic Zeeman shift evaluation campaign, due to limited availability of H-bridge and additional current sources. On a regular basis, the coils operate at a fixed current values that were mainly chosen with considerations about the red MOT position. The impact of this on the clock operation is discussed in chapter 4.

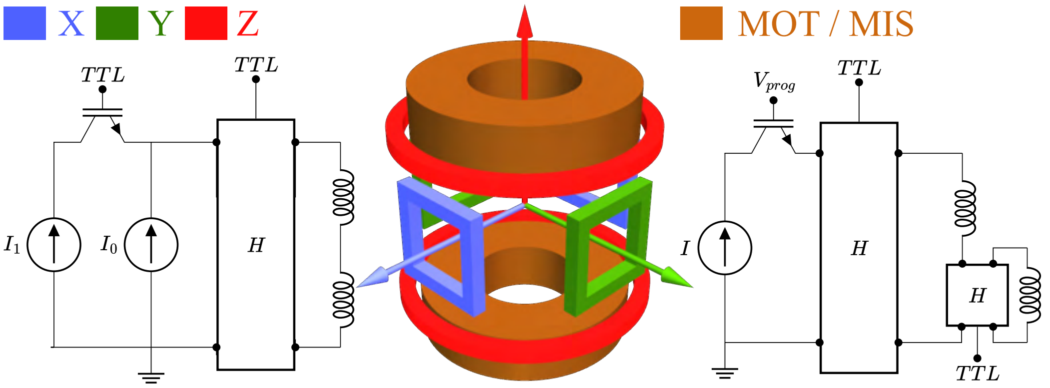

Fig. 3.2 Schematic of the coils system geometry and respective driving circuits.

Proximity optics and radiations. The system geometry is displayed in Fig. 3.3, where all the science chamber proximity optics and radiations reaching the atoms are shown. The main lattice beam propagates in the xy plane, orthogonal to gravity, and is delivered via a polarization-maintaining (PM) fiber. After the fiber, a series of beam shaping lenses focus the beam to a target waist $w_{0H} \approx 50\,\mu\text{m}$ at the atoms position (see Sec.5.1.1). After traversing the vacuum chamber, the beam is re-collimated and back-reflected with a short-pass dichroic mirror to form the optical lattice. An equal dichroic mirror is used in the input path, in order to avoid introducing clock laser standing wave components during the clock interrogation. The combination of $\lambda/2$ + PBS + $\lambda/2$ helps setting the polarization input at the other fiber end, which is chosen by minimizing the power fluctuations after the PBS. The final half-wave plate sets the lattice polarization to be vertical.

A similar optical path is replicated for the vertical lattice, which is aligned along the direction of gravity, as shown in the right panel of Fig. 3.3. For this configuration, the beam waist at the atomic sample is chosen to be $w_{0V} \approx 130\,\mu\text{m}$ (see Sec.5.1.2). The back-reflected beam is refocused directly by the back-reflector which is realized with a concave mirror. Unfortunately, clock spectroscopy along the vertical branch could not be implemented here, primarily due to limited available optical power at 698 nm, and the lack of a sufficiently strong and controllable magnetic field to effectively drive the clock transition. This additional lattice was primarily used to realize a non-interfering two-dimensional trap, where atoms are confined within a smaller spatial region, for the investigation of atom-atom interactions described in chapter 5.

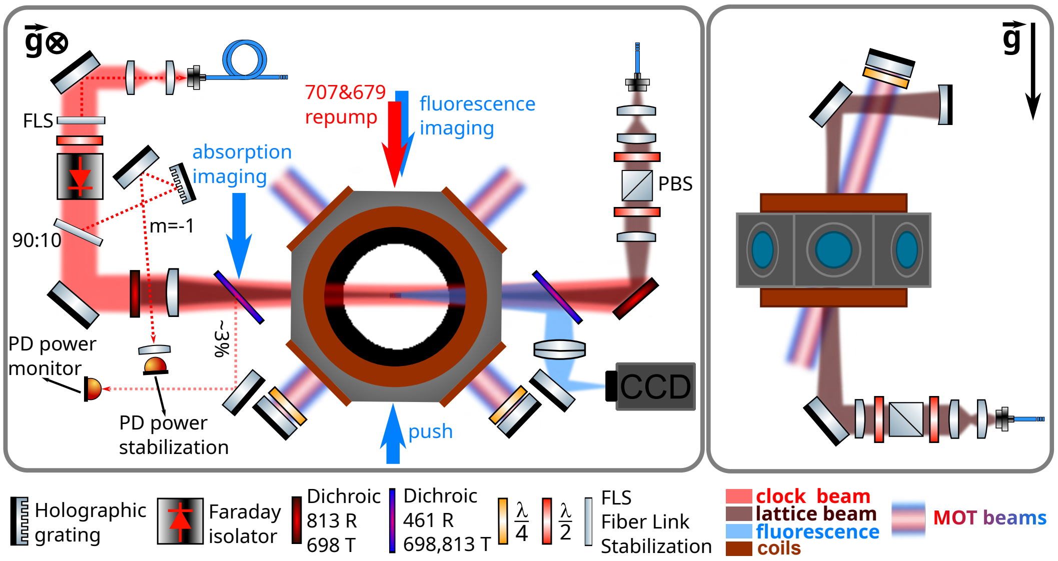

Fig. 3.3 Schematic of the science chamber and all the proximity optics and radiations. The main lattice, realized with the single back-reflected beam configuration, propagates in the horizontal direction. The power-stabilized clock laser reaches the atoms through the lattice back-reflector. An additional vertical lattice allows two-dimensional trapping. The detection system exploits a CCD for both fluorescence and absorption imaging of the atomic population.

The clock laser exits from a PM fiber and propagates along the main lattice direction, has a target waist at the atomic position $w_C \approx 150\,\mu\text{m}$ and it is vertically polarized at the entrance of the science cell in order to be parallel to the induced magnetic field. The vertical polarization is ensured by accurate angular positioning of the optical isolator shown in the left panel of Fig. 3.3. Beside the fiber link stabilization (FLS) back-reflector, which is used to perform fiber phase noise cancellation [155, 156], all the other optical elements shown are needed for a reliable clock laser power stabilization. The performance and impact on the clock operation of this control loop is discussed in chapter 4.

Finally, the core of the detection system is also shown in Fig. 3.3, and detailed in the next section. Both absorption and fluorescence imaging can be performed using a $5s^2\,{}^1\mathrm{S}_0 \leftrightarrow 5s5p\,{}^1\mathrm{P}_1$ resonant beam. Absorption imaging is carried out along the lattice axis and is mainly used for diagnostic purposes, such as time of flight (ToF) measurements. Fluorescence imaging, on the other hand, is employed during clock operation for fast detection of both $5s^2\,{}^1\mathrm{S}_0$ and $5s5p\,{}^3\mathrm{P}_0$ populations, the latter after repumping to the ground state. The fluorescence excitation beam propagates collinear with the repumping beams and orthogonal to the lattice axis. In both imaging modes, the 461 nm light is redirected onto the CCD sensor by custom made long pass dichroic mirrors placed along the lattice beam path.

3.2 Detection system

The atomic population detection system is based on a CCD camera (Stingray F201-B), which enables both absorption and fluorescence imaging of the atomic cloud. The detector has a 1624×1234 pixel matrix, with each pixel measuring $4.4\,\mu\mathrm{m} \times 4.4\,\mu\mathrm{m}$. The light is collected by an achromatic lens with a focal length of 100 mm, resulting in a numerical aperture of the imaging system of $\mathrm{NA} = 0.10(4)$. A dedicated frame grabber board with CameraLink connection is used for data acquisition, which is further accelerated by only reading a small portion of the sensor (300×180 pixels for absorption and 300×80 pixels for fluorescence). The imaging setup was already realized and mostly optimized before this work. In particular the choice of exposure time, probe-atoms interaction time, and the region of interest (ROI) dimensions for fluorescence imaging.

3.2.1 Absorption imaging

Atom number extraction from absorption imaging The absorption image is constructed by taking three camera exposures: one with atoms (I_{atoms}), one with the probe beam only (I_{probe}), and one background image (I_{bg}) without atoms and probe light. The probe beam is typically operated at 100-150 µW distributed over a large ($\approx$2 cm) cross section. This ensures saturation effects of the addressed transition can be neglected [157]. The optical density (OD) at each pixel is then extracted using the Lambert-Beer law [158] as

$$\mathrm{OD}(x,z) = \ln\left(\frac{I_{\mathrm{probe}}(x,z) - I_{\mathrm{bg}}(x,z) + \varepsilon}{I_{\mathrm{atoms}}(x,z) - I_{\mathrm{bg}}(x,z) + \varepsilon}\right), \tag{3.1}$$

where ε is a small regularization constant to avoid numerical divergences. The resulting OD map represents the column density of atoms integrated along the probe beam direction. To extract the total number of atoms $N \propto \int \mathrm{OD}(x,z)dxdz$, the integrated OD profiles along the horizontal (x) and vertical (z) directions are computed and fitted with Gaussian profiles

$$f(x) = A\exp\left[-\frac{(x-x_0)^2}{2\sigma_x^2}\right] + C, \tag{3.2}$$

and similarly for z. In principle, to count the atoms we could directly integrate the signal from each pixel, however fitting the signal allows for other key parameters of the atomic cloud, such as its width, to be extracted. From the fitted parameters, the atom number is obtained as

$$N_x = \sqrt{2\pi}A_x\sigma_x\frac{C_F^2}{\sigma_0}, \qquad N_z = \sqrt{2\pi}A_z\sigma_z\frac{C_F^2}{\sigma_0}, \tag{3.3}$$

where C_F is the effective pixel size in meters per pixel, and $\sigma_0 = \frac{3}{2\pi}\lambda^2$ is the resonant scattering cross-section for light of wavelength λ [100]. The final atom number N is taken as the average of N_x and N_z. This method assumes the atomic distribution is approximately Gaussian , that the probe beam is resonant with $5s^2\,{}^1\mathrm{S}_0 \leftrightarrow 5s5p\,{}^1\mathrm{P}_1$, and has an intensity negligible with respect to the transition saturation intensity. Also, to esnure linearity and a reliable estimate of the atom number high OD images are avoided [158] by giving the atomic cloud a few ms of expansion. Fig. 3.4 shows an example of absorption imaging of the red MOT and the lattice.

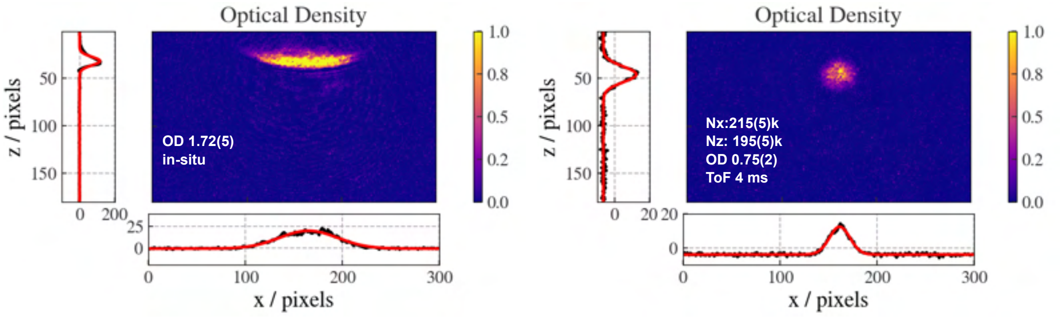

Fig. 3.4 Left: absorption imaging of the in-situ single frequency red MOT. Right: Absopriton imaging of the lattice after 4 ms of expansion.

Calibration of the imaging system and temperature extraction from time-of-flight imaging. The time-of-flight (ToF) sequence provides a direct means to determine both the imaging calibration factor C_F and the temperature of the atomic sample. In particular, given the geometry of our setup, absorption imaging give us access to the radial temperature only. After release from the confining potential, which can be the lattice or the MOT, the center-of-mass (CoM) position $z_{\mathrm{CoM}}(t)$ of the atom cloud evolves ballistically according to

$$z_{\mathrm{CoM}}(t) = z_0 + v_0 t + \frac{1}{2} a_{\mathrm{px}} t^2, \tag{3.4}$$

where a_{px}, v_0, and z_0 are the acceleration, initial velocity and position, expressed in px·s^{-2} , px·s^{-1}, and px, respectively. For a known acceleration, as the local gravitational acceleration g =9.8055 m s^{-2} [159, 160], the pixel-to-length calibration factor C_F is obtained as

$$C_F = \frac{g}{a_{\mathrm{px}}}. \tag{3.5}$$

This calibration links camera pixels to physical distances in the object plane and accounts for the overall imaging magnification. Figure 3.5 shows the evaluation of Eq. (3.5) for many ToF measurements acquired with different trap geometries over several months. The result is $C_F = 7.1746(11)\ \mu m \cdot \mathrm{px}^{-1}$.

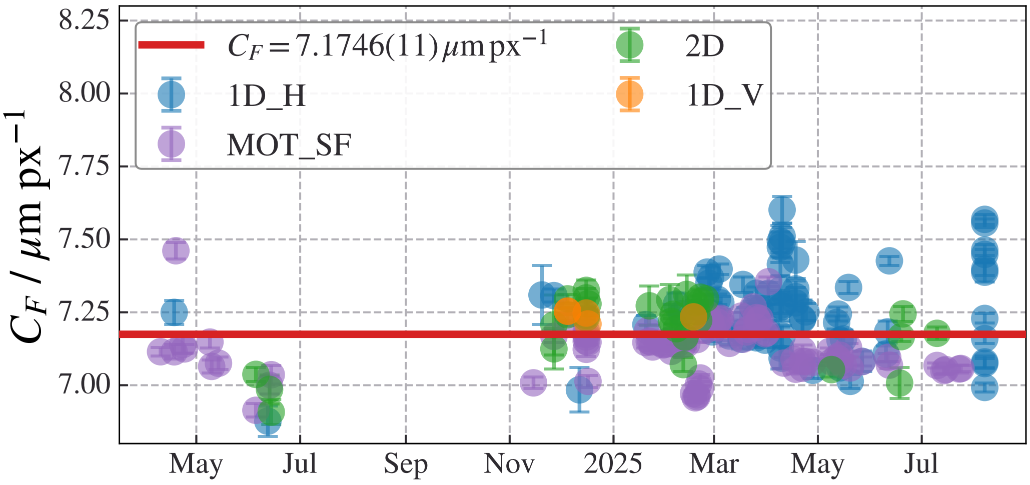

Fig. 3.5 Imaging system pixel calibration using free-fall measurement form different atomic samples: 1D horizontal lattice(lightblue), 1D vertical lattice (yellow), 2D lattice (green), single frequency (SF) red MOT (purple). The red solid line represents the weighted average.

Once C_F is established, the temperature can be extracted from the ballistic expansion of the atomic density distribution [158]. The observed Gaussian widths $\sigma_{x,z}(t)$ increase in time according to

$$\sigma_{x,z}^2(t) = \sigma_{0,x,z}^2 + \frac{k_B T_{x,z}}{m} t^2, \tag{3.6}$$

where $\sigma_{0,x,z}$ are the in-trap widths, m is the atomic mass, and $T_{x,z}$ are the temperatures along the horizontal and vertical directions, respectively. Experimentally, the measured widths (in px) are fit as

$$\sigma_{x,z}^2(t) = b_{x,z} t^2 + c_{x,z}, \tag{3.7}$$

giving the slopes $b_{x,z}$ in $\mathrm{px}^2 \cdot \mathrm{s}^{-2}$, which represents the average squared thermal velocity of the system. Using the previously determined calibration, the temperature follows as

$$T_{x,z} = \frac{m}{k_B} b_{x,z}^{(\mathrm{phys})} = \frac{m}{k_B} b_{x,z} C_F^2. \tag{3.8}$$

ToF imaging thus provides a self-consistent determination of both the imaging scale and the atomic temperature under identical experimental conditions. The same analysis also allows us to retrieve the in-trap cloud sizes $\sigma_{0,x,z}$ from the intercepts $c_{x,z}$, which can in principle be compared to the expected harmonic oscillator ground-state widths in the trapping potential. However, due to limited imaging resolution and the high optical densities encountered in in-situ absorption imaging, accurately extracting the cloud widths at zero expansion time remains difficult.

3.2.2 Fluorescence imaging

Fluorescence imaging is performed by exposing the atomic sample to a 50 µs resonant light pulse, while the emitted fluorescence is integrated over a 1 ms acquisition window on the CCD. The probe beam is focused to a 1 mm waist at the atomic cloud, and it is linearly polarized along the vertical direction in order to maximize the fluorescence emission along the CCD optical axis. This directionality arises from the selection rules for the emission and absorption of light by atoms, which lead to anisotropy in the emission that depends on the light polarization, the total angular momentum **J** and the magnetic quantum numbers m of the initial and final states [161, 162]. The total signal is obtained by summing the CCD counts within a 30×30 pixel region of interest (ROI) centered on the lattice fluorescence spot. The background level is estimated by integrating an identical ROI displaced by 120 pixels from the signal region. The net fluorescence signal is then calculated as the difference between the two integrated counts.

Increasing the fluorescence signal An optical band pass-filter is employed to prevent light at unwanted wavelengths from reaching the CCD sensor. During this work, in order to improve SNR, the fluorescence filter was changed from an FB460-10 (Thorlabs), which has a nominal transmission of 56.25% at 461 nm, to an FBH460-10 (Thorlabs) with a declared transmission of 95.62% at the same wavelength. This new filter has also a better declared suppression of 813 nm light, however spurious lattice light, and its second-order reflections, became visible on the CCD with an intensity comparable to the atomic signal when the filter was placed. This effect is shown in Fig. 3.6. The atomic fluorescence also appeared downshifted, suggesting a possible lensing effect introduced by the filter. Direct measurements of the 813 nm transmission at normal incidence confirmed this behavior: the FBH460-10 exhibits, on average over three tested samples, a transmission at 813 nm approximately 30(2) times higher than that of the FB460-10, thus resulting a bit worse with respect to what declared.

Switching off the lattice during the imaging sequence is not an option, since the introduction of the repumping laser (discussed in Sec. 3.4.3) to detect the excited fraction requires that the atoms in the ${}^3\mathrm{P}_0$ state remain trapped in the lattice while imaging the ${}^1\mathrm{S}_0$ population. The problem was solved by installing two FBH460-10 filters in series, effectively suppressing the spurious lattice light, and the atomic fluorescence signal returned almost to its original position. The gain obtained by this change is estimated to be roughly a factor 2.2 based on the fluorescence imaging signals (c) and (d) reported in Fig. 3.6, which have respectively 45×10^3 and 100×10^3 counts. The observed gain is higher than the expected by simply considering the declared transmission of the two filter models, this is likely due to a transmission loss of the old filter due to aging. This kind of filter is indeed particularly sensitive to moisture and the coating degrades over time. This problem should be less critical for this new hard-coated model.

A further increase in the detected atomic signal is obtained by increasing the probe optical power. As shown in Fig. 3.7, switching from fluorescence detection

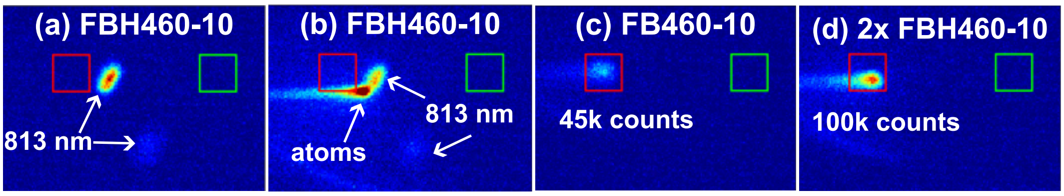

Fig. 3.6 (a) Spurious lattice light using the FBH460-10 filter. (b) Atomic signal and spurious lattice light using the FBH460-10 filter, the atomic signal is smaller and downshifted. (c) Atomic signal with FB460-10. (d) Atomic signal with two FBH460-10 placed in cascade. (c) and (d) were acquired with the same loading conditions, and therefore same number of atoms. The red and green squares represents the 30x30 ROIs over which the signal and background counts are integrated.

after a 4 ms time of flight (as performed prior to the introduction of the repumping lasers) to in-situ detection requires a slightly higher probe power to reach saturation. The in-situ fluorescence signal, however, saturates at a higher value. The resulting gain in signal is estimated to be a factor of 1.56(3).

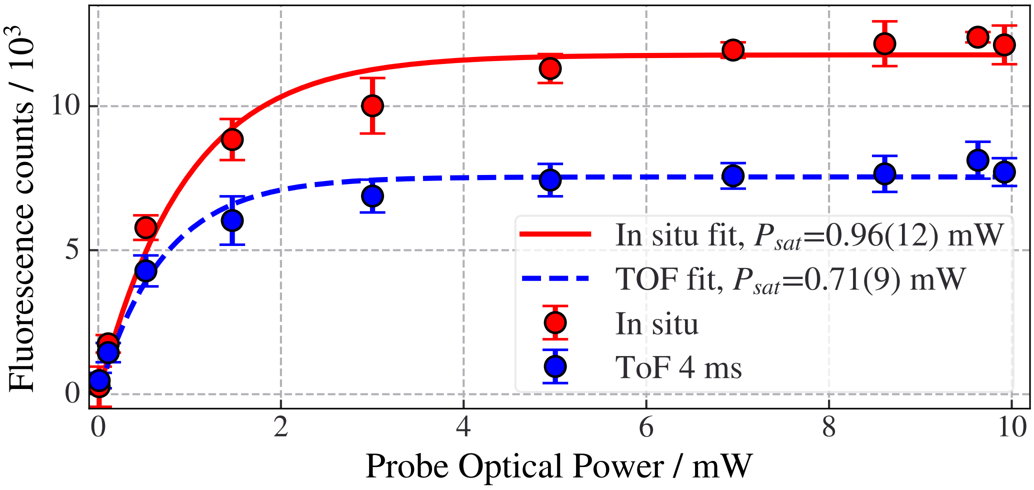

Fig. 3.7 In situ (red circles) versus ToF (blue circles) fluorescence imaging signal at different probe powers. In situ imaging results in a higher signal, but also with a higher effective optical power needed for saturation.

Fluorescence calibration of number of atoms In order to evaluate the number of atoms during clock operation, which relies on fluorescence imaging, the relationship between the atom number determined by absorption imaging, as described in the previous subsection, and the fluorescence signal was measured for different intensities of the 2D-MOT beams. For each value of the 2D-MOT intensity about 30 images are acquired to average down noise. Results are shown in Fig. 3.8: the conversion coefficient is estimated to be 0.846(5) atoms/count.

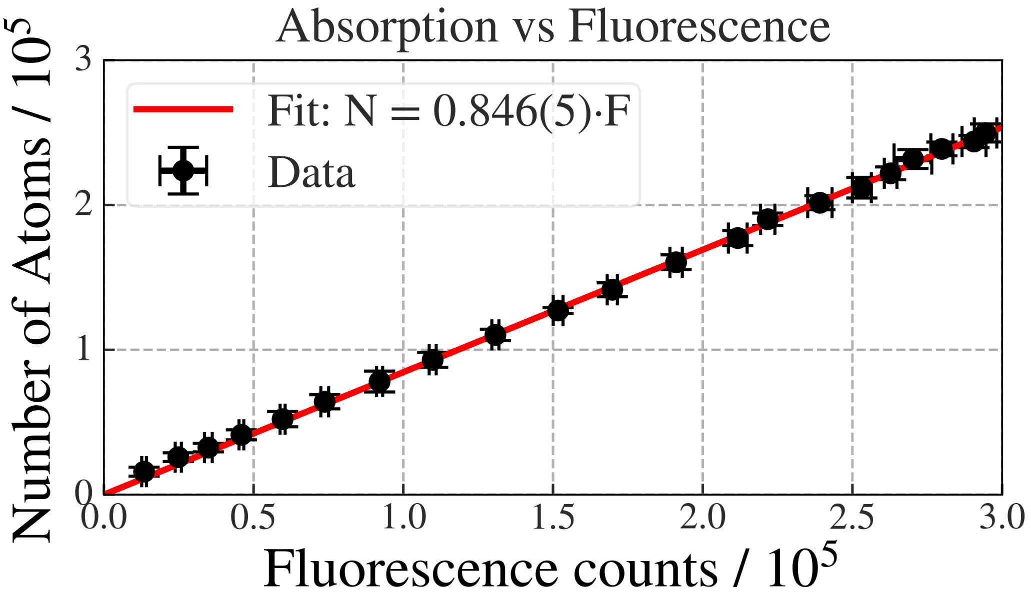

Fig. 3.8 Number of atoms versus fluorescence signal calibration. Each point represent the average of 30 images for both absorption and fluorescence and the uncertainty is one standard deviation. The solid line is a linear fit with the intercept forced to zero.

3.3 Optical radiations

This section describes how the necessary optical radiations are generated and delivered to the physics package. During this work, due to the installation of new laser sources at 461 nm and 813 nm, the respective optical layouts for the distribution across the experiment have been remade from scratch. Furthermore, repumping lasers at 707 nm and 679 nm were successfully integrated in the clock experimental sequence for the first time. The subsection dedicated to the repumpers (Sec. 3.3.3) also describes this integration process.

3.3.1 Laser cooling and trapping: 461 nm, 689 nm and 813 nm

461 nm The newly installed 461 nm source is a commercial frequency-doubling module (TA-SHG Pro, Toptica). The system delivers a maximum output power of 1.3 W, well above the requirements of a single lattice-clock experiment, even though the sideband-enhanced 2D-MOT is particularly demanding in terms of optical power. The output beam has an estimated beam quality of $\mathrm{M}^2 = 1.2(1)$ and a waist of $w_0 = 550(10)\,\mu\mathrm{m}$ at 2 m from the output port, with a slight residual astigmatism. This astigmatism is not corrected. Fiber coupling and AOM efficiencies are optimized by adjusting the positions of the beam-shaping lenses.

In routine operation we use 850 mW of total output power, distributed (see Fig. 3.9) among three main branches. At the end of the distribution chain, we obtain approximately 100 mW for the 2D-MOT beams, 70 mW for the sideband-enhancement beams, 20 mW for the 3D-MOT beams, 10 µW to 100 µW for the push beam, and 9 mW for the detection beam. The available output at the sub-harmonic wavelength (922 nm) is sent to a wavemeter and to a fiber-coupled EOM for laser-frequency stabilization at a detuning about 160 MHz from the atomic resonance.

This frequency-doubling stage is extremely robust and largely insensitive to acoustic or vibrational noise, providing the basis for an apparatus capable of continuous operation over several hours. The main limitation of the system is its sensitivity to residual humidity: water vapor inside the SHG cavity degrades the conversion efficiency and generally causes the system to operate at a suboptimal point. This issue is easily resolved by opening the resonator lid and replacing the desiccant bags with fresh ones, typically every 3-4 months.

689 nm The source for narrow-line laser cooling is a commercial external cavity diode laser (DL-pro, Toptica), which is sent to the reference cavity through a fiber-coupled EOM and locked at roughly 500 kHz from the atomic resonance. This master laser is used to injection-lock a slave diode, providing a net optical power of about 12 mW for narrow-line cooling of ^{88}Sr on the $5s^2\,{}^1\mathrm{S}_0 \leftrightarrow 5s5p\,{}^3\mathrm{P}_1$ transition. The possibility of efficient narrow-line cooling of ^{87}Sr it is predisposed but not completed as it was not a focus of this work.

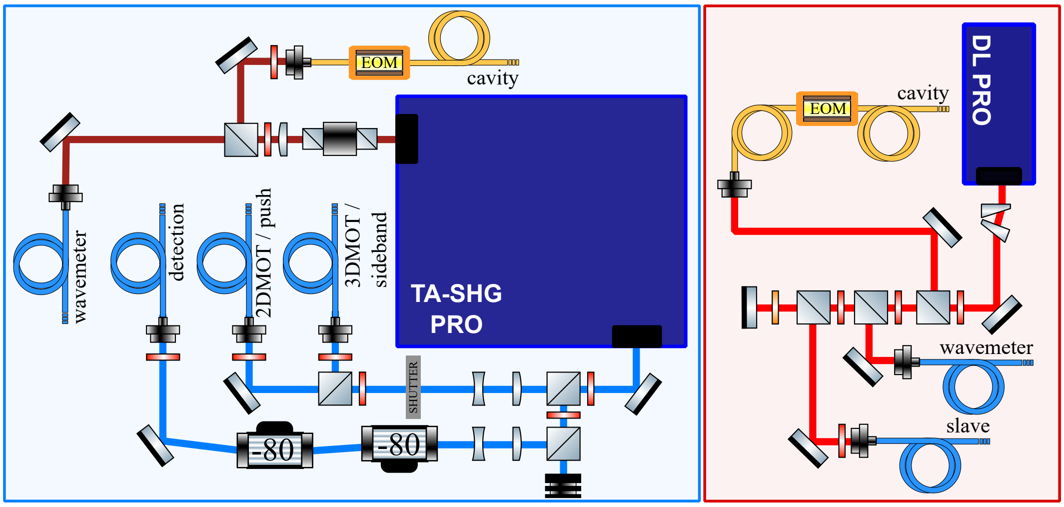

Fig. 3.9 461 nm and 689 nm optical radiation distribution setup.

813 nm The lattice laser was also replaced during this work. Initially, the system used a TiSa module from M Squared Lasers, externally pumped by a Verdi 532 nm laser, which produced less than 1 W at 813 nm. This 813 nm laser was later substituted with another M Squared product that features an integrated pump technology. The new laser system was installed in May 2023 and could deliver up to 6 W at 813 nm at maximum pump power. However, the conversion efficiency P_{813}/P_{pump} shows degradation over time, with the degradation rate increasing when the laser was operated at higher power for generation of a 2D lattice. At the moment of writing, the maximum output power is halved. This behavior is shown in Fig. 3.10, along with the implemented distribution setup.

The main output is distributed among two branches: one for the horizontal lattice, along which the clock interrogation is performed, and one for the vertical lattice. Together, we use them to form a non-interfering 2D lattice. The optical power delivered to the atoms is controlled by AOMs driven by 80 MHz DDSs. To avoid interference between the lattices, besides different polarizations, also opposite diffraction orders of the AOMs are used, resulting in a detuning of 160 MHz between the horizontal and vertical lattices. The auxiliary output (dashed line in Fig. 3.10 is used to send 813 nm light to a wavemeter and to the frequency stabilization system.

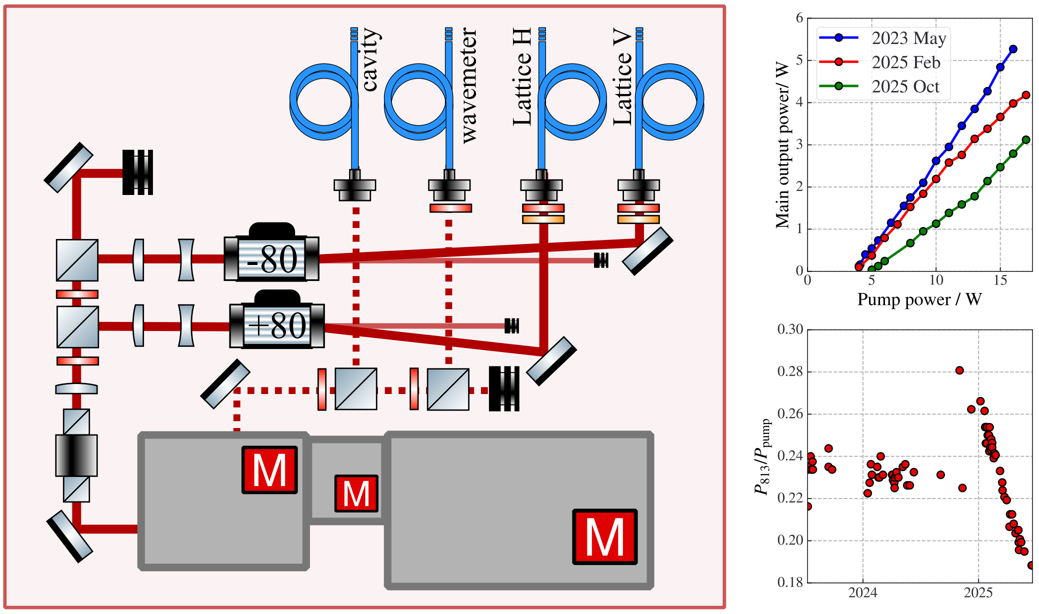

Fig. 3.10 Left: 813 nm distribution setup, Right: Output Power degradation over time-the top panel shows the output power characteristic acquired ad different time, the bottom panel shows daily evaluation of the slope P_{813}/P_{pump}.

3.3.2 Repumping - 679 nm and 707 nm

The repumping lasers addressing the transitions $5s5p\,^3\mathrm{P}_0 \leftrightarrow 5s6s\,^3\mathrm{S}_1$ at 679 nm and $5s5p\,^3\mathrm{P}_2 \leftrightarrow 5s6s\,^3\mathrm{S}_1$ at 707 nm are home-made external-cavity diode lasers (ECDLs) and were already introduced in [85], where the realization details of their construction are provided. However, both repumper lasers were later dismissed mainly due to issues with the 679 nm source, which required operation at very low temperatures around 5 °C. Such condition caused water condensation, that eventually damaged the ECDL enclosure.

679 nm. During the present work a replacement diode (HL6756MG, Thorlabs) was tested for operation near 679 nm. However, this diode required high temperatures (above 45 °C) to reach the target wavelength, and stable single-mode operation could not be achieved. The issue was the same: a significant misalignment between its gain spectrum and the desired emission frequency.

The solution was ultimately found with a ridge-waveguide tunable Fabry-Pérot anti-reflection (AR) coated laser diode (EYP-RWE-0690-00703-1000-SOT02-0000). Its declared wavelength tuning range is similar to the previously tested models, however, the key improvement here is the AR coating which suppresses self-lasing and provides a more stable external-cavity operation.

707 nm. For the 707 nm source, the HL7001MG laser diode is used. Although it is not AR-coated and requires operation at approximately 35 °C to lase at 707 nm, the diode gain spectrum allows for reasonably stable ECDL operation. For both lasers, coarse adjustment of the grating angle for wavelength selection and vertical tilt for injection optimization are required every two to three weeks.

Optical distribution. The optical distribution layout used to deliver the repumping light to the atoms is shown in Fig. 3.11. The output of both ECDLs first passes through an anamorphic prism pair to correct the characteristic elliptic beam profile of diode lasers, and to improve the transmission efficieny through the subsequent optical isolator, which is employed to prevent undesired optical feedback arising from spurious back-reflections. Before the two beams are combined, a small fraction of the optical power is sent to a wavelength meter, which is also used to stabilize the repumper frequencies through a slow feedback loop, as discussed in Sec. 3.4.3.

The beams are subsequently combined using a polarizing beam splitter (PBS), and the majority of the optical power is directed towards the path leading to the atomic sample. Along this path the beam is spatially filtered by a non-resonant mode cleaner composed of two f=45 mm lenses and a 300 µm pinhole. This stage improves the fiber-coupling efficiency, enhances the AOM diffraction efficiency, and suppresses residual beam-profile fringes. Despite this filtering, residual repumping light from the zeroth AOM order still couples into the fiber, therefore we had to introduce an electro-mechanical shutter to effectively prevent repumping photons to reach the atoms at unwanted times. At the fiber output, the repumper beam is reshaped to achieve a spot size of approximately 1 mm at the position of the atoms and is overlapped with the detection beam, as illustrated in Fig. 3.3.

A fraction of the light, transmitted at 707 nm and reflected at 679 nm by the combining PBS, is sent to a Fabry-Pérot scanning interferometer (SA200-2B, Thorlabs), which provides an immediate visual diagnostic of the ECDLs injection quality.

Diode Current Modulation. Before implementing active stabilization of the repumper lasers via the wavelength meter,described in Sec. 3.4.3 and which required

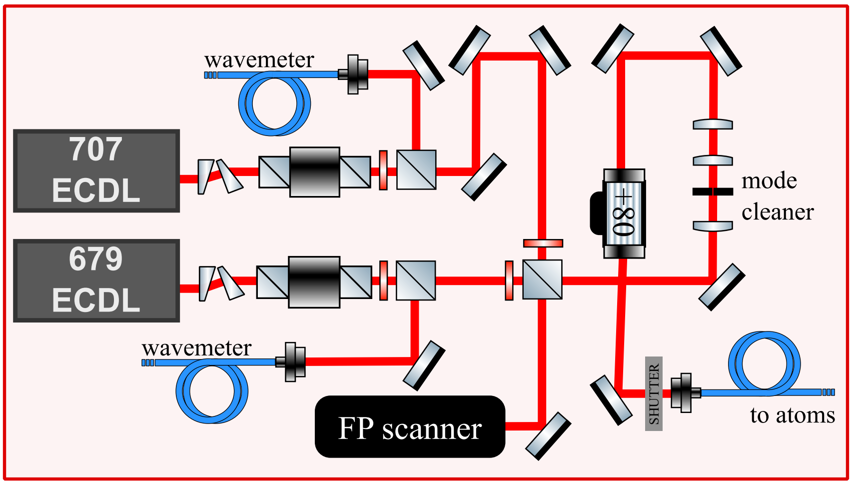

Fig. 3.11 679 nm and 707 nm optical radiation distribution layout.

the installation of a fiber-optic switch, short-term frequency noise was reduced by modulating the diode current with a 10 kHz ramp, as shown in Fig. 3.12. This modulation provided a frequency excursion of several hundred MHz, effectively reducing the impact of short-term laser drifts. The resulting robustness can be observed in the measurement of the repumping efficiency as a function of the central wavelengths of the two lasers reported in Fig. 3.14, which exhibits no appreciable variation over several picometers. Nevertheless, periodic manual readjustment of the central wavelengths remained necessary, limiting the system ability to operate continuously and without intervention over extended periods.

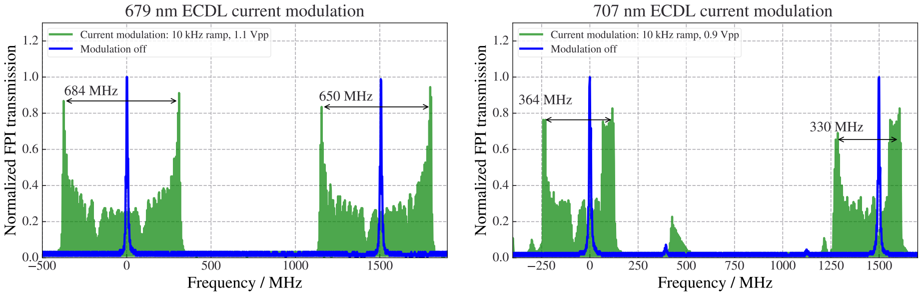

Fig. 3.12 Example of current modulated (green) and non-modulated (blue) repumpers transmission of the FP scanning interferometer.

Repumping efficiency. The optimization of the repumping process was carried out by analyzing the repumping efficiency, η, at different wavelengths, intensities, and pulse durations.

During the characterization, the clock laser frequency is scanned, and atoms are excited to the $5s5p\,^3\mathrm{P}_0$ state with a 3 ms clock pulse. The total $5s^2\,^1\mathrm{S}_0 + 5s5p\,^3\mathrm{P}_0$ population is then fitted using either a Lorentzian profile, $y_{0L} + L(\nu)$, or a Rabi profile, $y_{0R} + R(\nu)$, where y_0 is an offset and L and R denote the Lorentzian and Rabi contributions, respectively. The repumping efficiency is defined as

$$\begin{aligned} \eta_L &= 1 - \frac{L(\nu_0)}{y_{0L}}, \\ \eta_R &= 1 - \frac{R(\nu_0)}{y_{0R}}, \\ \eta &= \frac{1}{2}\left(\eta_L + \eta_R\right), \end{aligned} \tag{3.9}$$

where ν_0 is the resonance frequency extracted from the fit. The uncertainty in the efficiency is taken as the semi-difference between η_L and η_R. An example of the corresponding spectroscopy measurement is shown in Fig. 3.13.

The initial operating wavelengths for the characterization were chosen by identifying the maximum enhancement of the blue MOT atom number, occurring near $\lambda_{707} = 707.202\,\mathrm{nm}$ and $\lambda_{679} = 679.290\,\mathrm{nm}$. This choice is further supported by the results in Fig. 3.14, which also highlight the benefit of keeping the laser current modulated: consistent maximum efficiencies of around 80% are observed over a $\sim 3\,\mathrm{GHz}$ span, corresponding to roughly 5 pm of central wavelength deviation. For the particular measurement in Fig. 3.14, the repumping pulse lasts 5 ms and is applied immediately before fluorescence detection, which occurs 28 ms after the ground-state atom measurement.

After establishing the central operating wavelengths of the repumping lasers, we investigated different repumping durations and beam intensities. The results are summarized in Fig. 3.15. For all explored optical powers, the repumping efficiency reaches a plateau for pulse durations t_{rep} between 0.5 and 1.0 ms, after which it begins to decrease, likely due to heating effects and light-assisted collisions [146].

After optimizing both the central wavelengths and the repumping pulse duration, chosen to be $t_{\mathrm{rep}} = 0.8\,\mathrm{ms}$, the repumping efficiency was determined to be 87(3)% by averaging 50 spectroscopic profiles. No dependence on the clock interrogation time is observed; the efficiency remains within the experimental error even for longer interrogation times. This indicates that the missing population is unlikely to be

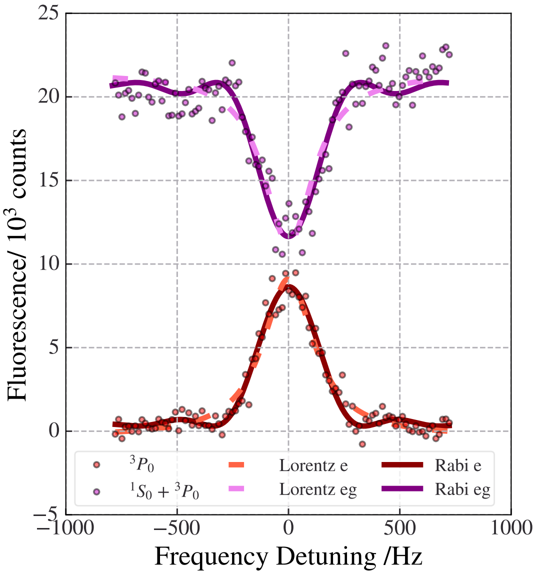

Fig. 3.13 Example of spectroscopy obtained during the repumping efficiency characterization, where the repumping process is not optimized. The clock interrogation time is 3 ms and, for this dataset, the repumping pulse is 5 ms long. The typical clock operation lineshape with optimized repumping process can be found in Fig.4.10.

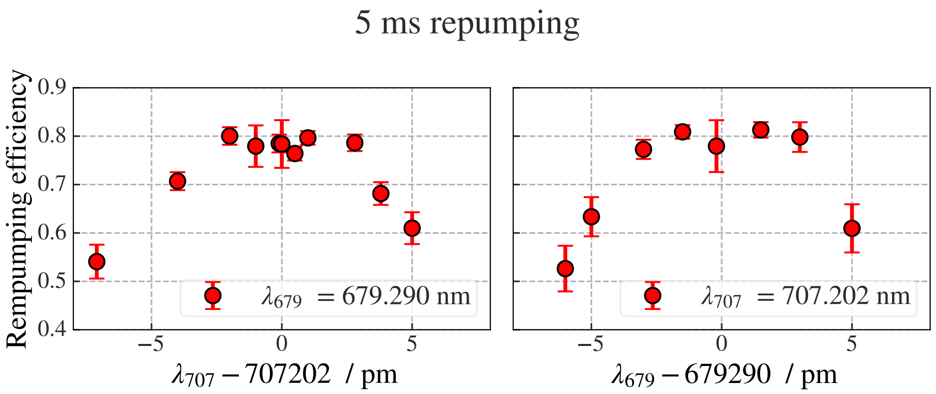

Fig. 3.14 Characterization of the repumping efficiency at different wavelengths, with a repumping pulse duration of 5 ms.

caused by clock-light-induced collisional effects, as observed in [163]. Instead, the main losses are most likely due to inelastic collisions between $5s5p\,^3\mathrm{P}_0$ atoms [145]
.

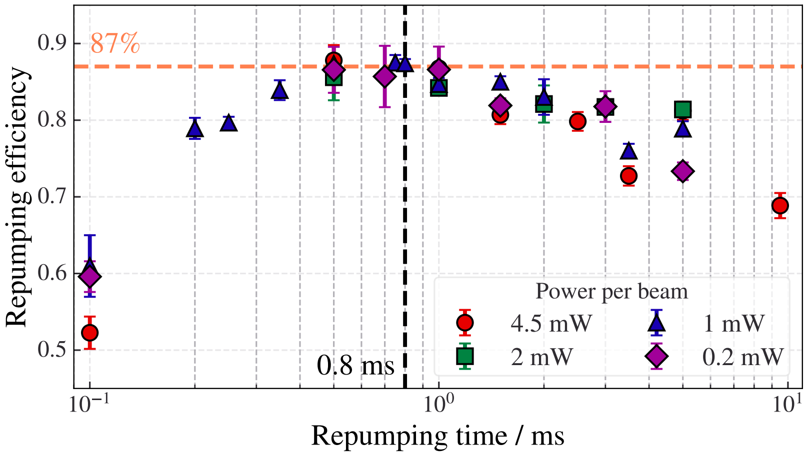

Fig. 3.15 Characterization of the repumping efficiency at different pulse durations and intensities.

3.3.3 Clock laser - 698 nm

The clock laser is a commercial DL-pro system (Toptica) operated near its maximum output power of approximately 35 mW. The available optical power is distributed among four main branches, as shown in Fig. 3.16.

One branch is directed to the wavelength meter, where the clock laser serves as a reference for stabilizing the repumper frequencies, as discussed in Section 3.4.3. A second branch is sent to the frequency-stabilization setup via a fiber-coupled electro-optic modulator (EOM). This EOM is driven with a high-frequency sawtooth waveform generated by a non-linear transmission line (NLTL) from Picosecond Pulse Labs model 7100 -110. This is used to perform a Serrodyne modulation [164, 165] which provides a frequency shift of the optical carrier, with high sideband suppresion [166], on top of which the Pound-Drever-Hall modulation is applied for laser stabilization in a similar way to the dual-sideband offset technique [167, 168].

A third portion of the light is delivered to an optical frequency comb [169] through a phase-stabilized 20 m fiber link. There, a virtual beatnote with the IT-Yb1 clock laser at 1156 nm [170] is produced. This beatnote is subsequently processed to perform spectral-purity transfer, improving the instability of the local clock laser by approximately one order of magnitude through feedback applied to the frequency of the sawtooth drive (see Sec 3.4.2).

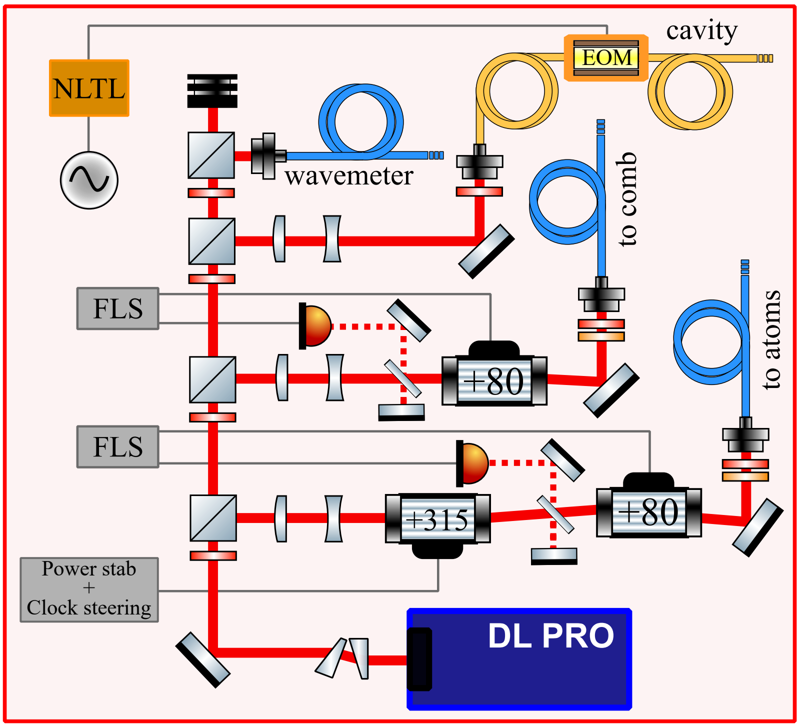

Fig. 3.16 Clock laser distribution layout. See main text for details. FLS: Fiber link stabilization, NLTL:non-linear transmission line.

Finally, the majority of the optical power (about 20 mW) is directed towards the branch ending at the atomic sample, where the net available maximum optical power is 4 mW. In this branch, two acousto-optic modulators (AOMs) are employed: an 80 MHz AOM used to phase-stabilize the 5 m fiber link, and a second AOM used to control the optical frequency delivered to the atoms. The drive signal for the latter AOM (approximately 315 MHz) is generated by a Siglent SDG6032x waveform generator connected to the experiment-control computer. This same signal is also used to implement power stabilization of the clock light.

To ensure that both the fiber link stabilization loop and the power stabilization loop remain continuously active, the light delivered to the atoms is never switched off. Instead, during the state-preparation phase, the clock laser is detuned by 200 kHz from the clock transition using the generator frequency-shift keying (FSK) modulation. Another reason to keep the AOM RF drive always on is to avoid the phase drifts due to thermal gradients induced by the power switching of the RF drive. Frequency switching does introduces phase noise too, but at a much smaller level so that the systematic frequency shift is at the level of 10^{-18} [170, 171].

Furthermore, since the AOM is located within the Doppler-noise cancellation (DNC) interferometer used for fiber noise suppression [172], any frequency modulation is interpreted by the stabilization loop as a phase perturbation to be compensated, leading to a residual systematic shift. In principle, this effect could be mitigated by symmetrizing the interrogation sequence (e.g. alternating red- and blue-detuned phases), thereby averaging the induced shift to zero [170]. However, given the small magnitude of the effect and the absence of detectable noise associated to the FSK modulation in our DNC system error signal, we do not perform switching between red and blue detuning and just keep a constant red detuning of 200 kHz.

3.4 Frequency stabilization and monitor

3.4.1 Multi-wavelength cavity

The core of the laser frequency stabilization system is an optical reference cavity (ORC), whose spacer is made of ultra-low-expansion (ULE) glass, of cylindrical shape with length $L = 10\,\mathrm{cm}$ and diameter $\phi = 5\,\mathrm{cm}$. The cavity mirrors are dielectric-coated to provide high reflectivity at 922 nm, 813 nm, and 689 nm, providing a finesse of approximately 10^4 at 689 nm and 10^3 at the other two wavelengths. Further details on the system can be found in [86], which remains accurate in describing the stabilization schemes for the cooling and trapping lasers. Here it is sufficient to note that the 689 nm and 922 nm lasers are locked to the ORC using the dual-sideband offset-locking technique [167], enabled by the use of large bandwidth fiber-coupled waveguide EOMs (Jenoptik PM705, PM905), which conveniently compensates for the cavity drift of approximately $95(2)\,\mathrm{mHz\,s^{-1}}$ estimated by long-term monitoring of the $5s^2\,{}^1\mathrm{S}_0 \leftrightarrow 5s5p\,{}^3\mathrm{P}_1$ resonance [86].

For the lattice laser, implementing dual-sideband offset locking is impractical due to the characteristics of the employed electro-optic modulator (EO-PM-NR-C1, Thorlabs). This device has a limited usable bandwidth of 100 MHz and a relatively large half-wave voltage V_π=136 V. This poses the major constraint, as achieving a sufficiently large modulation index at the desired offset frequency would require RF power levels well beyond what the modulator is designed to handle.

The clock laser is pre-stabilized to the same optical reference cavity (ORC), and Fig. 3.17 shows the performance of this resonator as measured by the frequency instability of the virtual beatnote generated via the frequency comb between our clock laser and the Yb clock laser at 1156 nm (see Sec. 3.4.2). The drift is not strictly linear on short timescales, which can be attributed to several effects, mainly uncompensated RAM, intracavity power fluctuations of all lasers locked to the cavity, and residual environmental seismic noise. Altogether, this ORC limits the short-term stability of our clock laser to approximately 1×10^{-14} at 1 s averaging time and exhibits an unpredictable drift behavior, both undesirable for clock operation. In contrast, the Yb clock laser demonstrates a greater short-term stability of 2×10^{-15} at 1 s averaging time, and its cavity drift is compensated via a feedforward that keeps the 1156 nm vs. comb beatnote at a fixed frequency, thus restricting the long-term drift to that of the H-Maser used to stabilize the comb repetition rate which is in the order of 6×10^{-16}/day [173]. We therefore use the virtual beatnote signal to transfer the 1156 nm laser stability to our clock laser, as described in the following subsection.

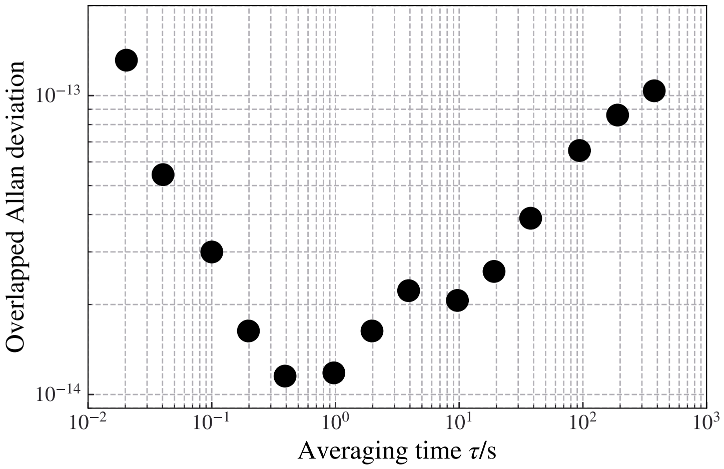

Fig. 3.17 Clock laser frequency instability measured via the virtual beatnote with the 1156 nm Yb clock laser.

3.4.2 Spectral purity transfer via serrodyne modulation

Spectral purity transfer. The consolidation of the spectral purity transfer between the 1156 nm Yb clock laser and our clock laser was an important part of the early stages of this work. A detailed description of the Serrodyne modulation setup and its efficiency characterization can be found in [166]. Figure 3.18, extracted from [166], illustrates both the setup for spectral purity transfer and the configuration used for phase-noise characterization of the NLTL.

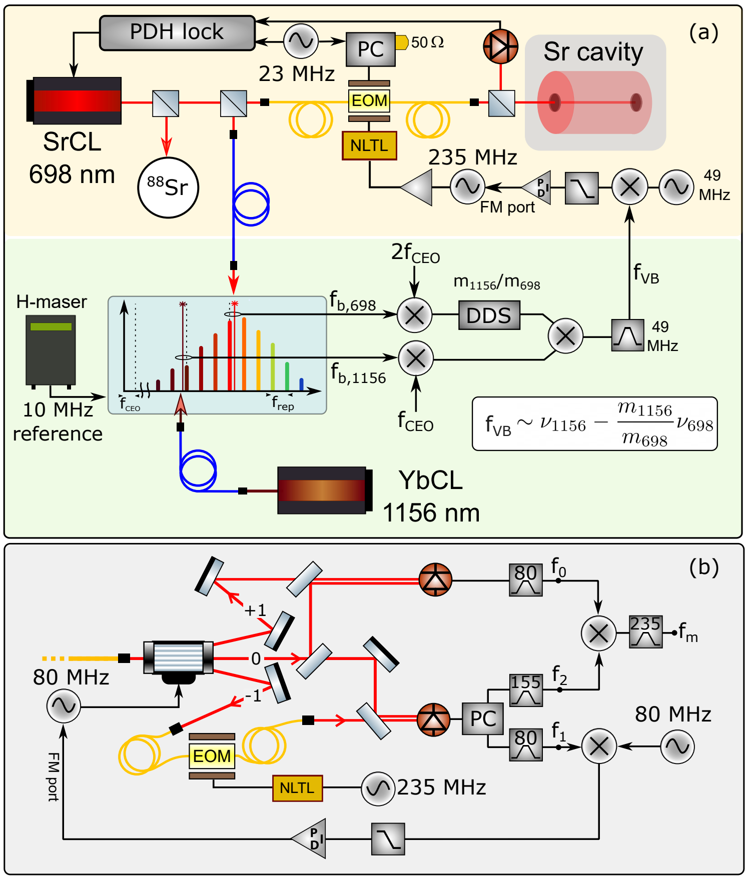

Fig. 3.18 From [166]. (a) Spectral purity transfer setup. (b) Raman-Nath interferometer used to characterize the serrodyne modulator noise.

In summary, the transfer mechanism operates as follows. The 689 nm laser is offset-locked to the ORC described in Section 3.4.1, with a 235 MHz offset provided by the NLTL. The NLTL is a nonlinear component that generates a radio-frequency (RF) comb containing harmonics of its input signal. Therefore, in the time domain, the NLTL output resembles a sawtooth waveform, whose quality depends on the NLTL performance. When this signal is applied to the EOM, it produces a nearly linear phase ramp. Since the instantaneous optical frequency is proportional to the time derivative of the phase, such a linear phase modulation results in a constant frequency shift of the optical field. This is in contrast with a sinusoidal drive, which produces a sinusoidal phase modulation and therefore generates symmetric sidebands around the carrier without shifting its central frequency.

The 698 nm laser is then sent to the same frequency comb as the 1156 nm laser, although their respective beatnotes arise from interaction with different comb branches. These two beatnotes are processed through RF chains designed to remove common-mode noise introduced by the frequency comb carrier-envelope offset frequency, f_{CEO}. The Sr clock laser beatnote is subsequently scaled by the ratio of the comb tooth numbers, m_{1156}/m_{698}. After rescaling, this signal is mixed with the output of the Yb clock laser beatnote processing chain, this time canceling the comb repetition rate noise and yielding the final signal of interest: the virtual beatnote, f_{VB}. Residual noise (below 1×10^{-17}) not related to the 1156 nm nor to the 698 nm lasers in this signal is due to uncorrelated noise in the two different comb branches.

Finally, a phase-locked-loop (PLL) is implemented and the spectral purity transfer is realized via frequency corrections on the 235 MHz driving signal of the NLTL. Performance of the transfer can be appreciated in Fig. 3.19 where the instabilities of the frequency corrections applied to our clock laser and to the Yb clock laser, during different and uncorrelated measurements, are compared.

Between 1-10 s, where the measurement noise is dominated by the clock lasers flicker noise floor, Sr data shows approximately 1.3 times higher instability. For longer times, the behavior is determined by the Yb clock laser drift correction [170] and the particular clock cycle loops of each clock.

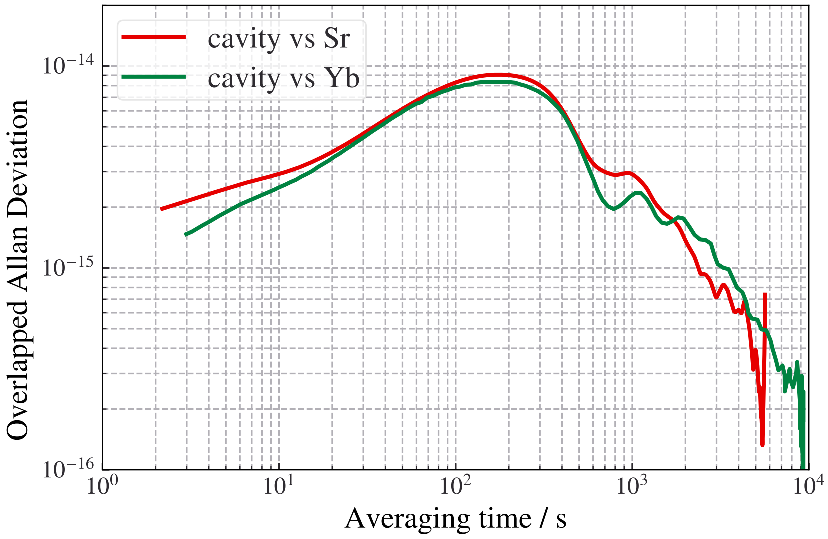

Fig. 3.19 Cavity vs atoms: Yb (red) data, Sr (green) data acquired during this work. The two measurements are acquired not simultaneously, but on the same day.

Serrodyne frequency shifter noise. We also experimentally evaluated the contribution of the serrodyne modulation to the overall phase noise of the optical system used to realize the spectral purity transfer. To assess this we implemented a composite self-heterodyne interferometer based on an AOM operating in the Raman-Nath (RN) regime, as shown in Fig. 3.18.

The interferometer consists of two Mach-Zehnder interferometers (MZIs) generated by a single beam incident on the AOM driven at 80 MHz. The reference arm is provided by the unshifted zeroth diffraction order of the AOM, while the ±1 diffraction orders produce two separate MZI beatnotes. The "-1" MZI includes the waveguided EOM with the serrodyne modulation, and generates two beatnote frequencies: f_2 at 155 MHz, corresponding to the frequency-shifted optical carrier, and f_1 at 80 MHz, corresponding to the residual unshifted fraction. The f_1 signal is used to actively stabilize common-path phase perturbations, as it only encodes optical path length fluctuations information. Consequently, the phase noise of f_2 reflects the contribution of the serrodyne shifter itself.

The "+1" MZI beatnote, f_0, is affected by both the phase noise compensation of the "-1" arm and the AOM intrinsic phase noise. By mixing f_0 and f_2, an RF signal f_m is obtained in which the anti-correlated AOM phase noise is largely canceled, providing a cleaner measure of the serrodyne induced phase noise.

The phase noise spectra of f_0, f_1, f_2, and f_m were measured using a phasemeter (Microsemi 5125A) and are shown in Fig. 3.20. For Fourier frequencies below the servo bump at approximately 2 kHz, the phase noise of f_2 is limited by the residual noise of the 235 MHz serrodyne oscillator, setting an upper bound for the serrodyne contribution, which is lower than the limit reported in [174] for frequencies above 10 Hz. For frequencies above 2 kHz, the mixed signal f_m provides an upper limit on the serrodyne induced phase noise. Between 2 and 40 kHz, the noise is dominated by residual environmental fluctuations, as indicated by the unlocked f_1 spectrum (blue trace). Above 40 kHz, f_m shows lower phase noise than both f_0 and f_2, corresponding to the uncompensated noise of the 80 MHz AOM driver. This demonstrates the effectiveness of common-mode noise rejection in the RN heterodyne interferometer. An estimate of the phase jitter due to serrodyne modulation can be obtained by integrating the spectral densities of f_2 and f_m over their respective frequency ranges, obtaining for 1 s of integration time $\phi_{serr}^{rms} \lesssim 3 \times 10^{-3}$ rad.

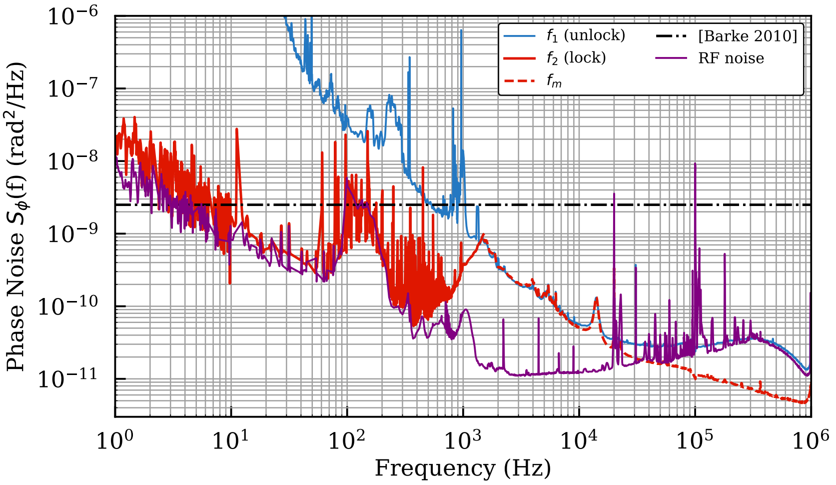

Fig. 3.20 From [166]: phase noise measured with RN heterodyne scheme. See main text for details.

The operation of the developed Raman-Nath interferometric scheme is then later expanded in detail in [175].

3.4.3 Wavelength meter frequency readout and stabilization

As mentioned in Sec. 3.4.2, the repumpers frequencies are actively stabilized using a wavelength meter (WM, Bristol Instruments 671B). Figure 3.21 shows a schematic of the stabilization loop together with the interface of the control program. The principle of operation is straightforward: the frequency measured by the wavemeter is stabilized by adjusting the voltage applied to the PZT actuator of the 707 nm and 679 nm ECDLs.

The stabilization setup makes use of an 8-channel fiber-optic switch (FOS), which routes all optical sources in the experiment to the WM. The control program, developed following the communication guidelines in [176], is built around a dedicated wavemeter-manager thread. This thread continuously cycles through six channels. For each channel, it allows approximately 0.35 s for the FOS to settle before acquiring four channel readings, one every 50 ms, resulting in a full scan period of of the six channels of roughly 2 s.

When PID stabilization is enabled for the repumpers channels, the feedback loop runs with a user-defined update period, typically set to 5 s. During each period, the system averages all frequency readings collected from a single channel since the previous update, and store the result into a buffer. The PID controller periodically reads the buffer, computes the deviation from the setpoint oof this averaged frequency, which is either an absolute reading or a the frequency difference with respect to the clock laser. The resulting proportional and integral terms produce a correction voltage that is sent to a the power supply controlling the repumpers ECDLs PZT drive voltage, thus correcting the ECDL grating position. Each stabilization loop can be activated or deactivated independently, allowing flexible operation of the system.

By default, the program stabilizes both repumpers relative to the clock laser. In this way the sensitivity to drifts and calibration errors of the wavemeter is reduced. A dedicated safety mechanism continuously checks whether the clock laser remains within its expected frequency range, and if for some reason the clock laser drifts outside this window, the system automatically switches to absolute stabilization, preventing the clock laser abrupt frequency change to be transferred to the repumpers.

A representative measurement of the stabilization performance is shown in the bottom panel of Fig. 3.21, where the frequency difference between each repumper and the clock laser remains stabilized over nearly two days. The noise on the stabilization is about 400 MHz peak-to-peak, consistent with the WM declared performances. After approximately 45 hours, the PID loop is deliberately switched off to show the long-term drift of the free-running repumper lasers. In this particular case we observe roughly 1 GHz drift in 10 hours for the 679 nm and about 0.4 GHz

3.5 Experimental control and typical sequence

The central hardware element of the experiment control architecture is an FPGA (Xilinx Spartan XC3S250E), clocked at 10 MHz, to which several TTL, programmable DDS, and DAC boards are connected through a 64-bit serial bus. The FPGA communicates with the experiment computer via USB and is operated using a Python based control system originally developed for Bose-Einstein condensate experiments at UNITN [177]. A detailed description of the hardware can be found in [85, 178]. Here it might be interesting to just recall that the system can sustain instruction rates up to 2.5 MHz, corresponding to a minimum time step of about 40 μs between two programmed actions.


Repumpers wavemeter lock

Reference - FOS channel 0
429.227675THz

FOS Channel 4
423.913477 THz
Setpoint / nm: 707,20200 — Lock — Unlock
Rigol CH 1: 8,479 V — Manual

FOS Channel 5
441.332062 THz
Setpoint / nm: 679,29000 — Lock — Unlock
Rigol CH 2: 24,710 V — Manual

PID Settings — Show Plot — Show Wavelength — Enable Logging

FOS Channel 1
325.519785 THz

FOS Channel 2
434.829181 THz

FOS Channel 3
368.554294 THz

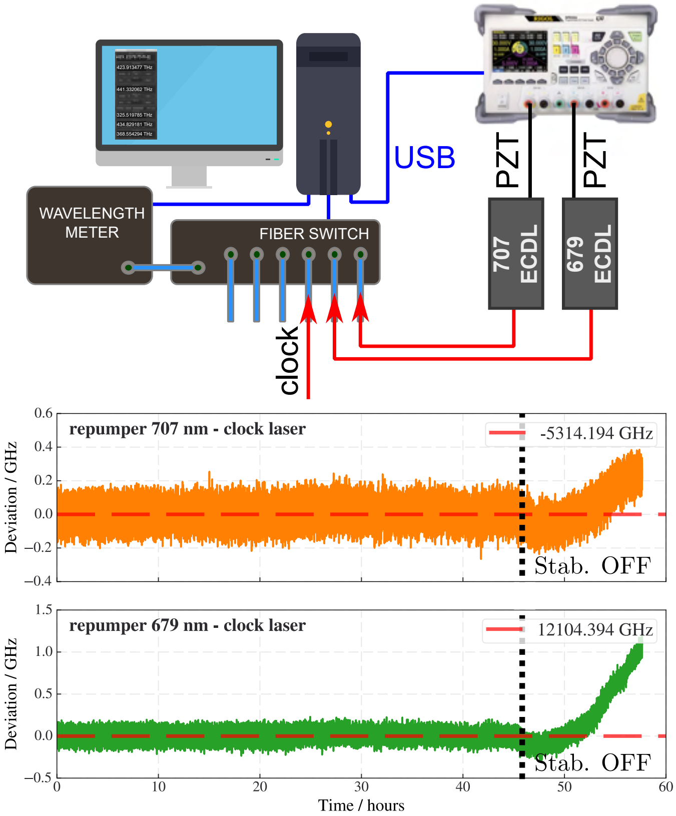

Fig. 3.21 Schematic of the repumping lasers stabilization setup together with the control program interface. Plot: Typical time trace of the frequency difference between each repumper and the clock laser as measured by the wavemeter. After $t = 45$ h, the stabilization loop is intentionally disabled to illustrate the drift of the 707 nm (orange trace) and 679 nm (green) lasers when operating without feedback.

During this work, a simple but effective control interface was developed to make operation of the clock more convenient. A GUI-based program was implemented to integrate the three main components of the experiment: the FPGA timing sequence, the CCD image acquisition and processing, and the control of the signal generator that drives the steering AOM of the clock laser which is also connected via USB to the experiment computer. The need for such an interface became evident when we realized that our previous way of coordinating these components suffered from subtle synchronization issues. These occasionally produced glitches in the sequence of frequencies that the signal generator had to produce during a clock interrogation. The root cause of the problem was that the program controlling the signal generator and the one handling the data acquisition were running in two parallel and independent loops. The solution implemented here, schematized in Fig. 3.22, eliminates this issue by merging the control of all components into a single program, clockmaster.py, which forces full sequentiality between the execution of each experimental cycle and any frequency update applied to the signal generator that drives the clock laser AOM.

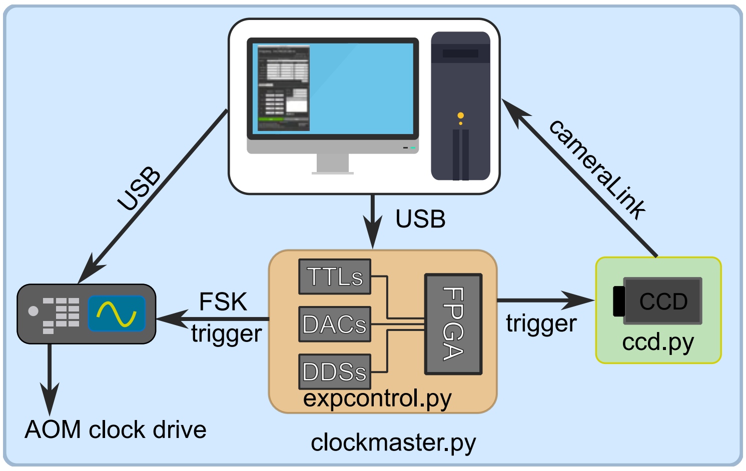

Fig. 3.22 Block diagram of the main experiment control system components. See main text for details.

The program clockmaster.py is designed to perform two main tasks: clock spectroscopy (graphical interface shown in Fig. 3.23) and interleaved clock operation (graphical interface shown in Fig. 3.24).

Clock spectroscopy. A typical sequence for acquiring a single spectroscopy point proceeds as follows. First, the experimental sequence and the selected experimental parameters are loaded into the FPGA. The FPGA then executes the full timing sequence, in particular it triggers the FSK modulation (see Sec. 3.3.3) that initiates the clock interrogation, and controls the triggering of the CCD camera. The CCD usually records two images per cycle: one for atoms in the ground state and one for atoms in the excited state. The camera, connected to the control computer via a CameraLink interface, acts as a server through the dedicated control program ccd.py. Once the images are acquired, the main control program analyzes them to retrieve the fluorescence counts and computes the excitation probability. Importantly, until this last step is not completed, updating the clock laser AOM driving frequency is not allowed. This strict sequentiality ensures that any frequency change applied to the AOM happens at the appropriate time.

● Reference variables ○ Measurement variables ○ Sideband variables

RUN: 4

Central frequency / Hz 8065.000

Span / Hz 100.00

Points 50

2.00 Hz

Hop frequency / Hz 0.00

Iterations 1

Notes:

☒ Save data

☐ Randomize array

0%

Fig. 3.23 Clock spectroscopy settings within the control graphical interface. From this panel, the central frequency of the scan, the frequency span, and the total number of points can be selected. The set of experimental variables to be used is chosen via one of the top radio buttons, and a quick fit of the spectroscopic profile can be performed with a single click. The plots on the right side are a representative output of a spectroscopy scan: blue points represent the ground state signal, red points represent the excited state signal, while the magenta and green point represent the total population and the excitation fraction respectively.

Interleaved operation. In interleaved operation, two independent clock loops run with slightly different experimental parameters, typically differing by only a single quantity, to evaluate relative frequency shifts [179, 180]. We refer to these two sets of parameters as the Reference and Measurement modes. Most key experimental parameters, including interrogation time, the magnetic field used to induce the clock transition, atom-number related settings, and lattice intensity, can be configured through the graphical interface shown in Fig. 3.25.

During interleaved operation, since the atom has no hyperfine structure, the clock is interrogated on two resonances only, which we denote as f_0 (Reference) and f_1 (Measurement). A single clock interrogation therefore consists of four experimental sequences, enumerated and illustrated in Fig. 3.24: sequences 1 and 2 correspond to the interrogation of the red-detuned side of f_0 (1) and f_1 (2), while sequences 3 and 4 correspond to the interrogation of the blue-detuned side of f_0 (3) and f_1 (4). The detuning is set via the hop parameter, which is usually chosen to lock the clock at the half-width at half-maximum (HWHM) point.

Once the four sequences are completed, the error is determined as

$$\varepsilon = p_b - p_r$$

	Reference f0	Measurement f1
f / Hz	314798066.035	314798061.851
hop / Hz	17.00	17.00
k / 1/Hz	-20.00	-20.00
Gp	0.280	0.280
Gi	0.0010	0.0010

Ref. Fluo 8000

Meas. Fluo 8000

Plot memory 50

Notes:

RUN: 0

Fig. 3.24 Clock interleaved operation settings within the control graphical interface. From this panel, the expected center frequencies of the resonances f_0 (reference) and f_1 (measurement), the detuning at which the interrogation happens (hop) and the loop gains can be set. The right side of the figure shows conceptually the procedure of the interleaved operation. Red-detuned side interrogation of the reference (1) and measurement (2) excitation profiles, blue-detuned side interrogation of the reference (3) and measurement (4) excitation profiles.

where p_b and p_r are the blue-detuned and red-detuned excitation probabilities, and the feedback is computed as

$$\delta f = k\left(\mathrm{G}_p\,\varepsilon + \mathrm{G}_i\,\varepsilon_{\mathrm{int}}\,dt\right),$$

where $\varepsilon_{\mathrm{int}}$ is the integrated error, dt is the duration of the four experimental sequences, and k is determined by the spectroscopic profile as the slope of the error signal. The parameters G_p and G_i are the proportional and integral gains of the loop, respectively, and have been optimized by minimizing the noise in the interleaved measurement. These gains are fixed and never changed during operation.

Figure 3.26 shows the typical experimental sequence used during the measurements presented in this work. Compared to the sequence reported in [86], the duration of the cooling phase is reduced from 280 ms to 215 ms, which does not sacrifice cooling performance in terms of the final temperature of the red MOT, although it slightly reduces atom loading capabilities. Additionally, instead of switching on the lattice early in the experimental sequence, it is ramped up over 2.5 ms and 20 ms before releasing the red MOT trap, ensuring loading from a MOT with a well-defined and measurable spatial extension. This approach is useful for modeling the atom number distribution along the lattice sites (see Sec.5.1.4).

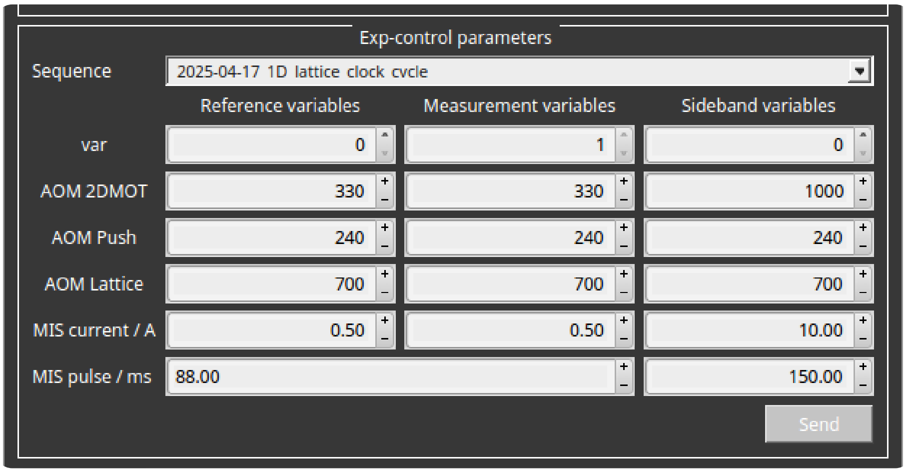

Sequence: 2025-04-17 1D lattice clock cvcle

	Reference variables	Measurement variables	Sideband variables
var	0	1	0
AOM 2DMOT	330	330	1000
AOM Push	240	240	240
AOM Lattice	700	700	700
MIS current / A	0.50	0.50	10.00
MIS pulse / ms	88.00		150.00

Fig. 3.25 Experimental parameter settings within the control graphical interface.

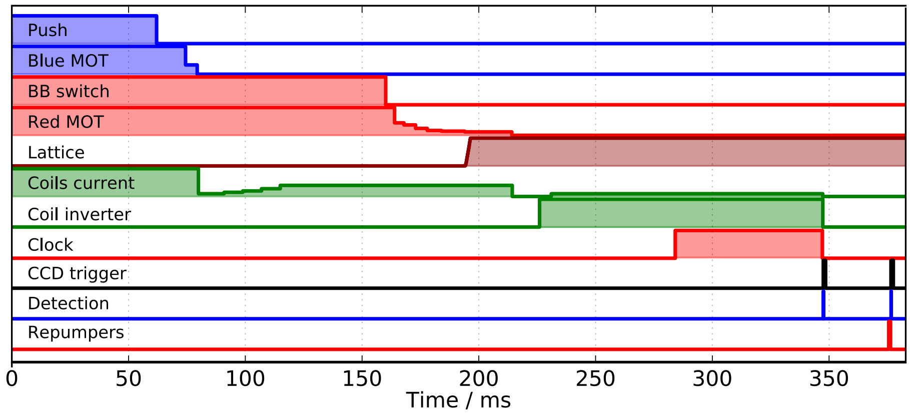

Fig. 3.26 Typical experimental sequence

After the lattice is formed, the MOT coils are switched to a Helmholtz configuration, the bias magnetic field for clock interrogation is activated, and the actual clock interrogation begins after 30 ms, allowing time for the magnetic field to stabilize. At the end of the interrogation pulse, which time can vary during the different measurements performed during this work, the ground and excited state populations are detected, with imaging times as described in Sec. 3.2.2. The time interval between the two images is limited to at least 29 ms due to a combination of the CCD frame rate and the repumpers' shutter opening time.

Chapter 4

Systematic evaluation of a ^{88}Sr optical lattice clock

Table 4.1 Accuracy budget of the INRiM ^{88}Sr optical lattice clock. All values are expressed in relative units of 10^{-16}.

Effect	Shift / 10^{-16}	Uncertainty / 10^{-16}
Clock AC Stark	-1144.0	1.9
Quadratic Zeeman	-689.0	2.0
BBR	-50.3	0.7
Lattice AC Stark	10.8	1.5
Collisions	3.3	1.9
Other shifts	0.0	1.0
Total	-1869.2	3.9

This chapter presents the results obtained during the evaluation of the uncertainty budget of the INRiM ^{88}Sr optical lattice, with particular attention to the quadratic Zeeman shift (Sec. 4.1) and the AC Stark shift induced by the clock-laser light (Sec. 4.2), which are particularly important in magnetically induced clock transitions. In this context, additional details are provided on how the relevant quantities are experimentally controlled, expanding on what already mentioned in 3.1. Then Sec. 4.3 combines the previous results, and clarifies the reference operating point choice, showing how the total combined uncertainty due to the corresponding shifts varies with the applied magnetic field and the clock laser intensity. The evaluation of lattice light induced AC Stark shift is presented in Sec. 4.4, while other systematic effects are discussed in 4.5.

The resulting uncertainty budget is summarized in Tab.4.1, the total fractional frequency uncertainty is estimated to be 3.9×10^{-16}, about one order of magnitude lower than the value recently declared by the UMK ^{88}Sr optical lattice clock [181]. The measurement and evaluation of the collisional shift is detailed separately in chapter 5.

4.1 Quadratic Zeeman shift

The quadratic, or second-order, Zeeman shift is one of the leading systematic effect affecting the ^{88}Sr clocks, where the clock transition is induced by the application of a bias magnetic field, as described in Sec. 2.2. Here, the shift contributions coming from magnetic fields along the three spatial directions X, Y, and Z (recall Fig. 3.2) are evaluated by performing relative frequency shift measurements with interleaved clock operation (Sec. 3.5). All the measurements presented in this chapter are fitted with the function

$$\Delta\nu_i(I_{\mathrm{meas}}) = y_0 + \beta_{88}\left(k_i I_{\mathrm{meas}} + B_{0i}\right)^2 \tag{4.1}$$

where $(k_i I_{\mathrm{meas}} + B_{0i})$ is the total field along the direction i, composed by residual/bias field B_{0i} and the one provided by the particular sets of coils $k_i I_{\mathrm{meas}}$, where I_{meas} is the coils' current and also the quantity changed during the interleaved operation. The parameter y_0 is a frequency offset arising from the differential nature of the measurement, and ultimately representing the absolute shift at the reference operating current I_{ref}. Finally, β_{88} is the quadratic Zeeman shift coefficient, for which we use the value $-23.38(3)\,\mathrm{MHz\,T^{-2}}$ provided in [129]. The resulting absolute shift at the generic operating current I will then be given by

$$\Delta\nu_i(I) = \beta_{88}\left(k_i I + B_{0i}\right)^2 - y_0. \tag{4.2}$$

Changing the magnetic field has the consequence to induce different Rabi frequencies (see Sec. 2.2) for the clock cycles of the interleaved measurement, which means that the optimal interrogation time T_π is different. In order to avoid having unequal cycle times, particularly during the measurements along the Z direction where the stronger magnetic field is applied, the interrogation time has been set to a value that provided similar excitation on both the interrogated clock lines.

4.1.1 Coils driving circuits

Before diving into the frequency shift measurements, let's add a few more details on the coils driving system already described in Sec. 3.1. The current noise of the coil drivers was characterized to assess its contribution to the clock frequency instability. The noise properties of an output current of $I_{out} = 1$ A, either provided by the X,Y coils driver or the Z and MOT/MIS coils driver, have been evaluated with a 6.5 digits digital multimeter (DMM,Keysight 34411A). The measured instabilities of the driving current are shown in the right panel of Fig. 4.1 and are translated into clock frequency instability using Eq. (4.1) as:

$$\sigma_y(I) \simeq \sigma_{yI} \frac{\partial}{\partial I} \left(\frac{\Delta \nu}{\nu_{88}} \right) \approx \frac{2 k_i^2 \beta_{88}}{\nu_{88}} \sigma_{yI} I, \tag{4.3}$$

where σ_{yI} denotes the fractional current instability and $\sigma_y(I)$ the corresponding fractional clock frequency instability. The coils coefficient is set to $k_i = 1\,\mathrm{mT\,A^{-1}}$ which is roughly what is expected, and measured, for the MIS coils. The measured current noise is compliant with manufacturer specifications. At an operating current $I = 1$ A, the introduced frequency instability at 1 s averaging time is slightly above 1×10^{-18}. Therefore, under the present operating conditions current noise is not a concern for the clock long-term stability. The noise of the output current might become a limiting factor if the clock laser available has extremely good noise properties, enabling several seconds of interrogation time and thus the operation at extremely weak magnetic fields. In this case, an active stabilization of the magnetic field may be realized [182, 183].

Being able to reverse the magnetic field is important for a more accurate determination of the vertex of Eq. (4.1), i.e. the zero magnetic field point, which is what we are interested in. A simple H-bridge was implemented to enable reliable and fast reversal of the magnetic field polarity and it is schematized in Fig. 4.1. The bridge is realized using insulated-gate bipolar transistors (IGBTs) and home made driver to control their gate voltage to realize the commutation table shown in Fig. 4.1. The control signals are two TTLs provided by the experiment control system: ON/OFF

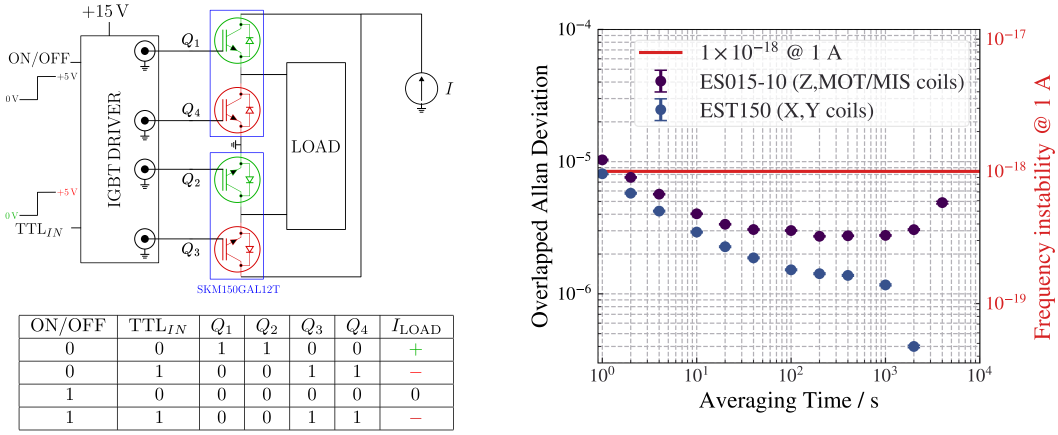

ON/OFF	TTL$_{IN}$	Q_1	Q_2	Q_3	Q_4	I_{LOAD}
0	0	1	1	0	0	+
0	1	0	0	1	1	−
1	0	0	0	0	0	0
1	1	0	0	1	1	−

Fig. 4.1 Left: IGBT (SKM150GAL12T) based H-bridge implemented to reverse the current into a generic coils pair. The voltages at the IGBTs gates Q_i satisfy the truth table realized via an home-made TTL controlled driver. Right: evaluated output current instability of the X,Y, an Z coils power supply, at an output current I = 1 A.

and TTL$_{IN}$. The ON/OFF signal mainly controls if the current flow is enabled and it is usually kept in the ON state, while the TTL$_{IN}$ signal is used to reverse the current flow. The circuit response time is less than 20 ms. When TTL$_{IN}$ =0 V (+5 V) the voltage at the gates Q_1, Q_2 (Q_3, Q_4) is high, and the current flow is positive (negative).

4.1.2 Transverse plane magnetic fields contribution

Recalling from Sec. 2.2 how the magnetic field determines the coupling strength between the clock states and, most importantly, their energy difference, it is desirable to operate in a condition where the total magnetic field is null if there is no mixing field applied. This might not always be possible due to technical reasons, and the total shift arising from the magnetic field in all directions must be evaluated. In the following, we first characterize the transverse Zeeman shifts, then we derive a calibration to correct for their contribution to the clock frequency.

On the transverse plane, orthogonal to the MIS magnetic field, there are two field components generated by two sets of coils in which the current flowing is $I_{0\mathrm{X}}$ =1.425 A and $I_{0\mathrm{Y}}$ =1.408 A, respectively. These values were previously chosen by consideration on the red MOT position in the imaging plane and its atom number. In particular, by reducing its position sensitivity to the applied field gradient during the MOT phase. This way, the magnetic field in a given direction can be minimized.

In order to evaluate the Zeeman shift along these directions, relative frequency shift measurements were performed by changing the coils current values around the working point defined above. When operating on the X (Y) coils, the Y (X) coils current was kept at $I_{0\mathrm{Y}}$ ($I_{0\mathrm{X}}$). Measurements were also performed at different MIS magnetic fields, consequently adjusting the clock laser intensity to have a Rabi frequency corresponding to an optimal interrogation time $T_\pi = 50\,\mathrm{ms}$. The results are shown in the top panel of Fig. 4.2, where each data point corresponds to a 30-40 minutes long measurement with a typical interleaved instability of $\sigma_y(\tau) \sim 6\times10^{-15}/\sqrt{\tau/\mathrm{s}}$.

Looking at the results it is found that the observed shift at different MIS current values do not overlap. This suggests that the MIS coils introduce unwanted field components in the horizontal plane whose strength depends on the applied MIS current I_{MIS}. These components may arise due to a combination of effects among which: a slight misalignment of the MIS coils centers, mechanical torques affecting the coils when switching from anti-Helmholtz to Helmholtz configuration and mutual inductance in the coils system. For each coil pair, the data are simultaneously fitted with Eq. (4.1) forcing the parameter k_i to be equal for each dataset finding $k_{\mathrm{X}} = 0.271(5)\,\mathrm{G\,A^{-1}}$ and $k_{\mathrm{Y}} = 0.289(3)\,\mathrm{G\,A^{-1}}$.

The bottom panel of Fig. 4.2 shows the fit parameter $B_{0\mathrm{X}}$ and $B_{0\mathrm{Y}}$, which is found to increase linearly as a function of I_{MIS}, with a proportionality constant that we define as $k_{i\mathrm{Z}}$, $i \in \{X, Y\}$, thus modeling the total field components as

$$B_{\mathrm{X}} = k_{\mathrm{X}} I_{\mathrm{X}} + k_{\mathrm{XZ}} I_{\mathrm{MIS}} + B_{BG,\mathrm{X}} \tag{4.4a}$$

$$B_{\mathrm{Y}} = k_{\mathrm{Y}} I_{\mathrm{Y}} + k_{\mathrm{YZ}} I_{\mathrm{MIS}} + B_{BG,\mathrm{Y}}. \tag{4.4b}$$

The values for k_{iZ} and $B_{BG,i}$, which represent the laboratory background field components along i, are extracted from a linear fit of offset fields retrieved by the simultaneous fit of the parabolas in Fig. 4.2. Results are reported in Tab. 4.2, together with the coils conversion factors k_i. Considering a total Earth's magnetic field $B_{\mathrm{E}} \simeq 0.48\,\mathrm{G}$, and given the experiment location in Turin (45°00'54.3"N 7°38'21.9"E) the expected magnetic inclination is around 61°, thus $B_{\mathrm{E,H}} = B_{\mathrm{E}}\cos 61^\circ \approx 0.23\,\mathrm{G}$. Using the background field estimated in Tab. 4.2 we found an experimental value $B_{\mathrm{H},exp} = 0.25(7)\,\mathrm{G}$ compatible with the expected terrestrial field.

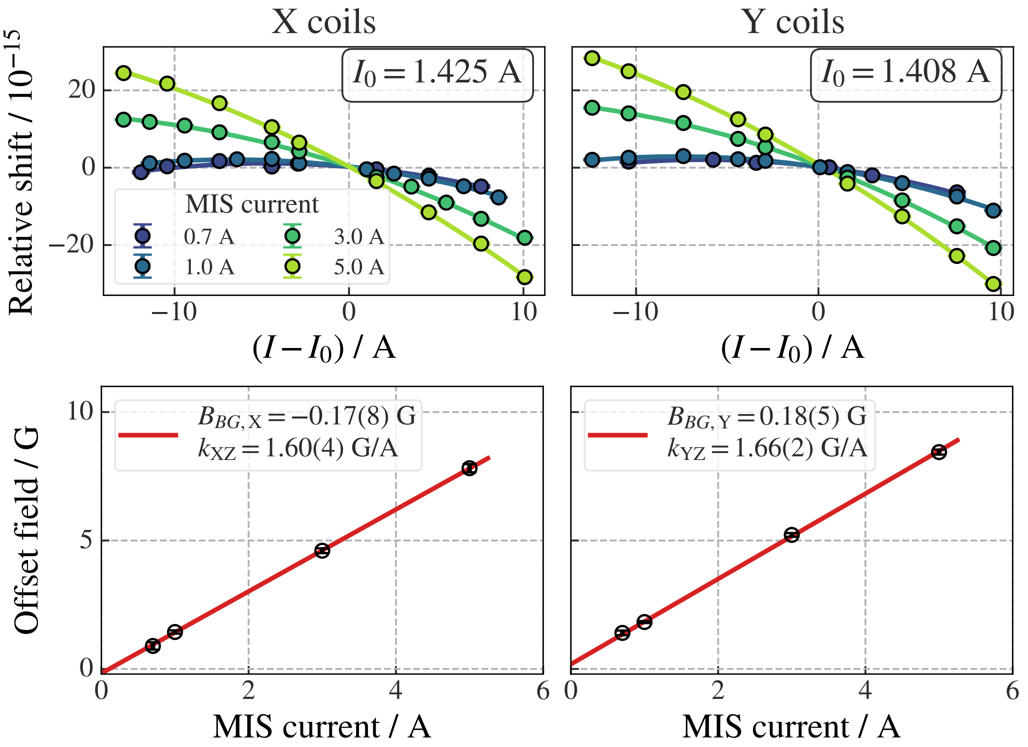

Fig. 4.2 Top: Relative frequency shift measurements changing the bias coils current around the references $I_{0\mathrm{X}}$ =1.425 A (left) and $I_{0\mathrm{Y}}$ =1.408 A (right), and at different I_{MIS}. Solid lines are simultaneous fits to Eq. (4.1) constraining the value of k_i to be equal for each dataset. Bottom: values of the offset fields B_{0i} fitted at different I_{MIS} for X (left) and Y (right) coils data. In both direction the offset fields linearly increase suggesting the MIS field introduces unwanted component in the orthogonal plane. Solid lines are linear fit to $B_{0i} = k_{\mathrm{iZ}} I_{\mathrm{MIS}} + B_{BG,i}$.

i	$k_i/\mathrm{G\,A}^{-1}$	$k_{i\mathrm{Z}}/\ \mathrm{G\,A}^{-1}$	$B_{BG,i}/$ G
X	0.271(5)	1.60(4)	-0.17(8)
Y	0.289(3)	1.66(2)	0.18(5)

Table 4.2 Parameters extracted from the data in Fig. 4.2

Now considering the most important part, the shift evaluation, we used Eq. (4.2) for each fitted parabola in Fig. 4.2, obtaining a correction that is dependent on the used I_{MIS} and shown in Fig. 4.3. The corrections are fitted with Eqs. 4.5 to obtain a calibration that is used when evaluating the shift contribute given by the MIS coils, as presented in the next section. In particular, we therefore evaluate the Zeeman shift correction that needs to be applied for the X and Y direction components as:

$$\Delta\nu_X^{corr}(I_{\mathrm{MIS}}) = \beta_{88}\,(k_{\mathrm{XZ}} I_{\mathrm{MIS}} + B_{0\mathrm{X}}) \tag{4.5a}$$

$$\Delta\nu_Y^{corr}(I_{\mathrm{MIS}}) = \beta_{88}\,(k_{\mathrm{YZ}} I_{\mathrm{MIS}} + B_{0\mathrm{Y}})\,, \tag{4.5b}$$

which are valid as long as the bias coils along X and Y are kept at currents $I_{0\mathrm{X}}$ and $I_{0\mathrm{Y}}$. The frequency offset parameters are set to zero by construction, the determined offset fields are consistent with the total fields expressed by Eqs. 4.4 at $I_{\mathrm{MIS}} = 0$, and finally the coefficients k_{XY} and k_{XZ} are consistent with the ones evaluated in Tab. 4.2. For completeness, the results are reported in Tab. 4.3. To give an idea of the correction magnitude and uncertainty, using I_{MIS} =1 A as a reference value the result is:

$$\frac{\Delta\nu_X^{corr}(I_{\mathrm{MIS}} = 1\,\mathrm{A})}{\nu_{88}} = -18(2)\times 10^{-16} \tag{4.6a}$$

$$\frac{\Delta\nu_Y^{corr}(I_{\mathrm{MIS}} = 1\,\mathrm{A})}{\nu_{88}} = -27.1(1.4)\times 10^{-16}. \tag{4.6b}$$

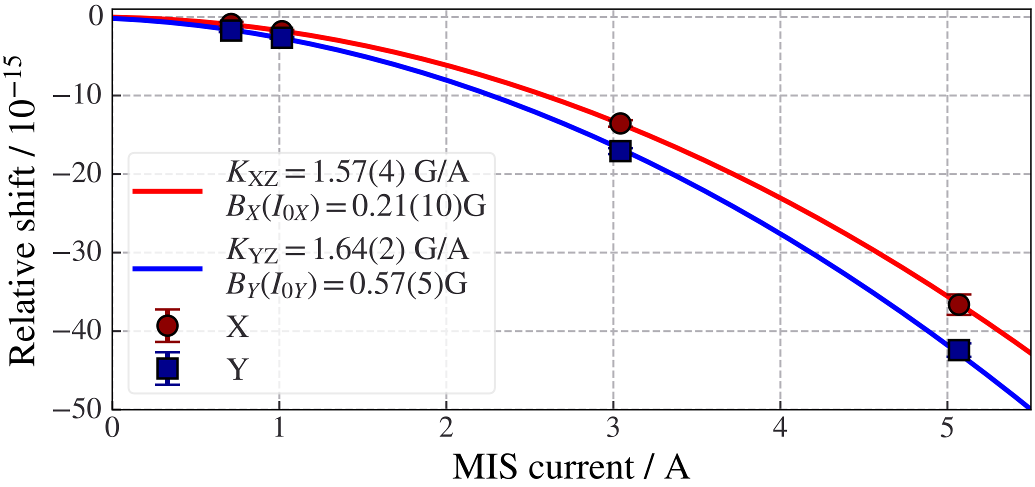

Fig. 4.3 $\Delta\nu_X^{corr}$ (left) and $\Delta\nu_Y^{corr}$ (right) as a function of the MIS current.

i	$k_{iZ}/\mathrm{G\,A}^{-1}$	$B_{0i}/$ G
X	1.57(4)	0.21(10)
Y	1.64(2)	0.57(5)

Table 4.3 Parameters extracted from the data in Fig. 4.3

4.1.3 Z direction: MIS field contribution and total Zeeman shift evaluation

Along the vertical direction Z, the total magnetic field is composed of three contributions: the background field, the field generated by the bias coils along Z, and the MIS magnetic field, which is typically the dominant one. The bias coils are primarily used to control the vertical position of the red MOT. We indicate the two first components as a single bias field B_{0Z}, thus expressing the total field along Z as

$$B_Z = K_Z I_{\mathrm{MIS}} + B_{0Z}. \tag{4.7}$$

We typically work at a non-zero vertical magnetic field B_{0Z} to maximize the overlap between the red MOT and the optical lattice, whose position has been selected to avoid unwanted speckle patterns from the optical window. While the same result could be obtained by changing the cooling light detuing and/or the MOT quadrupole field, these methods would affect the red MOT shape and consequently the atomic loading into the optical lattice. Hence for day to day adjustements we preferred to work with a non-zero compensation magnetic field in this direction. However, the contribution of this additional field is typically smaller than the bias MIS field used to induce the clock transition. Fortunately, the bias current I_{0Z} of these coils has to be changed rarely, usually after long shut down periods and only if the desired red MOT shape and position is not achieved adjusting the 689 nm laser detuning (to compensate for the cavity drift) and the trap beams alignment.

To evaluate the shift contribute given by B_Z, we proceeded as for the other directions but also accounting for the MIS field contribute in the orthogonal plane, which is different for each I_{MIS} value. For each measurement performed at I_{MIS} versus $I_{\mathrm{MIS}\,,ref}$ =1 A, the relative shift data is corrected by using the results of Eq. (4.5) with the parameters in Tab. 4.3. This way, we are able to isolate the effect of B_Z, and at the same time measuring the total 2$^{\mathrm{nd}}$-order Zeeman shift, since the effects along X and Y are automatically accounted for. The measurement results are shown in Fig. 4.4, together with a typical interleaved clock instability during the characterization. The fit results with Eq. (4.1) are summarized in Tab. 4.4. During the following measurement was kept I_{0Z} =1.65 A.

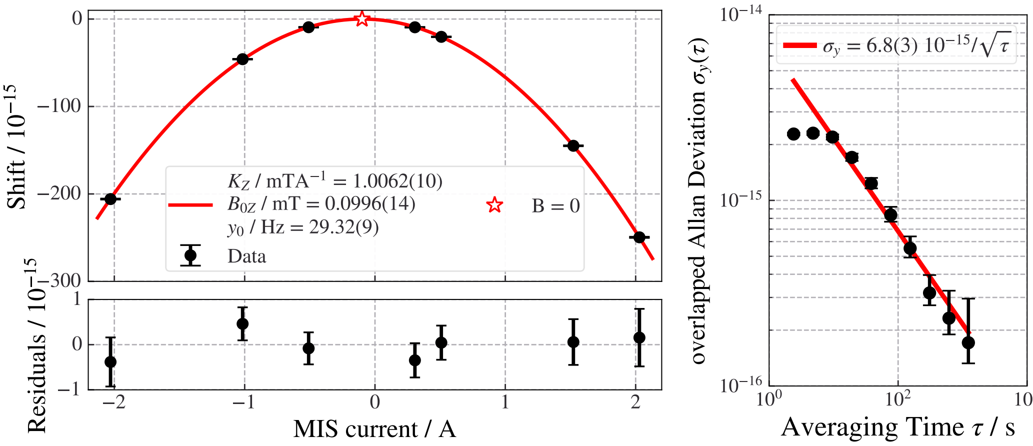

Fig. 4.4 Left:total quadratic Zeeman relative frequency shift measured at different I_{MIS} around the reference value of 1 A. The data are correct by the effect given by the orthogonal plane's field contribution, thus this measure represent the evaluation of the total shift. Right: typical interleaved instability of a 40-60 minutes long measurement.

y_0 / Hz	K_Z/G A^{-1}	B_{0Z}/ G
29.32(9)	10.062(10)	0.996(14)

Table 4.4 Fit parameters extracted from the data in Fig. 4.4 for the total quadratic Zeeman shift.

The resulting total quadratic Zeeman shift at the reference operation current I_{MIS} =1 A, evaluated through Eq. (4.2) with the parameters in Tab. 4.4 is

$$\left.\frac{\Delta_B}{\nu_{88}}\right|_{I_{\text{MIS}}=1\,\text{A}} = -686(3)\times 10^{-16}. \tag{4.8}$$

The observed offset field along the vertical direction, is a reasonable value compared with the expected magnitude of the combined field due to the bias coils and the Earth magnetic field component along Z. Coupling this with the considerations on the background fields in the transverse plane, it seems that the permanent magnets used for the 2D MOT,without magnetic shields, are not affecting the accuracy of the shift evaluation at the few parts in 10^{-16} level.

The total shift was evaluated another time, roughly 6 months apart from the measurement above, keeping the same conditions, besides eventual variations in the laboratory background field. Given the characterization along the X and Y directions, thus repeating only the interleaved measurement at different I_{MIS}, the shift is evaluated to be $\frac{\Delta_B}{\nu_{88}} = -691(3) \times 10^{-16}$. The two measurements are consistent within the experimental error, but differ by 5×10^{-16}, which allow us to estimate an eventual total field difference between the two measurements of

$$\delta B_{tot} = \left| \frac{\sqrt{|\Delta_{B,1}|} - \sqrt{|\Delta_{B,2}|}}{\sqrt{\beta_{88}}} \right| = 0.04(3)\,\mathrm{G}. \tag{4.9}$$

The shift value and its uncertainty reported in Tab.4.1 is the weighted mean of the two measurements presented here.

4.2 Clock laser light shift

4.2.1 Clock laser power stabilization

The clock laser intensity I_c determines, together with the total magnetic field, the coupling to the $^3\mathrm{P}_1$ state necessary to induce the clock transition through Eq. (2.1), and introduces a systematic light shift due to the differential polarizability of the clock states at 698 nm through Eq. (2.2). Recalling the clock laser light delivery setup of Fig. 3.16, the clock laser is sent to the atoms through a phase-stabilized and polarization-maintaining fiber link and then follows the optical path schematized in Fig. 3.9. In our setup, beside the intrinsic laser intensity noise, intensity fluctuations at the atomic cloud are mainly arising from polarization instability at the fiber output that affects subsequent polarization-dependent optics transmission. This instability is passively minimized by carefully aligning the clock laser input polarization, but temperature drifts and mechanical instabilities within the fiber environment pose a limit to the quality of this passive stabilization. To reach a reliable control on the induced Rabi frequency and consequently the clock laser light shift, power stabilization of the light that interrogates the atoms is required.

In Fig. 4.5 the optical and electronics power stabilization setup realized during this work are shown. The fine tuning of this setup required many trial and errors that lead to a substantial modification of the previous optical layout, except for the beam shaping lenses. In this final version, a fraction of the clock laser light is picked-off after an optical isolator (OI) with a 90:10 beam splitter, it is then filtered by an holographic reflective grating (GH13-18V, Thorlabs) and finally focused into the active area of a photodetector (PDA100A-EC, Thorlabs) producing a DC signal V_{PD}. The signal is then fed to a comparator that subtracts a reference voltage V_{ref}. The difference $V_{\text{PD}} - V_{\text{ref}}$ is fed to a proportional-integral (PI) controller which stabilizes it to 0 V by acting on the control voltage V_{ctrl} of a voltage variable attenuator (VVA , ZX73-2500-S+ Mini-Circuits), thus controlling the RF power that drives the AOM. The VVA attenuation is far from linear, depending on the the value of its bias voltage V_+ and the control voltage. For this particular VVA model, and considering the output dynamics of our PI, a balance between attenuation and linearity region is found by keeping V_+ = 5 V and biasing the PI output to make it work around V_{ctrl} = 6 V. Another important element is the time constant of the stabilization loop, it has to be kept small in order to allow fast stabilization switching (t_{rise} $\simeq$50 ms) to different values of V_{ref}. Our voltage reference is home-made and can switch between $V_{\text{ref}} = V_1$ and $V_{\text{ref}} = V_1 + V_2$ via a TTL control signal. Finally, a spurious reflection (about 3%) by the long pass dichroic mirror, used for absorption imaging, is sent to a photodiode to obtain an out-of-loop monitor V_{mon} of the optical power.

With respect to the optical setup presented in Fig. 4.5, both the diffraction grating and the OI revealed to be crucial in order to realize an effective stabilization loop. The OI prevents etalons to arise between the lattice and fiber link stabilization back-reflectors. The OI is oriented in such a way that the clock laser polarization at the input of the vacuum chamber is vertical, and parallel to the MIS magnetic field. However, we had to sacrifice some Doppler noise cancellation quality, since we had to move the fiber link stabilization before the OI, remaining with roughly 25 cm of uncompensated optical path between the two back-reflectors. The grating was also a crucial element: a small fraction of lattice light goes through the clock/lattice dichroic, and was back-reflected again by the FLS reflector, and finally ending on the stabilization loop photodiode. The OI decreased this effect, but some lattice light was still reflected back by the OI output facet and produce a visible signal on the detector. The addition of the diffraction grating in the setup, and using the $m = -1$ order as the stabilization signal, completely eliminated the issue.

The performance of the power stabilization can be appreciated in Fig. 4.6. There, measurements a few hours long of both free-running and stabilized (out-of-loop)

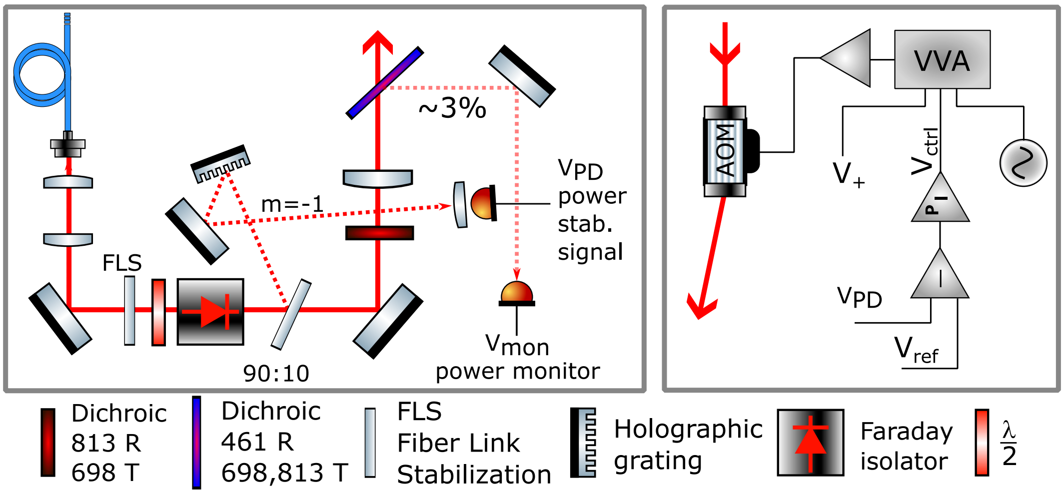

Fig. 4.5 Left: optical elements of the power stabilization loop. The pick-off light for power stabilization is taken after an optical isolator, oriented in un such a way that the polarization at the atoms is vertical. The pick-off light is filtered by a holographic reflective grating to avoid spurious lattice light coupling into the stabilization loop, and finally focused into a photodiode V_{PD}. Left: electronics of the stabilization loop. The difference between the signal V_{PD} and a voltage reference V_{ref} is fed to a PI controller acting on the control voltage V_{ctrl} voltage variable attenuator (VVA), thus controlling the RF power that drives the clock laser light acousto-optic modulator (AOM). A spurious reflection by the long pass dichroic mirror used for absorption imaging, is sent to a photodiode to obtain an out-of-loop monitor V_{mon} of the optical power

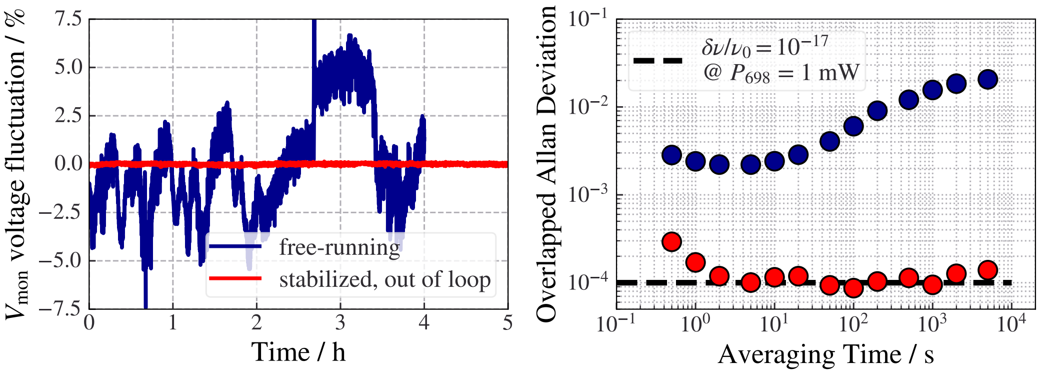

Fig. 4.6 Left: time trace of free-running (blue) and stabilized, out-of-loop (red) optical power fluctuations measured with V_{mon}. Right: overlapped Allan deviation of the respective time traces. The out-of-loop measurement reaches a flicker noise floor at $\sigma_{y,V} \simeq 1 \times 10^{-4}$, which correspond to an estimated clock frequency instability of $\delta\nu/\nu_0 \simeq 1 \times 10^{-17}$ for an optical power of 1 mW (dashed black line).

optical power monitored measuring V_{mon} with a DMM (Keysight 34411A). Both measurements acquired setting the clock laser power at the vacuum chamber to

1 mW. Without stabilization oscillations of the optical power greater than 5% peak-to-peak are observed over a $\simeq$1 h time scale. When the stabilization is active, short term fluctuations are reduced to 0.2% peak-to-peak and no long-term drifts of the optical power are observed. In the right panel of Fig. 4.6 this information is translated in instability using the overlapped Allan deviation estimator $\sigma_{y,V}(\tau)$, which reaches a flicker noise floor at $\sigma_{y,V}(\tau) = 1 \times 10^{-4}$ after 2 s averaging time. Using the probe shift calibration described in the next pages, it can be estimated that the corresponding limit to the clock frequency instability induced by the clock laser power instability is, at the reference power P_{clock} =1 mW, on the 1×10^{-17} level.

4.2.2 Relative frequency shift measurements

The procedure used to evaluate the probe shift is the same used for the quadratic Zeeman shift. A range of ±0.5 mW around the reference power P_{ref} =1 mW is explored during the relative frequency shift measurements. Since changing the clock power also changes the Rabi frequency, the interrogation time is set in order to have similar excitation on both interrogated transitions during the interleaved measurement. To keep this difference small, and don't change too much the interrogation time between each set of measurements, we increased the MIS magnetic field with respect to the reference point presented in the previous section, operating the coils at I_{MIS} =1.5 A. This way the magnetic field contribute to the Rabi frequency is stronger and, given its square root dependence on the clock laser intensity, this allowed us to not change much the interrogation time between each set of measurements. The range of explored Rabi frequencies is $\Omega/2\pi$= 9-15 Hz and the base interrogation time used was chose to be T =35 ms. It was changed at the extremes ends of the measurement only (lowest and highest clock power differences), to 45 ms and 25 ms respectively. For each measurement the in-loop excited fraction was 0.3(2), the total integration time was about 40-60 minutes with interleaved instabilities of 7-10$\times 10^{-15}\tau^{-1/2}$. The results are shown in Fig. 4.7.

The observed shift is linear as expected (Eq. (2.2)) and it is modeled as

$$\frac{\Delta_L}{\nu_{88}}(P_{\text{clock}}) = S(P_{\text{clock}} - P_{\text{ref}}) \tag{4.10}$$

where both S and P_{ref} are fit parameters, S being the most relevant one since it gives the slope of the shift, which is found to be $S = -114.40(18)\times10^{-15}\mathrm{mW}^{-1}$, or equivalently $-49.10(8)\,\mathrm{Hz\,mW}^{-1}$. The probe shift at the reference clock power P_{ref} =1 mW is thus evaluated to be

$$\left.\frac{\Delta_L}{\nu_{88}}\right|_{P_{\mathrm{ref}}=1\,\mathrm{mW}} = -1144.0(1.9)\times10^{-16}. \tag{4.11}$$

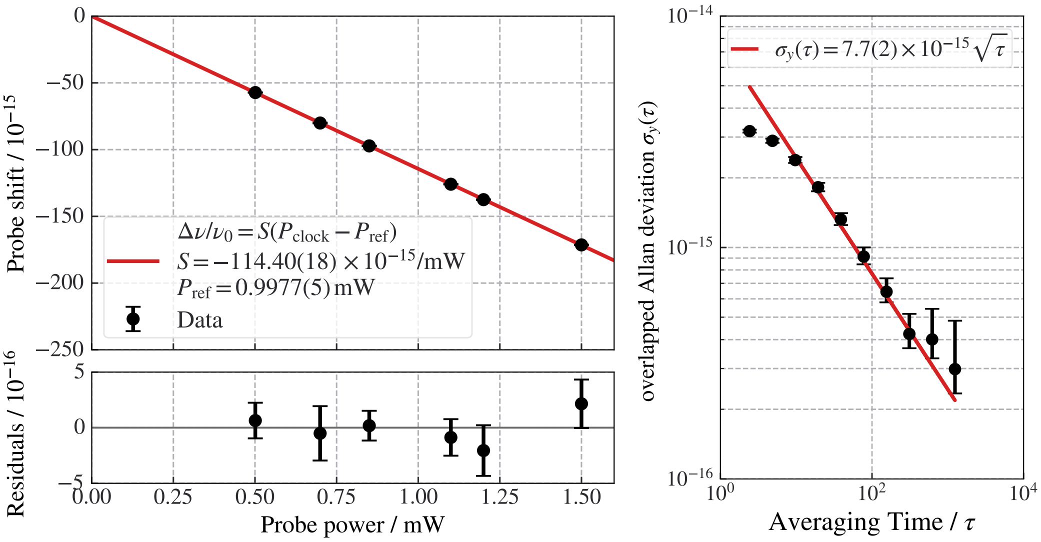

Fig. 4.7 Left: relative probe frequency shift around the reference power P_{ref} =1 mW and residuals to a linear fit (solid red line) to the data (black dots). Both data and fit are re-scaled by the estimated offset to show the absolute shift. Right: example of interleaved instability during the measurements.

4.2.3 Influences on the probe shift

The principal influence on the observed shift value is certainly the relative alignment between the lattice and clock laser. To minimize the influence of this contribute, the clock laser is systematically aligned by maximizing the light that is coupled into the lattice fiber. Another observed important influence in the probe shift evaluation in our system's geometry, turns out to be the lattice trap depth. This can be intuitively understood by the fact that our lattice is orthogonal with respect to gravity, therefore due to gravitational sag the trap minima position along the vertical direction is dependent on the trap depth, and gets further from the lattice beam center as the depth decreases. Thus, given the Gaussian profile of the local clock laser, the experienced intensity changes, decreasing as the trap depth is lowered. The measurement in Fig. 4.8 shows repeated interleaved evaluation of the probe shift between $P_{\text{ref}} = 1$ mW and $P_{\text{meas}} = 1.1$ mW at different trap depths, thus measuring the probe shift slope for a 0.1 mW power difference. In order to estimate the absolute shift at P_{ref} the result is multiplied by 10. The data in Fig. 4.8 is then scaled by subtracting the measured shift at the highest trap depth $U_0 = 158\,E_r$ to show the variation. Differences in at the 1×10^{-15} are observed. Although this does not represent a real limitation in the probe shift evaluation, as this can be still evaluated with 10^{-16} accuracy at each trap depth value, this interplay between trap depth and probe shift is problematic in the context of the lattice AC Stark shift evaluation, of which a preliminary evaluation is presented in Sec. 4.4. Given this information, it is clear that in the context of an eventual frequency ratio evaluation, the Probe shift would likely be the chosen measurement to run the clock, in order to have a strict monitor on it while the comparison goes on.

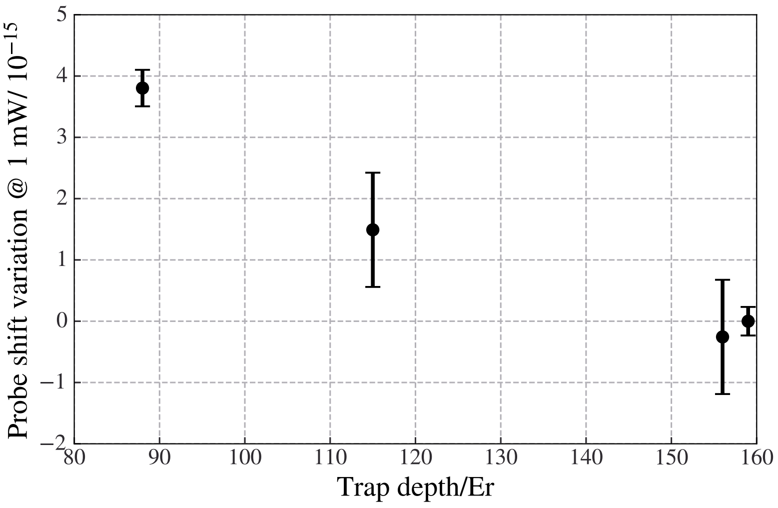

Fig. 4.8 Probe shift evaluation at different trap depths, see main text for details.

4.3 Induced Rabi frequency calibration and combined shift uncertainty

Combining the results of the two previous sections for the quadratic Zeeman and probe shifts, we may now give an idea of the achievable Rabi frequencies in our experiment and identify a typical operation point for the clock. Equations 2.1 and 2.2 can be combined to write the induced Rabi frequency as $\Omega = \xi\sqrt{|\Delta_L \Delta_B|}\cos\theta$, where ξ is a dimensionless factor combination of the atomic sensitivity to the applied fields, representing a quality factor since relates the strength of the induced coupling to the resulting frequency shift. For ^{88}Sr this parameter is calculated to be $\xi = 0.3$ [38].

Assuming $\cos\theta = 1$, and using the shifts Δ_L and Δ_B evaluated in the previous sections we define our experiment-friendly calibration of the Rabi frequency in terms of the applied MIS current I_{MIS} and clock power P_{clock} as

$$\Omega_0/2\pi = 10.23 \times \sqrt{\frac{P_{\text{clock}}}{\text{mW}}}\left(\frac{I_{\text{MIS}}}{A}\right)\text{Hz} \tag{4.12}$$

A visual representation of Eq. (4.12) is given in the left panel of Fig. 4.9. This result however does not account for collisional and thermal dephasing [139, 145] which degrade the coherence of the system resulting in a lower effective Rabi frequency $\Omega < \Omega_0$. An example of direct measurement of Ω through Rabi flopping can be found in Sec. 5.2.2.

The combination of quadratic Zeeman and probe shift and the resulting total uncertainty evaluated at different I_{MIS} and P_{clock} are shown in Fig.4.9. While choosing a sweet spot for the clock standard operation conditions it was considered that the target total uncertainty for the clock characterization during this work is set to be lower than 10^{-15}. To achieve so, low intensities of both magnetic and clock light fields must be used, thus reducing the coupling strength and enabling longer interrogation times. In principle, our clock laser coherence should enable interrogation times similar to the one employed in IT-Yb1 of 120 ms [170], however ^{88}Sr density dependent decoherence has to be also considered and in our system this requires to operate with the lowest possible number of atoms, thus sacrificing SNR. A reasonable operation point is set to the reference values used for the Probe and Zeeman shifts characterization: $I_{\text{MIS}} = 1$ A and $P_{\text{clock}} = 1$ mW, and with a total number $N \approx 7000$ of

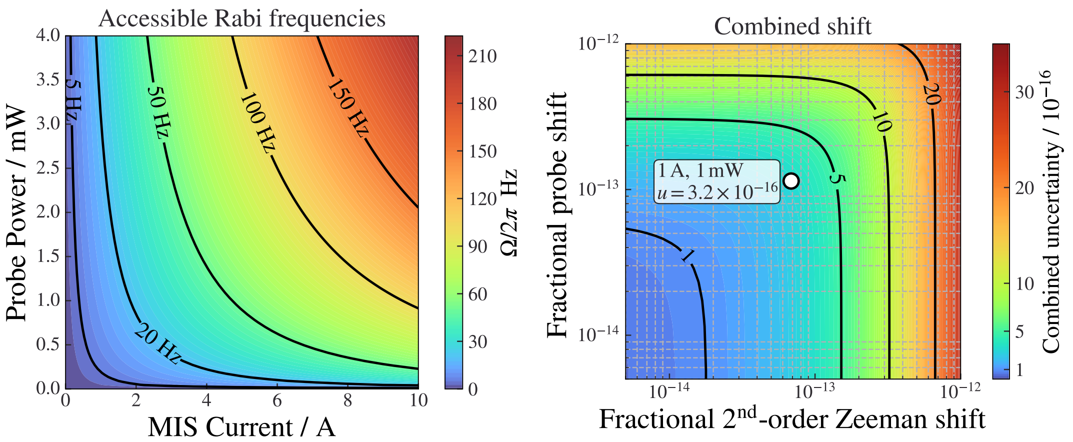

Fig. 4.9 Left: Induced Rabi frequency at the available experimental parameters P_{clock} and I_{MIS}. Right: Contour plot of the combined uncertainty on probe and quadratic Zeeman fractional induced shifts (y and x axes respectively). The white dot represents the identified suitable operation point where the total uncertainty is 3.2×10^{-16}, determined based on a trade-off considering clock laser noise properties and detection noise.

interrogated atoms. With this parameters the optimal interrogation time $T_{opt} = 65$ ms provides typical maximum excitation of 0.75 and linewidth of 15 Hz as shown in Fig. 4.10. At this working point, the total systematic uncertainty of the probe and quadratic Zeeman shift is estimated to be 3.2×10^{-16}, leaving room for similar uncertainty levels on other systematic shifts.

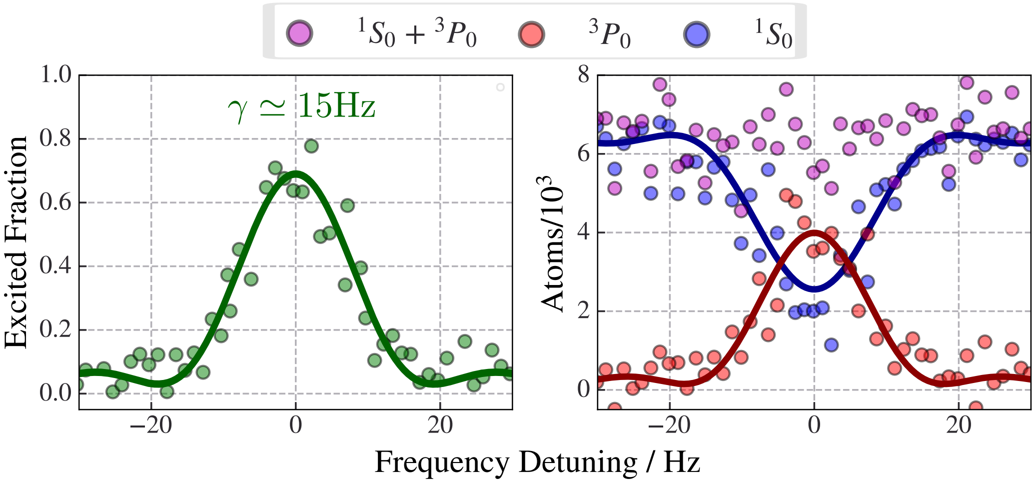

Fig. 4.10 Rabi spectroscopy at $I_{\text{MIS}} = 1$ A and $P_{\text{clock}} = 1$ mW, for a total of $N \approx 7 \times 10^3$ interrogated atoms.

4.4 Lattice AC Stark shift

Here we present a preliminary evaluation of the lattice AC stark shift realized during the final stage of this work, and performed via interleaved measurements at different lattice depths. Following the argument presented in the previous section, measurements were acquired with a Rabi frequency $\Omega/2\pi \simeq$7.5 Hz, induced with I_{MIS} = 3 A and P_{clock} =0.1 mW. In this way we reduced the systematic probe shift difference due to gravitational sag at different trap depths by a factor of 10, bringing it close, or lower, to the aimed statistical uncertainty of a few parts in 10^{-16} for the lattice shift measurements.

The lattice laser is referenced to the ORC described in Sec. 3.4.1, using the closest resonator mode to the magic frequency $\nu_{L,m} = 368\,554.778(8)$ GHz determined in Ref.[184]. The lattice frequency is monitored with a wavelength meter (Bristol 671B), providing a high uncertainty on the determined frequency $\nu_L = 368\,554.3(3)$ GHz. More accurate direct measurements of the lattice frequency were not implemented during the time of this work. The lattice light delivery (Sec. 3.2) is controlled via a 80 MHz AOM, of which the $m = +1$ diffraction order is used. Thus, the expected detuning from the magic frequency is $\nu_L + f_{\mathrm{AOM}} - \nu_{L,m}$ = $-0.4(3)$ GHz.

It is worth noting that the spectral purity of the lattice laser influences the determination of $\nu_{L,m}$. Broadband Amplified Spontaneous Emission (ASE) around the laser carrier introduces uncontrolled frequency shifts [92, 185, 186], particularly when using tapered amplifiers or diode sources, while Ti:Sapphire lasers are significantly less affected and are therefore usually preferred. Nevertheless, for high-accuracy clocks ASE is still something to be concerned with. The typical mitigation strategy exploits the spectral filtering provided by volume Bragg gratings [187, 188], often coupled with further spatial and spectral filtering provided by lattice build-up cavities [189, 190]. At this stage of our experiment, the influence of ASE in our system is not evaluated.

Interleaved measurements are performed between the available trap depth range 50-180 E_r, keeping $U_0 = 85E_r$ as the reference value. The data are then fitted with a linear model derived by [143], and summarized in Sec. 2.3, considering only the linear term in the lattice intensity, which should be the dominant at the expected detuning from the magic frequency. The detuning is left as a fit parameter, together with a frequency offset coming from the interleaved measurement. Results of the measurements are shown in Fig. 4.11, where the trap depth in the x-axis is computed as an effective trap depth accounting for the radial distribution of the atomic sample $U_{\mathrm{eff}} = U_0/(1 + k_B T_r/U_0)$ [191]. The radial temperature of the atomic sample is estimated via ToF imaging, and U_0 with sideband resolved spectroscopy (see Sec. 2.4.1 , 5.2).

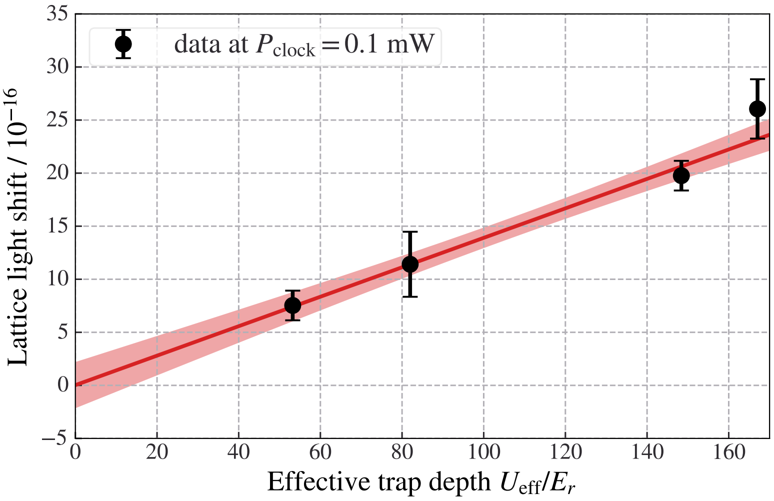

Fig. 4.11 Lattice shift interleaved measurement with respect to the reference trap depth $U_0 = 85\,E_r$. The solid line is a linear model with the detuning from the magic frequency [184] as a fit parameter. Measurement are acquired at P_{clock} =0.1 mW to reduce the effect described in Sec. 4.2.3.

The estimated lattice detuning from the magic frequency is $-0.31(4)$ GHz, which is about 100 MHz less than the expected one. Nevertheless it is still consistent with the wavelength meter expected value due to the latter one having an uncertainty of 300 MHz. By looking at the data positive trend we can confirm that the effect of the clock laser intensity has been reduced but it might not be made negligible, thus slightly reducing the effective slope of the observed trend. Further refinement of the lattice shift evaluation are currently ongoing at the moment of writing. At the moment, we evaluate the lattice light shift using the data presented in Fig. 4.11 at the reference trap depth $U_0 = 85\,E_r$ to be

$$\frac{\Delta\nu_{\mathrm{ACStark}}}{\nu_{88}} = 108(15) \times 10^{-17}. \tag{4.13}$$

4.5 BBR shift

The black body radiation shift arises as an AC Stark shift component induced by the emission spectra of the environment surrounding the atoms during the clock interrogation. In our system, thanks to 2D MOT atomic source configuration (Sec. 3.1) the BBR component of the hot oven is considered negligible at the current level of accuracy budget. The only component considered during this evaluation is the environment BBR shift, given by the finite temperature of the surroundings of the interrogation region. Considering an environment temperature T and a reference temperature $T_0 = 300\,\mathrm{K}$, the shift is evaluated through [91]:

$$\Delta\nu_{\mathrm{BBR}} = \Delta\nu_{stat}\left(\frac{T}{T_0}\right)^4 + \Delta\nu_{dyn}\left(\frac{T}{T_0}\right)^6 \tag{4.14}$$

where the first term represent the effect of the differential static polarizability between the clock states, and the second term is a dynamic correction that accounts for frequency dependence of the states polarizabilities across the BBR spectrum. Our laboratory temperature is stabilized to $T = 23.0(1)\,°\mathrm{C}$, however it must be pointed out some limiting factor that should bring this temperature uncertainty higher. There are no temperature monitor systems in the immediate vicinity of the science chamber and the MOT/MIS coils generating the necessary fields during the experiment are not temperature stabilized. For the latter argument, the heating effect is assumed to be negligible due to the typical low currents used during the clock interrogation and the low duty cycle [86]. If these effects were to be accurately considered one would probably find an effective temperature slightly higher. Nevertheless, assuming a conservative uncertainty on the temperature of $\pm 1\,°\mathrm{C}$ we quantify the shift as

$$\frac{\Delta\nu_{\mathrm{BBR}}}{\nu_{88}} = -50.3(7) \times 10^{-16}. \tag{4.15}$$

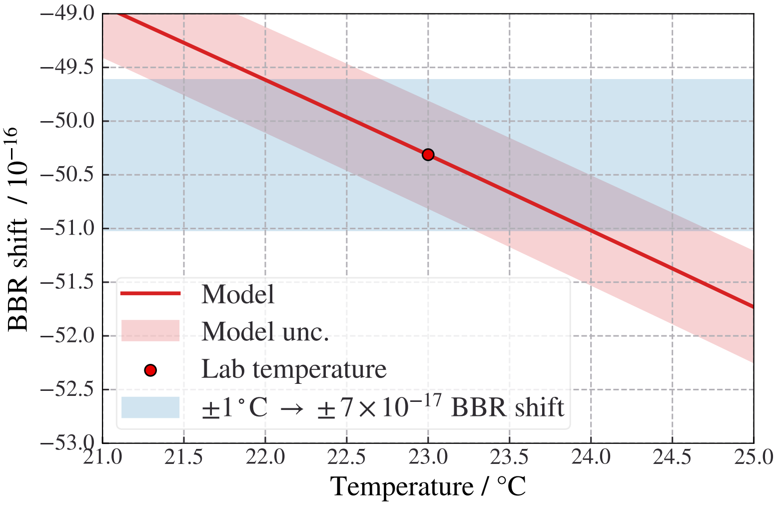

Fig. 4.12 BBR shift model [91] prediction around the laboratory temperature $T = 23.0(1)\,°\mathrm{C}$. The blue highlighted region represents a $\pm 7 \times 10^{-17}$ frequency interval corresponding to a $\pm 1\,°\mathrm{C}$ temperature difference.

4.6 Considerations on other systematics

4.6.1 Background gas collisions

The background gas collision shift arises from interactions with residual gases (mainly H_2 molecules) within the interrogation chamber and hot atoms coming from the oven. If the interaction does not result in an ejection from the trap, the remaining atom has an induced shift of the clock transition due to the process that scales linearly with the trap loss rate Γ [63, 192]. Thanks to the 2DMOT configuration and the optical loading of the atoms in the interrogation region the contribute from hot atoms is absent since there are no Sr atoms flowing into the chamber after the first stage cooling process. For the same reason an excellent vacuum quality is provided, enabling lattice lifetimes consistently observed to be $\Gamma^{-1} \gtrsim 14(2)\,\mathrm{s}$ (see 5.2.1). Evaluating the shift as [192]

$$\frac{\Delta\nu_{HC}}{\nu_{88}} = -30(3) \times 10^{-18} \frac{\mathrm{s}}{\Gamma^{-1}} = -2.1(4) \times 10^{-18}, \tag{4.16}$$

this contribute is completely negligible with respect to the other effects captured in the accuracy budget.

4.6.2 Doppler shift

Atoms trapped in the optical lattice are in the Lamb-Dicke regime (Sec.2.4.1), where they can be considered as effectively localized in the reference frame of the clock laser light. However, the clock laser phase noise accumulated during the free-space, or guided optical path, introduce Doppler shift and line broadening. In our system, as mentioned in Sec. 3.2, we employ an interferometric Doppler-noise cancellation (DNC) system to compensate the noise introduced by the fiber link. However, the back-reflecting mirror that creates the long arm of the interferometer for the cancellation scheme is not monolithically couplet to the lattice back-reflector, leaving a total uncompensated optical path of about 30 cm. A similar setup was employed in IT-Yb1 [171], and they demonstrated that this effect is negligible within a 5×10^{-17} uncertainty. However, considering that our interrogation time is roughly a factor of 2 lower than the typical interrogation time of IT-Yb1, we are exposed to a stronger Dick effect. To be conservative, an increased uncertainty on this shift is here given, estimating the residual Doppler shift as

$$\frac{\Delta\nu_{\mathrm{D1}}}{\nu_{88}} = 0(1) \times 10^{-16}. \tag{4.17}$$

4.6.3 Servo error shift

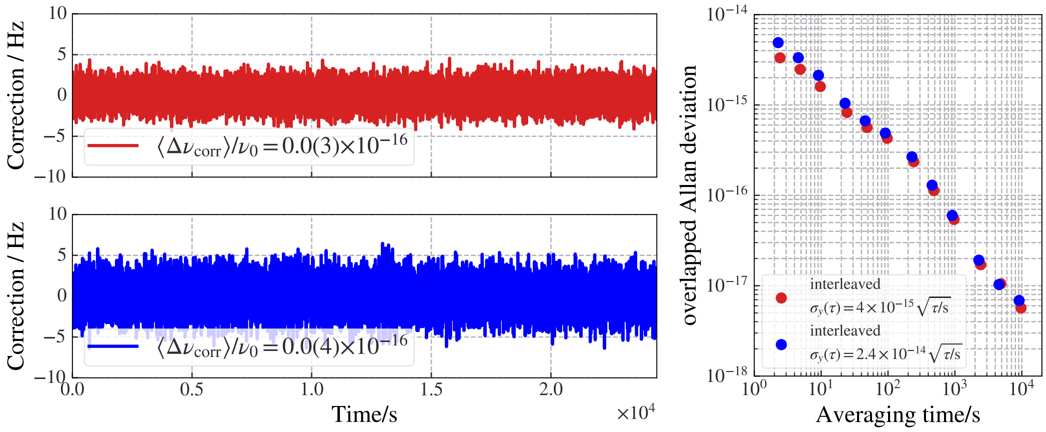

Fig. 4.13 Servo error shift estimation for two different measurement conditions with interleaved instability of 4×10^{-15} (red) and 2.4×10^{-14} (blue).

During the clock operation, the clock laser is frequency stabilized to the atomic resonance by a servo loop as described in Sec. 3.1. The error signal is produced by interrogating the atoms at two probe frequencies, obtained by shifting the laser frequency ν_l above or below the resonance ν_0 by a fixed amount $\Delta\nu_{\text{step}}$. The frequency stabilization loop then applies small additional corrections $\Delta\nu_{\text{corr}}$ to the probe frequency in order to satisfy the lock condition, so that the laser frequency becomes $\nu_l = \nu_0 \pm \Delta\nu_{\text{step}} + \Delta\nu_{\text{corr}}$. The clock laser drifts due to the reference cavity creep, and the finite gain of the loop produces a systematically biased error signal, thus resulting in an offset from the true resonance ν_0. In our system we benefit from a de-drifted clock laser (See 3.4.2). Otherwise, the typical approach to reduce the drift effect on the servo loop is to use the in-loop clock data to de-drift the laser while the clock operates or introduce in the error signal computation a time-dependent term to account for the cavity drift. The servo error shift can be computed [171] as the average clock laser detuning from resonance

$$\Delta\nu_{\text{servo}} = \langle \nu_l \rangle - \nu_0 = \langle \Delta_{\text{corr}} \rangle. \tag{4.18}$$

We evaluate the shift for two different typical measurements that have different interleaved instabilities to see if the interleaved measurement noise has some significant contribute to the shift evaluation. The results are shown in Fig. 4.13 were the red data correspond to an interleaved measurement with instability $\sigma_y(\tau) = 4 \times 10^{-15}/\sqrt{\tau/s}$ and the blue data to a measurement with $\sigma_y(\tau) = 2.4 \times 10^{-14}/\sqrt{\tau/s}$. The shift is evaluated computing the average of the corrections and the uncertainty as the standard error. In both cases a negligible shift is found: $\Delta\nu_{\text{servo}}/\nu_{88} = 0(3) \times 10^{-17}$ and $\Delta\nu_{\text{servo}}/\nu_{88} = 0(4) \times 10^{-17}$ respectively.

Chapter 5

Collisional shift and investigation of ^{88}Sr interaction properties

In this chapter density dependent interaction effects in a bosonic ^{88}Sr optical lattice clock are investigated. In contrast to fermionic systems, bosonic atoms typically exhibit strong s-wave interactions that cannot be mitigated by lowering the system temperature and lead to significant decoherence, measurable inelastic losses, distortion of the transition lineshape and, most importantly, collisional frequency shifts. The strength of these effects is strictly dependent on the atomic density within a single lattice site, which is determined by the confinement potential, the atomic temperature, and how the atoms are distributed among the lattice sites.

The chapter is organized as follows. Section 5.1 introduces the lattice configurations and the methods for determining the effective lattice sites density in our experiment, through a detailed characterization of the lattice beams waists and the atomic temperatures. Section 5.2 presents measurements of known inelastic losses and decoherence phenomena affecting ^{88}Sr, which provide validation of our density estimation approach. In Sec.5.3, interaction sidebands emerging over the clock transition are observed in a highly populated 2D lattice, and are used to constrain the sign of the ground-excited scattering length a_{eg}, as well as estimating its strength. Finally, Sec.5.4 discusses the results of collisional shift measurements in a 1D lattice. Through these measurements, the systematic shift and its contribute to the total uncertainty budget is evaluated to be $3.3(1.9)\times10^{-16}$, and we also provide estimates of the excited-excited and ground-excited scattering lengths by analyzing the data in light of what presented in Sec.2.5.

5.1 Traps geometry and thermodynamics characterization

In order to determine the effective lattice site volume entering interaction energies and loss rates, a precise characterization of the traps geometry is needed. In this section, we characterize the one and two dimensional lattice configurations used in this work by measuring, when possible, or estimating, the relevant trap frequencies and the atomic temperature. These quantities are then used to determine the effective lattice site volume employed throughout the following sections.

5.1.1 1D horizontal lattice waist measurement and temperatures characterization

The horizontal lattice beam waist was primarily characterized by optical dipole trap oscillation measurements, a well known technique in ultracold atom experiments[130] for measuring the radial confinement frequencies provided by a dipole trap, which are typically of the order of a few hundreds Hz.

In our setup the main optical lattice is horizontally oriented, such that gravity acts along one of the radial directions, denoted as z, and we can exploit it to excite the oscillations. The dipole trap is obtained by simply blocking the backward propagating lattice beam. In the experimental sequence, the trap is then switched off for a short 300 µs time interval, during which the atoms acquire a velocity kick due to gravity, but do not escape the trapping region. When the trap is subsequently switched back on, the atomic cloud is displaced from the equilibrium position and undergoes harmonic oscillation at the radial trap frequency before settling at the equilibrium.

The oscillatory motion is probed by measuring via absorption imaging the position of the atomic cloud at different hold times, counted from the moment the trap is switched back on. A representative example of the observed oscillations is shown in the inset of Fig. 5.2.

Figure 5.2 shows the measured radial oscillation frequency as a function of the input lattice power measured at the vacuum chamber window. The experimental data follow the expected scaling described in Sec.2.2, and in particular the presence of a minimum input power for successful trapping. A fit to the data, which combines Eq.(2.11) and Eq.(2.13), determines a lattice beam waist of

$$w_{0,\mathrm{H}} = 52.26(14)\,\mu\mathrm{m}, \tag{5.1}$$

where the quoted uncertainty corresponds to the statistical uncertainty of the fit.

In the fitting procedure, optical power losses arising from imperfect transmission through optical components and vacuum windows are considered, and the polarizability value used is the one provided in [143].

Denoting with P_{in} the lattice power measured at the input of the vacuum chamber, we find that the optical power of the forward-propagating lattice beam at the position of the atoms is $P_1 = T_{w,\mathrm{h}} P_{\mathrm{in}}$ where the transmission coefficient $T_{w,\mathrm{h}} = 0.86(2)$, is obtained by measuring the transmitted optical power through the science cell, and assuming both input and output windows contribute to the same degree. For the back-reflected lattice beam, additional losses due to the retro-reflector, refocusing lens and the long-pass dichroic (see Fig.3.9) are taken into account. Including these contributions, the effective power of the backward-propagating beam is found to be $P_2 = 0.63(3)\,P_{\mathrm{in}}$.

The axial confinement of the lattice was characterized using resolved sideband spectroscopy (SBS) on the clock transition (see 2.4). Figure 5.2 shows the measured axial trap frequency as a function of the input lattice power. The axial trap frequencies are extracted from the spectroscopic profiles shown in Fig.5.3 using the model proposed in [139] and summarized in Eq.(2.21). The experimental data are then compared to the expected axial frequencies obtained from a numerical simulation of two interfering Gaussian beams. The simulation includes the experimentally determined beam waist and accounts for the measured power imbalance between the lattice beams. In Fig.5.1 the simulated potentials at different lattice powers is shown.

The measured axial trap frequencies do not fully overlap with the simulated ones obtained using the beam waist retrieved from the dipole oscillation measurements. Better agreement with the experimental data is obtained by either assuming a slightly larger beam wist of 55 µm or by accounting for an additional $\simeq 10\%$ reduction in

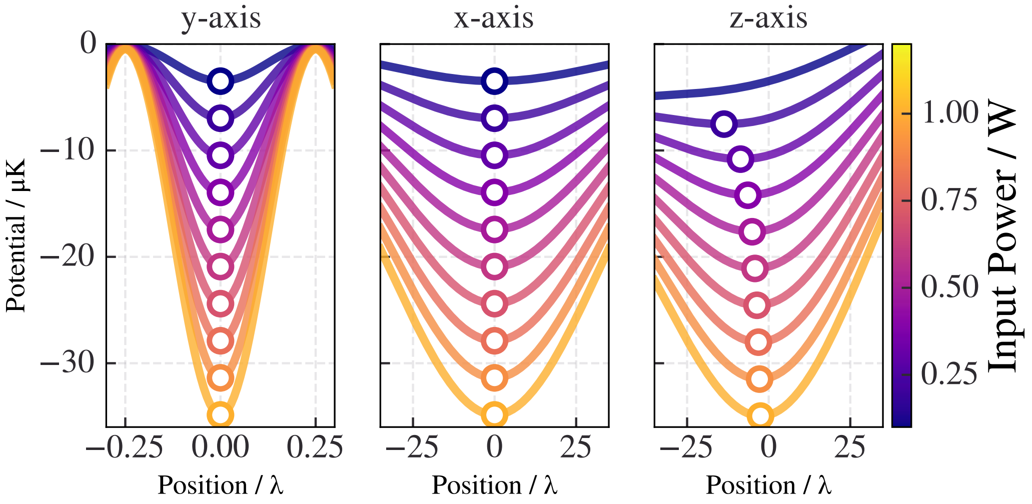

Fig. 5.1 Simulation of the lattice potential along the three spatial directions at different lattice powers. The white dots represent the numerically estimated equilibrium positions.

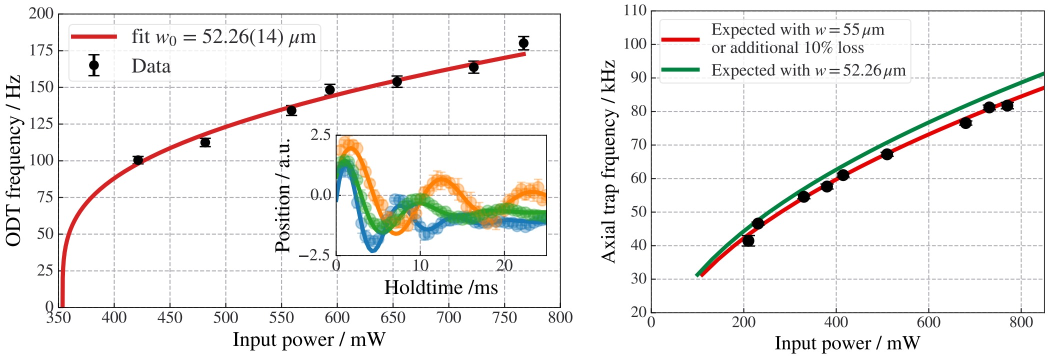

Fig. 5.2 Left: radial trap frequency obtained from optical dipole trap oscillation measurements as a function of the lattice input power. The solid line is a fit assuming a Gaussian beam profile, from which a beam waist of $w_0 = 52.26(14)\,\mu\text{m}$ is determined. The inset shows representative oscillations at input powers of 760 mw (blue), 430 mW (orange), and 560 mW (green). Right: axial trap frequency measured by resolved sideband spectroscopy compared with numerical simulations including the measured beam waist and the power imbalance between the lattice beams. The red curve, which best describe our data, requires either a slightly larger waist of 55 µm or an additional 10% loss, which could plausibly arise due to polarization mismatch.

the effective lattice depth. The first scenario is considered unlikely, as the position of the refocusing lens was carefully optimized by maximizing the number of trapped atoms. A more plausible explanation is an additional reduction of the lattice potential arising from imperfect match of the polarization vectors of the lattice beams, and/or a slight elliptical polarization induced by windows birefringence. Such polarization imperfections lead to a reduced interference amplitude between the beams and consequently to a lower effective lattice depth. Consistently with this interpretation, for all subsequent estimations that requires knowing the lattice waist, we use the result reported in Eq.(5.1), and for the trap frequency estimation we use the red curve in the right panel of 5.2.

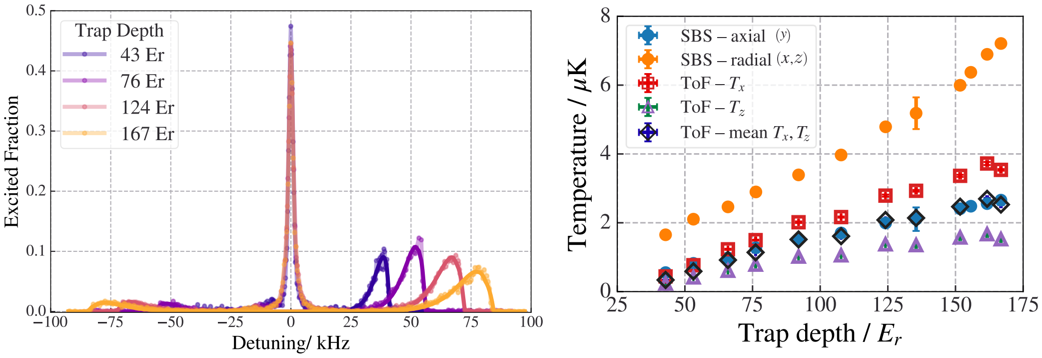

Fig. 5.3 Left: clock transition spectra showing the carrier and axial sidebands for different lattice trap depths. Right: temperatures extracted from sideband spectroscopy and from cloud expansion as a function of the lattice trap depth.

The left panel of Fig. 5.3 shows representative SBS spectra for different lattice depths U_0, covering the full available range of approximately $40\,E_r$ up to $170\,E_r$. Each spectrum consists of a central carrier and two motional sidebands, whose frequency separation and relative amplitudes encode information about the axial confinement and temperature. To observe the spectra, we typically excite the clock transition with an interrogation time of 150 ms, using the maximum available Rabi frequency achievable with 3-4 mW of clock laser power and an applied magnetic field of approximately 100 G. The relatively long interrogation time is chosen to enhance the signal of the sidebands, hence allowing for a reliable fit of the spectroscopic profile. However, long interrogation times also increase the sensitivity of the extracted sideband amplitudes to broadening mechanisms. These effects can lead to an overestimation of the motional excitation, and therefore the temperature, particularly for the weakly confined radial degrees of freedom.

The right panel of Fig. 5.3 shows the temperatures extracted from sideband spectroscopy along the axial and radial directions, together with temperature measurements obtained via time-of-flight (TOF) expansion. The increase of the atomic temperature with lattice depth is the result of both fundamental and technical effects.

From a fundamental perspective, in the case of adiabatic loading the motional state occupation $\langle n \rangle$ is preserved. Since the trapping frequency scales as $\omega \propto \sqrt{U_0}$, the mean motional energy $E \sim \hbar\omega\langle n \rangle$ increases as $\sqrt{U_0}$. This implies a corresponding scaling of the effective temperature as $T \propto \sqrt{U_0}$. However, this mechanism alone does not account for the approximately linear scaling observed in Fig. 5.3. A dominant contribution is instead provided by technical heating processes, in particular parametric heating induced by intensity noise of the trapping laser. The associated heating rate scales as $\Gamma \propto \omega^2 S_I(2\omega)$, where S_I is the relative intensity noise power spectral density evaluated at twice the trap frequency. Since $\omega^2 \propto U_0$, this leads to a heating rate approximately proportional to the lattice depth, provided that $S_I(2\omega)$ is slowly varying in the relevant frequency range. This mechanism naturally explains the observed linear increase of the temperature with U_0. The slight deviation from linearity at large lattice depths, visible in Fig.5.3, may be attributed to the decrease of the laser intensity noise at higher frequencies.

For the TOF measurements, the extracted temperatures along the two radial directions, T_x and T_z, are found to be systematically different. This asymmetry is probably due to a difference in the radial frequencies arising from gravitational sag, which breaks the cylindrical symmetry of the trap as it was shown in Sec.2.3. Also, the lack of elastic scattering between ground state atoms prevents the system thermalization within the experimental time scales. For practical purposes and when a single representative radial temperature is required, we assume a symmetric radial confinement and use the average temperature $(T_x + T_z)/2$, with the semi-dispersion as uncertainty. While the TOF based radial temperatures are preferred over the SBS derived ones, our only estimate of the axial temperature T_y remains the one extracted from sideband spectroscopy.

5.1.2 1D vertical lattice waist measurement

In addition to the horizontal lattice discussed in the previous section, our experimental setup includes an auxiliary one dimensional lattice oriented along the vertical direction, i.e. along gravity, implemented during this work. A precise characterization of the vertical lattice beam waist is also required, specifically for the determination of the trapping potential in the two dimensional lattice, and therefore for an accurate evaluation of atomic densities and interaction effects in such configuration.

Resolved sideband spectroscopy could not be used for the vertical lattice characterization. The main reasons for that are the limited clock laser power available, and the difficulty of generating sufficiently strong and controllable magnetic fields along the appropriate direction with the existing setup. Therefore, the axial trap frequency of the vertical lattice was measured using the parametric heating technique [193, 194], which is based on a controlled modulation of the lattice intensity. The technique relies on the fact that a periodic modulation of the trap depth at a frequency close to twice the harmonic trap frequency leads to a resonant excitation of the atomic motion, thus heating the atomic sample. The increased motional energy results in a corresponding loss of trapped atoms which can be readily detected.

In our measurements, the intensity of the vertical lattice beam is modulated for 100 ms with a modulation depth of approximately 3%. After the modulation, the remaining atomic population is measured with fluorescence imaging, and the resonance frequency is identified as the peak in the observed loss signal. Representative parametric heating spectra are shown in the inset of Fig. 5.4. Figure 5.4 shows the measured vertical lattice trap frequency as a function of the input optical power. The data follow the expected scaling with lattice power for a Gaussian beam, and from a

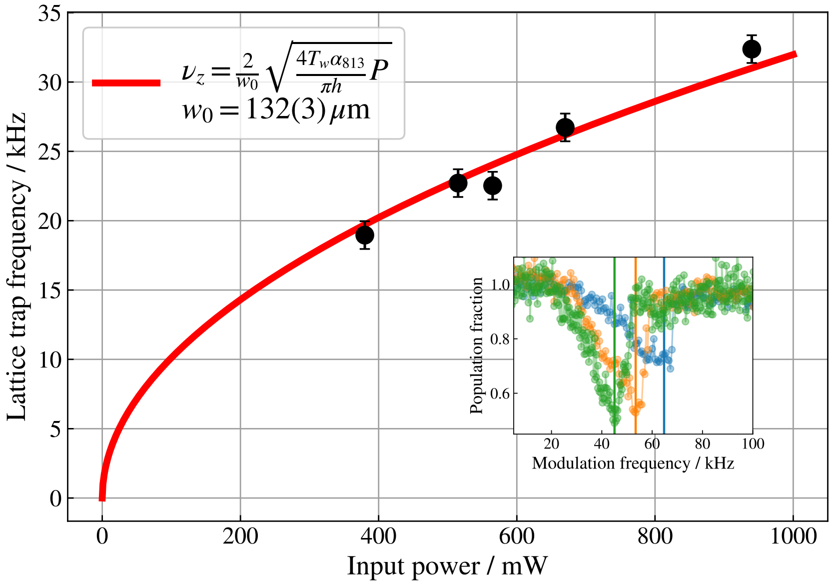

Fig. 5.4 Vertical lattice trap frequency measured via parametric heating as a function of the input optical power. The solid line is a fit with the expected scaling and considering power losses. The vertical lattice beam waist is estimated to be $w_{0,V} = 132(3)$ µm. The inset shows representative parametric heating spectra used to extract the resonance frequencies.

fit to the data we retrieve a vertical lattice beam waist of

$$w_{0,V} = 132(3)\,\mu\text{m}, \tag{5.2}$$

where the quoted uncertainty corresponds to the fit uncertainty.

As for the horizontal lattice, optical power losses along the beam path were characterized and considered. In particular, we determine a window transmission for the vertical lattice beam of $T_{w,V} = 0.96(2)\%$. The measured vertical lattice waist and effective power calibration complete the characterization of the trapping potential required for the two dimensional lattice configuration employed in the following sections.

5.1.3 2D lattice

The 2D lattice configuration employed in this work is realized by overlapping two independent one dimensional optical lattices oriented along orthogonal directions. Interference between the lattices is avoided by using orthogonal polarizations and a relative frequency detuning of $\Delta \simeq 160\,\text{MHz}$. As discussed in Sec.2.4, this choice removes the need to maintain a stable phase relation and polarization matching between the beams, which is challenging in free space setups. Also, it allows the total trapping potential to be approximated by the incoherent sum of the individual lattices contributes.

The 2D lattice loading experimental sequence is illustrated in Fig. 5.5: the loading begins during the final stage of the red MOT, with the vertical lattice being ramped up in 2.2 ms. After switching off the MOT beams, the horizontal lattice is ramped up to its final operating depth, using a ramp of 2.2 ms. The vertical lattice is then gradually switched off, to allow for atoms that are not trapped by the horizontal lattice to fall under the effect of gravity. About 8 ms suffice to remove unwanted atoms from the lattices intersection region. Finally, the vertical lattice is switched on again, leading to a pure 2D lattice sample [133, 195] with atoms confined in the intersection of the two lattices.

The 2D lattice loading procedure adopted in this work is motivated by the improved spectroscopic contrast of the clock transition obtained with this sequence. When the horizontal lattice is loaded first, the peak excitation of the clock transition is

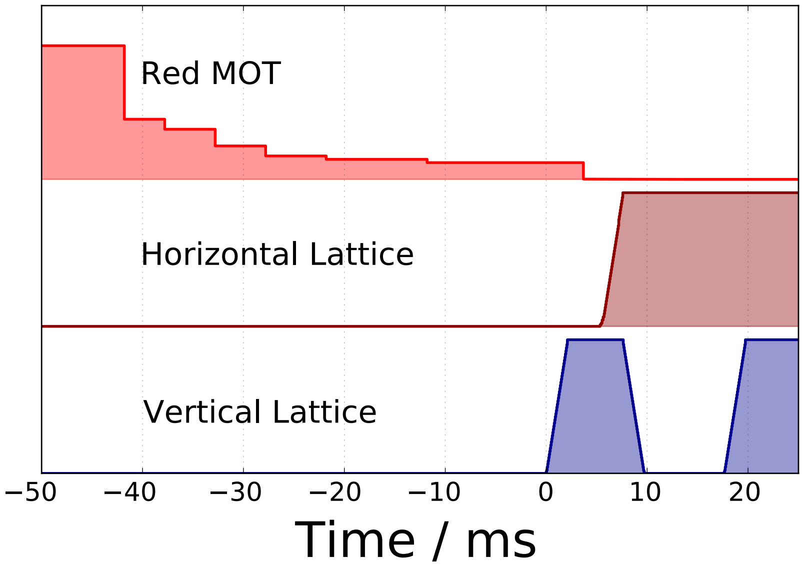

Fig. 5.5 Timing sequence for loading atoms into the 2D lattice. The vertical lattice is ramped up during the final stage of the red MOT, followed by the ramp-up of the horizontal lattice. The vertical lattice is then temporarily switched off to allow untrapped atoms to fall away, and subsequently restored to realize a pure 2D lattice configuration.

systematically reduced and decreases further as the vertical lattice depth is increased. This observation is quite surprising, as one would expect the loading process to be symmetric. Nevertheless, it seems that loading the horizontal lattice first results in more dense, and prone to decoherence, final atomic sample. The observed behavior at increasing vertical lattice powers may be qualitatively explained with arguments on the adiabaticity of the loading process. By loading atoms first into the tightly focused horizontal lattice, where gravitational sag and intensity inhomogeneity are significant along the radial direction, and then introducing the vertical lattice potentially leads to a less adiabatic redistribution of the atomic ensemble [196, 197]. In contrast, loading the vertical lattice first provides early strong confinement along the gravitational direction in a larger waist and more homogeneous trapping potential. This results in a gentler, more adiabatic, transfer when the horizontal lattice is introduced. Further investigation, for example by increasing the lattices ramp up times, was however not performed.

This behavior is illustrated in Fig. 5.6, which compares the observed peak excitation at a fixed horizontal lattice power and as function of the vertical lattice power. The vertical-first loading configuration shows consistently higher excitation and a weaker dependence on the vertical lattice depth, which led us to prefer it and use it for all subsequent 2D lattice measurements.

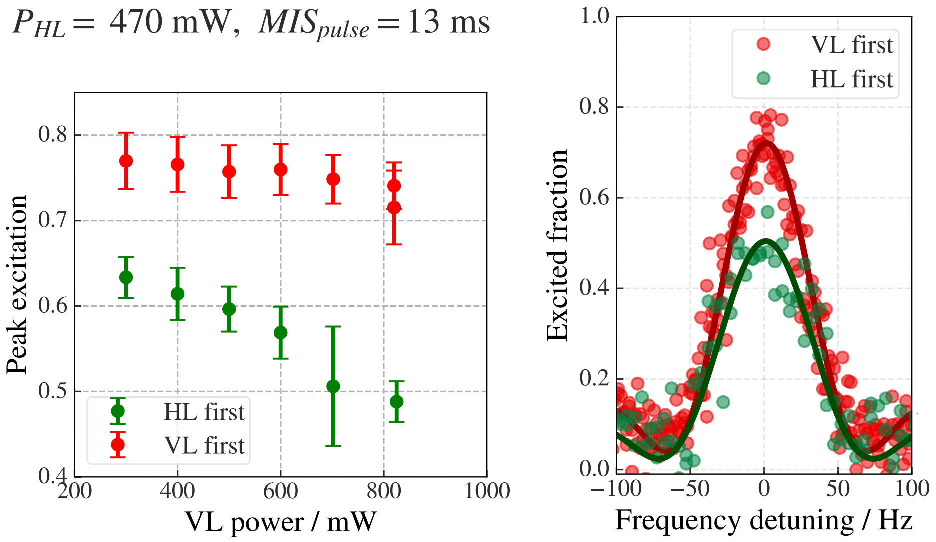

Fig. 5.6 Peak excitation of the clock transition as a function of the vertical lattice power for two different lattice loading sequences. Loading the horizontal lattice first results in a systematically reduced excitation that decreases with increasing vertical lattice depth, while loading the vertical lattice first shows higher and more stable excitation. Based on this comparison, the vertical first loading sequence was adopted for the 2D lattice operation.

Concerning the atomic sample temperatures, we directly access the weakly confined direction temperature with TOF thermonmetry. This is the dominant temperature correction to the spatial extent of the atomic wavefunction within the lattice site, and therefore plays the major role in determining the density. Instead, along the tightly confined directions thermal corrections to spatial extensions are comparatively small (see Eq.(2.28)), and are therefore neglected.

5.1.4 Modeling distribution across lattice sites

Knowing how the atoms distributes among the lattice sites, and therefore quantify how many atoms there are in a typical lattice site, is also required to model the density. Following the approach in [149] we model the loading of atoms into the lattice assuming that the occupation follows Poissonian statistics, with a spatially dependent average occupation number described by a Gaussian envelope, whose width is determined by the relevant loading mechanism and the lattice configuration.

One dimensional lattice. In the 1D lattice configuration, we reasonably assume the atomic distribution along the lattice axis is determined by the spatial extension of the final red MOT stage. Which, under typical operating conditions is determined to be $\sigma_{\mathrm{MOT}} \simeq 200\,\mu\mathrm{m}$ via absorption imaging. The mean atom number at lattice site i is modeled as

$$G(i) = \frac{N_0}{\sqrt{2\pi}\sigma} \exp\left(-\frac{i^2}{2\sigma^2}\right), \quad \sigma = \frac{\sigma_{\mathrm{MOT}}}{d_{\mathrm{lat}}} \tag{5.3}$$

where N_0 is the total atom number, and σ is a dimensionless width expressed in lattice site units $d_{\mathrm{lat}} = \lambda_L/2$.

Assuming independent loading, the occupation number distribution for a random lattice site is obtained by summing over the Poisson probabilities:

$$P(m) = \frac{1}{N_{\mathrm{sites}}} \sum_i P_i(m) = \frac{1}{N_{\mathrm{sites}}} \sum_i \frac{G(i)^m}{m!} e^{-G(i)}, \tag{5.4}$$

where dividing by the number of non-negligibly occupied lattice sites ensures normalization. From the equation above, the average site occupation number is determined as $\langle m \rangle = \sum_m mP(m)$, while the peak occupation number m_{peak} is determined as the m value for which $mP(m)$ is maximum.

Two dimensional lattice. The 2D lattice modeling comes as a natural extension of the 1D geometry, with the only difference that the spatial distribution shall not be determined by the red MOT cloud width. Instead, we model the relevant spatial extensions to be determined by the harmonic confinement provided by each of the two lattices in the weak radial direction.

Extending Eq.(5.3) in two dimensions, the mean occupation at the lattice site (i, j) is modeled as

$$G(i,j) = \frac{N_0}{2\pi\sigma_y\sigma_z} \exp\left(-\frac{i^2}{2\sigma_y^2} - \frac{j^2}{2\sigma_z^2}\right), \tag{5.5}$$

where σ_y and σ_z denote the dimensionless widths, along the horizontal and vertical lattices axes, that have to be considered and reasonably estimated.

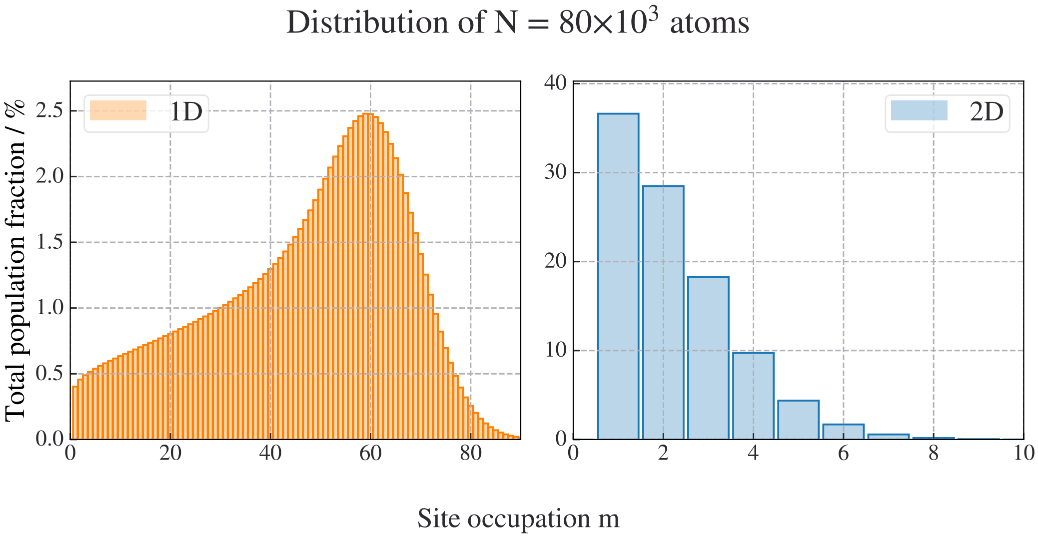

Fig. 5.7 Comparison of the modeled lattice site occupation number distributions for $N = 8 \times 10^4$ atoms in 1D and 2D lattice configurations. The 2D lattice strongly suppresses highly occupied sites, resulting in a significantly reduced peak occupation.

Assuming again Poissonian loading, the occupation number distribution for a 2D lattice site is obtained as:

$$P(m) = \frac{1}{N_{\text{sites}}} \sum_{i,j} P_{ij}(m) = \frac{1}{N_{\text{sites}}} \sum_{i,j} \frac{G(i,j)^m}{m!} e^{-G(i,j)}. \tag{5.6}$$

In order to provide reasonable values for the widths in Eq.(5.5), as mentioned above we proceed estimating how extended the wavefunction would be, along the radial direction, if confinement is provided by one of the two lattices only. The representative temperature to be used is the one along the weakly confined direction of the atomic sample in the 2D lattice, and it is determined by TOF measurements. Under the typical operating conditions, with approximately 500 mW in the horizontal lattice and 500 mW in the vertical lattice, the temperature is about $T \simeq 1.5\,\mu$K. Assuming this temperature value to be representative of the radial temperature also in the individual lattices configurations, the spatial distribution widths are then estimated from the radial extension of a thermal atomic cloud in a harmonic potential via Eq. (2.28). The radial trap frequencies are obtained from the characterization of the individual lattices. For the horizontal lattice, ω_r is derived from the measured axial trap frequencies using Eq. (2.16) and the waist value reported in the previous section. For the vertical lattice, the axial trap frequency is estimated from the fitted lattice parameters shown in Fig.5.4. This results in the estimated relevant spatial extensions to be $\sigma_z = 12\,\mu\mathrm{m}/d_{\mathrm{lat}}$ and $\sigma_y = 70\,\mu\mathrm{m}/d_{\mathrm{lat}}$, corresponding to the horizontal and vertical lattices confinements, respectively.

As displayed in Fig. 5.7 the site occupancy distribution is sensibly different when comparing $N = 8 \times 10^4$ atoms distributed in 1D and 2D lattices. In the 1D lattice, the distribution is broad and there are many multi-occupied lattice sites, while in the 2D lattice, thanks to the increased number of available sites ($N^{2D}_{sites}/N^{1D}_{sites} \simeq 80$) atoms are predominantly in a low-occupation number site.

5.2 Inelastic losses and decoherence measurements

As an internal validation of our approach for estimating density, we performed measurement of inelastic excite-state losses and collisional decoherence on the clock transition of ^{88}Sr and compare the extracted coefficients with literature values [110, 145, 146].

5.2.1 Excited state inelastic loss measurements

Inelastic collisions between atoms in the $^3\mathrm{P}_0$ state lead to irreversible atom loss from the trap mainly due to the high kinetic energy acquired by the atoms after the collision process. Measuring the corresponding loss rate coefficient therefore constitutes an indirect probe of the density within the lattice sites, and provide an important validation of the approach of estimating the lattice site volume and modeling the population distribution introduced in the previous section.

The dynamic of the excited state population in a lattice site $n_{e,i}(t)$ at a time t, is modeled using a rate equation that includes one body and two body loss processes:

$$\dot{n}_{e,i} = -\Gamma_{\mathrm{vac}}\, n_{e,i} - \Gamma_2\, n^2_{e,i}, \tag{5.7}$$

where Γ_{vac} accounts for the one body losses due to background gas collisions and finite trap lifetime, while Γ_2 is the coefficient we are interested in, as it describes the two body inelastic collisions between $^3\mathrm{P}_0$ atoms. Introducing the site volume V_{site},

Γ_2 is expressed as:

$$\Gamma_2 = \frac{\gamma_{ee}}{V_{\text{site}}} \tag{5.8}$$

where γ_{ee} is the density normalized inelastic loss rate coefficient. Equation (5.8) highlights the dominant role of the volume determination in extracting meaningful values of the loss rate coefficient. Given an initial population $n_{e,i}(0) = n^0_{e,i}$, the rate equation has the analytical solution

$$n_{e,i}(t) = \frac{n^0_{e,i}\, e^{-\Gamma_{\text{vac}}t}}{1 + n^0_{e,i}\frac{\Gamma_2}{\Gamma_{\text{vac}}}\left(1 - e^{-\Gamma_{\text{vac}}t}\right)}. \tag{5.9}$$

The dynamics for an initial total population N_0 in the 1D lattice is then obtained by summing Eq.(5.9) over the lattice sites, defining $n^0_{e,i} = G(i)$ through Eq.(5.3). To correctly retrieve the total number of atoms at $t = 0$, the summation is carried out considering lattice sites within $\pm 3\sigma_{\text{MOT}}$, which is found to be the minimum condition that does not introduce errors in the population estimation. The same argument is extended for the 2D lattice, this time the summation is performed over then indexes i, j, and the initial populations at the site (i, j) are defined through Eq.(5.5).

The one body loss rate Γ_{vac} is determined by the decay of the ground state atoms, fitting the data with a pure exponential decay, and it is subsequently fixed in the analysis of the excited population loss measurements. The extracted one body loss rates are consistent across both lattice configurations and are determined to be $\Gamma^{-1}_{\text{vac,1D}} = 14.5(1.1)\,\text{s}$ and $\Gamma^{-1}_{\text{vac,2D}} = 14.2(4)\,\text{s}$. From the fit of the excited population data instead, we retrieve Γ_2, and later compute the loss rate γ_{ee} using Eq.(5.8).

To perform the excited state measurements, atoms are transferred to the $^3\text{P}_0$ state by a resonant 5 ms long π-pulse, corresponding to a Rabi frequency $\Omega \approx 2\pi \times 100\,\text{Hz}$. To reduce sensitivity to slow frequency drift of the clock laser, its frequency is weakly modulated around the resonance with a $\pm 20\,\text{Hz}$ amplitude. This way, we can maintain a stable fraction of excited atoms over the time span of the measurement, and avoid the introduction of fictitious losses due to a less efficient population transfer caused by clock laser noise. Immediately after the excitation pulse, the remaining ground state atoms are wiped away with a resonant 461 nm pulse and the excited state population is later detected via fluorescence imaging after an hold time t.

Table 5.1 Summary of relevant trap parameters during the $^3P_0$ inelastic loss measurements. The spatial directions y and z are the axial directions of the horizontal and vertical lattices respectively. Volumes are estimated through Eq. (2.29).

Parameter	Unit	1D Lattice	2D Lattice
$\omega_x/2\pi$	Hz	217(10)	208(30)
$\omega_y/2\pi$	kHz	62.0(5)	60.5(9)
$\omega_z/2\pi$	kHz	0.217(10)	22.8(2)
Temperature T	µK	1.2(3)	1.5(2)
Volume $V_{\text{site}}/(2\pi)^{3/2}$	µm^3	5.8(18)	0.08(2)
Loss coeff. γ_{ee}	µm^3/s	21(7)	10.0(15)

Both 1D and 2D lattice loss measurements were performed with an initial excited state population of about 8×10^4 atoms, while the traps parameters during the measurements are summarized in Tab.5.1. In particular, in the 1D lattice configuration the trap depth is about $78(2)\,E_r$, with a TOF estimated temperature of 1.2(3) µK, hence a resulting lattice site volume of $V_{\text{site}}^{\text{1D}} = (2\pi)^{3/2}\times 5.8(18)\,\mu\text{m}^3$. For the 2D lattice configurations the horizontal and vertical depths are respectively $73(4)\,E_r$ and $11(2)\,E_r$, the radial temperature is measured to be 1.5 µK, providing an estimated lattice site volume of $V_{\text{site}}^{\text{2D}} = (2\pi)^{3/2}\times 0.08(2)\,\mu\text{m}^3$.

The excited state decay data in Fig.5.8 are fitted using the procedure explained above. The extracted loss rate coefficients are

$$\gamma_{ee}^{\text{1D}} = 21(7)\,\mu\text{m}^3/\text{s} \quad , \quad \gamma_{ee}^{\text{2D}} = 10(1.5)\,\mu\text{m}^3/\text{s} \tag{5.10}$$

The value of γ_{ee}^{1D} is consistent within the uncertainty with the coefficient measured by Traverso *et al.* [146]. In addition, considering also the relatively large uncertainty of our measurement, we find agreement with the recent measurement reported by Dolde *et al.* [110]. We also note that in the latter work, they approach differently to the problem of retrieving the total population dynamic from the single site dynamic. They provide an approximate solution for the sum of each lattice site contribution to the decay, which we also implemented with our data and find slightly lower but consistent values with our first used approach: $\gamma_{ee}^{\text{1D}} = 17(4)\,\mu\text{m}^3/\text{s}$ and $\gamma_{ee}^{\text{2D}} = 7(2)\,\mu\text{m}^3/\text{s}$.

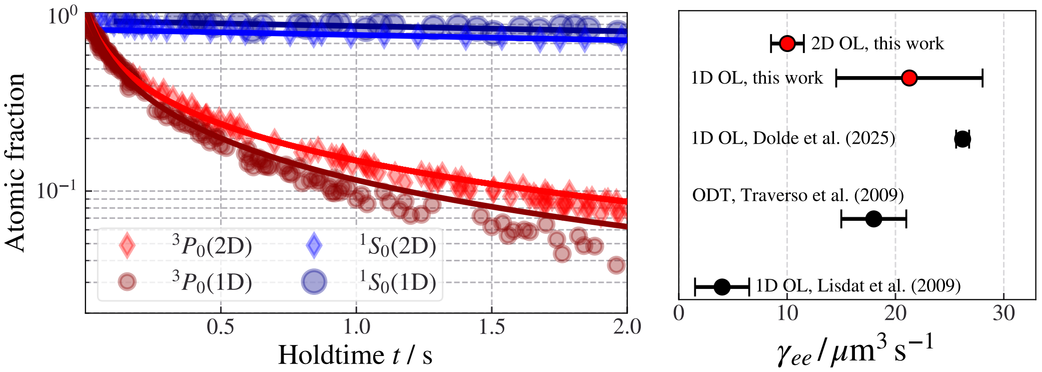

Fig. 5.8 Left: measured losses in the $^3\mathrm{P}_0$ (red) and $^1\mathrm{S}_0$ (blue) states. Darker(lighter) shades represent the 1D(2D) measurements. Solid lines are decay fits with a pure exponential (ground state data), or with Eq.(5.9) (excited state data). Right: comparison of the extracted loss rate γ_{ee} with literature values [110, 145, 146].

In contrast, the value reported by Lisdat *et al.*[145] seems to be underestimated compared to this work and others estimates. It is curious that, in our case, measurements differs by approximately a factor $\sqrt{8}$, and that the same level of discrepancy is observed in the decoherence measurement presented in the next section.

In the 2D configuration instead, we extract a loss coefficient that appears to be smaller. It is worth mentioning here that in the 2D case the extracted loss coefficient strongly depends on the assumed spatial widths entering the Gaussian envelope in the population distribution mode. In particular, since the inelastic losses originates exclusively from lattice sites with occupation $m \geq 2$, the site averaged decay is dominated by the tail of the probability distribution in Fig.5.7, which is quite sensitive to the choice of the considered spatial extensions. For instance, we could find agreement between the 1D and 2D measurements if accounting for larger (in the order of the lattice waists) spatial widths in Eq.(5.5). By doing so the $m \geq 2$ sites weights in the averaging process is reduced, and the overall observed decay requires a larger γ_{ee}^{2D} value to reproduce the data. However, such widths are considered to be not truthful based on the arguments made in the previous section based on the harmonic confinement and the 2D lattice loading process.

The observed discrepancy between 1D and 2D inelastic loss rates with the approach described above could also arise due to inhomogeneities not being considered. In the 1D lattice configuration atoms are trapped roughly in 1/10 of the beam Rayleigh range, therefore neglecting trap frequencies variations over the atomic sample is a fairly good approximation. In the 2D lattice instead, the resulting potential is characterized by a higher degree of spatial inhomogeneity due to the characteristic frequencies variation being dictated by the scale of the beams waists rather than the Rayleigh range. An estimate of the inhomogeneity can be obtained by simulating the resulting potential of the 2D lattice with the typically used input powers, and computing the resulting trap frequencies over the lattice sites grid defined by the spatial extensions introduced in Sec.5.1.4. By doing so, we estimate a ratio $\overline{V}/V_p \simeq 1.25$, where V_p is the volume computed at the grid center and $\overline{V}$ is the average volume. Thus, the inhomogeneity can account for roughly a 25% increase of the loss rate, which would still be lower than the 1D lattice measured ones. These observations suggest the interpretation that increasing the lattice dimensionality, thereby reducing the effective space over which atoms can move and interact, results in a suppression of the observed loss rate.

5.2.2 Collisional decoherence measurements

Beyond inelastic losses, elastic collisions in ^{88}Sr lead to decoherence which manifests as a damping and dephasing of Rabi flopping of the populations. Following the approach proposed in [145], we characterize the decoherence in our system by measuring Rabi oscillations at different atom numbers while keeping fixed the lattice depth.

All the measurements reported in this section are performed in the 1D lattice configuration, which is operated at a trap depth of about $80E_r$, with corresponding axial and radial trap frequencies $\omega_{\mathrm{ax},r}/2\pi = \{61.4(5), 0.215(10)\}\,\mathrm{kHz}$. The axial temperature determined via SBS is $T_{ax} = 1.7(2)\,\mu\mathrm{K}$ while the transverse temperature measured by TOF expansion is $T_r = 1.7(3)\,\mu\mathrm{K}$. Combining all this, the estimated lattice site volume is $V_{\mathrm{site}}^{\mathrm{1D}}/(2\pi)^{3/2} = 9(2)\,\mu\mathrm{m}^3$ (Eq.(2.29)).

The Rabi oscillations are driven using an estimated induced Rabi frequency $\Omega_0 \simeq 2\pi \times 43\,\mathrm{Hz}$, achieved with (see Eq.(4.12)) $2\,\mathrm{mW}$ of clock laser power and $I_{\mathrm{MIS}} = 3\,\mathrm{A}$ of current flowing into the MIS coils (about $30\,\mathrm{G}$). The population evolution is recorded at increasing interrogation times, and the total number of atoms is retrieved using fluorescence imaging and the calibration presented in Sec.3.2.2. To reduce noise, a few spectroscopic profiles are acquired at each interrogation time and the populations at $\Delta = 0$ are estimated by averaging the signal over a $\pm 10Hz$ window around the central frequency.

Experimental data shown in Fig. 5.9 are analyzed using the density dependent decoherence model proposed in [145], which is also summarized in 2.5.1. For each lattice site occupation, the dynamics defined by the sets of ordinary differential equations arising from Eq.(2.30) is numerically integrated up to the interrogation time, and the total observed populations are computed by summing over all the lattice sites, accounting for the probability distribution described in Sec.5.1.4.

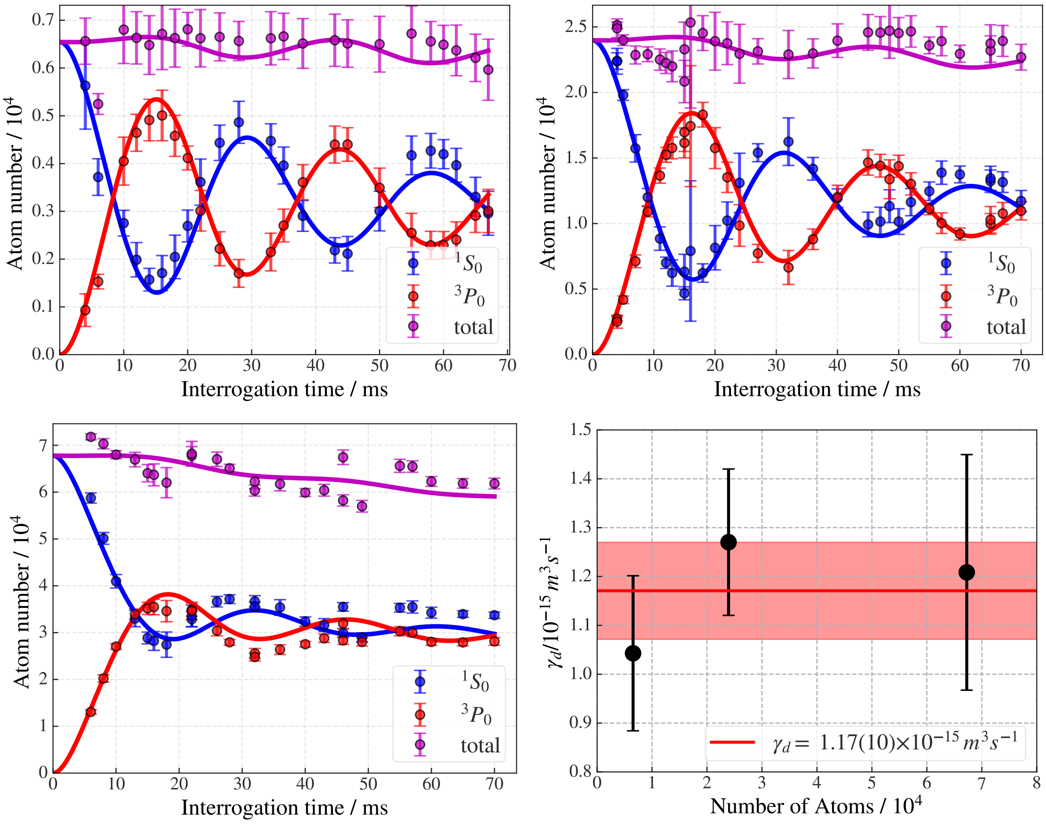

Fig. 5.9 Rabi oscillations of the clock transition measured in the 1D lattice configuration for different atom numbers. Solid lines show fits to the density dependent decoherence model of [145], obtained by averaging the site-resolved dynamics over the lattice site occupation distribution.

In the fitting procedure, all the free parameters of the model, besides the elastic dephasing coefficient γ_d and the effective Rabi frequency Ω_{eff} are fixed to measured or estimated values. In particular the two body loss rate γ_{ee} is fixed by the 1D measurement presented in the previous section, while the $e-g$ loss rate coefficient is fixed to $\gamma_{ge} = \gamma_{ee}/10$ assuming valid the scaling observed in [145]. The vacuum limited lifetime Γ_{vac}, although of negligible contribute is measured and fixed, while the effective laser linewdith L in Eq.(2.31) is estimated as $L/2\pi = 1.5\,\text{Hz}$ via the noise properties of our laser.

The experimental data together with the fitted curves are shown in Fig.5.9. In the lower-right panel of the figure, the extracted dephasing coefficients are shown to average around the value

$$\gamma_d = 1.17(10) \times 10^{-15}\text{m}^3\,\text{s}^{-1}, \tag{5.11}$$

which is, again, about a factor $\sqrt{8}$ higher than the $\gamma_d = 0.32(1) \times 10^{-15}\text{m}^3\,\text{s}^{-1}$ reported in [145], repeating the discrepancy observed for the γ_{ee} loss rate. This likely indicates a different convention in the site volume definition, or the average density within a lattice site, for which we here follow the approach presented in [149] and discussed in the previous sections. It is worth to mention however, that the measurement of this phenomenological coefficient in different experiments, for example in the work by Bishof *et al.* [198], is not fully understood. In particular, the experiment in [198] shows how the observed dephasing in ^{87}Sr could not be reproduced unless introducing an explicit dependence of γ_d on the effective Rabi frequency. This suggest that additional effects, likely arising from the many-body nature of the system, prevents this dephasing mechanism to be fully described with this approach.

Concerning the effective Rabi frequency extracted from the three datasets, it is estimated as the average from the three measurements to be $\Omega_{\text{eff}}/2\pi = 34(2)\,\text{Hz}$, which is lowered with respect to the estimated Ω_0 by this elastic dephasing mechanism, and additional thermal dephasing and inhomogeneities [139].

5.3 Interaction sidebands in a 2D lattice

Recalling the per-particle pair interaction energies definition in Sec.2.5.1, is easy to see how interactions can be enhanced by simply confining the atoms in a smaller space region. Doing so, can make interaction-induced many body features observable in the clock transition lineshape. In particular, the transition lineshape can be asymmetrically distorted, with the asymmetry originating from multi-occupied

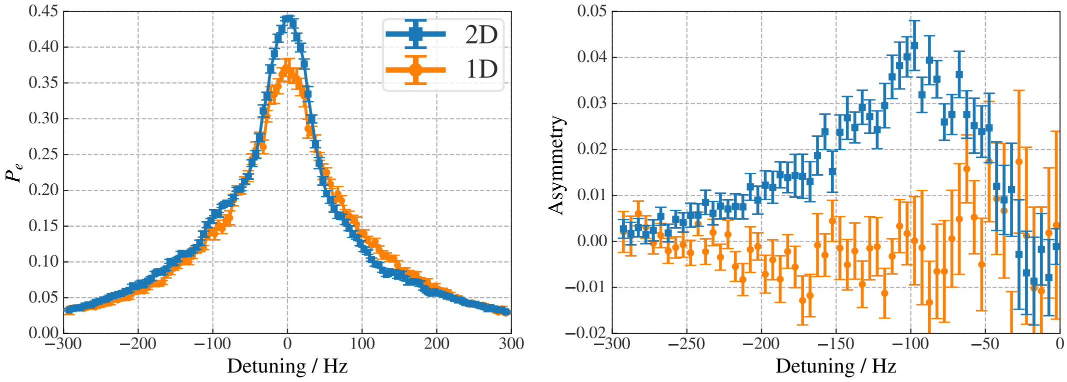

Fig. 5.10 Clock transition spectra recorded in highly populated (8×10^4) 1D and 2D lattice configurations. While the 1D spectrum remains symmetric, the 2D spectrum shows a pronounced asymmetry indicative of interaction-induced contributions.

lattice sites which are energy shifted by the interactions and therefore resonate at a slightly different frequencies. These shifted resonances around the unperturbed transition constitute what commonly referred to as *interaction sidebands* (ISB). Such spectroscopic features have been previously observed and quantitatively analyzed in ultracold ^{87}Sr in a 2D trap by Bishof *et al.* [195]. In ^{88}Sr, a glimpse of the interaction induced asymmetry has been observed on ultra-narrow spectroscopy of the clock transition in a 1D lattice confined sample [199]. The asymmetry, although not fully resolved due to the weak confinement, appeared at negative detunings, suggesting that the interspecies interaction energy U_{eg} is negative.

In order to confirm and better resolve this observation, we investigate the ISB emerging in a 2D lattice configuration following the approach in [195]. The trap is operated with horizontal and vertical depths of $90(4)\,E_r$ and $17(2)\,E_r$, respectively, corresponding to trap frequencies of $\omega_{x,y,z}/2\pi \simeq \{0.23,\,66,\,17\}\,\mathrm{kHz}$. Considering the measured transverse temperature $1.6(2)\,\mu\mathrm{K}$, the lattice site volume for this measurements is estimated to be $V^{2\mathrm{D}}/(2\pi)^{3/2} = 0.06(1)\,\mu\mathrm{m}^3$ (Eq.(2.29)).

Spectra exciting the clock transition on $N \approx 8 \times 10^4$ atoms with a Rabi π-pulse of 15 ms, in both 1D and 2D lattices, are shown in Fig.5.10. In the 1D lattice, the observed lineshape do not present asymmetries, while in the 2D lattice the asymmetry becomes evident at negative detunings. Moreover, the overall peak excitation is slightly enhanced, in agreement with the expected dominance of singly occupied sites in the 2D lattice.

To construct and isolate the signal of interest, the ISB, a few spectra are acquired. By averaging and binning them symmetrically with respect to the fitted resonance position, the resulting averaged spectra is then flipped around the resonance and the excitation difference $P_e(\delta_-) - P_e(\delta_+)$ is regarded as the experimentally retrieved ISB.

The resulting signal is modeled as a weighted sum of Lorentzian contributions from lattice sites with different occupancies,

$$S_{\mathrm{ISB}}(\delta) = A \sum_{m\geq 2} w_m \left[L(\delta - (m-1)u_{eg}) - L(\delta + (m-1)u_{eg})\right], \tag{5.12}$$

where $u_{eg} = U_{eg}/h$ is the frequency shift deriving from the interaction energy U_{eg}, w_m are the occupation weights derived from the population distribution model of Sec. 5.1.4, δ is the clock laser detuning, and $L(\delta)$ is a Lorentzian lineshape with linewidth γ.

The modeling of the signal through Eq.(5.12) is a direct consequence of the many-body model introduced in Sec.2.5.1 (see also Ref.[195]). In the simplest picture of a single-photon excitations, the excitation of a single atom in a m-occupied lattice site leads to a transition between the many-body states $|g^m\rangle$ to $|e\,g^{m-1}\rangle$. With the latter resulting energy shifted by $\Delta E_m = (m-1)(C-\chi) = (m-1)U_{eg}$, proportionally to the remaining ground state atoms in the lattice site. Since only single photon processes are considered, there is no expected contribution from the excite-excited interaction energy U_{ee}. Therefore, sites with different occupancies give rise to a ladder of transitions spaced by the interaction energy U_{eg}, which are however broadened due to the finite temperature of the system [195] and hence not fully resolvable. Nevertheless, their combined contribution leads to an observable distortion of the lineshape.

Proceeding as described above, we observe the ISB asymmetry at different total number of trapped atoms (Fig.5.11), and by a simultaneous global fit with Eq.(5.12) the per-particle interaction energy shift is determined to be

$$\frac{U_{eg}}{h} = -31(6)\,\mathrm{Hz}, \tag{5.13}$$

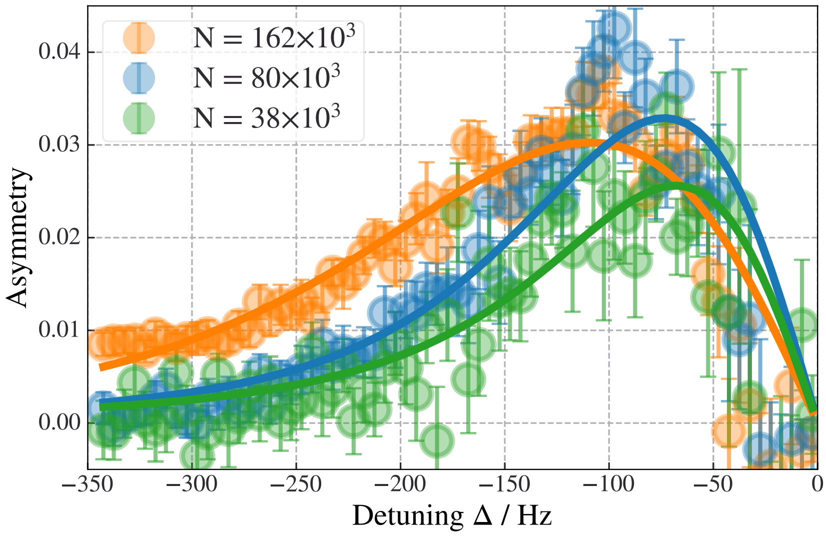

Fig. 5.11 ISB asymmetry measured for different total atom numbers in the 2D lattice. Solid lines show a simultaneous global fit of the asymmetry model, with shared interaction parameter U_{eg}.

corresponding to an excited-ground scattering length

$$a_{eg} = \frac{1}{2}\frac{mU_{eg}}{4\pi\hbar^2}V^{2\mathrm{D}} = -180(50)\,a_0, \tag{5.14}$$

where a_0 is the Bohr radius, and the factor $1/2$ comes from having set $\alpha_{ge}^{(2)} = 2$ (see Sec.2.5.1, Eq.(2.38)). The uncertainty on the interaction energy is the 1σ uncertainty from the fit, while the scattering length uncertainty includes propagation of the site volume error. The negative sign indicates an attractive excited-ground interaction, which is consistent with the sign inferred in [199], and also with the results evinced in this work from the density frequency shift measurements presented in the next section.

5.4 Collisional shift measurements

The density dependent frequency shift arising from atomic interactions represents one of the critical aspects for the accuracy of bosonic optical lattice clocks. Beyond the metrological relevance, the study of collisions induced shift is a powerful tool that provides direct experimental access to the interaction properties of the atom under consideration by performing high-precision frequency measurements.

In this section collisional shift measurements for ^{88}Sr trapped in a 1D lattice are presented and discussed. Differential shift measurements are performed, at different lattice depths, via clock self-comparison changing the total number of interrogated atoms with respected to a reference value, which denotes our typical operating condition of $N_{\text{ref}} \approx 7 \times 10^3$ atoms, determined by fluorescence imaging and its calibration (see Sec.3.2.2). The experimental procedure and observations are qualitatively reported in Sec.5.4.1, where it can be clearly seen that all the data share the common feature of reaching a non-linearity region, where the shift changes sign. The interpretation of this feature comes in the following sections, where besides estimating the impact of the shift on the accuracy budget, we provide estimates of both excited-excited and ground-excited scattering lengths of ^{88}Sr.

5.4.1 Measurement conditions and qualitative considerations

In order to maintain a suitable excitation probability P_e for the clock operation over a large span of atom numbers we limit the influence of decoherence and inelastic losses by choosing a relatively short interaction timescale, and select the working effective Rabi frequency at $\Omega/2\pi = 34(2)\,\text{Hz}$, as estimated during the decoherence measurements, and corresponding to a π-pulse duration of 15 ms. The Rabi oscillations and the typical lineshape at the reference atom number $N_{\text{ref}} \approx 7 \times 10^3$ is shown in Fig. 5.12. However, the peak excitation and linewidth cannot be maintained over the whole explored range, as displayed in the right panel of Fig. 5.12, which shows how these two features scales with the total atom number. For instance, at the reference atom number, the typical linewidth is 50 Hz, increasing up to 120 Hz when the clock is operated at the highest densities, while peak excitation ranges roughly from 0.9-0.3. Nevertheless, independently on the particular lineshape, the detuning at which the clock is interrogated to realize the stabilization loop (see. Sec.3.5) is kept constant throughout all the measurements at $\delta_{\text{lock}} = 25\,\text{Hz}$, to ensure that the Rabi driving term in the system hamiltonian in Eq.(2.35) is not affected.

For each measurement series the lattice depth is fixed and the total number of atom is varied by adjusting the 2D MOT beams intensity. At the beginning of each data acquisition run, sometimes in-between too, several important experimental

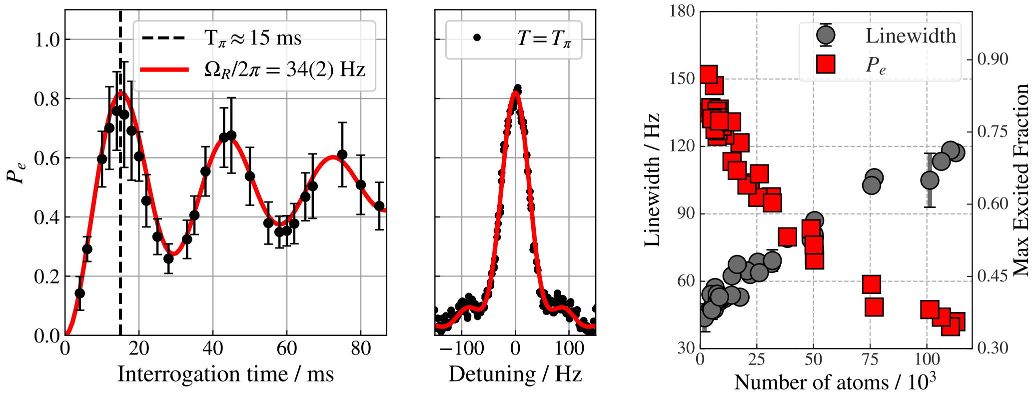

Fig. 5.12 Left: Rabi oscillation at $N \approx 7 \times 10^3$,the data is the same of Fig.5.9 just expressed as excitation probability P_e. Center: representative spectroscopic line shape $N \approx 7 \times 10^3$ recorded with a $T_\pi = 15\,\text{ms}$ interrogation pulse, solid line is a fit to the master equation Eq.(2.30). Left: variation of linewdith and maximum excitation probability with the interrogated atom number.

parameters are kept under control. In particular, the axial trap frequency measured via SBS, the clock laser intensity, and the spatial extension of the red MOT. The latter is important to ensure that the same loading statistic, as described in Sec.5.1.4, can be applied to all measurements, and it is kept at around $\sigma_{\text{MOT}} \simeq 200(5)\,\mu\text{m}$. All of these parameters are found to be sufficiently stable over the course of a day. The MOT width, which is particularly important, is mainly determined by the cooling laser detuning, the quality of the beams alignment and the transfer efficiency from the blue MOT. Fortunately, the environment temperature is stable and guarantees both lattice and MOT beams alignment do not suffer from thermal hysteresis due to temperature fluctuations. The alignment of both is anyway checked and optimized prior to the start of every data acquisition run, while the cooling laser detuning has to be adjusted once every 2-3 days to compensate for the drift of the reference cavity. Although the lattice is not power stabilized and shows less than 5% short term fluctuations, the long term stability observed over the course of a day of the measured trap depth is about $\leq 3\,E_r$. Also, the detection beam power was frequently monitored to ensure saturation of the fluorescence signal (see Sec.3.2.2), in order to suppress the effect of power fluctuations which would compromise the fluorescence-atom number calibration. The radial temperature of the atoms is typically measured once via TOF expansion, and kept as the representative radial temperature during a daily set of measurements.

Typical duration of a single interleaved measurement is on the order of 40-120 minutes, depending on the starting fractional frequency instability. A representative Allan deviation of the interleaved measurements, together with the instability of the measured atom number difference, is shown in Fig. 5.13, while in general the achieved instabilities varied between 0.4-2 $\times 10^{-14}\sqrt{\tau/\mathrm{s}}$. The target statistical uncertainty for each measurement is in the order of 2×10^{-16}.

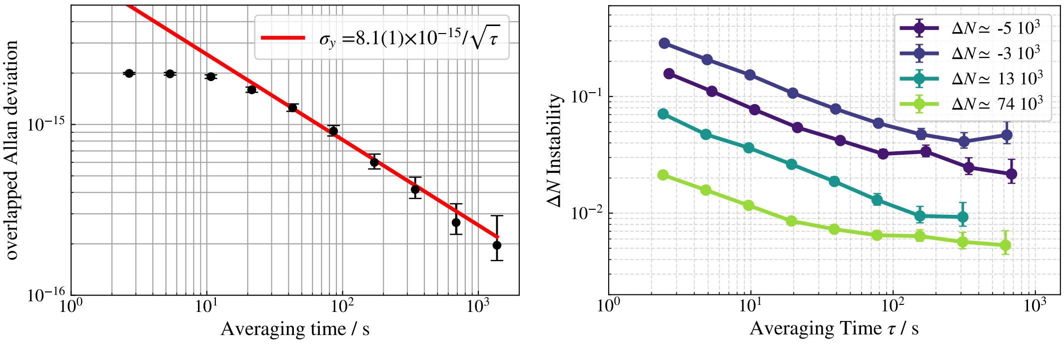

Fig. 5.13 Clock frequency instability during density-shift measurements. Left: overlapping Allan deviation of the differential measurement. Right: typical instabilities of the atom number difference.

Figure 5.14 shows the measured relative clock frequency shift as a function of atom number at different lattice depths. In all cases, the frequency shift shows a non-linear behavior characterized by a change in slope.

The non-linearity is the central feature of all the acquired measurements. From a theoretical perspective one can explain the arise of such non linearity with both the many-body spin model and mean-field treatments introduced in Sec.2.5. In the many-body model it is an explicit consequence of the presence of the quadratic term $\hat{S}_z^2$ proportional to the interaction energies. As anticipated, this non-linear features can emerge also in mean-field treatments, for example as the one proposed by Harber *et al.* in [200], by an implicit dependence of the excitation probability with density, which is the case for ^{88}Sr.

5.4.2 Data analysis with the many-body spin model

Within the many-boady approach introduced in Sec. 2.5.2, bosonic atoms occupying the same lattice site are treated as a collective spin-$1/2$ system with two-body contact elastic interactions described by the Hamiltonian in Eq. (2.35). The model accounts

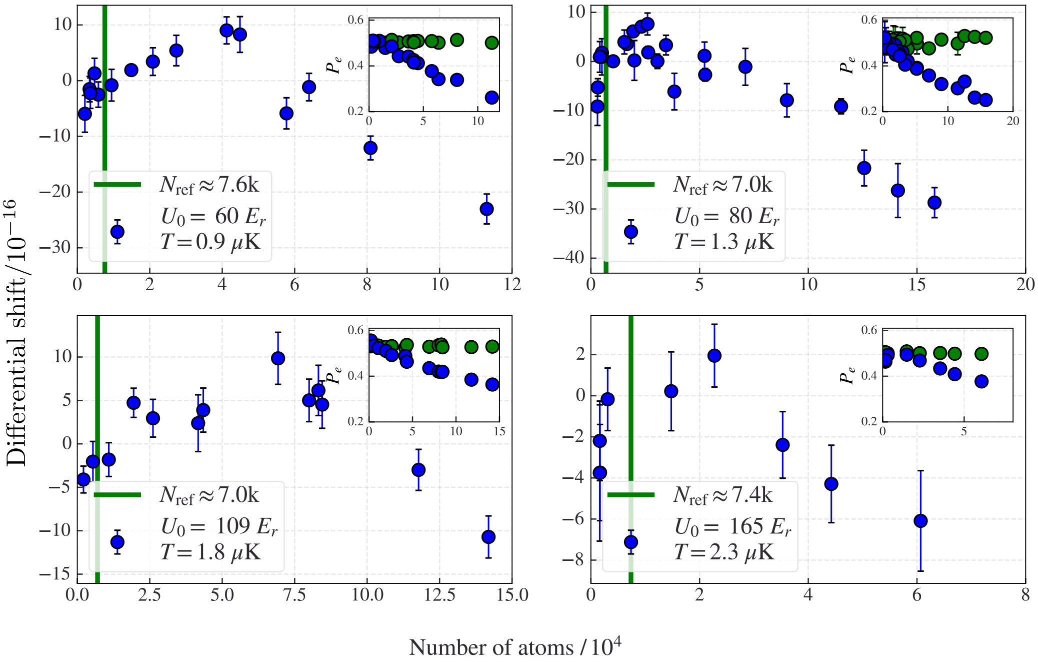

Fig. 5.14 Relative clock frequency shift as a function of total atom number for different lattice depths. Insets show the corresponding excitation probability as a function of atom number, here blue dots correspond to the measured atom number, while green dots represent the excitation at the reference atom number. The vertical green line indicates the reference atom number N_{ref}.

for s-wave interaction energies U_{gg}, U_{ee} and U_{eg}, among which the ground-ground is here neglected, or at least considered as a small correction, due to the small value of the ground state scattering length a_{gg} for ^{88}Sr [148].

To construct the model predictions for the density shift at a given total number of atom, the Hamiltonian of the system is solved using QuTip python library by integrating the evolution up to the interrogation pulse duration. The model evaluates the excitation probability at the lock-points $P_e(\delta \pm \delta_{\text{lock}})$ and finds the value of δ, i.e. the clock laser detuning, for which $P_e(\delta + \delta_{\text{lock}}) = P_e(\delta - \delta_{\text{lock}})$, thus effectively simulating the working principle of the clock stabilization loop. To reduce the computational complexity, instead of averaging over the lattice sites occupation, the lattice is assumed to be uniformly populated with the average site occupation number determined from the distribution defined by Eq.(5.4). The parameters of the model are the interaction energies U_{ee} and U_{eg}, and a global frequency offset that accounts for the differential nature of the measurement, and which represents the collisional shift at N_{ref}.

For some measurement series, data points at the highest atom numbers were excluded from the fit. This choice was motivated by the general argument of "poor" fitting, but most importantly because if the points were included, the low-density trend of the data could not be faithfully reproduced, hence failing in a correct estimation of the frequency shift at the reference atom number. A possible explanation could be that these points correspond to regimes where strong inhomogeneity of the lattice site occupation is expected, and therefore our uniformly occupied lattice approximation becomes not applicable. Also, the absence of losses and collisional decoherence in the spin-model probably start to be relevant in this regime, and cannot be neglected. The fitting results of the data with the procedure explained above is shown in Fig.5.15.

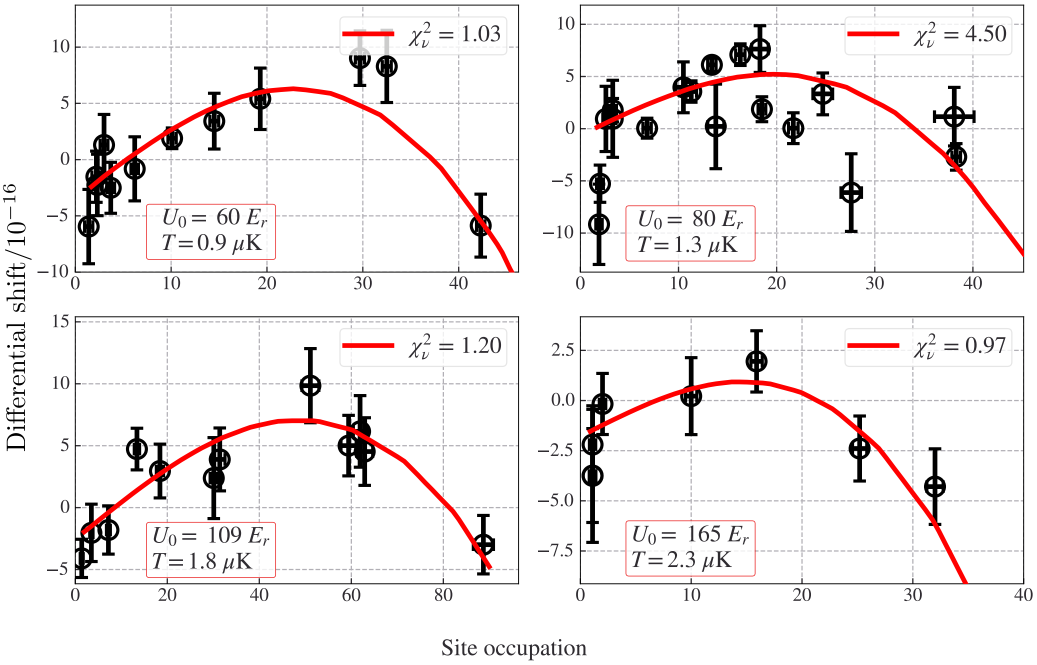

Fig. 5.15 Spin-Model fit curves of the data shown in Fig.5.14. Only the fitted range is shown. The exclusion of points is discussed in the main text.

It must be noted that despite the model being strictly lossless, it naturally predicts a decrease of excitation at increasing number of atoms. This effect is a consequence of the effective detuning in Eq. (2.35) depending on the instantaneous population imbalance. As a consequence many-body interactions alone can produce a density dependent suppression of excitation qualitatively consistent with the behavior shown in the insets of Fig. 5.14.

The quantitative results of the spin-model analysis, together with a comparison to the mean-field treatment are presented in Sec. 5.4.4.

5.4.3 Data interpretation with the mean-field model

Following the derivation outlined in [200], the mean-field collisions induced frequency shift for non-condensed thermal bosons can be written directly in terms of the excitation probability as:

$$\Delta\nu = \frac{2\hbar}{M}\left[a_{ee} - a_{gg} + (1-2P_e)\,(2a_{eg} - a_{ee} - a_{gg})\right] n, \tag{5.15}$$

where n is the atomic density within a lattice site, M is the ^{88}Sr mass. In Eq. (5.15) the non-linearity is encoded in the excitation probability P_e itself, since it is density dependent. Indeed, one may in principle couple the mean-field shift equation with the Bloch equations introduced by Lisdat *et al.*[145], including both inelastic and elastic dephasing processes, and summing the solution over the lattice sites. Doing so within a fitting routine would be however computationally intensive. Here instead, the excitation probability at increasing number of atom is treated with a phenomenological model chosen to reproduce our experimental data at increasing densities. To capture the observed behavior of the excitation probability shown in Fig. 5.12, for a lattice site with occupation m we model it as

$$P_e(m,\Delta,\Omega) = P_{\mathrm{R}}(\Delta,\Omega) \times P_0\, e^{-m\,\alpha_{\mathrm{eff}}(\Delta)}, \tag{5.16}$$

where $P_{\mathrm{R}}(\Delta,\Omega)$ is the single particle Rabi response, P_0 is an effective low-density excitation probability and $\alpha_{\mathrm{eff}}(\Delta)$ is an effective damping coefficient. To account for the dependence on the interrogation detuning, α_{eff} is further parameterized as

$$\alpha_{\mathrm{eff}}(\Delta) = \alpha_0\,(1-\beta\,\Delta)\,, \tag{5.17}$$

with α_0 and β as free, non-negative parameters.

For a given total atom number N, the experimentally relevant excitation probability is obtained by averaging Eq. (5.16) over the lattice site occupation distribution

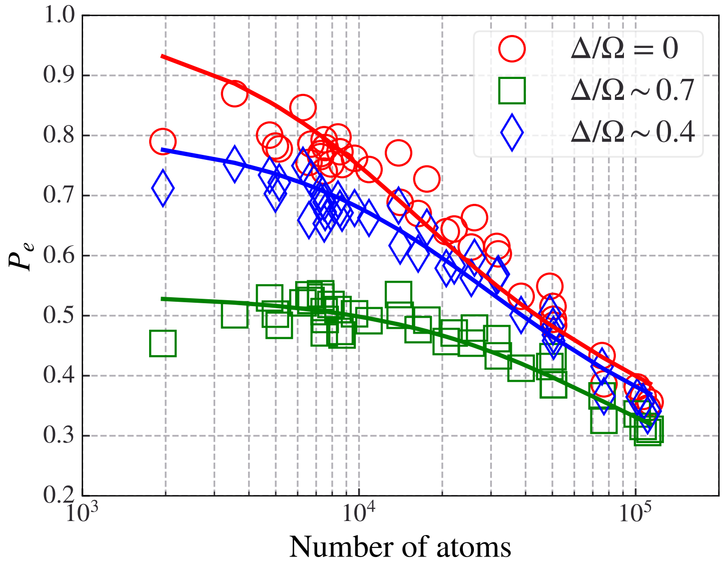

Fig. 5.16 Phenomenological model of the excitation probability adopted to perform the mean-field fitting procedure. Experimental data are excitation probabilities at different detunings retrieved from spectroscopic profiles acquired at increasing number of interrogated atoms. Solid lines represent the simultaneous best fit of the data with Eq.(5.18).

described in Sec. 5.1.4:

$$P_e(N,\Delta,\Omega) = \sum_m P(m)\, P_e(m,\Delta,\Omega), \tag{5.18}$$

where $P(m)$ is the normalized occupation number distribution for a total atom number N. For the data show in Fig.5.16, corresponding to the operating conditions at $\Omega = 2\pi \times 34\,\text{Hz}$, the fitting procedure determines $P_0 = 1.00(2)$, $\alpha_0 = 0.153(12)$, and $\beta = 50(2) \times 10^{-3}\,\text{Hz}^{-1}$.

This averaged excitation probability is then combined with the mean-field expression for the density shift in Eq. (5.15). In analogy with the spin-model analysis, the atomic density that enters the mean-field equation is determined using the uniformly occupied lattice approximation. Thus, for a given total atom number N, the mean lattice site occupation $\langle m \rangle_N$ is obtained from the loading model described in Sec. 5.1.4, and the corresponding density is therefore

$$n(N) = \frac{\langle m \rangle_N}{V_{\text{site}}}, \tag{5.19}$$

where the lattice site volume V_{site} is experimentally determined from the trap frequencies and temperatures as discussed previously.

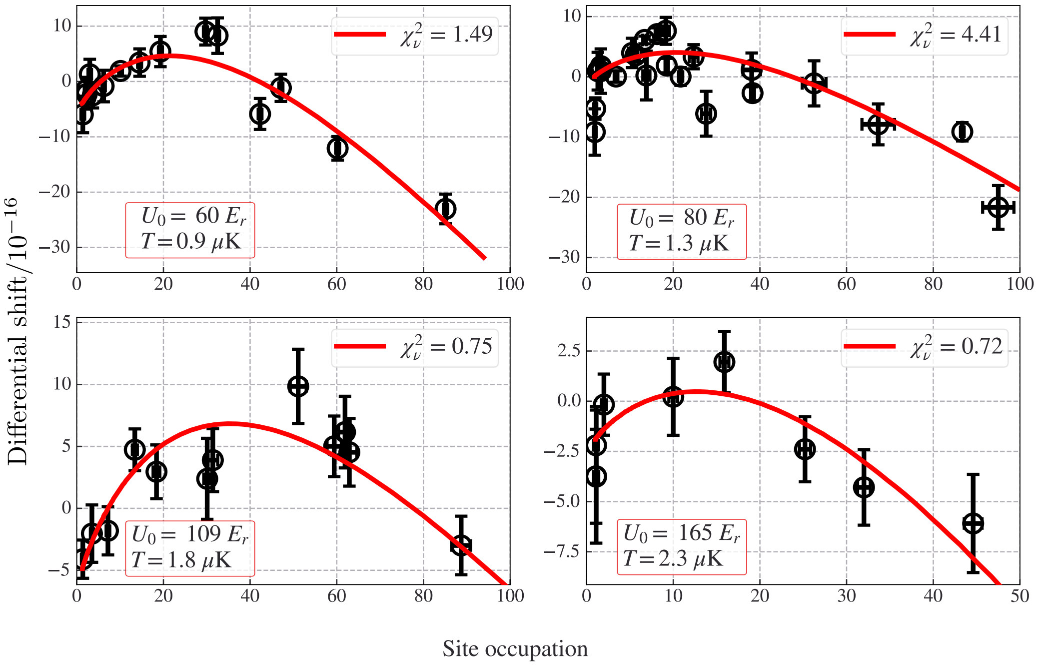

Fig. 5.17 Mean-field fit curves of the data shown in Fig.5.14. In contrast to the spin-model fit, the mean-field with the phenomenological added losses can well reproduce the data over the whole explored range of number of atoms.

The mean-field fitting procedure is performed combining Eq. (5.15) with Eq.(5.18), and using the experimentally determined densities $n(N)$. The free parameters of the fit are the scattering lengths a_{ee} and a_{eg}, together with a global frequency offset accounting for the differential nature of the shift measurement. The scattering length a_{gg} is fixed to its known negligible value $a_{gg} = -1.4(5)a_0$ [148].

The model fit to our data is shown in Fig.5.17, and quantitative results and their comparison with the spin-model interpretation are discussed in the next subsection.

5.4.4 Results and comparison

This section summarizes the interaction parameters of ^{88}Sr extracted from the density-shift data using the two analysis methods described in the previous sections: the spin model (SM, Sec. 5.4.2) and the mean-field (MF, Sec. 5.4.3). The evaluation of the systematic collisional shift affecting our clock at the typical operating density is discussed towards the end of the section.

Single-particle density calibration

For each measurement series performed at fixed trap depth the lattice site volume V_{site}, or equivalently the single-particle density $n_0 \equiv V_{\text{site}}^{-1}$, is obtained from the measured trap frequencies and temperatures as described in Sec. 5.1. The values of n_0 relative to each data set of the density shift measurements, together with the expected trend from the trap characterization, are shown in Fig. 5.18.

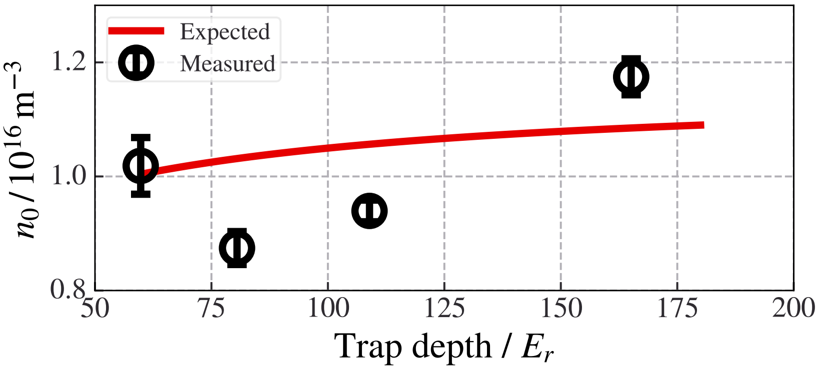

Fig. 5.18 Single-particle density $n_0 = V_{\text{site}}^{-1}$ used to convert atom number to density for the different density-shift data sets. Black points: values obtained from the measured trap frequencies and temperatures for each measurement series. Red line and shaded band: expected density from the lattice characterization, including the dominant uncertainties (temperature, trap frequencies, and waist).

As it can be seen in the plot above, over the range of the explored trap depths, the single-particle density does not vary dramatically. This is consistent with the fact that V_{site} is set by a combination of the three confinement frequencies and by the finite temperature broadening in Eq. 2.28. In practice, the increase of confinement with depth is partially compensated by the observed increase of temperature, so that the net density scaling with the trap depth is weaker.

Extracted interaction parameters

The interaction energies and corresponding scattering lengths extracted from the SM and MF fits are shown in Fig.5.19. The reported uncertainties of the fit parameters

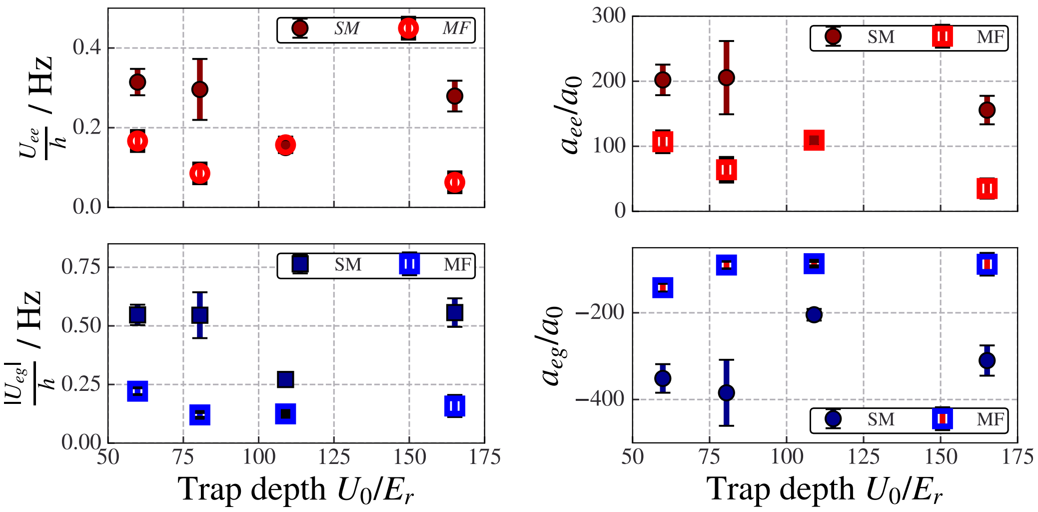

Fig. 5.19 Interaction parameters extracted from density shift measurements at different lattice depths. Right: scattering lengths a_{ee} and a_{eg} obtained from the spin-model (filled markers) and mean-field (open markers) analyses. Left: corresponding on-site interaction energies U_{ee}/h and $|U_{eg}|/h$. Error bars include the fit uncertainty rescaled by $\sqrt{\chi^2_\nu}$ when $\chi^2_\nu > 1$.

have been inflated by $\sqrt{\chi^2_\nu}$ whenever the reduced chi-squared χ^2_ν exceeded unity to account for underestimated experimental uncertainties. For ease of reference, the interaction parameters and the relevant experimental measurement conditions are summarized in tables 5.2, 5.3,and 5.4.

Table 5.2 Experimental parameters and density calibration for the density shift measurements. The single particle density $n_0 = V_{\mathrm{site}}^{-1}$ is estimated through Eq. (2.29).

U_0/E_r	$T/\mu\mathrm{K}$	$n_0/10^{10}\,\mathrm{cm}^{-3}$	$N_{\mathrm{ref}}/10^3$
60(2)	0.90(12)	1.02(5)	7.6(2)
80(1)	1.28(14)	0.87(3)	7.0(3)
109(2)	1.84(12)	0.94(2)	7.0(2)
165(2)	2.33(14)	1.17(3)	7.4(2)

The interaction parameters extracted from both the SM and MF analyses display a significant scatter when comparing measurements across different lattice depths. However, no particular experimental reason was identified to justify the exclusion of any point. Most reasonably, the scatter is related to the ability to precisely determine the lattice site volume, and the degree of experimental control we have on it over weekly timescales.

Table 5.3 Interaction parameters extracted using the many-body spin model. The fit parameters are the interaction energies U_{ij}/h, expressed in Hz, the scattering lengths are determined from U_{ij}.

U_0/E_r	U_{ee}/h	U_{eg}/h	a_{ee}/a_0	a_{eg}/a_0
60(2)	0.31(3)	−0.55(4)	202(23)	−350(33)
80(1)	0.30(8)	−0.50(10)	205(55)	−384(75)
109(2)	0.150(13)	−0.27(2)	110(6)	−204(14)
165(2)	0.28(4)	−0.56(6)	156(21)	−310(35)

Table 5.4 Interaction parameters extracted using the mean-field analysis. The fit parameters are the scattering lengths a_{ij}, energies U_{ij}/h are expressed in Hz and are determined from a_{ij}.

U_0/E_r	U_{ee}/h	U_{eg}/h	a_{ee}/a_0	a_{eg}/a_0
60(2)	0.166(28)	−0.222(24)	107(15)	−142(13)
80(1)	0.086(22)	−0.120(34)	64(17)	−90(12)
109(2)	0.158(16)	−0.124(12)	109(11)	−87(8)
165(2)	0.064(22)	−0.158(38)	35(12)	−88(22)

Regarding the interaction energies U_{ee} and U_{eg}, their increase with lattice depth is in principle expected due to the enhanced confinement, although weakened by the increase in temperature. Such a trend is not evinced from our data, likely due to the limited depth range explored and the weak expected dependence of n_0 on the confinement. The scattering lengths however, should not depend on the confinement. Assuming that the observed scatter is due to likely underestimated uncertainties, a conservative approach might be to report the scattering lengths determined via the two models as a simple average of the values obtained from each data set. The corresponding uncertainty is then taken as the sample standard deviation, thus:

$$\begin{aligned} \mathrm{SM}: &\quad a_{ee} = 168(40)\,a_0,\, a_{eg} = -312(70)\,a_0, \\ \mathrm{MF}: &\quad a_{ee} = 80(30)\,a_0,\, a_{eg} = -102(23)\,a_0. \end{aligned} \tag{5.20}$$

Notably, for the excited-excited interaction, our extracted value of a_{ee} from the MF and SM approaches is consistent with the estimate reported by Traverso *et al.* [146], who obtained $|a_{ee}| = 100(50)\,a_0$.

Leaving the scatter aside, the interaction parameters extracted with the spin-model are typically higher then the mean-field ones. This behavior, somehow expected, reflects the fundamental difference in how the two models account for density dependent excitation dynamics. The spin model describes a coherent many-body evolution with elastic interactions, is intrinsically lossless, and the shift derivation from the model accounts for the time dependent evolution of the population imbalance. On the other hand, the mean-field approach used here accounts phenomenologically for the observed reduction of excitation with density, which might be ultimately described by the sets of equations Eq.(2.30) that accounts for dissipation and decoherence, but the time dependence is neglected as in Eq.5.15, and only the final value of P_e after the excitation pulse is considered. This probably tends to favor smaller effective interaction energies required to reproduce our collisional shift data. Although in principle there should be a way to incorporate such losses also in a single lattice site many-body hamiltonian, and produce a more accurate description of the interaction within a lattice site, for instance by introducing Lindbladian dissipation terms (see for example [201]), this theoretical effort is left for future work. A further point of comparison is the interspecies scattering length a_{eg} determined from the interaction sideband (ISB) measurements discussed in Sec. 5.3, which was estimated as $a_{eg} = -180(50)\,a_0$. This value is marginally consistent with both MF and SM models within the experimental uncertainties, while lying closer to the MF result.

Despite these differences, all approaches consistently indicate a negative value of a_{eg}. Together with the determination of a_{ee}, in this work we therefore resolve the relative sign of the scattering lengths in bosonic ^{88}Sr, providing a novel constraint on its interaction properties.

As a further check for predictive power of the extracted interaction parameters from the density-shift analysis, we performed additional measurements by operating the clock at different interrogation detunings with respect to the reference lock point $\delta_{\text{lock}} = 25\,\text{Hz}$, and measured the resulting differential frequency shift. In these measurements, the atom number is kept fixed at $N_{\text{ref}} \simeq 7 \times 10^3$, while the error signal is generated at different detunings Δ from resonance. Figure 5.20 shows the resulting clock frequency shifts as a function of the normalized detuning Δ/Ω for both the 1D and 2D lattice configurations. In the 1D case, we were able to correct the reference point with the experimentally measured density shift at the reference atom number, the experimental data is therefore re-scaled by this offset. For the 2D configuration we were unfortunately unable to measure the shift at the reference point due to technical issues, thus in this case only the differential shift is shown. The solid lines correspond to the predictions of the mean-field model, evaluated using the MF scattering lengths at the reference operating point and without any additional free parameters. The shaded bands represent the associated uncertainty propagated from the interaction parameters and the density estimation.

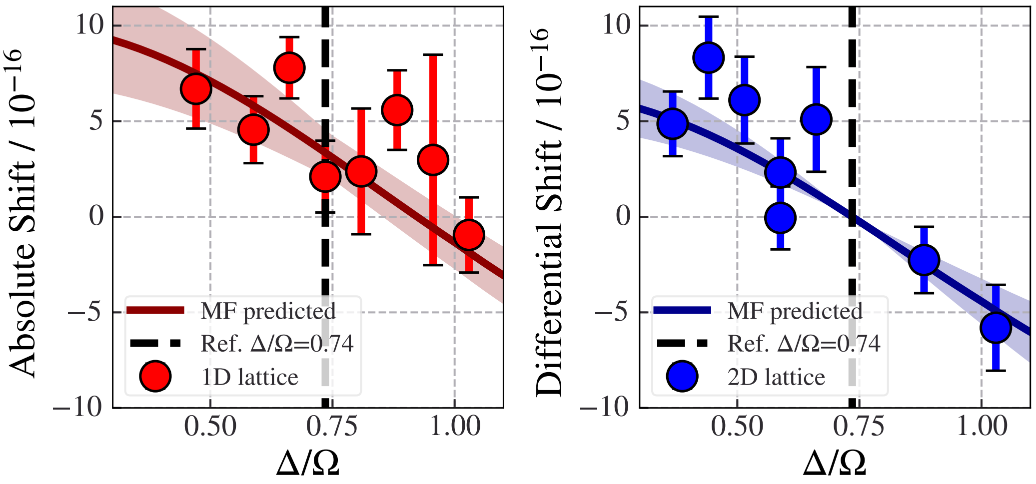

Fig. 5.20 Absolute (right) and differential (left) frequency shift as a function of the normalized interrogation detuning Δ/Ω, obtained by locking the clock at different detunings with respect to the reference lock point $\delta_{\text{lock}} = 25\,\text{Hz}$, in a 1D (right) and 2D (left) lattice sample. Solid lines show the mean-field predictions evaluated using the interaction parameters extracted at the reference operating conditions, while shaded areas indicate the corresponding uncertainty. Vertical dashed lines are placed at the reference detuning.

The observed dependence of the shift on the interrogation detuning is a direct consequence of the excitation fraction entering Eq. (5.15), even without introducing losses, and is therefore expected within the mean-field framework. Probably, a similar behavior would be obtained also with the spin-model description if evaluated using the corresponding interaction parameters. The good agreement between the experimental data and the predicted curves over the explored range of detunings provides an additional cross-check for the density calibration and for the interaction parameters extracted from the density-shift measurements.

Evaluation of the collisional frequency shift

The spin-model (SM) and mean-field (MF) analyses estimate collisional shifts of comparable order at the reference operating point, typically of the order of a few

$\times 10^{-16}$. While the two approaches return different interaction parameters, the extracted shift at the reference operating conditions is, as it should, less sensitive to these differences because it is constrained by the same experimental data.

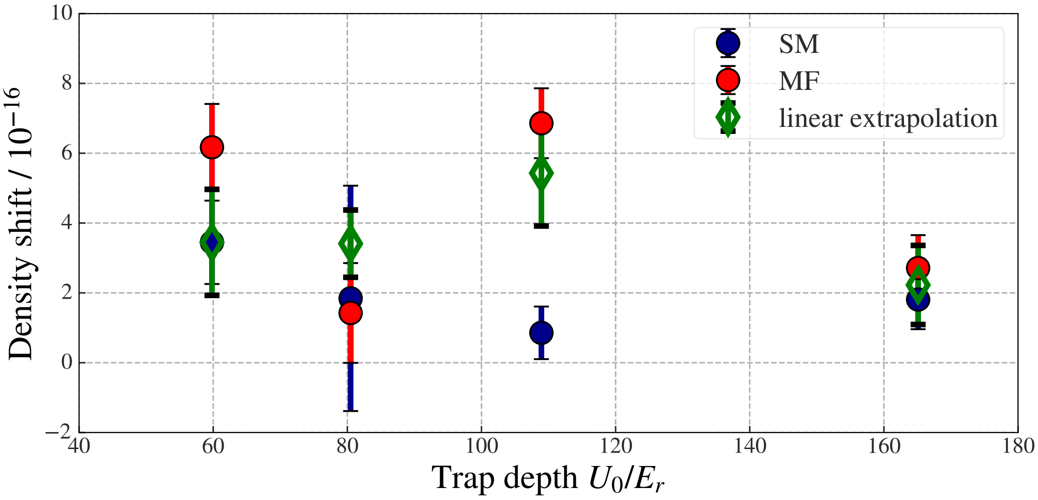

Fig. 5.21 Density shift evaluated at the reference atom number $N_{\text{ref}} \simeq 7 \times 10^3$ as a function of lattice trap depth U_0. Blue circles show the shifts extracted from the many-body spin-model (SM), red circles correspond to the mean-field (MF), and green diamonds represent values obtained from a linear extrapolation of the measured density shift for atom numbers $N \leq 2.5 \times 10^4$. Error bars include statistical uncertainties from the fits, inflated when the reduced χ^2 exceeds unity.

As an additional comparison point for the shift evaluation, we extract a more independent estimate of the shift by simply performing a linear fit of the measured frequency shift in the low-density range ($N \lesssim 2.5 \times 10^4$), where and decoherence and losses effects are reduced. The three extraction methods results are shown in Fig. 5.21.

Within the explored trap depth range, there is no clear trend of the shift with respect to U_0 at the current level of uncertainty, although a weak dependence is expected. To provide a representative shift value at the typical operation conditions we combine the three determinations (SM, MF, and linear) across all the trap depths. Considering the unweighted mean and the standard deviation as the uncertainty the result is:

$$\left.\frac{\Delta\nu_{\text{coll}}}{\nu_{88}}\right|_{N_{\text{ref}}} = 3.3(1.9) \times 10^{-16}. \tag{5.21}$$

Considerations

A glimpse of the nonlinearity emerging in density-shift experimental data is already suggested by the measurements reported in Ref. [145] and in the corresponding PhD thesis [150]. There, the authors state that beyond a certain atom number ($\simeq 5 \times 10^4$) the density shift tends to saturate, although no further measurements are shown in that regime. Moreover, the magnitude of the shifts observed in those works is of the order of 10^{-14}, almost two orders of magnitude larger than what we measured here. Shifts of comparable magnitude were, however, reported in the early characterization of the INRiM ^{88}Sr clock [86], where the clock was operated without a control on the excited state population due to the absence of repumping lasers. In contrast, in Refs. [145, 150] the clock is operated by locking to the excitation profile obtained from the detection of excited atoms only, in order to shorten the experimental cycle time. To assess whether the choice of spectroscopic signal influences the observed density shift, we generate the error signal using the three available profiles: the ground state population, the excited state population, and the normalized excitation fraction. By extracting the corresponding lock point positions for each profile, and looking at differences, there was no significant dependence. Actual density-shift measurements performed using different locking signals were, however, not carried out during this work.

Other key literature references reporting experimentally determined density shifts in ^{88}Sr include Takano *et al.* [184] and Origlia *et al.* [199]. In those works, the observed shifts are linear, about one order of magnitude smaller than our measured shift, and with a negative slope. However, in both cases photoassociation pulses on the ^{3}P$_1$ transition [202] are applied to perform parity selection of the lattice site occupancy, resulting in lattices dominated by singly occupied sites. This substantially modifies the interaction picture, suppressing on-site interactions and potentially making significant the role of weaker inter-site interactions that are here neglected, and ultimately leading to a different density shift behavior.

Chapter 6

Towards a hybrid cavity-lattice clock

This chapter describes the design and the initial construction of a cavity-enhanced extension of the INRiM Sr optical lattice clock. The upgrade introduces an optical cavity system designed to provide strong and homogeneous coupling between the atomic ensemble and the optical cavity fundamental mode. The aim is to enable collective atom-cavity interactions and exploit them to achieve a quantum-enhanced clock operation, based on the realization of strongly correlated atomic states. This will allow us to study possible novel state preparation and interrogation protocols, and provide a direct experimental platform for recent research investigations carried out by our theory group [203, 204].

6.1 Atom-cavity coupled ensembles for optical clocks

As mentioned in the Introduction, one of the fundamental limits to clocks stability is the projection noise associated with the standard preparation and detection of the atomic state in atomic clocks. For an ensemble of N uncorrelated atoms this noise scales as $N^{-1/2}$ and defines the *standard quantum limit* (SQL). A possible route to overcome this limitation, requires the generation of non-classical atomic states, where correlations within the atomic ensemble are introduced, typically via an interaction with an external system. As a result, squeezed states [69, 70] which show a reduced uncertainty on the observable of interest can be realized. In atomic clocks, the observable of interest is the population imbalance between the clock states, identified with the total spin operator $\hat{S}_z$. Spin squeezed state with up to 20 dB below SQL uncertainty have been demonstrated on the RF clock transition of ^{87}Rb [71, 72]. In optical clock transitions the metrological gains experimentally achieved until now are moderate and very recent [74, 205, 206], and this reflects the ongoing experimental interest and effort that is being directed towards the realization of quantum-enhanced optical clocks.

The most widespread approach to generate squeezed states with reduced uncertainty on $\hat{S}_z$ exploits optical cavities and their interaction with the atomic system which is described in the framework of cavity quantum electrodynamics (cQED). A detailed theoretical treatment of atom-cavity coupled systems is beyond the scope of this manuscript and is not required for understanding the majority of the concepts discussed in this chapter. This section is limited to a qualitative description of the physical mechanisms behind cavity-assisted measurements and introduces the relevant figures of merit that led to the conceptual design described in the next section. Finally, here we clarify how quantum non-demolition (QND) measurements are enabled in such a system and can be exploited for the generation of spin-squeezed states relevant for optical clocks applications.

In the cQED context, the cavity mode acts as a mediator of collective light-matter interactions, coupling simultaneously to all atoms located within its mode volume. When the atomic ensemble is tightly confined, with frozen motional degrees of freedom, and the spatial overlap with the cavity mode is homogeneous, the coupling becomes collective.

The strength of the interaction between a single atom and the cavity field is quantified by the atom-cavity coupling constant g (see for example [207–210]), whose strength mainly depends on the optical mode spatial profile, and the atomic dipole moment. However, the main figure of merit of the atom-cavity system is represented by the cooperativity. The single atom cooperativity C_0 is defined as the ratio between the rate of spontaneous emission into the resonator mode and the decay rate into all other free-space modes and has the expression given by [210]

$$C_0 = \frac{4g^2}{\kappa\Gamma} = \frac{24\mathscr{F}}{\pi k^2 w_0^2}, \tag{6.1}$$

where the second equality is retrieved from semi-classical arguments [210] and shows how the cooperativity depends on the optical resonator properties such as the finesse $\mathscr{F}$, the cavity mode waist w_0 and the cavity light wavevector k. From this, it is clear that the cooperativity can be enhanced by decreasing the cavity mode volume, hence its mode waist, and increasing the cavity finesse.

In contrast to typical laser cavities, where the active medium decay rate is much larger than the cavity decay which in turn dictates the final coherence of the radiation, in the cQED system in order to extract information from the cavity, either in the case of QND measurements or to detect superradiance, it is important to work in the so called bad cavity regime, defined by $\kappa \gg \Gamma$. In this limit, the intracavity field decays on a timescale much shorter than the atomic dynamics and therefore quasi-adiabatically follows the evolution of the atomic ensemble. This regime is particularly favorable for metrological applications, as it allows information about collective atomic observables to be extracted from the cavity output field with minimal perturbation on the atomic system. Furthermore, if the cavity is far-detuned from the atomic resonance, the system is in the dispersive regime, where the presence of atoms inside the cavity substantially leads to a shift of the cavity resonance frequency that depends on the internal state of the atoms. At an effective level, this interaction can be described by a coupling Hamiltonian of the form [75]

$$\hat{H} = \hbar \frac{g^2}{\Delta} \hat{a}^\dagger \hat{a} \hat{S}_z, \tag{6.2}$$

where $\hat{a}^\dagger \hat{a}$ is the intracavity photon number, $\hat{S}_z$ denotes the collective population imbalance and Δ is the cavity detuning from atomic resonance. This expression highlights the key feature enabling cavity assisted measurements: the cavity resonance frequency depends on the collective spin projection $\hat{S}_z$. As a consequence, measuring the phase of the light transmitted by the cavity provides direct information about this collective observable and since $\left[\hat{S}_z, \hat{H}\right] = 0$ such a measurement constitutes a quantum non-demolition (QND) measurement of $\hat{S}_z$ [211].

As a back-action of the cavity light field onto the atoms, repeated or continuous QND measurements can reduce the fluctuations of $\hat{S}_z$ below the SQL, leading to the generation of spin-squeezed states [203, 212, 213]. From a physical perspective, the cavity mediates an effective long-range interaction among the atoms, correlating their internal states through the shared cavity field. The degree of squeezing that can be achieved, usually quantified by the Wineland's parameter [69, 214]

$$\xi^2 = 2J \frac{\Delta^2 \hat{S}_z}{|\langle \mathbf{S} \rangle|^2} = N \frac{\Delta^2 \hat{S}_z}{|\langle \mathbf{S} \rangle|^2}, \tag{6.3}$$

depends on the collective cooperativity (which is NC_0 for N homogeneously coupled atoms [210]), the probing strength, and the balance between information gain and decoherence.

Given the considerations above, a desirable realization of the atom-cavity system that aims at maximal and optimal spin-squeezing should therefore target a strong coupling regime, and the highest degree of coupling homogeneity, in order to reduce the coupling differences arising between atoms positioned in different regions of the intracavity field. Based on these considerations, the cavity-enhanced system developed at INRiM is designed to achieve strong collective coupling on the $^3\mathrm{P}_1$ intercombination transition [215], while coupling homogeneity across the atomic ensemble is ensured by trapping the atoms in a magic-wavelength optical lattice commensurate [72, 216] with the cavity standing wave. The main goal of the experiment upgrade is to exploit the strongly coupled and homogeneous system to study the benefits of using highly correlated collective atomic states during the clock state preparation and read-out.

6.2 Dual-cavity architecture and experimental concept

The experimental platform conceptualized for the INRiM hybrid cavity-lattice clock is based on a dual cavity architecture, in which atomic confinement and atom-cavity coupling are provided by two distinct optical resonators. The central element of the setup is a nearly confocal Fabry-Pérot (FP) optical cavity, namely the cQED cavity, designed to enable strong collective coupling between the atomic ensemble and its fundamental mode. The second cavity serves the purpose of generating a magic-wavelenth optical lattice, with spatial periodicity commensurate with the standing wave of the cQED cavity. This is important to stress: given the argument presented in the previous sections it is clear that the cooperativity, and ultimately the degree of achievable squeezing, depends on the atom-cavity mode overlap. Since the probe field of the cQED cavity has nodes and anti-nodes, a generically trapped ensemble of atoms within the cavity field would have regions that do not experience coupling due to the absence of the cavity field. The commensurate lattice therefore is built to provide a precise geometric relation between the trapping potential and the cavity field in order to maximize the coupling and make it more homogeneous. Since the lattice and probe wavelengths lie in different spectral regions, this commensurability cannot be achieved with a simple collinear geometry and it is therefore generated by a bow-tie resonator. The design and optimization of the cavities has been carried out prior to this work [216], here we summarize the procedure and results that lead to the choice of cavity parameters, as explained below and summarized in Tab.6.1 and 6.2. A 3D render of the final system is shown in Fig. 6.1, and it will be detailed in the next section.

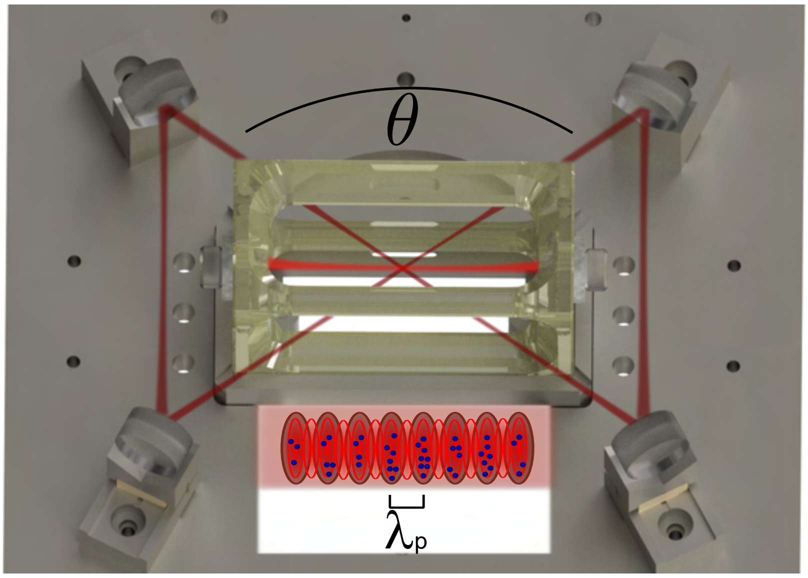

Fig. 6.1 Cavity-enhanced system with commensurate lattice.

cQED cavity design The role of the cQED cavity is to mediate the interaction between the atomic ensemble and a single optical mode on the $5s^2\,{}^1\mathrm{S}_0 \leftrightarrow 5s5p\,{}^3\mathrm{P}_1$ intercombination transition. The relevant figure of merit that has been optimized is not the single atom-cavity coupling strength g, but the single atom cooperativity C_0. The design strategy targets a near unity per atom cooperativity, such that for N atoms the total cooperativity is $C = NC_0 \gg 1$. At the same time, the cavity finesse is kept below 10^5 to avoid technical complications associated with ultra-high finesse resonators, and most importantly to allow operation in the bad-cavity regime, where the cavity loss rate κ is stronger than the atomic transition free-space spontaneous emission rate Γ. The considerations above led to a final cavity length $L = 66\,\mathrm{mm}$, with spherical mirrors characterized by a radius of curvature $\mathrm{RoC} = 75\,\mathrm{mm}$, and finesse $\mathscr{F} = 88 \times 10^4$. The cavity length and mirrors RoC determine a cavity mode waist of $w_0 = 90.4\,\mu\text{m}$ at 689.4 nm. The cQED cavity spacer is realized by an external company (Stable Laser Systems) and it is made by a low-expansion glass (Clearceram). A piezo actuator is glued on each mirror to allow for both cavity stabilization (by driving the piezo elements differential voltage), and for eventually tuning the cooperativity by driving the piezo elements common mode, thus changing the overlap between the atomic sample, trapped at the anti-nodes of the magic-wavelength optical lattice, and the cavity mode profile (see Fig.6.1). The cavity mirrors are coated to have high reflectivity (HR) at 698 nm, to leave open the possibility of studying collective emission phenomena on both the intercombination cooling and clock transitions [65, 66, 217, 218].

Table 6.1 Expected cQED cavity properties at 689.4 nm.

L / mm	66
FSR / GHz	2.27
RoC / mm	75
$\mathscr{F}$	88×10^4
w_0 / µm	90.4

Lattice bow-tie cavity design Since the atoms must be trapped at the center of the cQED cavity, the lattice bow-tie resonator has been designed to surround the linear cavity and with a fully-symmetric configuration so that the crossing point correspond to a cavity waist, therefore minimizing waveform aberrations. The commensurability criterion requires having at least a precise integer relation between the lattice and the cQED cavity standing wave spacings. This is achieved by tuning the crossing angle of the bow-tie cavity lattice beams to $\theta = 107.7^\circ$ [216]. This choice leads to a 1:2 commensurate lattice, with atoms trapped every other anti-node of the probe cavity, as pictorially shown in Fig.6.1. Fixing the crossing angle automatically constraints the mirrors angle of incidence to be $\alpha = 26.93^\circ$, leaving in principle three degrees of freedom remaining: two distances and at least one mirror radius of curvature (RoC). However, as stated above, the fully symmetric constraint further reduces the degrees of freedom, that are chosen to be the short arm of the cavity length and the mirrors RoC. The optimization of these two parameters is carried out by minimizing the cavity waist to increase the trap depth at the crossing point, and at the same time reducing the cavity sensitivity to mirrors misalignment. This procedure led to a short arm distance $d_1 = 63.8\,\mathrm{mm}$ and mirrors RoC = 50 mm. Furthermore,

Table 6.2 Lattice bow-tie cavity expected properties. The cavity waists w_{0S} and w_{0T} are the sagittal and tangential waists at the crossing point, where the atoms are trapped, α is the mirrors angle of incidence constrained by the commensurability requirement.

d_1 / mm	63.8
d_2 / mm	108.15
α / °	26.93
FSR / MHz	871.7
RoC / mm	50
w_{0T} / µm	80.8
w_{0S} / µm	132.7
$\mathscr{F}$	174

all mirrors are chosen to have the same coating reflectivity $R = 0.991$ resulting in a low cavity finesse $\mathscr{F} \approx 174$. The full symmetry of the cavity does not define a preferential input coupler, and allows pumping of the cavity modes from different directions. This is important considering that pumping a single cavity mode results in a 1D lattice with periodicity along the cQED cavity axis (see for example [130, 219]). Lamb-Dicke regime clock interrogation in such a geometry is prevented by the cQED cavity being HR coated at the clock laser wavelength. Therefore, an additional motion quantization axis is needed. It can be realized by either pumping the counter-propagating mode of the lattice resonator, obtaining a 2D lattice similar to the one shown in Fig. 2.3(d), that would allow Doppler and recoil free clock interrogation in any direction co-planar to the lattice beams. In this case, the clock laser is intended to be propagated co-axially to the lattice beam in the direction of the long cavity arm. An additional possibility is to add an external lattice, orthogonal to the bow-tie cavity plane [74].

6.3 Design of the in-vacuum components

6.3.1 Optical access and space constraints

The design of the in-vacuum mechanical components is primarily constrained by the requirement of precise and stable relative alignment between the Fabry-Pérot cQED cavity and the lattice bow-tie cavity. Since the atomic ensemble must be simultaneously located at the waist of the probe cavity mode and at the crossing point of the lattice beams, the mutual alignment of the two cavities represents the dominant geometrical constraint. The two cavities, being decoupled systems, complicates things even more, and at the same time makes searching for extreme machining tolerances uselessly expensive.

Additional constraints arise from the optical access provided by the vacuum chamber. The chamber body is made of titanium and has an octagonal shape, with the largest distance between opposite viewports of approximately 270 mm and an overall height of 114 mm. A detailed technical drawing of the chamber is shown in Fig. A.1. Optical access is provided by four CF63 viewports and three CF40 viewports distributed along the octagon faces, as well as two additional CF63 viewports located on the top and bottom of the chamber body. These two viewports are connected to the main chamber through CF200 flanges. The remaining port along the octagonal body is reserved for the connection to the atomic source.

The viewport arrangement, together with the presence of both optical cavities inside the chamber, prevent a straightforward implementation of the MOT and lattice beam paths. As a consequence, a non-orthogonal MOT configuration in the horizontal plane must be adopted, and additional in-vacuum folding mirrors are required to route the lattice beams to and from the bow-tie cavity. Furthermore, these constraints place strict limits on the size and positioning of all in-vacuum optical mounts, and also restrict the MOT beam diameter, which is limited to a maximum value of approximately 1 cm.

The final beams geometry adopted to satisfy these constraints is shown in Fig. 6.2, where the overall layout of the designed system can also be appreciated. In the figure, the MOT beams are shown in blue, while the lattice cavity pump and possible reflection/transmission beams are shown in red. Four possible pumping directions for the lattice cavity are identified: two accessible through CF63 viewports used for the MOT beams, and two additional directions available at the edges of one of the CF40 viewports.

These space and access constraints impact the mechanical design of the lattice cavity mirror mounts. In particular, they make it impractical to employ, as done in other experiments including [220, 221], engineered UHV-compatible mirror mounts for the 1/2" bow-tie cavity mirrors, as the limited available volume leave minimal freedom for bulky adjustment mechanisms. As a result, the mirror holders are designed as compact elements featuring a simple V-groove geometry, which defines, in principle, the mirror position and angle by construction. The mirrors are aligned using external tools and subsequently glued to the holders during the alignment procedure described in Sec. 6.3.4. A similar approach is for example used in [222].

For the same reasons, shear piezoelectric actuators are chosen for cavity length control. Compared to stack actuators, shear actuators allow a much more compact implementation, compatible with the restricted space available around the bow-tie cavity mirrors.

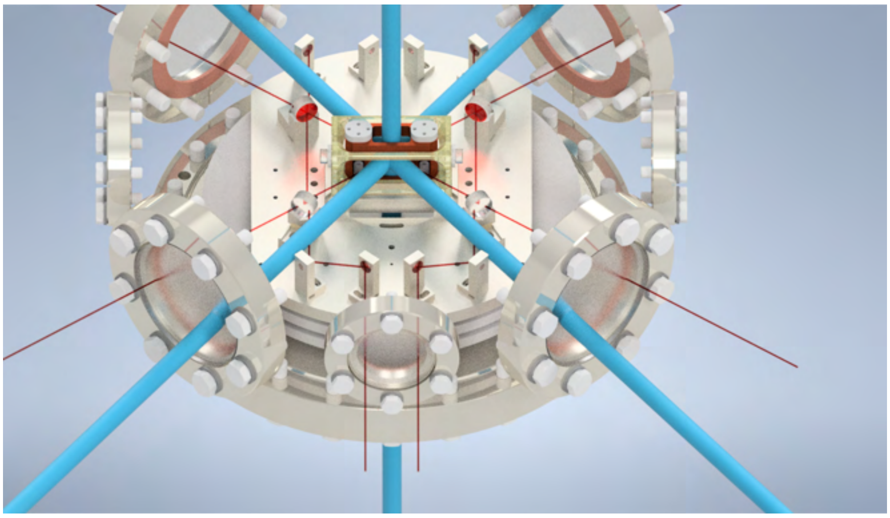

Fig. 6.2 3D render od the realized system with beam paths.

6.3.2 Materials selection

All the components are required to be UHV compatible and also non-magnetic, to prevent the uncontrolled magnetization of elements that would impact on the atomic system. For this reason, essentially all the critical components are machined from titanium, specifically the Ti6Al4V alloy, which besides excellent non-magnetic properties also shows a good mechanical stability, a relatively low thermal expansion coefficient, and a low outgassing rate. An exception is made for the passive vibration damping stage detailed in Sec. 6.3.3 which in a non-magnetic tungsten alloy (Wolfmet HA 190). This choice was inspired by the work in Ref.[223]. The high density $\rho \approx 17\,\mathrm{g\,cm^{-3}}$ of this material allows the mechanical frequency of the vibration damping support to be lowered without increasing the overall volume of the assembly.

Always for vibration damping purposes, elastomeric material (FKM) elements are also included in the design.

Piezoelectric components are ceramic based actuators, specifically we used NAC-2123 for the cQED cavity, and NAC2403-H3.4 for the bow-tie cavity.

Adhesive bonding will be required for mounting optical components and piezoelectric actuators. Several low-outgassing epoxy options were evaluated, taking into account both manufacturer specifications and reported experience from similar atomic physics experiments with the stringent vacuum level requirements, including Refs.[224–226]. The details reported in Yu-Ting Cheng PhD thesis [227] about gluing optics and other element were also particularly helpful in the selection. Based on this survey and the current commercial availability EPO-TEK H77 is selected as the primary epoxy adhesive, due to its suitable mid-high viscosity and favorable handling properties.

Additional elements introduced with the aim of supporting an in-vacuum temperature monitoring system, and a control system on possible stray electric fields are realized using oxyngen-free high conductivity (OFHC) copper and PEEK, a UHV compatible semi-crystalline thermoplastic material.

6.3.3 Final assembly

The machined components arrived in our laboratory during between late November and early December 2025. A test assembly of the machined components is shown in Fig. 6.3. Here all the elements, besides the cQED cavity, are shown in their intended final configuration on the titanium support platform, of which complete technical drawings are shown in figures A.2,A.3,A.4.

Mirror mounts. A total of eight folding mirror mounts are disposed symmetrically with respect to the platform center. Although only four of them are actually needed, this choice is made to minimize the mass distribution asymmetry. These mounts are realized to host glued mirrors with diameter $\phi = 3\,\mathrm{mm}$, and have a prefixed design position, but are left with a rotational degree of freedom. This feature can be appreciated in the technical drawing of Fig. A.6, and can eventually be exploited before screwing the mounts onto the science platform.

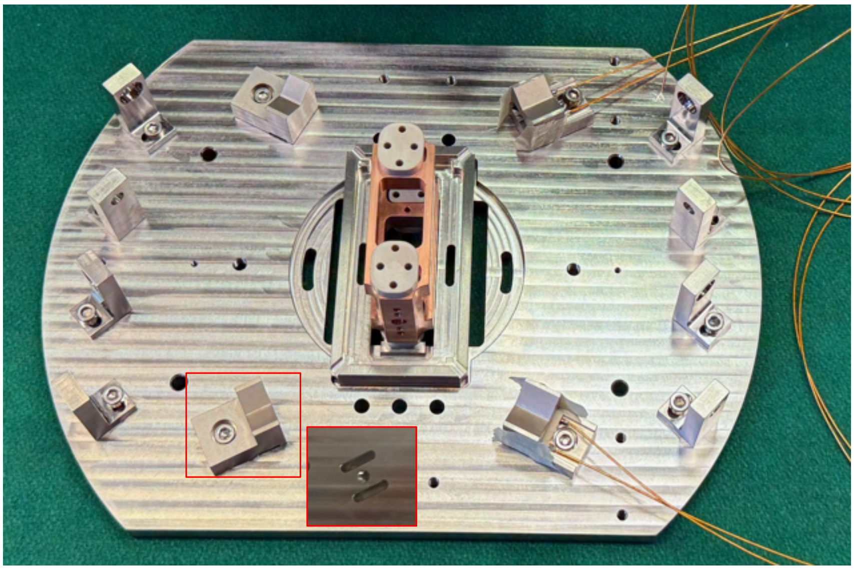

Fig. 6.3 Test assembly of the final machined parts onto the science platform.

Two kinds of bow-tie cavity mirror mounts are realized: monolithic mounts (Fig. A.7), and composite mounts (Fig. A.8,A.9), the latter being used for hosting the piezoelectric element. Both mount types will be fixed to the science platform via appropriate UHV compatible screws, with their positioning guided by the slotted features highlighted in red in Fig. 6.3. The composite mirror mounts feature a slotted region where the epoxy will be placed. This serves the purpose of guiding the glue expansion during the cure process and also to provide a way out for the epoxy outgassing products.

cQED cavity holder. How to hold and position the cQED cavity has been a concern, both in terms of the alignment requirements and sensitivity to environmental noise. Caged solutions, in which the cavity is held in place and partially isolated from external vibration via elastomeric elements have initially been considered. However, this was soon discarded as it will result in increased difficulties and uncertainty in the cavity positioning and most importantly on its long-term stability. In the end, we concluded that the safest option was to let the cavity define a reference point, by fixing it onto the science platform, and developed the alignment tool described in the next section and inspired by the work presented in [228]. In order to avoid directly gluing the spacer on the platform, a dedicated cavity holder (Fig. A.5) was designed. The holder features four contact points to which the cavity will be glued, while the holder itself will be epoxy-bonded to the platform. This minimize the risk of directly damaging the spacer if, for some reason, dismount of the part is needed.

Temperature sensors and electrodes housing. The experiment upgrade targets to reach fractional accuracy at least in the low 10^{-17} region. Thus, the presence of in-vacuum temperature sensor is planned for a better estimation of the BBR shift, as well as a set of 8 electrodes to generate electric fields in all the spatial directions. The electrodes serves the purpose of quantifying and eventually cancel the DC Stark shift [229–231] arising from stray electric fields. Due to the high content of glass material and piezoelectric elements in the vacuum chamber, it would be surprising to not observe this issue. The housing for these elements is designed as a OFHC copper support, to provide a minimal shielding and high thermal conductivity. It is placed within the cQED cavity in the proximity of the atomic sample, and its structure can be appreciated in the picture of Fig. 6.3. A detailed technical drawing can be found in Fig.A.10.

Vibration damping system. Finally, in order to provide a passive system for environmental vibration damping is developed. The system exploits three heavy tungsten alloy plates, each one separated from the next via three Viton spheres of diameter ϕ =6.35 mm. Each sphere sits on a 4.5 mm flared through hole which also has an extended slot to prevent trapping of gas molecules. The science platform lays on top of the three plates separated by four Viton spheres. The system is shown in Fig.6.4, where the simulated damping properties with a $\approx$10 Hz cut-off frequency are displayed. Several other shapes and arrangements of the damping stages have been tested via finite-element-modeling (FEM), in particular the use of cylinders instead of spheres to separate each stage, as done in [223], has been considered but resulted in higher mechanical resonances in the order of 100 Hz. With the limited space availability the volume, hence the mass, of the plates is constrained and reaching simulated lower mechanical resonances is prevented with the designed simple structure.

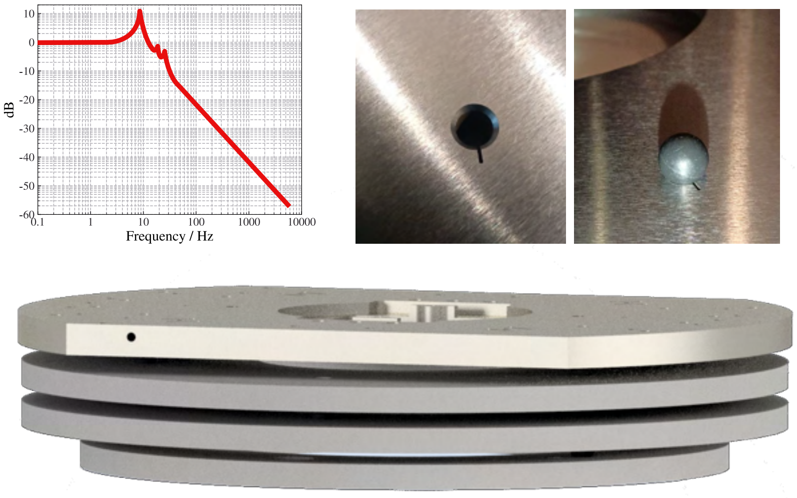

Fig. 6.4 Vibration damping system and its simulated frequency response.

6.3.4 Alignment tool and preliminary procedure

Given the constraints described in Sec. 6.3.1 and how the cavities system has been conceptualized, in order to achieve the requested mutual positioning of the cavities, an alignment tool is designed. Detailed technical drawings of the system are shown in figures A.11 to A.14, while in Fig.6.5 the machined components can be appreciated.

The key elements of the tool are two complementary parts (right side of Fig.6.5) which have both cavities paths engraved with a semi-circular cross section of diameter $a = 1$ mm. The engraved paths diameter is chosen to balance the level of guidance provided to the beams, and their undesired diffraction. The estimated beam radius at the apertures of $w_{\mathrm{BT}} \approx 160\,\mu\mathrm{m}$ and $w_{FP} \approx 275\,\mu\mathrm{m}$, respectively for the bow-tie and Fabry-Pérot cavities. This results in a worst-case power clipping for the FP cavity, giving a power clip of $P_{clip} = e^{-a^2/2w_{\mathrm{FP}}^2} \approx 0.13\%$. If this will result as a limiting factor, the engravings can be enlarged. The third component of the alignment tool is screwed on top of the parts with the engraved optical paths, as shown in the left side of Fig. 6.5. Here, four provisional kinematic mounts will be attached, as shown in Fig. 6.6, to held the bow-tie mirrors in place and allow for alignment of the cavity.

The strategy to mutually align the two cavities exploits the fully-symmetric configuration of each cavity, which means that when the two cavities meet at the crossing point, the crossing points itself becomes a symmetry point. The procedure will likely require many attempts and tests with a prototype spacer simulating the

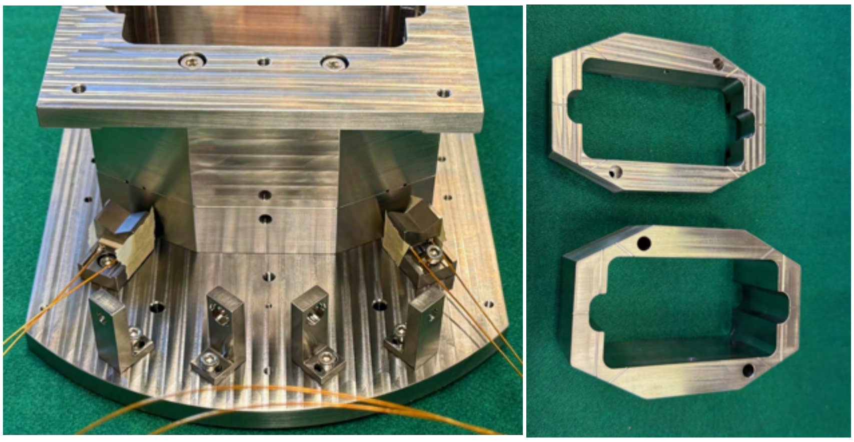

Fig. 6.5 Left: picture of the alignment tool positioned in the assembly. Right: details of the cavity path engraved in the alignment tool.

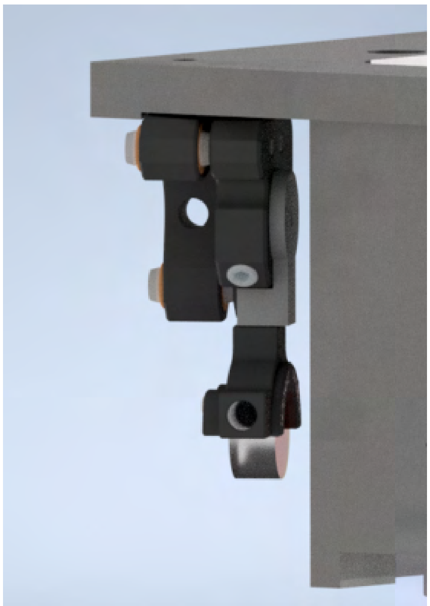

Fig. 6.6 Provisional kinematic mount for the bow-tie mirrors alignment.

cQED cavity, but the general idea, developed until now, requires the following steps to find the center of the system:

- The input beam of the FP cavity is aligned to resonate within it.
- An additional plane mirror is placed along the cavity axis, and its position is scanned until it forms a new resonant cavity with the FP cavity input mirror. This mirror now sets the center point of the system, which the bow-tie circulating beam must go through.

- The additional mirror is replaced with a precision pin-hole, and the bow-tie cavity is aligned exploiting the alignment tool and ensuring that the circulating beam overlaps at the pin-hole position.
- If the two cavity centers are overlapped, placing back the additional mirror should form a resonant three mirrors cavity with the bow-tie mirrors and a resonant linear cavity with the FP input mirror.

The weak point of this procedure is the delicate requirement to place and remove an auxiliary mirror multiple times. An alternative option could be to directly use the pin-hole to find the cQED cavity center by looking at its transmission signal. However, this would require a relatively large pin-hole in order to disturb, but not destroy, the resonant cavity through additional diffraction losses. As a consequence, the condition of overlapping at the center point for the bow-tie beam would be also relaxed. While the general idea behind the alignment strategy is defined, detailed behavior of the system in the intermediate steps is not fully characterized here. In particular, the interplay between cavity symmetry, temporary optical elements and alignment tolerances is expected to introduce non-idealities that cannot be easily predicted. Experimental trial and error will naturally lead to the optimization of the cavities alignment procedure.

Chapter 7

Conclusions

This thesis presented the work I carried out on the ^{88}Sr optical lattice clock at INRiM over the past three years, with one of the major goals being to improve the clock robustness and reduce its overall uncertainty budget, while establishing a reliable operating system to investigate the interaction properties of ^{88}Sr exploiting frequency measurements and higher dimensionality confinement.

The total uncertainty budget of the clock evaluated during this work shows a total fractional frequency uncertainty of 3.9×10^{-16} (Tab.4.1). Most of the evaluated systematic shifts contribute equally to the total uncertainty, at a level comparable with the typical statistical uncertainty of 2×10^{-16}. The dominant net systematic shifts are the quadratic Zeeman shift and the clock laser light induced AC Stark shift, which are a direct consequence of the magnetic field mixing technique used to induce the strictly forbidden $5s^2\,{}^1\mathrm{S}_0 \leftrightarrow 5s5p\,{}^3\mathrm{P}_0$ transition in bosonic ^{88}Sr. Despite the high values of the shifts, their control at the 10^{-16} level demonstrated in this work is the results of a careful three-dimensional characterization of the Zeeman shift and of a reliable optical power stabilization system realized for the clock laser.

These results will be soon used to perform the first local frequency ratio $^{171}\mathrm{Yb}/^{88}\mathrm{Sr}$ measurement between the two INRiM optical lattice clocks. Reduction of the dominant shifts requires operation at lower Rabi frequencies, thus longer interrogation times, which is ultimately limited by the joint coherence of our clock laser system and the atomic system itself. In order to lower these limits, there is currently work in progress towards a more effective detection system that will allow the clock to operate at lower densities, without sacrificing signal-to-noise ratio, and in parallel reducing the collisional shift contribute. From the clock laser side, INRiM is developing a new ultra-stable optical reference cavity to which both Yb and Sr clock lasers will be referenced. The cavity is based on a 30 cm long ULE spacer which is foreseen to provide short-term stability of $\simeq 10^{-16}$, about a factor 10 better than the current performance.

The investigation of ^{88}Sr interaction properties performed within this work allowed to provide novel insights on the s-wave scattering lengths of the atom. Specifically, by observing the interaction-induced sidebands (ISB) in a tightly-confined atomic sample this work constraints the sign of the interspecies scattering length to be negative and provides the estimate $a_{ge} = -180(50)a_0$. Moreover, through the interpretation of density shift measurements with a lossless many-body spin model (SM) and a mean-field (MF) approach, that includes losses and decoherence, this works provides estimates for both the excited-excited and ground-excited scattering lengths, obtaining $a_{ge} = -312(70)a_0$, $a_{ee} = 168(40)a_0$ for the SM and $a_{ge} = -102(23)a_0$, $a_{ee} = 80(30)a_0$ for the MF. The observed discrepancies between the two approaches are attributed to how losses and decoherence are handled in the two models. Despite this, all the methods agree on the scattering lengths sign, which was previously undetermined.

Improvements on these estimates might be obtained, for instance, in the ISB observation by employing deeper confinement and most importantly by lowering the system temperature below the μK regime, while still being able to operate in a regime where doubly occupied sites exist. A further theoretical refinement of the many-body picture which correctly incorporates losses and elastic decoherence channels is also needed.

Finally, in the last part of this work I presented the future direction towards which the INRiM strontium apparatus is evolving, by the finalization of the in-vacuum system design of the hybrid-cavity lattice clock architecture. Several mechanical and optical constraints were addressed during the design. The new system is conceived to enable strong and homogeneous collective coupling between lattice trapped atoms and an optical cavity targeting the $5s^{2}\,{}^{1}\mathrm{S}_0 \leftrightarrow 5s5p\,{}^{3}\mathrm{P}_1$ transition. This platform will enable the implementation of non-destructive measurement schemes and the generation of collective quantum states, such as spin-squeezed states, with the prospect of reducing quantum projection noise and the development of novel interrogation protocols in optical lattice clocks. Furthermore, it opens the way to the exploration of collective emission phenomena such as superradiance, which is at the core of the concept of active optical atomic clocks.

References

[1] E. Rubiola. *Phase Noise and Frequency Stability in Oscillators*. Cambridge University Press, 2010, p. 228. ISBN: 9780521153287 (cit. on p. 2).

[2] I. I. Rabi, J. R. Zacharias, S. Millman, and P. Kusch. "A New Method of Measuring Nuclear Magnetic Moment". In: *Physical Review* 53.4 (Feb. 1938), pp. 318–318. ISSN: 0031-899X. DOI: 10.1103/physrev.53.318 (cit. on p. 3).

[3] N. F. Ramsey. "A Molecular Beam Resonance Method with Separated Oscillating Fields". In: *Physical Review* 78.6 (June 1950), pp. 695–699. DOI: 10.1103/physrev.78.695 (cit. on p. 3).

[4] L. Essen and J. V. L. Parry. "An Atomic Standard of Frequency and Time Interval: A Cæsium Resonator". In: *Nature* 176.4476 (Aug. 1955), pp. 280–282. DOI: 10.1038/176280a0 (cit. on p. 3).

[5] B. I. des Poids et Mesures. *Le Système international d'unités/The International System of Units [Brochure]. 9th edition.* 2019. DOI: 10.59161/auez1291 (cit. on p. 3).

[6] S. Chu, L. Hollberg, J. E. Bjorkholm, A. Cable, and A. Ashkin. "Three-dimensional viscous confinement and cooling of atoms by resonance radiation pressure". In: *Physical Review Letters* 55.1 (July 1985), pp. 48–51. ISSN: 0031-9007. DOI: 10.1103/physrevlett.55.48 (cit. on p. 3).

[7] J. Dalibard and C. Cohen-Tannoudji. "Atomic motion in laser light: connection between semiclassical and quantum descriptions". In: *Journal of Physics B: Atomic and Molecular Physics* 18.8 (Apr. 1985), pp. 1661–1683. DOI: 10.1088/0022-3700/18/8/019 (cit. on p. 3).

[8] C. Cohen-Tannoudji, J. Dupont-Roc, and G. Grynberg. *Atom-Photon Interactions*. Wiley-VCH Verlag GmbH, Apr. 1998. DOI: 10.1002/9783527617197 (cit. on p. 3).

[9] J. Dalibard and C. Cohen-Tannoudji. "Laser cooling below the Doppler limit by polarization gradients: simple theoretical models". In: *Journal of the Optical Society of America B* 6.11 (Nov. 1989), p. 2023. DOI: 10.1364/josab.6.002023 (cit. on p. 3).

[10] M. A. Kasevich, E. Riis, S. Chu, and R. G. DeVoe. "rf spectroscopy in an atomic fountain". In: *Physical Review Letters* 63.6 (Aug. 1989), pp. 612–615. DOI: 10.1103/physrevlett.63.612 (cit. on p. 3).

[11] A. Clairon, C. Salomon, S. Guellati, and W. D. Phillips. “Ramsey Resonance in a Zacharias Fountain”. In: *Europhysics Letters (EPL)* 16.2 (Sept. 1991), pp. 165–170. DOI: 10.1209/0295-5075/16/2/008 (cit. on p. 3).

[12] K. Szymaniec, S. E. Park, G. Marra, and W. Chałupczak. “First accuracy evaluation of the NPL-CsF2 primary frequency standard”. In: *Metrologia* 47.4 (June 2010), pp. 363–376. ISSN: 1681-7575. DOI: 10.1088/0026-1394/47/4/003 (cit. on p. 3).

[13] F. Levi, D. Calonico, C. E. Calosso, A. Godone, S. Micalizio, and G. A. Costanzo. “Accuracy evaluation of ITCsF2: a nitrogen cooled caesium fountain”. In: *Metrologia* 51.3 (May 2014), pp. 270–284. DOI: 10.1088/0026-1394/51/3/270 (cit. on p. 3).

[14] J. Guéna et al. “First international comparison of fountain primary frequency standards via a long distance optical fiber link”. In: *Metrologia* 54.3 (May 2017), pp. 348–354. ISSN: 1681-7575. DOI: 10.1088/1681-7575/aa65fe (cit. on p. 3).

[15] S. Weyers, V. Gerginov, M. Kazda, J. Rahm, B. Lipphardt, G. Dobrev, and K. Gibble. “Advances in the accuracy, stability, and reliability of the PTB primary fountain clocks”. In: *Metrologia* 55.6 (Oct. 2018), pp. 789–805. DOI: 10.1088/1681-7575/aae008 (cit. on p. 3).

[16] V. Gerginov, G. W. Hoth, T. P. Heavner, T. E. Parker, K. Gibble, and J. A. Sherman. “Accuracy evaluation of primary frequency standard NIST-F4”. In: *Metrologia* 62.3 (Apr. 2025), p. 035002. ISSN: 1681-7575. DOI: 10.1088/1681-7575/adc7bd (cit. on p. 3).

[17] R. W. P. Drever, J. L. Hall, F. V. Kowalski, J. Hough, G. M. Ford, A. J. Munley, and H. Ward. “Laser phase and frequency stabilization using an optical resonator”. In: *Applied Physics B Photophysics and Laser Chemistry* 31.2 (June 1983), pp. 97–105. ISSN: 1432-0649. DOI: 10.1007/bf00702605 (cit. on p. 3).

[18] B. C. Young, F. C. Cruz, W. M. Itano, and J. C. Bergquist. “Visible Lasers with Subhertz Linewidths”. In: *Physical Review Letters* 82.19 (May 1999), pp. 3799–3802. ISSN: 1079-7114. DOI: 10.1103/physrevlett.82.3799 (cit. on p. 3).

[19] K. Numata, A. Kemery, and J. Camp. “Thermal-Noise Limit in the Frequency Stabilization of Lasers with Rigid Cavities”. In: *Physical Review Letters* 93.25 (Dec. 2004). DOI: 10.1103/physrevlett.93.250602 (cit. on pp. 3, 4).

[20] R. Holzwarth, T. Udem, T. W. Hänsch, J. C. Knight, W. J. Wadsworth, and P. S. J. Russell. “Optical Frequency Synthesizer for Precision Spectroscopy”. In: *Physical Review Letters* 85.11 (Sept. 2000), pp. 2264–2267. ISSN: 1079-7114. DOI: 10.1103/physrevlett.85.2264 (cit. on p. 3).

[21] T. Udem, R. Holzwarth, and T. W. Hänsch. “Optical frequency metrology”. In: *Nature* 416.6877 (Mar. 2002), pp. 233–237. ISSN: 1476-4687. DOI: 10.1038/416233a (cit. on p. 3).

[22] D. J. Jones, S. A. Diddams, J. K. Ranka, A. Stentz, R. S. Windeler, J. L. Hall, and S. T. Cundiff. "Carrier-Envelope Phase Control of Femtosecond Mode-Locked Lasers and Direct Optical Frequency Synthesis". In: *Science* 288.5466 (Apr. 2000), pp. 635–639. ISSN: 1095-9203. DOI: 10.1126/science.288.5466.635 (cit. on p. 3).

[23] E. Oelker et al. "Demonstration of 4.8×10^{-17} stability at 1s for two independent optical clocks". In: *Nature Photonics* 13.10 (July 2019), pp. 714–719. DOI: 10.1038/s41566-019-0493-4 (cit. on pp. 4, 5).

[24] N. Huntemann, C. Sanner, B. Lipphardt, C. Tamm, and E. Peik. "Single-Ion Atomic Clock with 3×10^{-18} Systematic Uncertainty". In: *Physical Review Letters* 116.6 (Feb. 2016). DOI: 10.1103/physrevlett.116.063001 (cit. on pp. 4, 6).

[25] T. Bothwell, D. Kedar, E. Oelker, J. M. Robinson, S. L. Bromley, W. L. Tew, J. Ye, and C. J. Kennedy. "JILA SrI optical lattice clock with uncertainty of 2.0×10^{-18}". In: *Metrologia* 56.6 (Oct. 2019), p. 065004. ISSN: 1681-7575. DOI: 10.1088/1681-7575/ab4089 (cit. on pp. 4, 16).

[26] A. Aeppli, K. Kim, W. Warfield, M. S. Safronova, and J. Ye. "Clock with $8{\times}10^{-19}$ Systematic Uncertainty". In: *Physical Review Letters* 133.2 (July 2024), p. 023401. ISSN: 1079-7114. DOI: 10.1103/physrevlett.133.023401 (cit. on p. 4).

[27] W. M. Itano, J. C. Bergquist, J. J. Bollinger, J. M. Gilligan, D. J. Heinzen, F. L. Moore, M. G. Raizen, and D. J. Wineland. "Quantum projection noise: Population fluctuations in two-level systems". In: *Physical Review A* 47.5 (May 1993), pp. 3554–3570. DOI: 10.1103/physreva.47.3554 (cit. on p. 4).

[28] G. Santarelli, C. Audoin, A. Makdissi, P. Laurent, G. Dick, and A. Clairon. "Frequency stability degradation of an oscillator slaved to a periodically interrogated atomic resonator". In: *IEEE Transactions on Ultrasonics, Ferroelectrics and Frequency Control* 45.4 (July 1998), pp. 887–894. ISSN: 0885-3010. DOI: 10.1109/58.710548 (cit. on p. 4).

[29] M. Notcutt, L.-S. Ma, A. D. Ludlow, S. M. Foreman, J. Ye, and J. L. Hall. "Contribution of thermal noise to frequency stability of rigid optical cavity via Hertz-linewidth lasers". In: *Physical Review A* 73.3 (Mar. 2006). DOI: 10.1103/physreva.73.031804 (cit. on p. 4).

[30] A. L. Parke and M. Schioppo. "Three hundred microsecond optical cavity storage time and 10-7 active RAM cancellation for 10-19 laser frequency stabilization". In: *Optics Letters* 50.10 (May 2025), p. 3405. ISSN: 1539-4794. DOI: 10.1364/ol.560815 (cit. on p. 4).

[31] T. Kessler, C. Hagemann, C. Grebing, T. Legero, U. Sterr, F. Riehle, M. J. Martin, L. Chen, and J. Ye. "A sub-40-mHz-linewidth laser based on a silicon single-crystal optical cavity". In: *Nature Photonics* 6.10 (Sept. 2012), pp. 687–692. ISSN: 1749-4893. DOI: 10.1038/nphoton.2012.217 (cit. on p. 4).

[32] D. Matei et al. “1.5 μm Lasers with Sub-10 mHz Linewidth”. In: *Physical Review Letters* 118.26 (June 2017). DOI: 10.1103/physrevlett.118.263202 (cit. on p. 4).

[33] D. Lee et al. “Frequency stability of 2.5×10^{-17} in a Si cavity with AlGaAs crystalline mirrors”. In: (Sept. 2025). arXiv: 2509.13503 `[physics.optics]` (cit. on p. 4).

[34] H. Katori, M. Takamoto, V. G. Pal’chikov, and V. D. Ovsiannikov. “Ultrastable Optical Clock with Neutral Atoms in an Engineered Light Shift Trap”. In: *Physical Review Letters* 91.17 (Oct. 2003). DOI: 10.1103/physrevlett.91.173005 (cit. on pp. 5, 25).

[35] H. Katori. “Spectroscopy of Strontium Atoms in the Lamb-Dicke Confinement”. In: *Frequency Standards and Metrology*. WORLD SCIENTIFIC, May 2002. DOI: 10.1142/9789812777713_0036 (cit. on pp. 5, 11, 25).

[36] R. Santra, E. Arimondo, T. Ido, C. H. Greene, and J. Ye. “High-Accuracy Optical Clock via Three-Level Coherence in Neutral Bosonic ^{88}Sr”. In: *Physical Review Letters* 94.17 (May 2005). DOI: 10.1103/physrevlett.94.173002 (cit. on pp. 5, 14).

[37] T. Hong, C. Cramer, W. Nagourney, and E. N. Fortson. “Optical Clocks Based on Ultranarrow Three-Photon Resonances in Alkaline Earth Atoms”. In: *Physical Review Letters* 94.5 (Feb. 2005). DOI: 10.1103/physrevlett.94.050801 (cit. on pp. 5, 14).

[38] A. Taichenachev, V. Yudin, C. Oates, C. Hoyt, Z. Barber, and L. Hollberg. “Magnetic Field-Induced Spectroscopy of Forbidden Optical Transitions with Application to Lattice-Based Optical Atomic Clocks”. In: *Physical Review Letters* 96.8 (Mar. 2006). DOI: 10.1103/physrevlett.96.083001 (cit. on pp. 5, 14–16, 80).

[39] T. Zanon-Willette, A. D. Ludlow, S. Blatt, M. M. Boyd, E. Arimondo, and J. Ye. “Cancellation of Stark Shifts in Optical Lattice Clocks by Use of Pulsed Raman and Electromagnetically Induced Transparency Techniques”. In: *Physical Review Letters* 97.23 (Dec. 2006). DOI: 10.1103/physrevlett.97.233001 (cit. on pp. 5, 14).

[40] V. D. Ovsiannikov, V. G. Pal’chikov, A. V. Taichenachev, V. I. Yudin, H. Katori, and M. Takamoto. “Magic-wave-induced $^1S_0$–$^3P_0$ transition in even isotopes of alkaline-earth-metal-like atoms”. In: *Physical Review A* 75.2 (Feb. 2007). DOI: 10.1103/physreva.75.020501 (cit. on pp. 5, 14).

[41] E. A. Alden, K. R. Moore, and A. E. Leanhardt. “Two-photonE1-M1optical clock”. In: *Physical Review A* 90.1 (July 2014), p. 012523. ISSN: 1094-1622. DOI: 10.1103/physreva.90.012523 (cit. on pp. 5, 14).

[42] Y. S. Hassan et al. “Cryogenic Optical Lattice Clock with 1.7×10^{-20} Blackbody Radiation Stark Uncertainty”. In: *Physical Review Letters* 135.6 (Aug. 2025). ISSN: 1079-7114. DOI: 10.1103/4tky-jmsm (cit. on p. 5).

[43] I. Nosske, C. Vishwakarma, T. Lücke, J. Rahm, N. Poudel, S. Weyers, E. Benkler, S. Dörscher, and C. Lisdat. “Transportable strontium lattice clock with 4×10^{-19} blackbody radiation shift uncertainty”. In: *Quantum Science and Technology* 10.4 (Oct. 2025), p. 045076. ISSN: 2058-9565. DOI: 10.1088/2058-9565/ae1161 (cit. on p. 5).

[44] K. Beloy et al. “Atomic Clock with 1×10^{-18} Room-Temperature Blackbody Stark Uncertainty”. In: *Physical Review Letters* 113.26 (Dec. 2014). DOI: 10.1103/physrevlett.113.260801 (cit. on p. 5).

[45] I. Ushijima, M. Takamoto, M. Das, T. Ohkubo, and H. Katori. “Cryogenic optical lattice clocks”. In: *Nature Photonics* 9.3 (Feb. 2015), pp. 185–189. ISSN: 1749-4893. DOI: 10.1038/nphoton.2015.5 (cit. on p. 5).

[46] J. C. Bergquist, W. M. Itano, and D. J. Wineland. “Recoilless optical absorption and Doppler sidebands of a single trapped ion”. In: *Physical Review A* 36.1 (July 1987), pp. 428–430. ISSN: 0556-2791. DOI: 10.1103/physreva.36.428 (cit. on p. 5).

[47] W. Paul. “Electromagnetic traps for charged and neutral particles”. In: *Reviews of Modern Physics* 62.3 (July 1990), pp. 531–540. DOI: 10.1103/revmodphys.62.531 (cit. on p. 5).

[48] F. Diedrich, J. C. Bergquist, W. M. Itano, and D. J. Wineland. “Laser Cooling to the Zero-Point Energy of Motion”. In: *Physical Review Letters* 62.4 (Jan. 1989), pp. 403–406. DOI: 10.1103/physrevlett.62.403 (cit. on p. 5).

[49] J. Stuhler et al. “Opticlock: Transportable and easy-to-operate optical single-ion clock”. In: *Measurement: Sensors* 18 (Dec. 2021), p. 100264. ISSN: 2665-9174. DOI: 10.1016/j.measen.2021.100264 (cit. on p. 6).

[50] A. D. Ludlow, M. M. Boyd, J. Ye, E. Peik, and P. Schmidt. “Optical atomic clocks”. In: *Reviews of Modern Physics* 87.2 (June 2015), pp. 637–701. DOI: 10.1103/revmodphys.87.637 (cit. on pp. 6, 26).

[51] C. Chou, D. Hume, J. Koelemeij, D. Wineland, and T. Rosenband. “Frequency Comparison of Two High-Accuracy Al^+ Optical Clocks”. In: *Physical Review Letters* 104.7 (Feb. 2010). DOI: 10.1103/physrevlett.104.070802 (cit. on p. 6).

[52] S. M. Brewer, J.-S. Chen, A. M. Hankin, E. R. Clements, C. W. Chou, D. J. Wineland, D. B. Hume, and D. R. Leibrandt. “$^{27}Al^+$ Quantum-Logic Clock with a Systematic Uncertainty below 10^{-18}”. In: *Phys. Rev. Lett.* 123.033201 (3 July 2019), p. 033201. DOI: 10.1103/PhysRevLett.123.033201 (cit. on p. 6).

[53] N. Huntemann, M. Okhapkin, B. Lipphardt, S. Weyers, C. Tamm, and E. Peik. “High-Accuracy Optical Clock Based on the Octupole Transition inYb+171”. In: *Physical Review Letters* 108.9 (Feb. 2012), p. 090801. ISSN: 1079-7114. DOI: 10.1103/physrevlett.108.090801 (cit. on p. 6).

[54] C. Lisdat et al. “A clock network for geodesy and fundamental science”. In: *Nature Communications* 7.1 (Aug. 2016). ISSN: 2041-1723. DOI: 10.1038/ncomms12443 (cit. on p. 6).

[55] C. Clivati et al. “Coherent Optical-Fiber Link Across Italy and France”. In: *Physical Review Applied* 18.5 (Nov. 2022), p. 054009. ISSN: 2331-7019. DOI: 10.1103/physrevapplied.18.054009 (cit. on p. 6).

[56] T. Lindvall et al. “Coordinated international comparisons between optical clocks connected via fiber and satellite links”. In: *Optica* 12.6 (June 2025), p. 843. ISSN: 2334-2536. DOI: 10.1364/optica.561754 (cit. on p. 6).

[57] N. Dimarcq et al. “Roadmap towards the redefinition of the second”. In: *Metrologia* 61.1 (Jan. 2024), p. 012001. ISSN: 1681-7575. DOI: 10.1088/1681-7575/ad17d2 (cit. on p. 6).

[58] M. I. Bodine et al. “Optical atomic clock comparison through turbulent air”. In: *Physical Review Research* 2.3 (Sept. 2020), p. 033395. ISSN: 2643-1564. DOI: 10.1103/physrevresearch.2.033395 (cit. on p. 6).

[59] T. Takano et al. “Geopotential measurements with synchronously linked optical lattice clocks”. In: *Nature Photonics* 10.10 (Aug. 2016), pp. 662–666. ISSN: 1749-4893. DOI: 10.1038/nphoton.2016.159 (cit. on p. 6).

[60] J. Grotti et al. “Geodesy and metrology with a transportable optical clock”. In: *Nature Physics* 14.5 (Feb. 2018), pp. 437–441. DOI: 10.1038/s41567-017-0042-3 (cit. on p. 6).

[61] N. Ohmae et al. “Transportable Strontium Optical Lattice Clocks Operated Outside Laboratory at the Level of 10^{-18} Uncertainty”. In: *Advanced Quantum Technologies* 4.8 (May 2021), p. 2100015. DOI: 10.1002/qute.202100015 (cit. on p. 6).

[62] M. Takamoto, I. Ushijima, N. Ohmae, T. Yahagi, K. Kokado, H. Shinkai, and H. Katori. “Test of general relativity by a pair of transportable optical lattice clocks”. In: *Nature Photonics* (Apr. 2020). DOI: 10.1038/s41566-020-0619-8 (cit. on p. 6).

[63] W. F. McGrew et al. “Atomic clock performance enabling geodesy below the centimetre level”. In: *Nature* 564.7734 (Nov. 2018), pp. 87–90. DOI: 10.1038/s41586-018-0738-2 (cit. on pp. 6, 85).

[64] Y. Tanaka and H. Katori. “Exploring potential applications of optical lattice clocks in a plate subduction zone”. In: *Journal of Geodesy* 95.8 (July 2021). ISSN: 1432-1394. DOI: 10.1007/s00190-021-01548-y (cit. on p. 6).

[65] R. H. Dicke. “Coherence in Spontaneous Radiation Processes”. In: *Physical Review* 93.1 (Jan. 1954), pp. 99–110. DOI: 10.1103/physrev.93.99 (cit. on pp. 7, 130).

[66] M. Gross and S. Haroche. “Superradiance: An essay on the theory of collective spontaneous emission”. In: *Physics Reports* 93.5 (Dec. 1982), pp. 301–396. DOI: 10.1016/0370-1573(82)90102-8 (cit. on pp. 7, 130).

[67] G. A. Kazakov and T. Schumm. “Active optical frequency standard using sequential coupling of atomic ensembles”. In: *Physical Review A* 87.1 (Jan. 2013), p. 013821. ISSN: 1094-1622. DOI: 10.1103/physreva.87.013821 (cit. on p. 7).

[68] G. A. Kazakov, S. Dubey, A. Bychek, U. Sterr, M. Bober, and M. Zawada. "Ultimate stability of active optical frequency standards". In: *Physical Review A* 106.5 (Nov. 2022). DOI: 10.1103/physreva.106.053114 (cit. on p. 7).

[69] D. J. Wineland, J. J. Bollinger, W. M. Itano, F. L. Moore, and D. J. Heinzen. "Spin squeezing and reduced quantum noise in spectroscopy". In: *Physical Review A* 46.11 (Dec. 1992), R6797–R6800. ISSN: 1094-1622. DOI: 10.1103/physreva.46.r6797 (cit. on pp. 7, 125, 127).

[70] M. Kitagawa and M. Ueda. "Squeezed spin states". In: *Physical Review A* 47.6 (June 1993), pp. 5138–5143. ISSN: 1094-1622. DOI: 10.1103/physreva.47.5138 (cit. on pp. 7, 125).

[71] K. C. Cox, G. P. Greve, J. M. Weiner, and J. K. Thompson. "Deterministic Squeezed States with Collective Measurements and Feedback". In: *Physical Review Letters* 116.9 (Mar. 2016), p. 093602. ISSN: 1079-7114. DOI: 10.1103/physrevlett.116.093602 (cit. on pp. 7, 126).

[72] O. Hosten, N. J. Engelsen, R. Krishnakumar, and M. A. Kasevich. "Measurement noise 100 times lower than the quantum-projection limit using entangled atoms". In: *Nature* 529.7587 (Jan. 2016), pp. 505–508. DOI: 10.1038/nature16176 (cit. on pp. 7, 126, 128).

[73] E. Pedrozo-Peñafiel et al. "Entanglement on an optical atomic-clock transition". In: *Nature* 588.7838 (Dec. 2020), pp. 414–418. ISSN: 1476-4687. DOI: 10.1038/s41586-020-3006-1 (cit. on p. 7).

[74] J. M. Robinson, M. Miklos, Y. M. Tso, C. J. Kennedy, T. Bothwell, D. Kedar, J. K. Thompson, and J. Ye. "Direct comparison of two spin-squeezed optical clock ensembles at the 10-17 level". In: *Nature Physics* 20.2 (Jan. 2024), pp. 208–213. ISSN: 1745-2481. DOI: 10.1038/s41567-023-02310-1 (cit. on pp. 7, 126, 131).

[75] W. Bowden, A. Vianello, I. R. Hill, M. Schioppo, and R. Hobson. "Improving the Q Factor of an Optical Atomic Clock Using Quantum Nondemolition Measurement". In: *Physical Review X* 10.4 (Dec. 2020), p. 041052. ISSN: 2160-3308. DOI: 10.1103/physrevx.10.041052 (cit. on pp. 7, 127).

[76] H. N. Hausser et al. "$^{115}\mathrm{In}^{+}$–$^{172}\mathrm{Yb}^{+}$ Coulomb Crystal Clock with 2.5×10^{-18} Systematic Uncertainty". In: *Physical Review Letters* 134.2 (Jan. 2025), p. 023201. ISSN: 1079-7114. DOI: 10.1103/physrevlett.134.023201 (cit. on p. 7).

[77] E. Peik and C. Tamm. "Nuclear laser spectroscopy of the 3.5 eV transition in Th-229". In: *Europhysics Letters (EPL)* 61.2 (Jan. 2003), pp. 181–186. ISSN: 1286-4854. DOI: 10.1209/epl/i2003-00210-x (cit. on p. 7).

[78] C. J. Campbell, A. G. Radnaev, A. Kuzmich, V. A. Dzuba, V. V. Flambaum, and A. Derevianko. "Single-Ion Nuclear Clock for Metrology at the 19th Decimal Place". In: *Physical Review Letters* 108.12 (Mar. 2012), p. 120802. ISSN: 1079-7114. DOI: 10.1103/physrevlett.108.120802 (cit. on p. 7).

[79] B. Seiferle et al. “Energy of the 229Th nuclear clock transition”. In: *Nature* 573.7773 (Sept. 2019), pp. 243–246. ISSN: 1476-4687. DOI: 10.1038/s41586-019-1533-4 (cit. on p. 7).

[80] J. Tiedau et al. “Laser Excitation of the Th-229 Nucleus”. In: *Physical Review Letters* 132.18 (Apr. 2024), p. 182501. ISSN: 1079-7114. DOI: 10.1103/physrevlett.132.182501 (cit. on p. 7).

[81] C. Zhang et al. “Frequency ratio of the 229mTh nuclear isomeric transition and the 87Sr atomic clock”. In: *Nature* 633.8028 (Sept. 2024), pp. 63–70. ISSN: 1476-4687. DOI: 10.1038/s41586-024-07839-6 (cit. on p. 7).

[82] S. Schiller. “Hydrogenlike Highly Charged Ions for Tests of the Time Independence of Fundamental Constants”. In: *Physical Review Letters* 98.18 (Apr. 2007), p. 180801. ISSN: 1079-7114. DOI: 10.1103/physrevlett.98.180801 (cit. on p. 7).

[83] M. G. Kozlov, M. S. Safronova, J. R. Crespo López-Urrutia, and P. O. Schmidt. “Highly charged ions: Optical clocks and applications in fundamental physics”. In: *Reviews of Modern Physics* 90.4 (Dec. 2018), p. 045005. ISSN: 1539-0756. DOI: 10.1103/revmodphys.90.045005 (cit. on p. 7).

[84] M. S. Safronova, D. Budker, D. DeMille, D. F. J. Kimball, A. Derevianko, and C. W. Clark. “Search for new physics with atoms and molecules”. In: *Rev. Mod. Phys.* 90 (2 June 2018), p. 025008. DOI: 10.1103/RevModPhys.90.025008 (cit. on p. 7).

[85] M. Barbiero. “Novel techniques for a Strontium Optical Lattice Clock”. PhD thesis. Politecnico of Turin, 2019. URL: http://hdl.handle.net/11583/2750550 (cit. on pp. 8, 32, 33, 46, 59).

[86] M. Barbiero, D. Calonico, F. Levi, and M. G. Tarallo. “Optically Loaded Strontium Lattice Clock With a Single Multi-Wavelength Reference Cavity”. In: *IEEE Transactions on Instrumentation and Measurement* 71 (2022), pp. 1–9. DOI: 10.1109/TIM.2022.3165292 (cit. on pp. 8, 53, 63, 84, 124).

[87] K. S. Krane. *Introductory nuclear physics*. Wiley, 1987, p. 845. ISBN: 047180553X (cit. on p. 10).

[88] T. Johnson and W. Kulp. “Nuclear Data Sheets for A = 87”. In: *Nuclear Data Sheets* 129 (Nov. 2015), pp. 1–190. ISSN: 0090-3752. DOI: 10.1016/j.nds.2015.09.001 (cit. on p. 10).

[89] J. E. Sansonetti and G. Nave. “Wavelengths, Transition Probabilities, and Energy Levels for the Spectrum of Neutral Strontium (SrI)”. In: *Journal of Physical and Chemical Reference Data* 39.3 (Sept. 2010), p. 033103. DOI: 10.1063/1.3449176 (cit. on p. 10).

[90] A. D. Ludlow et al. “Sr Lattice Clock at 1 × 10 –16 Fractional Uncertainty by Remote Optical Evaluation with a Ca Clock”. In: *Science* 319.5871 (Mar. 2008), pp. 1805–1808. ISSN: 1095-9203. DOI: 10.1126/science.1153341 (cit. on p. 11).

[91] T. Middelmann, S. Falke, C. Lisdat, and U. Sterr. “High Accuracy Correction of Blackbody Radiation Shift in an Optical Lattice Clock”. In: *Phys. Rev. Lett.* 109 (26 Dec. 2012), p. 263004. DOI: 10.1103/PhysRevLett.109.263004 (cit. on pp. 11, 84, 85).

[92] R. L. Targat et al. “Experimental realization of an optical second with strontium lattice clocks”. In: *Nature Communications* 4.1 (July 2013). DOI: 10.1038/ncomms3109 (cit. on pp. 11, 82).

[93] S. L. Campbell et al. “A Fermi-degenerate three-dimensional optical lattice clock”. In: *Science* 358.6359 (Oct. 2017), pp. 90–94. DOI: 10.1126/science.aam5538 (cit. on pp. 11, 21).

[94] M. K. Tey, S. Stellmer, R. Grimm, and F. Schreck. “Double-degenerate Bose-Fermi mixture of strontium”. In: *Physical Review A* 82.1 (July 2010), p. 011608. ISSN: 1094-1622. DOI: 10.1103/physreva.82.011608 (cit. on p. 11).

[95] S. Stellmer, R. Grimm, and F. Schreck. “Production of quantum-degenerate strontium gases”. In: *Physical Review A* 87.1 (Jan. 2013), p. 013611. ISSN: 1094-1622. DOI: 10.1103/physreva.87.013611 (cit. on p. 11).

[96] L. Sonderhouse, C. Sanner, R. B. Hutson, A. Goban, T. Bilitewski, L. Yan, W. R. Milner, A. M. Rey, and J. Ye. “Thermodynamics of a deeply degenerate SU(N)-symmetric Fermi gas”. In: *Nature Physics* 16.12 (Aug. 2020), pp. 1216–1221. ISSN: 1745-2481. DOI: 10.1038/s41567-020-0986-6 (cit. on p. 11).

[97] A. J. Daley, M. M. Boyd, J. Ye, and P. Zoller. “Quantum Computing with Alkaline-Earth-Metal Atoms”. In: *Physical Review Letters* 101.17 (Oct. 2008), p. 170504. ISSN: 1079-7114. DOI: 10.1103/physrevlett.101.170504 (cit. on p. 11).

[98] A. V. Gorshkov, A. M. Rey, A. J. Daley, M. M. Boyd, J. Ye, P. Zoller, and M. D. Lukin. “Alkaline-Earth-Metal Atoms as Few-Qubit Quantum Registers”. In: *Physical Review Letters* 102.11 (Mar. 2009), p. 110503. ISSN: 1079-7114. DOI: 10.1103/physrevlett.102.110503 (cit. on p. 11).

[99] A. V. Gorshkov et al. “Two-orbital S U(N) magnetism with ultracold alkaline-earth atoms”. In: *Nature Physics* 6.4 (Feb. 2010), pp. 289–295. ISSN: 1745-2481. DOI: 10.1038/nphys1535 (cit. on p. 11).

[100] H. J. Metcalf and P. van der Straten. *Laser Cooling and Trapping*. Springer New York, 1999. DOI: 10.1007/978-1-4612-1470-0 (cit. on pp. 11, 38).

[101] T. Binnewies, G. Wilpers, U. Sterr, F. Riehle, J. Helmcke, T. E. Mehlstäubler, E. M. Rasel, and W. Ertmer. “Doppler Cooling and Trapping on Forbidden Transitions”. In: *Physical Review Letters* 87.12 (Aug. 2001). DOI: 10.1103/physrevlett.87.123002 (cit. on p. 11).

[102] T. H. Loftus, T. Ido, A. D. Ludlow, M. M. Boyd, and J. Ye. “Narrow Line Cooling: Finite Photon Recoil Dynamics”. In: *Physical Review Letters* 93.7 (Aug. 2004). DOI: 10.1103/physrevlett.93.073003 (cit. on pp. 11, 12).

[103] T. H. Loftus, T. Ido, M. M. Boyd, A. D. Ludlow, and J. Ye. “Narrow line cooling and momentum-space crystals”. In: *Physical Review A* 70.6 (Dec. 2004). DOI: 10.1103/physreva.70.063413 (cit. on pp. 11, 12).

[104] S. Stellmer. “Degenerate quantum gases of strontium”. PhD thesis. University of Innsbruck, 2013 (cit. on p. 11).

[105] M. Yasuda, T. Kishimoto, M. Takamoto, and H. Katori. “Photoassociation spectroscopy of ^{88}Sr: Reconstruction of the wave function near the last node”. In: *Physical Review A* 73.1 (Jan. 2006). DOI: 10.1103/physreva.73.011403 (cit. on pp. 11, 12).

[106] S. B. Nagel, P. G. Mickelson, A. D. Saenz, Y. N. Martinez, Y. C. Chen, T. C. Killian, P. Pellegrini, and R. Côté. “Photoassociative Spectroscopy at Long Range in Ultracold Strontium”. In: *Physical Review Letters* 94.8 (Mar. 2005). DOI: 10.1103/physrevlett.94.083004 (cit. on p. 12).

[107] T. Nicholson et al. “Systematic evaluation of an atomic clock at 2×10^{18} total uncertainty”. In: *Nature Communications* 6.1 (Apr. 2015). DOI: 10.1038/ncomms7896 (cit. on p. 12).

[108] A. Heinz, A. J. Park, N. Šantić, J. Trautmann, S. G. Porsev, M. S. Safronova, I. Bloch, and S. Blatt. “State-Dependent Optical Lattices for the Strontium Optical Qubit”. In: *Physical Review Letters* 124.20 (May 2020), p. 203201. ISSN: 1079-7114. DOI: 10.1103/physrevlett.124.203201 (cit. on p. 12).

[109] J. A. Muniz, D. J. Young, J. R. K. Cline, and J. K. Thompson. “Cavity-QED measurements of the Sr87 millihertz optical clock transition and determination of its natural linewidth”. In: *Physical Review Research* 3.2 (May 2021), p. 023152. ISSN: 2643-1564. DOI: 10.1103/physrevresearch.3.023152 (cit. on pp. 12, 13).

[110] J. Dolde, D. Ganapathy, X. Zheng, S. Ma, K. Beloy, and S. Kolkowitz. “Direct measurement of the P03 clock state natural lifetime in Sr87”. In: *Physical Review A* 112.2 (Aug. 2025). ISSN: 2469-9934. DOI: 10.1103/f6pt-flnt (cit. on pp. 12, 13, 100, 102, 103).

[111] M. Yasuda and H. Katori. “Lifetime Measurement of the $^3P_2$ Metastable State of Strontium Atoms”. In: *Physical Review Letters* 92.15 (Apr. 2004). DOI: 10.1103/physrevlett.92.153004 (cit. on p. 12).

[112] R. Santra, K. V. Christ, and C. H. Greene. “Properties of metastable alkaline-earth-metal atoms calculated using an accurate effective core potential”. In: *Physical Review A* 69.4 (Apr. 2004), p. 042510. ISSN: 1094-1622. DOI: 10.1103/physreva.69.042510 (cit. on pp. 12, 13).

[113] N. Poli, R. E. Drullinger, G. Ferrari, J. Léonard, F. Sorrentino, and G. M. Tino. “Cooling and trapping of ultracold strontium isotopic mixtures”. In: *Physical Review A* 71.6 (June 2005). DOI: 10.1103/physreva.71.061403 (cit. on p. 13).

[114] P. G. Mickelson, Y. N. M. de Escobar, P. Anzel, B. J. DeSalvo, S. B. Nagel, A. J. Traverso, M. Yan, and T. C. Killian. "Repumping and spectroscopy of laser-cooled Sr atoms using the (5s5p)$^3P_2$–(5s4d)$^3D_2$ transition". In: *Journal of Physics B: Atomic, Molecular and Optical Physics* 42.23 (Nov. 2009), p. 235001. DOI: 10.1088/0953-4075/42/23/235001 (cit. on p. 13).

[115] S. Stellmer and F. Schreck. "Reservoir spectroscopy of $5s5p\,^3P_2$–$5snd\,^3D_{1,2,3}$ transitions in strontium". In: *Physical Review A* 90.2 (Aug. 2014). DOI: 10.1103/physreva.90.022512 (cit. on p. 13).

[116] F. Hu, I. Nosske, L. Couturier, C. Tan, C. Qiao, P. Chen, Y. H. Jiang, B. Zhu, and M. Weidemüller. "Analyzing a single-laser repumping scheme for efficient loading of a strontium magneto-optical trap". In: *Physical Review A* 99.3 (Mar. 2019), p. 033422. ISSN: 2469-9934. DOI: 10.1103/physreva.99.033422 (cit. on p. 13).

[117] N. Okamoto, T. Aoki, and Y. Torii. "Limitation of single-repumping schemes for laser cooling of Sr atoms". In: *Physical Review Research* 6.4 (Nov. 2024), p. 043088. ISSN: 2643-1564. DOI: 10.1103/physrevresearch.6.043088 (cit. on p. 13).

[118] J. Samland, S. Bennetts, C.-C. Chen, R. G. Escudero, F. Schreck, and B. Pasquiou. "Optical pumping of 5s4d1D2 strontium atoms for laser cooling and imaging". In: *Physical Review Research* 6.1 (Mar. 2024), p. 013319. ISSN: 2643-1564. DOI: 10.1103/physrevresearch.6.013319 (cit. on p. 13).

[119] S. Zhang, P. Ramchurn, M. Menchetti, Q. Ubaid, J. Jones, K. Bongs, and Y. Singh. "Novel repumping on 3P0 → 3D1 for Sr magneto-optical trap and Landé g factor measurement of 3D1". In: *Journal of Physics B: Atomic, Molecular and Optical Physics* 53.23 (Oct. 2020), p. 235301. ISSN: 1361-6455. DOI: 10.1088/1361-6455/abbe2c (cit. on p. 13).

[120] H. S. Margolis, G. Panfilo, G. Petit, C. Oates, T. Ido, and S. Bize. "The CIPM list "Recommended values of standard frequencies": 2021 update". In: (Jan. 2024). DOI: `10.48550/ARXIV.2401.14537`. arXiv: `2401.14537 [physics.atom-ph]` (cit. on p. 14).

[121] M. M. Boyd. "High precision spectroscopy of strontium in an optical lattice: Towards a new standard for frequency and time". PhD thesis. University of Colorado, Boulder, 2007. URL: https://ui.adsabs.harvard.edu/abs/2007PhDT......201B (cit. on p. 14).

[122] G. Panelli, S. C. Burd, E. J. Porter, and M. Kasevich. "Doppler-free three-photon spectroscopy on narrow-line optical transitions". In: *Physical Review A* 111.3 (Mar. 2025), p. 033112. ISSN: 2469-9934. DOI: 10.1103/physreva.111.033112 (cit. on p. 14).

[123] S. P. Carman et al. "Collinear Three-Photon Excitation of a Strongly Forbidden Optical Clock Transition". In: *Physical Review X* 15.3 (Aug. 2025). ISSN: 2160-3308. DOI: 10.1103/qk3v-46y8 (cit. on p. 14).

[124] Z. Barber, C. Hoyt, C. Oates, L. Hollberg, A. Taichenachev, and V. Yudin. "Direct Excitation of the Forbidden Clock Transition in Neutral Yb 174 Atoms Confined to an Optical Lattice". In: *Physical Review Letters* 96.8 (Mar. 2006). DOI: 10.1103/physrevlett.96.083002 (cit. on p. 14).

[125] X. Baillard, M. Fouché, R. Le Targat, P. G. Westergaard, A. Lecallier, Y. Le Coq, G. D. Rovera, S. Bize, and P. Lemonde. "Accuracy evaluation of an optical lattice clock with bosonic atoms". In: *Optics Letters* 32.13 (June 2007), p. 1812. ISSN: 1539-4794. DOI: https://doi.org/10.1364/OL.32.001812 (cit. on p. 14).

[126] A. Kulosa et al. "Towards a Mg Lattice Clock: Observation of the $^1S_0$–$^3P_0$ Transition and Determination of the Magic Wavelength". In: *Physical Review Letters* 115.24 (Dec. 2015). DOI: 10.1103/physrevlett.115.240801 (cit. on p. 14).

[127] C. Zyskind, T. Lauprêtre, H. Shang, B. Pointard, R. L. Targat, J. Lodewyck, and S. Bize. "First observation and measurement of the ^{198}Hg bosonic transition in an optical lattice clock". In: (Dec. 2025). arXiv: 2512.04920 `[physics.atom-ph]` (cit. on p. 14).

[128] X. Baillard et al. "An optical lattice clock with spin-polarized 87Sr atoms". In: *The European Physical Journal D* 48.1 (Dec. 2007), pp. 11–17. DOI: 10.1140/epjd/e2007-00330-3 (cit. on p. 16).

[129] B. Lu, X. Lu, J. Li, and H. Chang. "Theoretical calculation of the quadratic Zeeman shift coefficient of the 3P0o clock state for strontium optical lattice clock". In: *Chinese Physics B* 31.4 (Mar. 2022), p. 043101. ISSN: 1674-1056. DOI: 10.1088/1674-1056/ac29a6 (cit. on pp. 16, 66).

[130] R. Grimm, M. Weidemüller, and Y. B. Ovchinnikov. "Optical dipole traps for neutral atoms". In: *Advances in Atomic, Molecular and Optical Physics Vol. 42, 95-170 (2000)* (Feb. 24, 1999). arXiv: http://arxiv.org/abs/physics/9902072v1 `[physics.atom-ph]` (cit. on pp. 16, 89, 131).

[131] D. G.-O. Claude Cohen-Tannoudji. *Advances In Atomic Physics: An Overview*. World Scientific Publishing Co Pte Ltd, Sept. 5, 2011. 796 pp. ISBN: 9812774971. URL: https://www.ebook.de/de/product/11434066/claude_cohen_tannoudji_david_guery_odelin_advances_in_atomic_physics_an_overview.html (cit. on pp. 16, 27).

[132] R. W. Gosper. "The solutions of ye y 2 = x and ye y = x". In: *ACM SIGSAM Bulletin* 32.1 (Mar. 1998), pp. 8–10. ISSN: 0163-5824. DOI: 10.1145/294833.294837 (cit. on p. 18).

[133] N. D. Lemke, J. von Stecher, J. A. Sherman, A. M. Rey, C. W. Oates, and A. D. Ludlow. "p-Wave Cold Collisions in an Optical Lattice Clock". In: *Physical Review Letters* 107.10 (Aug. 2011). DOI: 10.1103/physrevlett.107.103902 (cit. on pp. 21, 95).

[134] L. Franchi, L. F. Livi, G. Cappellini, G. Binella, M. Inguscio, J. Catani, and L. Fallani. "State-dependent interactions in ultracold174Yb probed by optical clock spectroscopy". In: *New Journal of Physics* 19.10 (Nov. 2017), p. 103037. ISSN: 1367-2630. DOI: 10.1088/1367-2630/aa8fb4 (cit. on p. 21).

[135] T. Akatsuka, M. Takamoto, and H. Katori. “Optical lattice clocks with non-interacting bosons and fermions”. In: *Nature Physics* 4.12 (Oct. 2008), pp. 954–959. ISSN: 1745-2481. DOI: 10.1038/nphys1108 (cit. on p. 21).

[136] S. Okaba, R. Takeuchi, S. Tsuji, and H. Katori. “Continuous generation of an ultracold atomic beam using crossed moving optical lattices”. In: *Physical Review Applied* 21.3 (Mar. 2024). ISSN: 2331-7019. DOI: 10.1103/physrevapplied.21.034006 (cit. on p. 21).

[137] R. H. Dicke. “The Effect of Collisions upon the Doppler Width of Spectral Lines”. In: *Physical Review* 89.2 (Jan. 1953), pp. 472–473. DOI: 10.1103/physrev.89.472 (cit. on pp. 22, 23).

[138] D. J. Wineland and W. M. Itano. “Laser cooling of atoms”. In: *Physical Review A* 20.4 (Oct. 1979), pp. 1521–1540. ISSN: 0556-2791. DOI: 10.1103/physreva.20.1521 (cit. on p. 23).

[139] S. Blatt, J. W. Thomsen, G. K. Campbell, A. D. Ludlow, M. D. Swallows, M. J. Martin, M. M. Boyd, and J. Ye. “Rabi spectroscopy and excitation inhomogeneity in a one-dimensional optical lattice clock”. In: *Physical Review A* 80.5 (Nov. 2009), p. 052703. ISSN: 1094-1622. DOI: 10.1103/physreva.80.052703 (cit. on pp. 23, 80, 90, 106).

[140] K. Beloy, W. F. McGrew, X. Zhang, D. Nicolodi, R. J. Fasano, Y. S. Hassan, R. C. Brown, and A. D. Ludlow. “Modeling motional energy spectra and lattice light shifts in optical lattice clocks”. In: *Physical Review A* 101.5 (May 2020). ISSN: 2469-9934. DOI: 10.1103/physreva.101.053416 (cit. on p. 24).

[141] I. Goti, T. Petrucciani, S. Condio, F. Levi, D. Calonico, and M. Pizzocaro. *Atomic thermometry in optical lattice clocks*. 2025. DOI: 10.48550/ARXIV.2508.08164 (cit. on p. 24).

[142] A. Derevianko and H. Katori. “Colloquium: Physics of optical lattice clocks”. In: *Reviews of Modern Physics* 83.2 (May 2011), pp. 331–347. DOI: 10.1103/revmodphys.83.331 (cit. on p. 25).

[143] H. Katori, V. D. Ovsiannikov, S. I. Marmo, and V. G. Palchikov. “Strategies for reducing the light shift in atomic clocks”. In: *Physical Review A* 91.5 (May 2015). DOI: 10.1103/physreva.91.052503 (cit. on pp. 26, 82, 90).

[144] N. Lemke et al. “Spin-1/2Optical Lattice Clock”. In: *Physical Review Letters* 103.6 (Aug. 2009), p. 063001. ISSN: 1079-7114. DOI: 10.1103/physrevlett.103.063001 (cit. on p. 26).

[145] C. Lisdat, J. S. R. V. Winfred, T. Middelmann, F. Riehle, and U. Sterr. “Collisional Losses, Decoherence, and Frequency Shifts in Optical Lattice Clocks with Bosons”. In: *Physical Review Letters* 103.9 (Aug. 2009). DOI: 10.1103/physrevlett.103.090801 (cit. on pp. 27, 29, 50, 80, 100, 103–106, 115, 124).

[146] A. Traverso, R. Chakraborty, Y. N. M. de Escobar, P. G. Mickelson, S. B. Nagel, M. Yan, and T. C. Killian. “Inelastic and elastic collision rates for triplet states of ultracold strontium”. In: *Physical Review A* 79.6 (June 2009). DOI: 10.1103/physreva.79.060702 (cit. on pp. 27, 28, 49, 100, 102, 103, 120).

[147] D. Jaksch, C. Bruder, J. I. Cirac, C. W. Gardiner, and P. Zoller. “Cold Bosonic Atoms in Optical Lattices”. In: *Physical Review Letters* 81.15 (Oct. 1998), pp. 3108–3111. ISSN: 1079-7114. DOI: 10.1103/physrevlett.81.3108 (cit. on pp. 27, 30).

[148] Y. N. M. de Escobar, P. G. Mickelson, P. Pellegrini, S. B. Nagel, A. Traverso, M. Yan, R. Côté, and T. C. Killian. “Two-photon photoassociative spectroscopy of ultracold ^{88}Sr”. In: *Physical Review A* 78.6 (Dec. 2008). DOI: 10.1103/physreva.78.062708 (cit. on pp. 28, 113, 117).

[149] M. D. Swallows, M. J. Martin, M. Bishof, C. Benko, Y. Lin, S. Blatt, A. M. Rey, and J. Ye. “Operating a 87Sr optical lattice clock with high precision and at high density”. In: *IEEE Transactions on Ultrasonics, Ferroelectrics and Frequency Control* 59.3 (Mar. 2012), pp. 416–425. ISSN: 0885-3010. DOI: 10.1109/tuffc.2012.2210 (cit. on pp. 28, 97, 106).

[150] J. S. R. V. Winfred. “Investigation of collisional losses and decoherence in a 1-D optical lattice clock with”. PhD thesis. Leibniz University Hannover, 2010 (cit. on pp. 29, 124).

[151] A. Bonnin, C. Solaro, X. Alauze, and F. Pereira dos Santos. “Magic density in a self-rephasing ensemble of trapped ultracold atoms”. In: *Physical Review A* 99.2 (Feb. 2019), p. 023627. ISSN: 2469-9934. DOI: 10.1103/physreva.99.023627 (cit. on p. 29).

[152] A. Rey et al. “Probing many-body interactions in an optical lattice clock”. In: *Annals of Physics* 340.1 (Jan. 2014), pp. 311–351. DOI: 10.1016/j.aop.2013.11.002 (cit. on pp. 30, 31).

[153] G. Lamporesi, S. Donadello, S. Serafini, and G. Ferrari. “Compact high-flux source of cold sodium atoms”. In: *Review of Scientific Instruments* 84.6 (June 2013), p. 063102. DOI: 10.1063/1.4808375 (cit. on p. 32).

[154] M. Barbiero, M. G. Tarallo, D. Calonico, F. Levi, G. Lamporesi, and G. Ferrari. “Sideband-Enhanced Cold Atomic Source for Optical Clocks”. In: *Physical Review Applied* 13.1 (Jan. 2020). DOI: 10.1103/physrevapplied.13.014013 (cit. on p. 33).

[155] L.-S. Ma, P. Jungner, J. Ye, and J. L. Hall. “Delivering the same optical frequency at two places: accurate cancellation of phase noise introduced by an optical fiber or other time-varying path”. In: *Optics Letters* 19.21 (Nov. 1994), p. 1777. ISSN: 1539-4794. DOI: 10.1364/ol.19.001777 (cit. on p. 36).

[156] B. Rauf, M. C. Vélez López, P. Thoumany, M. Pizzocaro, and D. Calonico. “Phase noise cancellation in polarisation-maintaining fibre links”. In: *Review of Scientific Instruments* 89.3 (Mar. 2018). ISSN: 1089-7623. DOI: 10.1063/1.5016514 (cit. on p. 36).

[157] G. Reinaudi, T. Lahaye, Z. Wang, and D. Guéry-Odelin. “Strong saturation absorption imaging of dense clouds of ultracold atoms”. In: *Optics Letters* 32.21 (Oct. 2007), p. 3143. ISSN: 1539-4794. DOI: 10.1364/ol.32.003143 (cit. on p. 37).

[158] W. Ketterle, D. S. Durfee, and D. M. Stamper-Kurn. “Making, probing and understanding Bose-Einstein condensates”. In: (Apr. 2, 1999). arXiv: http://arxiv.org/abs/cond-mat/9904034v2 `[cond-mat]` (cit. on pp. 37, 38, 40).

[159] H. Moritz. “Geodetic reference system 1980”. In: *Bulletin Géodésique* 54.3 (Sept. 1980), pp. 395–405. ISSN: 1432-1394. DOI: 10.1007/bf02521480 (cit. on p. 39).

[160] URL: https://www.ptb.de/cms/ptb/fachabteilungen/abt1/fb-11/fb-11-sis/g-extractor.html (cit. on p. 39).

[161] A. S. Davydov. *Quantum mechanics*. Pergamon Pr., 1969. ISBN: 9780080131436 (cit. on p. 40).

[162] R. Zinkstok, E. J. v. Duijn, S. Witte, and W. Hogervorst. “Hyperfine structure and isotope shift of transitions in Yb I using UV and deep-UV cw laser light and the angular distribution of fluorescence radiation”. In: *Journal of Physics B: Atomic, Molecular and Optical Physics* 35.12 (June 2002), pp. 2693–2701. ISSN: 0953-4075. DOI: 10.1088/0953-4075/35/12/305 (cit. on p. 40).

[163] R. Bouganne, M. B. Aguilera, A. Dareau, E. Soave, J. Beugnon, and F. Gerbier. “Clock spectroscopy of interacting bosons in deep optical lattices”. In: *New Journal of Physics* 19.11 (Nov. 2017), p. 113006. ISSN: 1367-2630. DOI: 10.1088/1367-2630/aa8c45 (cit. on p. 50).

[164] L. Johnson and C. Cox. “Serrodyne optical frequency translation with high sideband suppression”. In: *Journal of Lightwave Technology* 6.1 (1988), pp. 109–112. DOI: 10.1109/50.3974 (cit. on p. 51).

[165] D. M. S. Johnson, J. M. Hogan, S.-w. Chiow, and M. A. Kasevich. “Broadband optical serrodyne frequency shifting”. In: *Optics Letters* 35.5 (Feb. 2010), p. 745. DOI: 10.1364/ol.35.000745 (cit. on p. 51).

[166] M. Barbiero, J. P. Salvatierra, M. Risaro, C. Clivati, D. Calonico, F. Levi, and M. G. Tarallo. “Broadband serrodyne phase modulation for optical frequency standards and spectral purity transfer”. In: *Optics Letters* 48.7 (Mar. 2023), p. 1958. DOI: 10.1364/ol.485064 (cit. on pp. 51, 54, 55, 58).

[167] J. I. Thorpe, K. Numata, and J. Livas. “Laser frequency stabilization and control through offset sideband locking to optical cavities”. In: *Optics Express* 16.20 (Sept. 2008), p. 15980. DOI: 10.1364/oe.16.015980 (cit. on pp. 51, 53).

[168] R. Kohlhaas, T. Vanderbruggen, S. Bernon, A. Bertoldi, A. Landragin, and P. Bouyer. “Robust laser frequency stabilization by serrodyne modulation”. In: *Optics Letters* 37.6 (Mar. 2012), p. 1005. DOI: 10.1364/ol.37.001005 (cit. on p. 51).

[169] P. Barbieri, C. Clivati, M. Pizzocaro, F. Levi, and D. Calonicoha. “Spectral purity transfer with 5×10^{-17} instability at 1 s using a multibranch Er:fiber frequency comb”. In: *Metrologia* (June 2019). DOI: 10.1088/1681-7575/ab2b0f (cit. on p. 51).

[170] I. Goti. “High accuracy Yb optical lattice clock: frequency comparisons and contributions to International Atomic Time”. PhD thesis. Politecnico of Turin, 2023. URL: https://iris.polito.it/handle/11583/2983198 (cit. on pp. 51–53, 56, 80).

[171] F. Bregolin. “^{171}Yb optical frequency standardstowards the redefinition of thesecond”. PhD thesis. Politecnico di Torino, 2019 (cit. on pp. 52, 86, 87).

[172] S. Falke, M. Misera, U. Sterr, and C. Lisdat. “Delivering pulsed and phase stable light to atoms of an optical clock”. In: *Applied Physics B* 107.2 (Mar. 2012), pp. 301–311. DOI: 10.1007/s00340-012-4952-6 (cit. on p. 53).

[173] V. Formichella et al. “Year-long optical time scale with sub-nanosecond capabilities”. In: *Optica* 11.4 (Apr. 2024), p. 523. ISSN: 2334-2536. DOI: 10.1364/optica.509706 (cit. on p. 54).

[174] S. Barke, M. Tröbs, B. Sheard, G. Heinzel, and K. Danzmann. “EOM sideband phase characteristics for the spaceborne gravitational wave detector LISA”. In: *Applied Physics B* 98.1 (Aug. 2009), pp. 33–39. DOI: 10.1007/s00340-009-3682-x (cit. on p. 57).

[175] M. Barbiero, J. P. Salvatierra, D. Calonico, F. Levi, and M. G. Tarallo. “Composite Raman-Nath heterodyne interferometry with relevance for precise spectroscopy”. In: *Optics & Laser Technology* 181 (Feb. 2025), p. 111613. ISSN: 0030-3992. DOI: 10.1016/j.optlastec.2024.111613 (cit. on p. 58).

[176] URL: https://github.com/shiragolda/bristol_fiber_optic_switch (cit. on p. 58).

[177] BEC-Trento. *exp-control*. https://github.com/BEC-Trento/exp-control. 2018 (cit. on p. 59).

[178] S. Donadello. “Observation of the Kibble-Zurek mechanism in a bosonic gas”. PhD thesis. Università di Trento, 2016 (cit. on p. 59).

[179] C. Degenhardt, H. Stoehr, U. Sterr, F. Riehle, and C. Lisdat. “Wavelength-dependent ac Stark shift of theS01-P13transition at657nmin Ca”. In: *Physical Review A* 70.2 (Aug. 2004), p. 023414. ISSN: 1094-1622. DOI: 10.1103/physreva.70.023414 (cit. on p. 62).

[180] C. Degenhardt et al. “Calcium optical frequency standard with ultracold atoms: Approaching10-15relative uncertainty”. In: *Physical Review A* 72.6 (Dec. 2005), p. 062111. ISSN: 1094-1622. DOI: 10.1103/physreva.72.062111 (cit. on p. 62).

[181] P. Morzyński et al. “Intercontinental frequency ratio measurement of ^{171}Yb and ^{88}Sr optical lattice clocks”. In: *Metrologia* 61.4 (Aug. 2024), p. 045009. ISSN: 1681-7575. DOI: 10.1088/1681-7575/ad6a1e (cit. on p. 66).

[182] S. Origlia. “A high-performance bosonic optical lattice clock”. PhD thesis. Heinrich-Heine-Universität Düsseldorf, 2018 (cit. on p. 67).

[183] S. Tiengo, R. Eid, M. Apfel, G. Brulin, and T. Bourdel. "A simple magnetic field stabilization technique for atomic Bose–Einstein condensate experiments". In: *Review of Scientific Instruments* 96.6 (June 2025). ISSN: 1089-7623. DOI: 10.1063/5.0258855 (cit. on p. 67).

[184] T. Takano, R. Mizushima, and H. Katori. "Precise determination of the isotope shift of88Sr–87Sr optical lattice clock by sharing perturbations". In: *Applied Physics Express* 10.7 (June 2017), p. 072801. ISSN: 1882-0786. DOI: 10.7567/apex.10.072801 (cit. on pp. 82, 83, 124).

[185] M. Pizzocaro, F. Bregolin, P. Barbieri, B. Rauf, F. Levi, and D. Calonico. "Absolute frequency measurement of the $^1S_0 - {}^3P_0$ transition of ^{171}Yb with a link to international atomic time". In: *Metrologia* 57.3 (May 2020), p. 035007. DOI: 10.1088/1681-7575/ab50e8 (cit. on p. 82).

[186] S. B. Koller, J. Grotti, S. Vogt, A. Al-Masoudi, S. Dörscher, S. Häfner, U. Sterr, and C. Lisdat. "Transportable optical lattice clock with 7×10^{-17} uncertainty". en. In: *Phys. Rev. Lett.* 118.7 (Feb. 2017) (cit. on p. 82).

[187] R. Fasano, Y. Chen, W. McGrew, W. Brand, R. Fox, and A. Ludlow. "Characterization and Suppression of Background Light Shifts in an Optical Lattice Clock". In: *Physical Review Applied* 15.4 (Apr. 2021), p. 044016. ISSN: 2331-7019. DOI: 10.1103/physrevapplied.15.044016 (cit. on p. 82).

[188] Z.-P. Jia, X.-Y. Cui, Y.-J. Xie, X. Zhang, G.-Z. Niu, X.-Y. Liu, Q.-Q. Zhu, J. Li, and H.-N. Dai. "Suppressing background spectra of lattice lasers in strontium optical clocks". In: *Physical Review Applied* 23.1 (Jan. 2025), p. 014014. ISSN: 2331-7019. DOI: 10.1103/physrevapplied.23.014014 (cit. on p. 82).

[189] M. Takamoto et al. "Frequency ratios of Sr, Yb, and Hg based optical lattice clocks and their applications". In: *Comptes Rendus. Physique* 16.5 (Apr. 2015), pp. 489–498. ISSN: 1878-1535. DOI: 10.1016/j.crhy.2015.04.003 (cit. on p. 82).

[190] T. Bothwell, C. J. Kennedy, A. Aeppli, D. Kedar, J. M. Robinson, E. Oelker, A. Staron, and J. Ye. "Resolving the gravitational redshift across a millimetre-scale atomic sample". In: *Nature* 602.7897 (Feb. 2022), pp. 420–424. ISSN: 1476-4687. DOI: 10.1038/s41586-021-04349-7 (cit. on p. 82).

[191] J. Siegel, W. McGrew, Y. Hassan, C.-C. Chen, K. Beloy, T. Grogan, X. Zhang, and A. Ludlow. "Excited-Band Coherent Delocalization for Improved Optical Lattice Clock Performance". In: (Feb. 7, 2024). DOI: https://doi.org/10.1103/PhysRevLett.132.133201. arXiv: 2402.04968v1 `[physics.atom-ph]` (cit. on p. 83).

[192] B. X. R. Alves, Y. Foucault, G. Vallet, and J. Lodewyck. "Background Gas Collision Frequency Shift on Lattice-Trapped Strontium Atoms". In: *2019 Joint Conference of the IEEE International Frequency Control Symposium and European Frequency and Time Forum (EFTF/IFC)*. IEEE, Apr. 2019, pp. 1–2. DOI: 10.1109/fcs.2019.8856042 (cit. on p. 85).

[193] T. A. Savard, K. M. O'Hara, and J. E. Thomas. "Laser-noise-induced heating in far-off resonance optical traps". In: *Physical Review A* 56.2 (Aug. 1997), R1095–R1098. ISSN: 1094-1622. DOI: 10.1103/physreva.56.r1095 (cit. on p. 94).

[194] S. Friebel, C. D'Andrea, J. Walz, M. Weitz, and T. W. Hänsch. "CO2-laser optical lattice with cold rubidium atoms". In: *Physical Review A* 57.1 (Jan. 1998), R20–R23. DOI: 10.1103/physreva.57.r20 (cit. on p. 94).

[195] M. Bishof, Y. Lin, M. D. Swallows, A. V. Gorshkov, J. Ye, and A. M. Rey. "Resolved Atomic Interaction Sidebands in an Optical Clock Transition". In: *Physical Review Letters* 106.25 (June 2011), p. 250801. ISSN: 1079-7114. DOI: 10.1103/physrevlett.106.250801 (cit. on pp. 95, 107, 108).

[196] M. Glück. "Wannier–Stark resonances in optical and semiconductor superlattices". In: *Physics Reports* 366.3 (Aug. 2002), pp. 103–182. ISSN: 0370-1573. DOI: 10.1016/s0370-1573(02)00142-4 (cit. on p. 96).

[197] P. Lemonde and P. Wolf. "Optical lattice clock with atoms confined in a shallow trap". In: *Physical Review A* 72.3 (Sept. 2005). DOI: 10.1103/physreva.72.033409 (cit. on p. 96).

[198] M. Bishof, M. J. Martin, M. D. Swallows, C. Benko, Y. Lin, G. Quéméner, A. M. Rey, and J. Ye. "Inelastic collisions and density-dependent excitation suppression in a ^{87}Sr optical lattice clock". In: *Physical Review A* 84.5 (Nov. 2011). ISSN: 1094-1622. DOI: 10.1103/physreva.84.052716 (cit. on p. 106).

[199] S. Origlia et al. "Towards an optical clock for space: Compact, high-performance optical lattice clock based on bosonic atoms". In: *Physical Review A* 98.5 (Nov. 2018). DOI: 10.1103/physreva.98.053443 (cit. on pp. 107, 109, 124).

[200] D. M. Harber, H. J. Lewandowski, J. M. McGuirk, and E. A. Cornell. "Effect of cold collisions on spin coherence and resonance shifts in a magnetically trapped ultracold gas". In: *Physical Review A* 66.5 (Nov. 2002), p. 053616. ISSN: 1094-1622. DOI: 10.1103/physreva.66.053616 (cit. on pp. 112, 115).

[201] E. Braaten, H.-W. Hammer, and G. P. Lepage. "Lindblad equation for the inelastic loss of ultracold atoms". In: *Physical Review A* 95.1 (Jan. 2017), p. 012708. ISSN: 2469-9934. DOI: 10.1103/physreva.95.012708 (cit. on p. 121).

[202] T. Zelevinsky, M. M. Boyd, A. D. Ludlow, T. Ido, J. Ye, R. Ciuryło, P. Naidon, and P. S. Julienne. "Narrow Line Photoassociation in an Optical Lattice". In: *Physical Review Letters* 96.20 (May 2006). DOI: 10.1103/physrevlett.96.203201 (cit. on p. 124).

[203] A. Caprotti, M. Barbiero, M. G. Tarallo, M. G. Genoni, and G. Bertaina. "Analysis of spin-squeezing generation in cavity-coupled atomic ensembles with continuous measurements". In: *Quantum Science and Technology* 9.3 (May 2024), p. 035032. ISSN: 2058-9565. DOI: 10.1088/2058-9565/ad4584 (cit. on pp. 125, 127).

[204] S. Giaccari, G. Dellea, M. G. Genoni, and G. Bertaina. “Higher-Order Adiabatic Elimination in Atom-Cavity Systems and Its Impact on Spin-Squeezing Generation”. In: (June 2025). DOI: 10.48550/ARXIV.2506.22383. arXiv: `2506.22383 [quant-ph]` (cit. on p. 125).

[205] B. Braverman et al. “Near-Unitary Spin Squeezing in Yb171”. In: *Physical Review Letters* 122.22 (June 2019). DOI: 10.1103/physrevlett.122.223203 (cit. on p. 126).

[206] Y. A. Yang, M. Miklos, Y. M. Tso, S. Kraus, J. Hur, and J. Ye. “Clock Precision beyond the Standard Quantum Limit at 10 - 18 Level”. In: *Physical Review Letters* 135.19 (Nov. 2025). ISSN: 1079-7114. DOI: 10.1103/6v93-whwq (cit. on p. 126).

[207] E. Jaynes and F. Cummings. “Comparison of quantum and semiclassical radiation theories with application to the beam maser”. In: *Proceedings of the IEEE* 51.1 (1963), pp. 89–109. ISSN: 0018-9219. DOI: 10.1109/proc.1963.1664 (cit. on p. 126).

[208] H. J. Kimble. “Strong Interactions of Single Atoms and Photons in Cavity QED”. In: *Physica Scripta* T76.1 (1998), p. 127. ISSN: 0031-8949. DOI: 10.1238/physica.topical.076a00127 (cit. on p. 126).

[209] D. A. Steck. *Quantum and Atom Optics*. (revision 0.16.6,17 October 2025). URL: https://atomoptics.uoregon.edu/~dsteck/teaching/ (cit. on p. 126).

[210] H. Tanji-Suzuki, I. D. Leroux, M. H. Schleier-Smith, M. Cetina, A. T. Grier, J. Simon, and V. Vuletić. “Interaction between Atomic Ensembles and Optical Resonators”. In: *Advances in Atomic, Molecular, and Optical Physics*. Elsevier, 2011, pp. 201–237. DOI: 10.1016/b978-0-12-385508-4.00004-8 (cit. on pp. 126, 128).

[211] V. B. Braginsky and F. Y. Khalili. “Quantum nondemolition measurements: the route from toys to tools”. In: *Reviews of Modern Physics* 68.1 (Jan. 1996), pp. 1–11. ISSN: 1539-0756. DOI: 10.1103/revmodphys.68.1 (cit. on p. 127).

[212] A. Kuzmich, L. Mandel, and N. P. Bigelow. “Generation of Spin Squeezing via Continuous Quantum Nondemolition Measurement”. In: *Physical Review Letters* 85.8 (Aug. 2000), pp. 1594–1597. ISSN: 1079-7114. DOI: 10.1103/physrevlett.85.1594 (cit. on p. 127).

[213] M. H. Schleier-Smith, I. D. Leroux, and V. Vuletić. “Squeezing the collective spin of a dilute atomic ensemble by cavity feedback”. In: *Physical Review A* 81.2 (Feb. 2010), p. 021804. ISSN: 1094-1622. DOI: 10.1103/physreva.81.021804 (cit. on p. 127).

[214] D. J. Wineland, J. J. Bollinger, W. M. Itano, and D. J. Heinzen. “Squeezed atomic states and projection noise in spectroscopy”. In: *Physical Review A* 50.1 (July 1994), pp. 67–88. DOI: 10.1103/physreva.50.67 (cit. on p. 127).

[215] M. A. Norcia and J. K. Thompson. “Strong coupling on a forbidden transition in strontium and nondestructive atom counting”. In: *Physical Review A* 93.2 (Feb. 2016), p. 023804. ISSN: 2469-9934. DOI: 10.1103/physreva.93.023804 (cit. on p. 128).

[216] M. G. Tarallo. “Toward a quantum-enhanced strontium optical lattice clock at INRIM”. In: *EPJ Web of Conferences* 230 (2020). Ed. by E. Puppin, p. 00011. DOI: 10.1051/epjconf/202023000011 (cit. on pp. 128–130).

[217] S. L. Kristensen, E. Bohr, J. Robinson-Tait, T. Zelevinsky, J. W. Thomsen, and J. H. Müller. “Subnatural Linewidth Superradiant Lasing with Cold Sr88 Atoms”. In: *Physical Review Letters* 130.22 (May 2023), p. 223402. ISSN: 1079-7114. DOI: 10.1103/physrevlett.130.223402 (cit. on p. 130).

[218] M. A. Norcia, M. N. Winchester, J. R. K. Cline, and J. K. Thompson. “Superradiance on the millihertz linewidth strontium clock transition”. In: *Science Advances* 2.10 (Oct. 2016), e1601231. DOI: 10.1126/sciadv.1601231 (cit. on p. 130).

[219] O. Morsch and M. Oberthaler. “Dynamics of Bose-Einstein condensates in optical lattices”. In: *Reviews of Modern Physics* 78.1 (Feb. 2006), pp. 179–215. ISSN: 1539-0756. DOI: 10.1103/revmodphys.78.179 (cit. on p. 131).

[220] S. Bernon. “Trapping and nondemolition measurement of cold atoms in a high-finesse ring cavity”. PhD thesis. Ecole Polytechnique X, 2011 (cit. on p. 132).

[221] E. Perego. “A novel setup for trapping and cooling Barium ions for atom-ion experiments”. PhD thesis. Politecnico di Torino, 2019 (cit. on p. 132).

[222] E. Wang. “Cavity-enhanced measurement for the generation of spin squeezed states in strontium atom interferometry”. PhD thesis. Università degli Studi di Firenze, 2020 (cit. on p. 133).

[223] A. Öttl, S. Ritter, M. Köhl, and T. Esslinger. “Hybrid apparatus for Bose-Einstein condensation and cavity quantum electrodynamics: Single atom detection in quantum degenerate gases”. In: *Review of Scientific Instruments* 77.6 (June 2006). ISSN: 1089-7623. DOI: 10.1063/1.2216907 (cit. on pp. 133, 136).

[224] A. J. Kollár, A. T. Papageorge, K. Baumann, M. A. Armen, and B. L. Lev. “An adjustable-length cavity and Bose–Einstein condensate apparatus for multimode cavity QED”. In: *New Journal of Physics* 17.4 (Apr. 2015), p. 043012. ISSN: 1367-2630. DOI: 10.1088/1367-2630/17/4/043012 (cit. on p. 134).

[225] N. Bruno, L. C. Bianchet, V. Prakash, N. Li, N. Alves, and M. W. Mitchell. “Maltese cross coupling to individual cold atoms in free space”. In: *Optics Express* 27.21 (Oct. 2019), p. 31042. ISSN: 1094-4087. DOI: 10.1364/oe.27.031042 (cit. on p. 134).

[226] K. Roux, V. Helson, H. Konishi, and J. P. Brantut. “Cavity-assisted preparation and detection of a unitary Fermi gas”. In: *New Journal of Physics* 23.4 (Apr. 2021), p. 043029. ISSN: 1367-2630. DOI: 10.1088/1367-2630/abeb91 (cit. on p. 134).

[227] Y.-T. chen. “A Platfrom for Cavity Quantum Electrodynamics with Rydberg Atom Arrays”. PhD thesis. Harvard University Graduate School of Arts and Sciences, 2022 (cit. on p. 134).

[228] Y. Cai, D. G. Allman, J. Evans, P. Sabharwal, and K. C. Wright. “Monolithic bowtie cavity traps for ultracold gases”. In: *Journal of the Optical Society of America B* 37.12 (Nov. 2020), p. 3596. ISSN: 1520-8540. DOI: 10.1364/josab.401262 (cit. on p. 135).

[229] J. Lodewyck, M. Zawada, L. Lorini, M. Gurov, and P. Lemonde. “Observation and cancellation of a perturbing dc stark shift in strontium optical lattice clocks”. In: *IEEE Transactions on Ultrasonics, Ferroelectrics and Frequency Control* 59.3 (Mar. 2012), pp. 411–415. DOI: 10.1109/tuffc.2012.2209 (cit. on p. 136).

[230] J. A. Sherman, N. D. Lemke, N. Hinkley, M. Pizzocaro, R. W. Fox, A. D. Ludlow, and C. W. Oates. “High-Accuracy Measurement of Atomic Polarizability in an Optical Lattice Clock”. In: *Physical Review Letters* 108.15 (Apr. 2012), p. 153002. ISSN: 1079-7114. DOI: 10.1103/physrevlett.108.153002 (cit. on p. 136).

[231] K. Beloy et al. “Faraday-Shielded dc Stark-Shift-Free Optical Lattice Clock”. In: *Physical Review Letters* 120.18 (May 2018), p. 183201. ISSN: 1079-7114. DOI: 10.1103/physrevlett.120.183201 (cit. on p. 136).

Appendix A

Hybrid cavity-lattice technical drawings

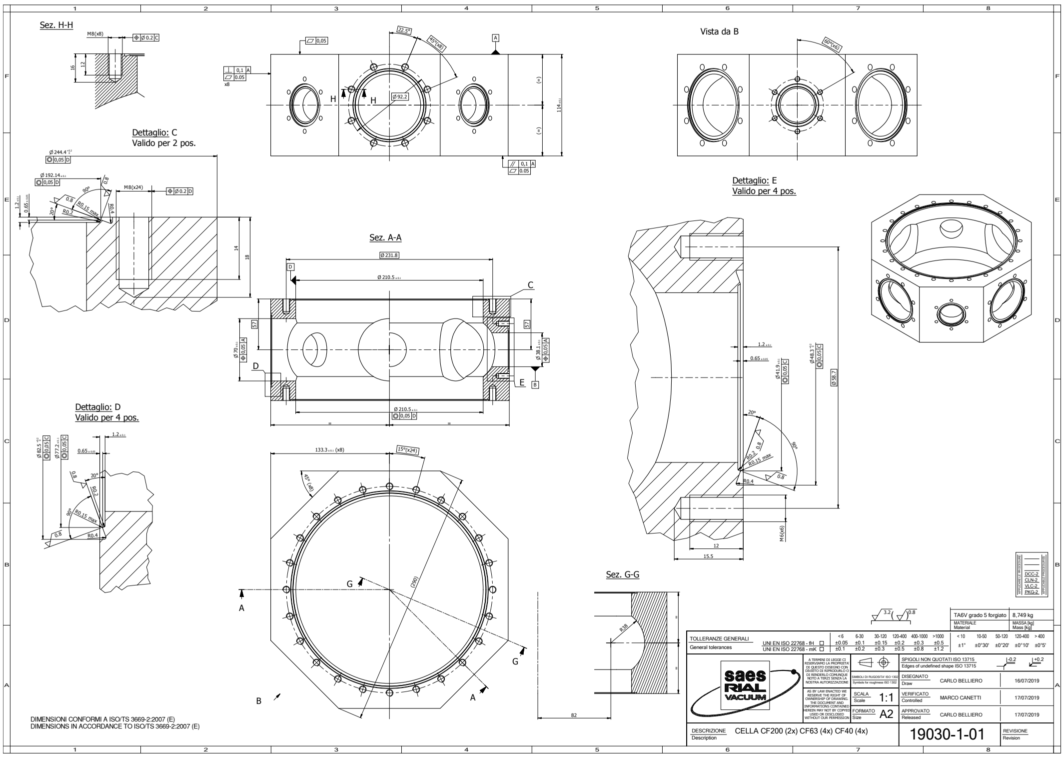

Fig. A.1 Technical drawing of the vacuum chamber.

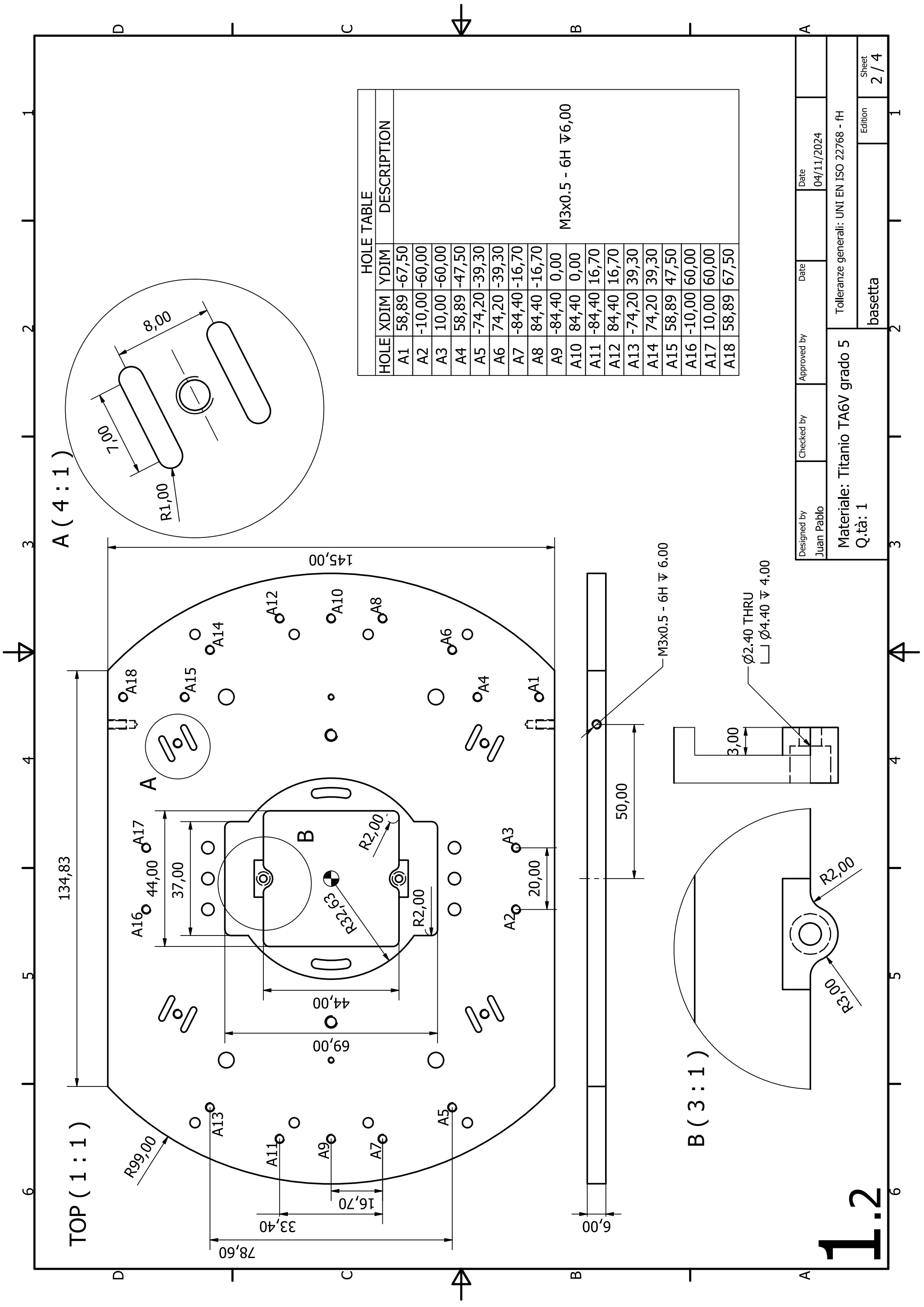

HOLE TABLE

HOLE	XDIM	YDIM	DESCRIPTION
A1	58,89	-67,50	M3x0.5 - 6H ↧6,00
A2	-10,00	-60,00	
A3	10,00	-60,00	
A4	58,89	-47,50	
A5	-74,20	-39,30	
A6	74,20	-39,30	
A7	-84,40	-16,70	
A8	84,40	-16,70	
A9	-84,40	0,00	
A10	84,40	0,00	
A11	-84,40	16,70	
A12	84,40	16,70	
A13	-74,20	39,30	
A14	74,20	39,30	
A15	58,89	47,50	
A16	-10,00	60,00	
A17	10,00	60,00	
A18	58,89	67,50	

Designed by Juan Pablo	Checked by	Approved by	Date	Date 04/11/2024	
Materiale: Titanio TA6V grado 5 Q.tà: 1			Tollerance generali: UNI EN ISO 22768 - fH basetta	Edition	Sheet 2 / 4

Fig. A.2 Technical drawing of the science platform.

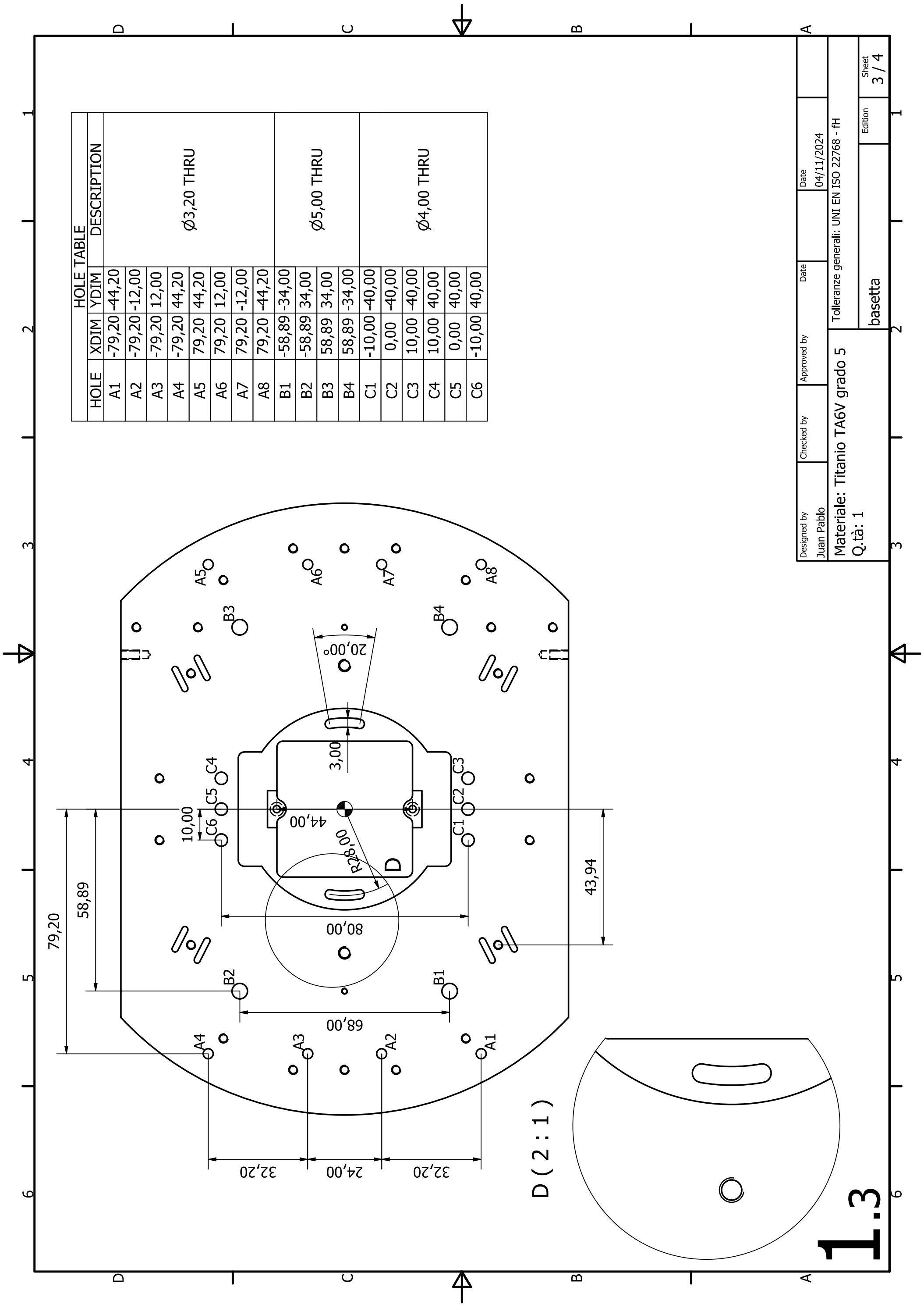

HOLE TABLE

HOLE	XDIM	YDIM	DESCRIPTION
A1	-79,20	-44,20	Ø3,20 THRU
A2	-79,20	-12,00	
A3	-79,20	12,00	
A4	-79,20	44,20	
A5	79,20	44,20	
A6	79,20	12,00	
A7	79,20	-12,00	
A8	79,20	-44,20	
B1	-58,89	-34,00	Ø5,00 THRU
B2	-58,89	34,00	
B3	58,89	34,00	
B4	58,89	-34,00	
C1	-10,00	-40,00	Ø4,00 THRU
C2	0,00	-40,00	
C3	10,00	-40,00	
C4	10,00	40,00	
C5	0,00	40,00	
C6	-10,00	40,00	

Fig. A.3 Technical drawing of the science platform.

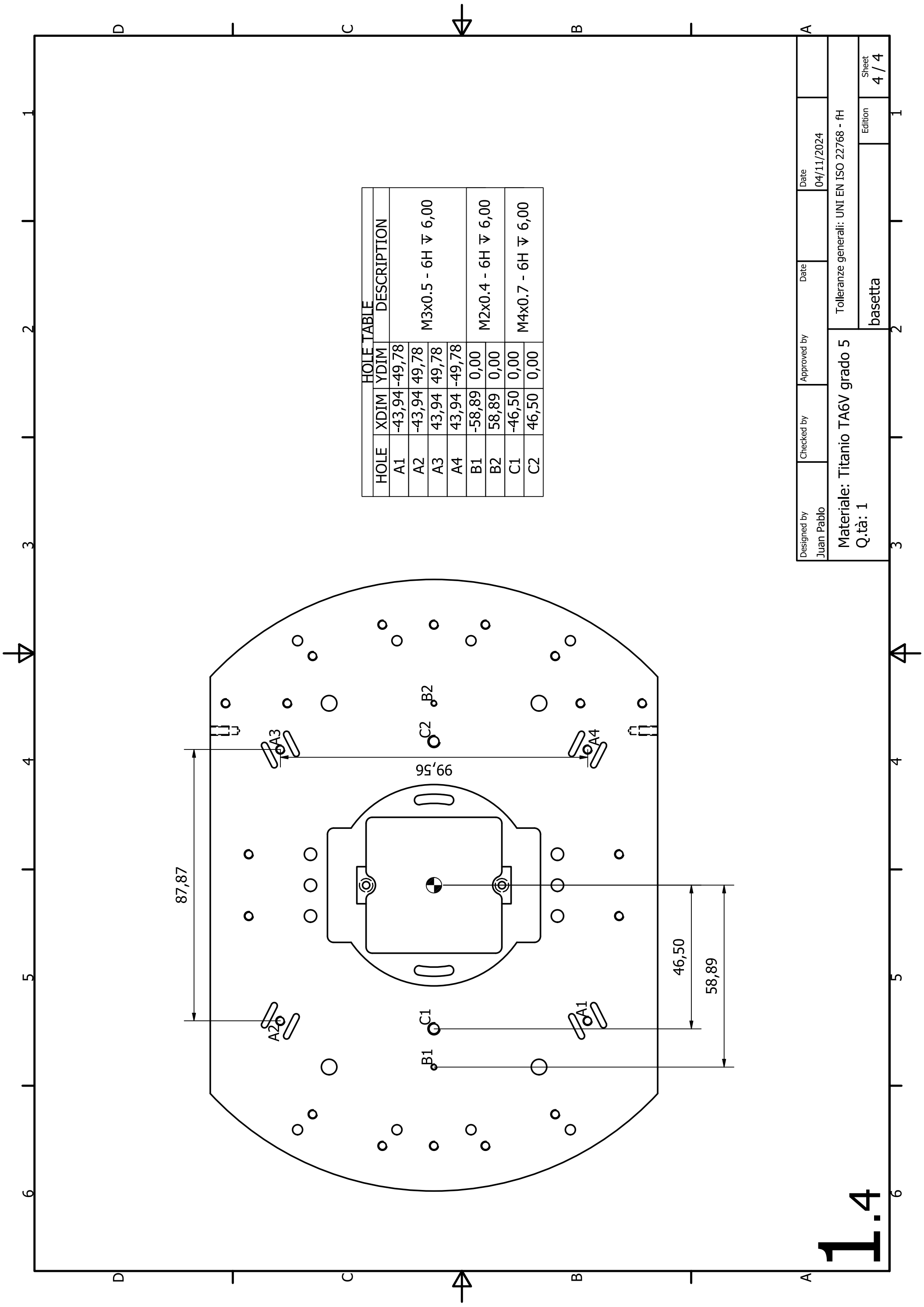

HOLE TABLE

HOLE	XDIM	YDIM	DESCRIPTION
A1	-43,94	-49,78	M3x0.5 - 6H ↧ 6,00
A2	-43,94	49,78	
A3	43,94	49,78	
A4	43,94	-49,78	
B1	-58,89	0,00	M2x0.4 - 6H ↧ 6,00
B2	58,89	0,00	
C1	-46,50	0,00	M4x0.7 - 6H ↧ 6,00
C2	46,50	0,00	

Designed by: Juan Pablo
Checked by:
Approved by:
Date:
Date: 04/11/2024
Materiale: Titanio TA6V grado 5
Q.tà: 1
Tolleranze generali: UNI EN ISO 22768 - fH
basetta
Edition: 1
Sheet: 4 / 4

Fig. A.4 Technical drawing of the science platform.

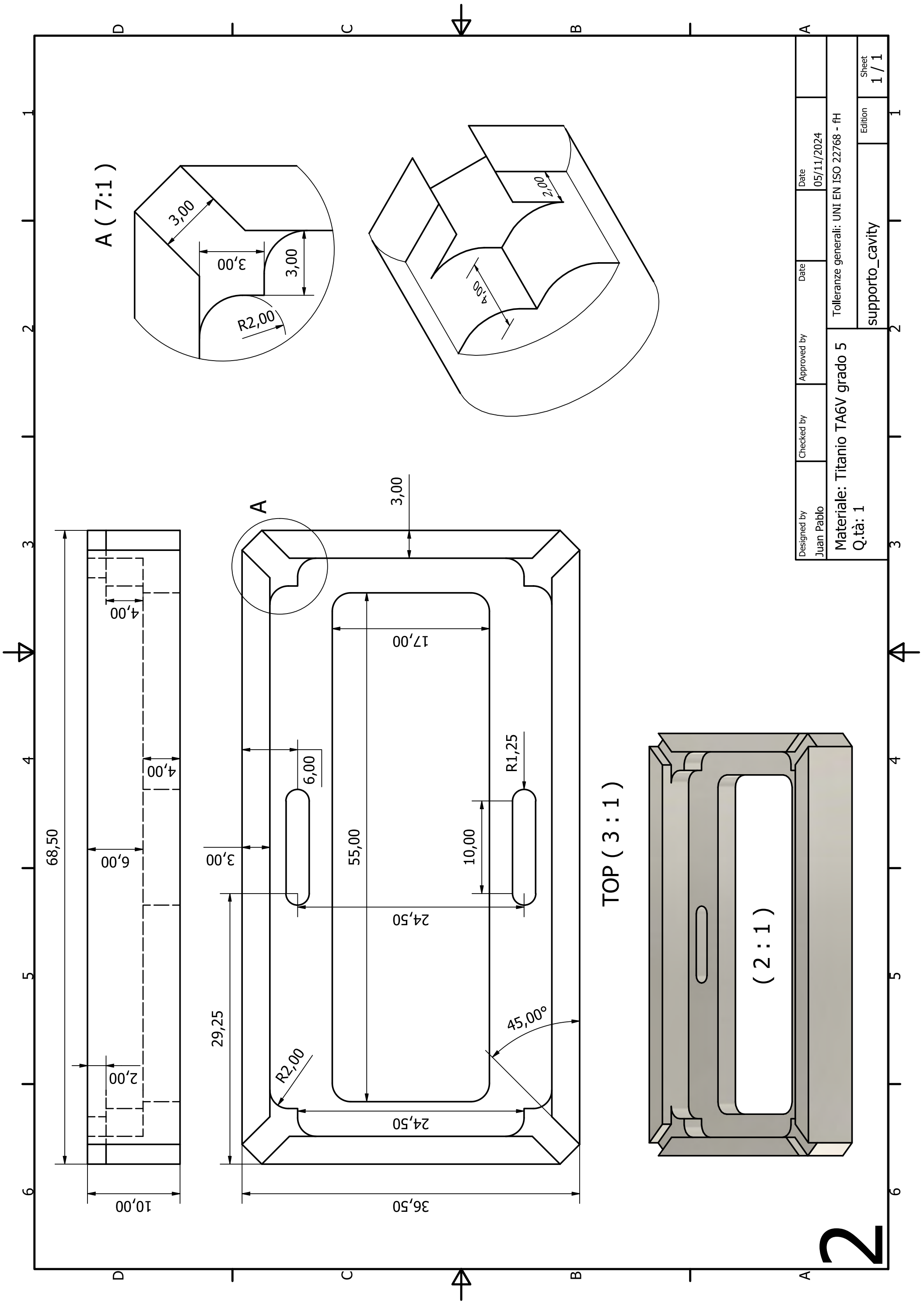

Fig. A.5 Technical drawing of the cQED cavity holder.

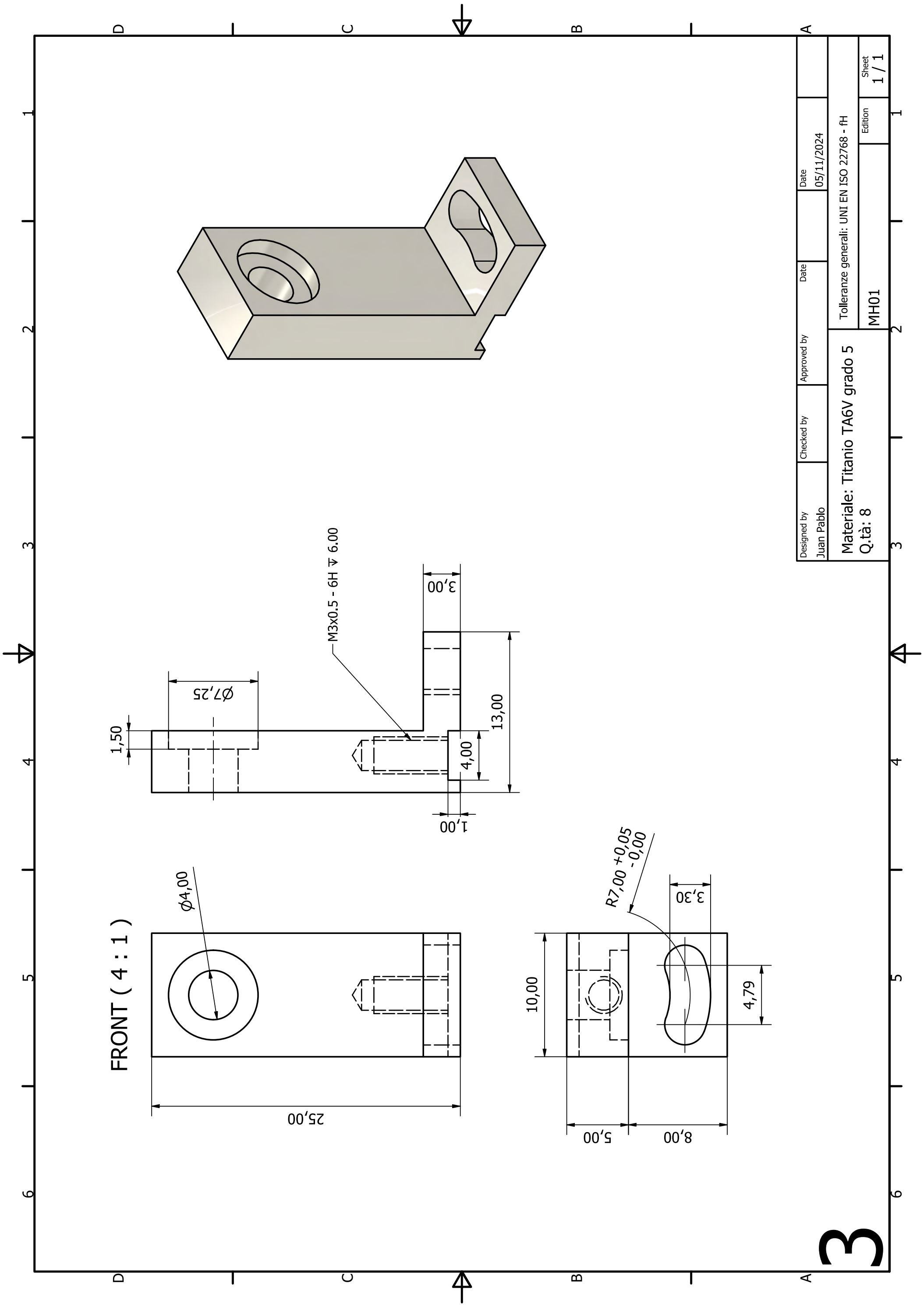

Fig. A.6 Technical drawing of the folding mirrors holder.

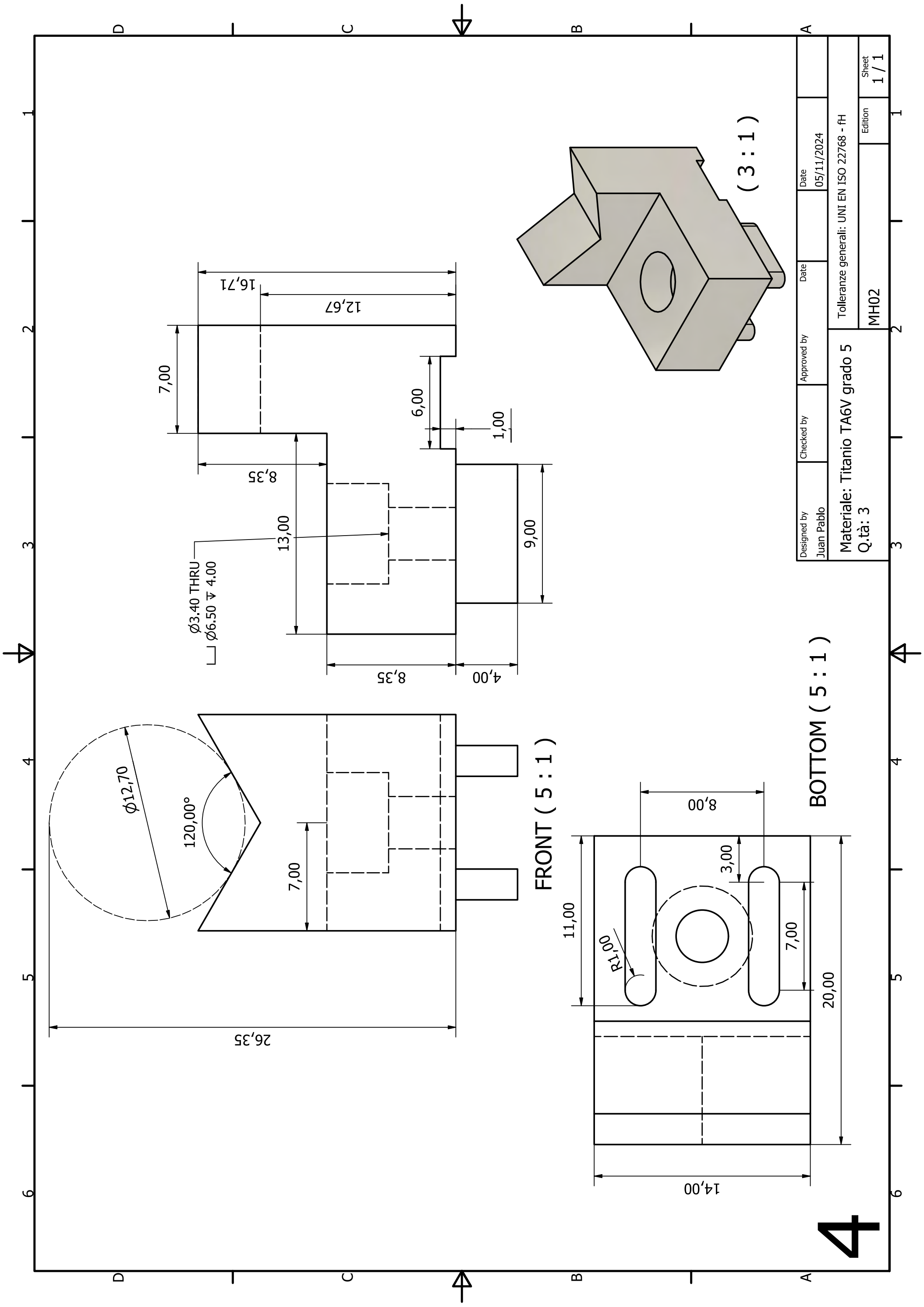

Fig. A.7 Technical drawing of the monolithic mirror holders for the bow-tie cavity.

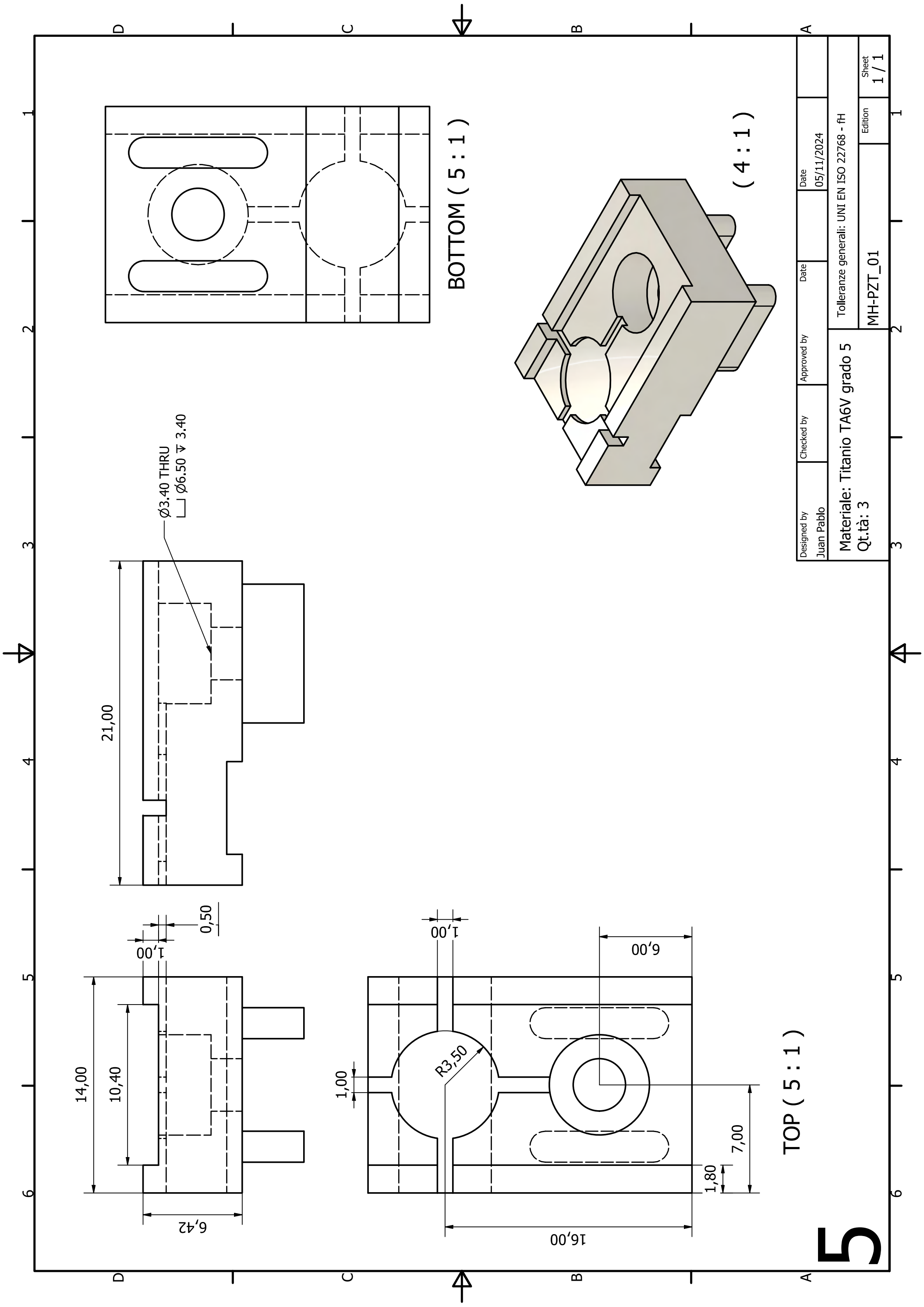

Fig. A.8 Technical drawing: bottom part of the composite mirror holder for the bow tie cavity.

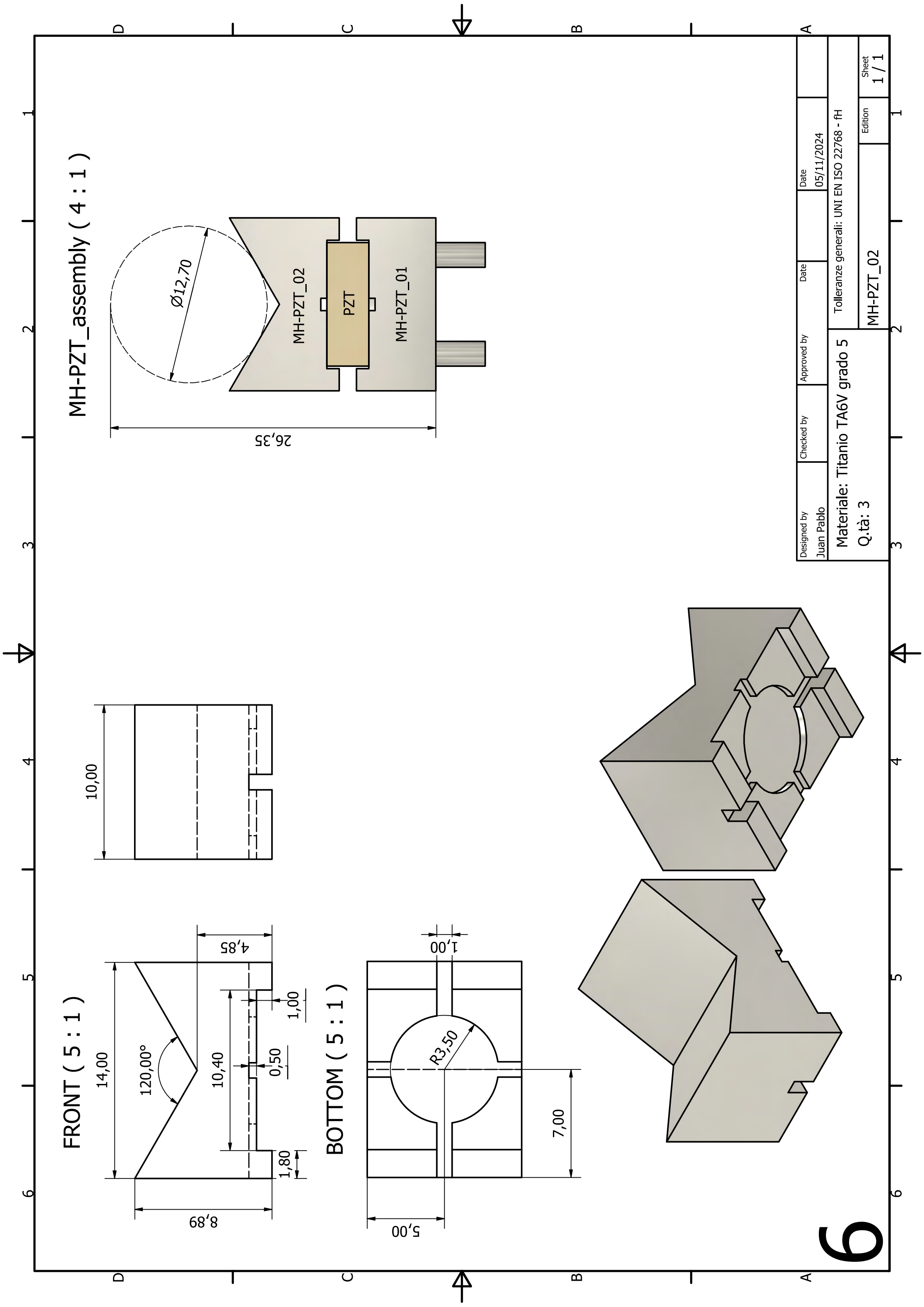

Fig. A.9 Technical drawing: top part of the composite mirror holder for the bow tie cavity.

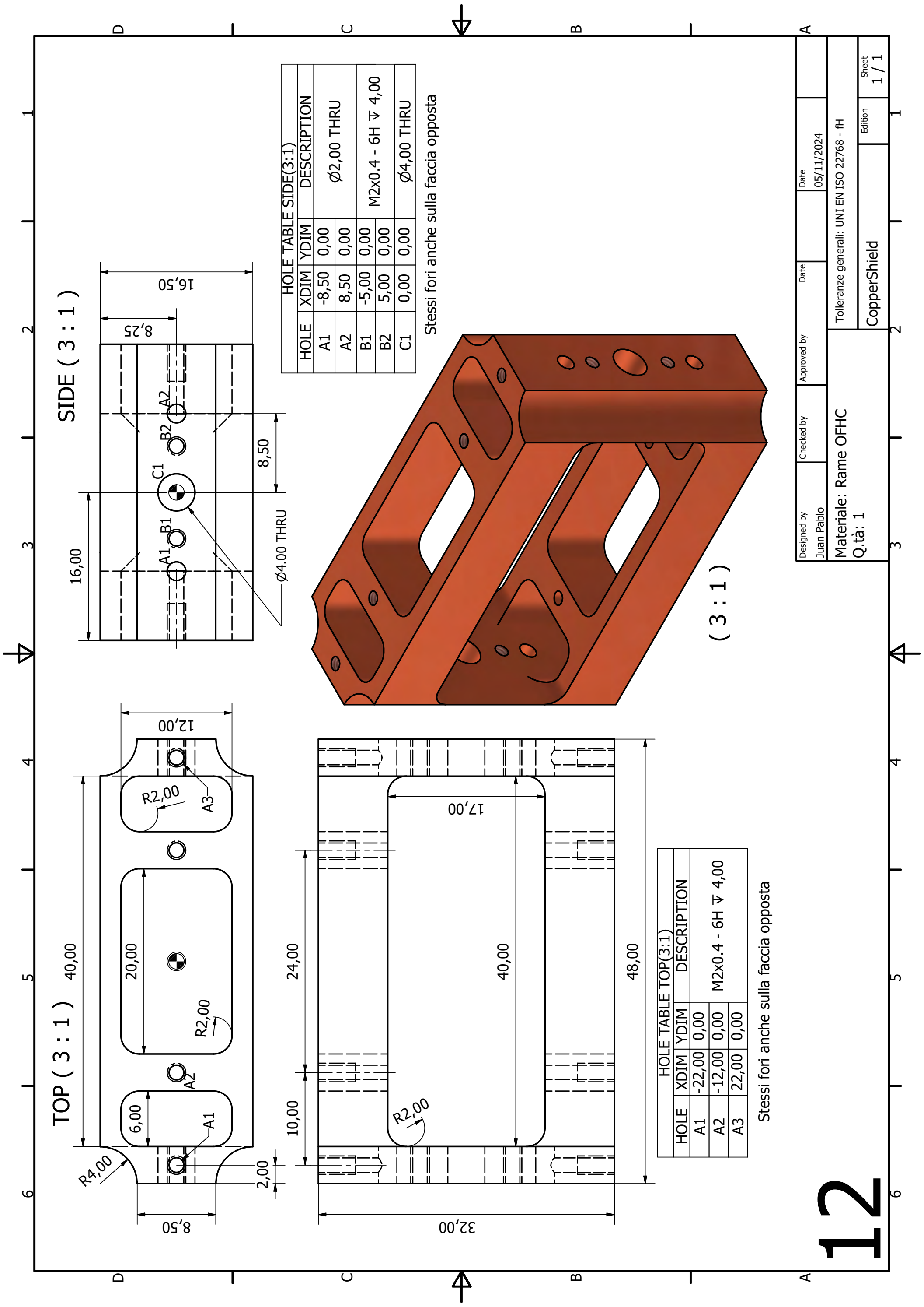

Fig. A.10 Technical drawing of the OFHC copper structure which will host electrodes and temperature sensors.

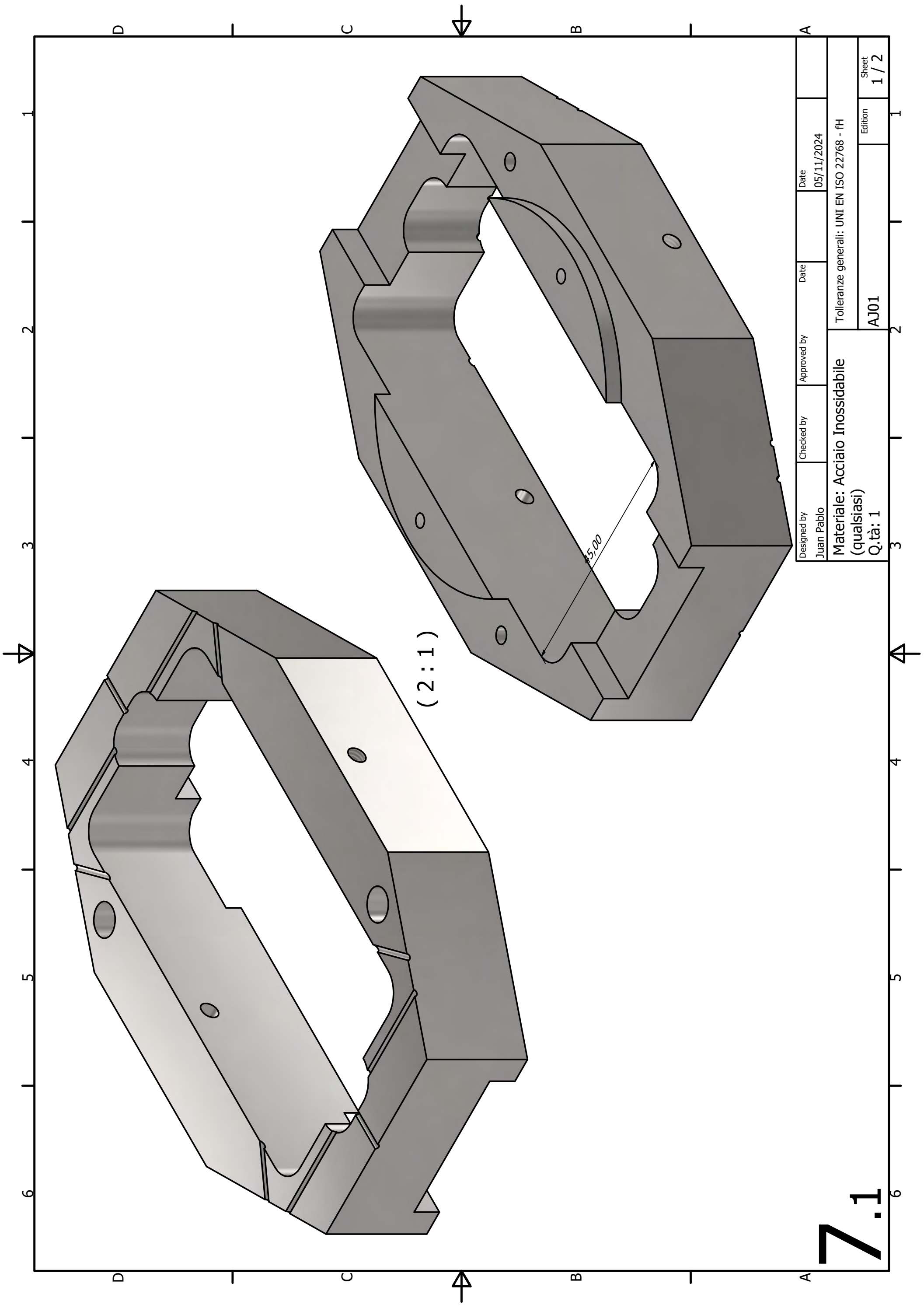

Fig. A.11 Technical drawing: part of the alignment tool.

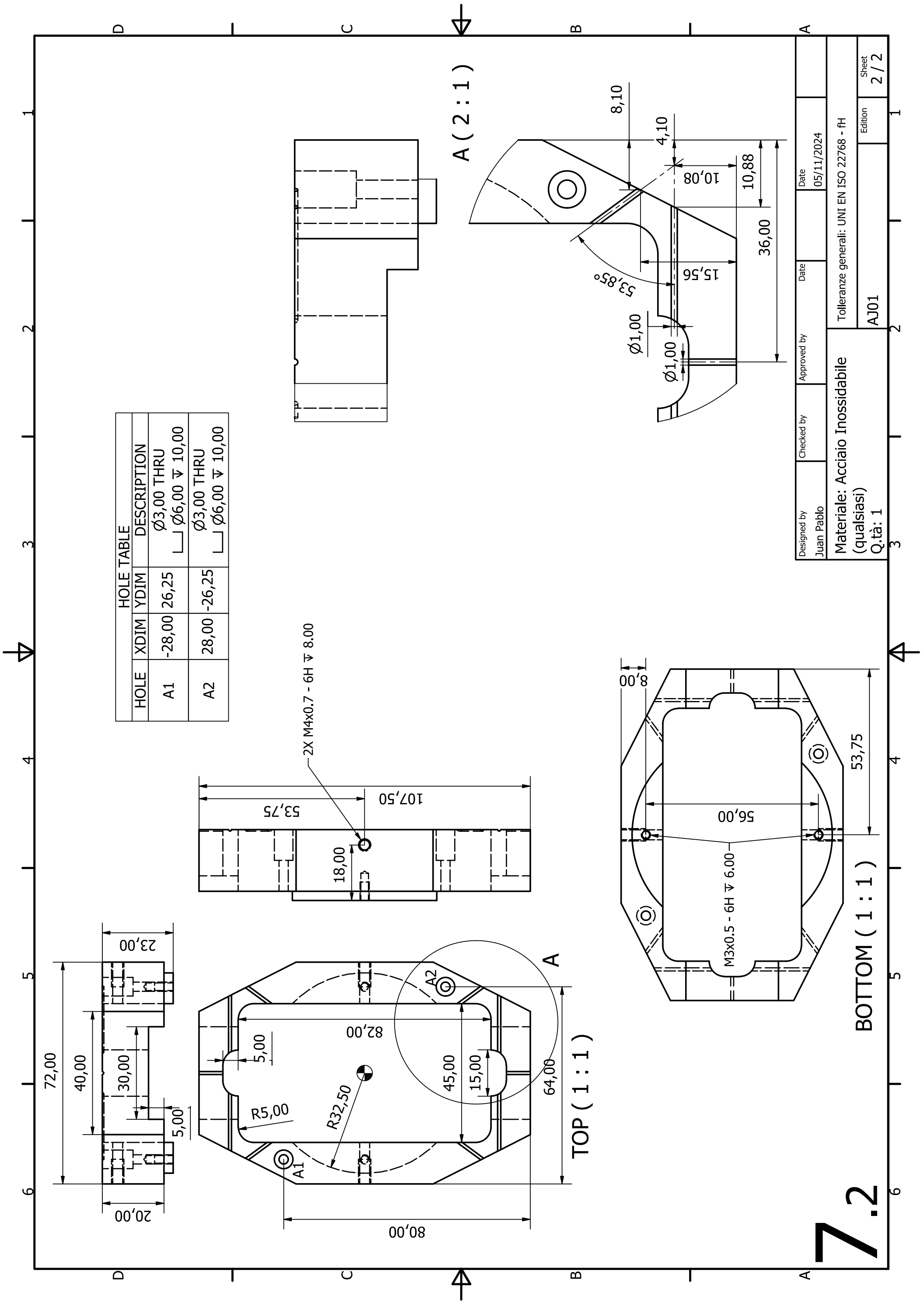

HOLE	XDIM	YDIM	DESCRIPTION
A1	-28,00	26,25	Ø3,00 THRU ⌴ Ø6,00 ↧ 10,00
A2	28,00	-26,25	Ø3,00 THRU ⌴ Ø6,00 ↧ 10,00

Fig. A.12 Technical drawing: part of the alignment tool.

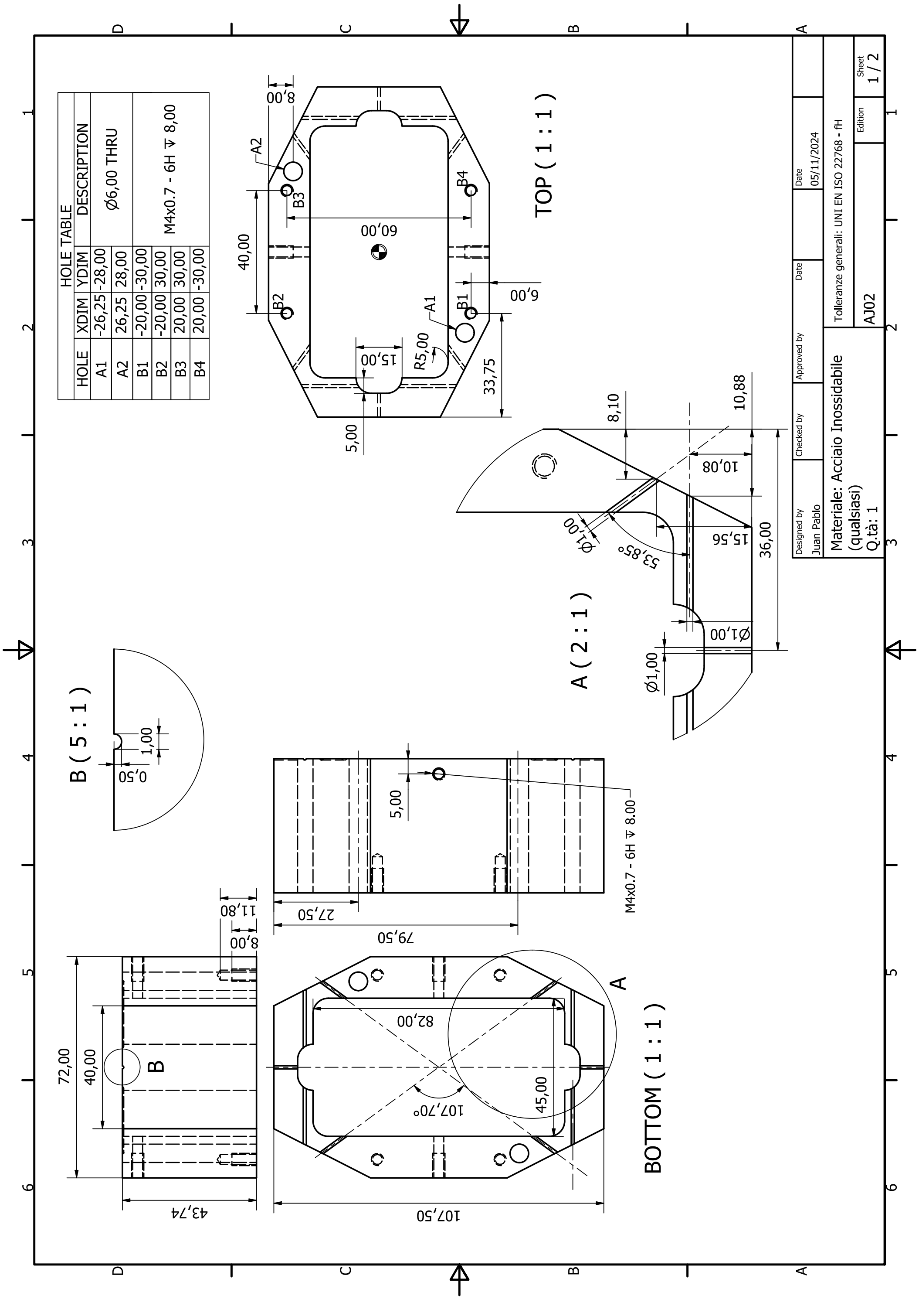

HOLE TABLE

HOLE	XDIM	YDIM	DESCRIPTION
A1	-26,25	-28,00	Ø6,00 THRU
A2	26,25	28,00	
B1	-20,00	-30,00	M4x0.7 - 6H ↧ 8,00
B2	-20,00	30,00	
B3	20,00	30,00	
B4	20,00	-30,00	

Designed by	Checked by	Approved by	Date	Date
Juan Pablo				05/11/2024

Materiale: Acciaio Inossidabile (qualsiasi)
Q.tà: 1

Tolleranze generali: UNI EN ISO 22768 - fH

AJ02

Edition

Sheet 1 / 2

Fig. A.13 Technical drawing: part of the alignment tool.

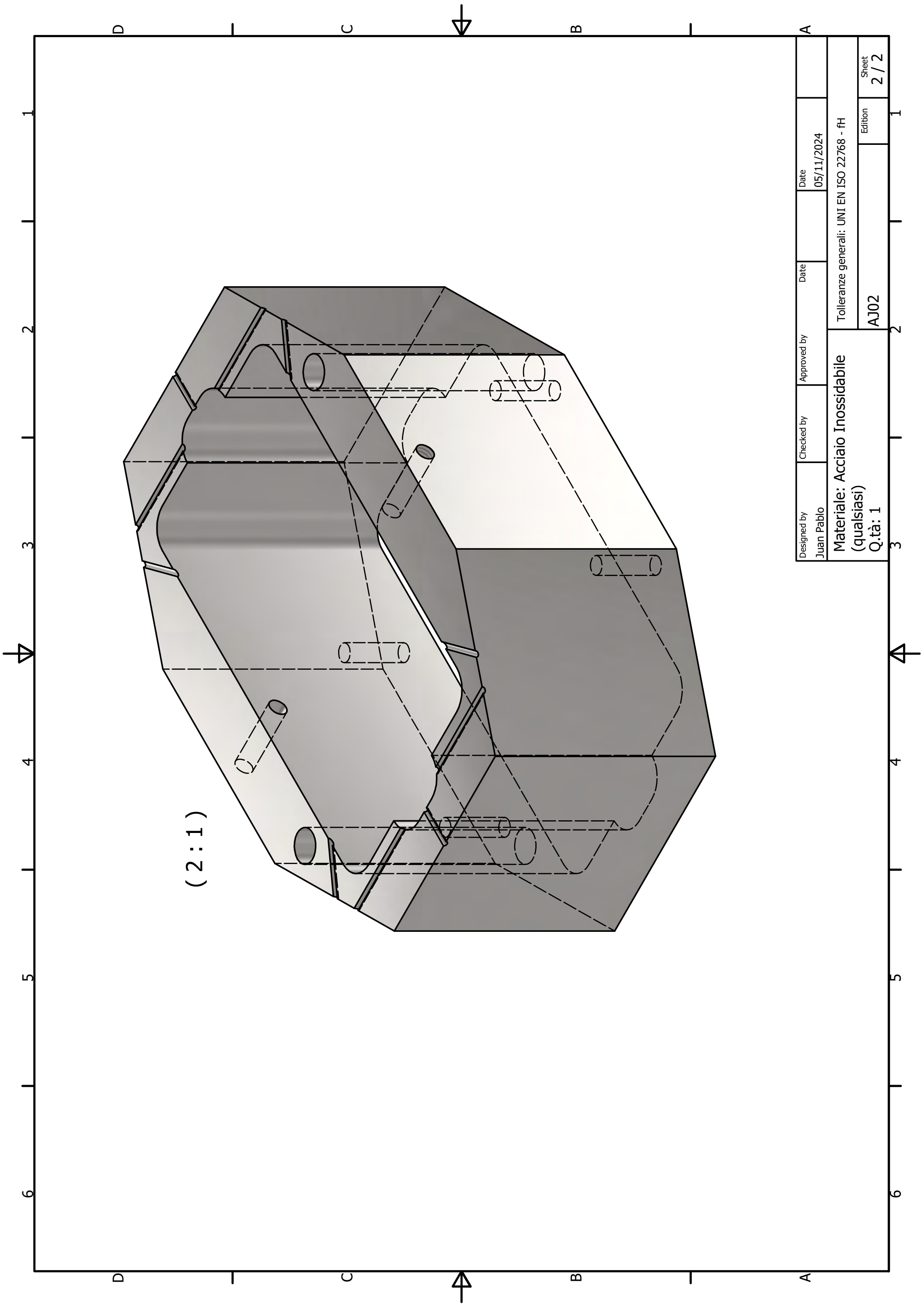

Fig. A.14 Technical drawing: part of the alignment tool.